MULTI-BAND AND DUAL-POLARISED ULTRA-WIDE BAND HORN ANTENNA FOR LANDMINE DETECTION USING GROUND PENETRATING RADAR TECHNIQUE

Amin Amiri

A thesis submitted for the degree of

Doctor of Philosophy

of

University College London

Department of Security and Crime Science

Department of Electronic and Electrical Engineering

2015

I, Amin Amiri, confirm that the work presented in this thesis is my own. Where information has been derived from other sources, I confirm that this has been indicated in the thesis.

Signature.....

Abstract

Anti-Personnel (AP) and Anti-Vehicle (AV) landmines are considered as a problem of global proportions and it is estimated that about 60-70 million landmines are scattered within at least 70 countries all over the world. Many of the landmines are made with minimum metal content so that certain detection methods, such as metal detectors, often tend to fail. A promising concept for the detection of buried non-metallic objects is Ground Penetrating Radar (GPR). Although GPR has shown some promising results, the diversity and complexity of the problem inflict certain challenges on the operation of GPR systems. The investigations discussed in this thesis cover important aspects of GPR with particular focus on design of a new Ultra-Wideband (UWB) antenna. A systematic approach is adopted to show the GPR modelling process, and understanding the fundamental principles of GPR technology. The resolution of GPR highlights the importance of operating bandwidth. RF characterisation of materials is another aspect of GPR that will be addressed by the measurement of the relative permittivity of the materials. A novel multifunctional, multi-channel antenna design is proposed to enable the investigation of multi-band imaging technique in GPR. The antenna is fabricated and the experimental measurements verify the performance of the designed antenna. The GPR results of 3D printed landmine models and real landmines in various environmental conditions have confirmed, the detection capability of the designed antenna. The GPR results of the landmines have also been investigated to study characteristic signatures of the landmines under certain system parameters.

To my dearest Mum, Dad, Sister and Maloos

Acknowledgment

Firstly, I would like to express my deepest gratitude to my supervisor, Dr Kenneth Tong. He has been incredibly supportive throughout the project and has always been there to offer guidance and push me towards my goals. I like to thank Prof. Hugh Griffiths for his valuable teachings and passion for radar. My appreciation goes to Dr Chin-Pang Liu, Prof. Ralph Benjamin, Prof. Paul Brennan and Dr Kevin Chetty for their assistance, insightful suggestions and counsel throughout the research. I would like to thank Mr George Matich and Dr Jeremy Langley from SELEX GALILEO, UK for their inputs and suggestions from an industrial perspective. Also, I would like to thank Dr Alessio Balleri for arranging a visit to Cranfield University, which allowed me to field test my antenna and GPR system in a different environment other than the lab. Last but not least I would like to thank my family and friends for all their support and unwavering encouragement in my studies.

Table of Contents

List of Figures

List of Tables

List of Symbols

ε_r	Relative permittivity
ε	Absolute permittivity
ε_0	Permittivity of free space
ε_r'	Real part of relative permittivity
$\varepsilon_r^{"}$	Imaginary part of relative permittivity
j	Imaginary unit
μ_r	Relative permeability
μ	Absolute permeability
μ_0	Permeability of free space
μ_r'	Real part of relative permeability
$\mu_r^{"}$	Imaginary part of relative permeability
σ	Conductivity
ω_0	Angular frequency
$\theta\ (t)$	Phase term
φ_0	Phase constant
λ	Wavelength
v_r	Relative propagation velocity
τ	Time interval
$tan\ \delta$	Loss tangent
BW	Bandwidth
G	Antenna Gain
A_{eff}	Antenna effective aperture
t	Time
ω_0	Frequency in radians per second
s	Signal
$a(t)$	Amplitude

$\theta\ (t)$	Phase term
P_r	Average peak power
$D\ (\theta_t\ \varphi_t)$	Directivity in spherical coordinates
L_t	Power loss from transmitter
L_{ch}	Channel loss
L_{rad}	Radiation loss
d	Distance
c	Speed of light
R_{res}	Range Resolution
f_{max}	Maximum frequency
f_{min}	Minimum frequency
L_{res}	Lateral Resolution
r	Distance from antenna
D	Antenna aperture
h	Antenna height from the ground
A	Antenna footprint
f	Frequency
δ	Skin depth
ρ	Resistivity
P_{out}	Output power
P_{in}	Input power
G_{ANT}	Antenna gain
G_{AUT}	AUT gain

List of Acronyms

AM	Additive Manufacturing
AP	Anti-Personnel
AV	Anti-Vehicle
AUT	Antenna Under Test
CNC	Computer Numerical Control
CW	Continuous Wave
CST	Computer Simulation Technology
CSP	Common Source Point
CRP	Common Receiver Point
CM	Common Midpoint
CO	Common Offset
CBRN	Chemical, Biological, Radiological, Nuclear
DMLS	Direct Metal Laser Sintering
EM	Electromagnetic
EoS	Earth observing System
ERT	Electrical Resistivity Tomography
EMI	Electromagnetic Induction
FIT	Finite Integration Technique
FDTD	Finite Difference Time Domain
FEM	Finite Element
FDM	Fused Deposition Modelling
FMCW	Frequency Modulated Continues Wave
FM	Frequency Modulation
GPR	Ground Penetrating Radar
IED	Improvised Explosive Devices
IDFT	Inverse Discrete Fourier Transform

IED	Improvised Explosive Device
MIMO	Multiple Input Multiple Output
MD	Metal Detector
MoM	Moments of Movements
NBS	Neutron Back Scattering
UN	United Nations
UHF	Ultra High Frequency
PCB	Printed Circuit Board
PRF	Pulse repetition frequency
RF	Radio Frequency
Rx	Receiver
RS	Remote Sensing
RCS	Radar Cross Section
RAM	Radar Absorbent Material
RBW	Resolution Bandwidth
RUAV	Rotary Unmanned Aerial Vehicle
RDX	Research Department Explosive
SPR	Surface Penetrating Radar
SAR	Synthetic Aperture Radar
SCR	Signal to Clutter Ratio
SNR	Signal to Noise Ratio
SCR	Signal to Clutter Ratio
SNR	Signal to Noise Ratio
SFCW	Step Frequency Continues Wave
SLA	Stereolithographic
SLS	Selective Laser Sintering
TEM	Transverse Electromagnetic
TNT	Trinitrotoluene

3D	Three-Dimensional
2D	Two-Dimensional
Tx	Transmitter
UXO	Unexploded Ordnances
UWB	Ultra-Wideband
UXO	Unexploded Ordnances
VSWR	Voltage Standing Wave Ratio
VNA	Vector Network Analyser

Chapter 1

Introduction

1.1 Overview and Motivation

Wars should end when fighting stops, yet landmines and explosive remnants kill or maim and continue to cause tragic and unintended consequences long after conflicts have ended. Every day around ten people, across 70 countries face threats of losing their life or limb *(ICBL, 2015)*. Landmines cannot distinguish between civilians and soldiers; families, communities, as well as lands and the countries' development, can be affected for decades. Although the majority of countries worldwide have renounced landmines and have joined the Mine Ban Treaty, signed in 1997 (Ottawa Treaty), 35 countries remain non-signatories, reserving the right to use landmines at any time *(GICHD, 2006)*. According to Landmine Monitor and the United Nations, there were around 250 million landmines stockpiled in the arsenals of 108 countries in 1998; over the years, this number has reduced substantially owning to the obligations set by the Mine Ban Treaty.

Due to the confusion of warfare, the exact number of landmines is unknown. However, it is estimated that more than 70 million landmines are still buried under the ground; for example, there are 10 million landmines remaining from various conflicts in Afghanistan since 1978. There are 10 million landmines in Angola, 8-10 million in Cambodia and 2 millions in Iraq. 3 million landmines lie under the ground in Mozambique, 1 million in Somalia, and 1-2 million in Sudan. In Africa alone there are 18 - 30 million landmines. In Europe, the Second World War ordnance and landmines still haunt people, with 3 million landmines in Yugoslavia, 0.2 million in Bosnia, 1 million in Croatia and 0.5-1 million in Serbia *(VVAF, 2007)*. Figure 1.1 illustrates the worldwide distribution of landmine-contaminated countries in 2015.

The estimated landmine-related casualties are reported to be approximately 26,000 people per year. Common injuries include blindness, burns, shrapnel wounds and those involving limbs. The other inadvertent victims of landmines are animals; it is reported that the Afghans suffered a total loss of more than 75,000 animals due to landmines, more than 50% of the livestock. In addition to humans and animals, landmines result in large areas of fertile farmland and waterways to be inaccessible; for example in Cambodia, between 20 and 40% of villages and rice fields have been

mined and abandoned. This is a serious problem considering that most landmine-affected areas are still in poverty *(Boutwell and T.Klare, 1999)*.

Arms dealers sell most landmines on the black market, and it is almost impossible to implement a worldwide monitoring scheme. The cost of producing a single landmine is estimated to be around £1, and yet the cost of removing a landmine is estimated to be up to £750 *(BBC, 1999)*.

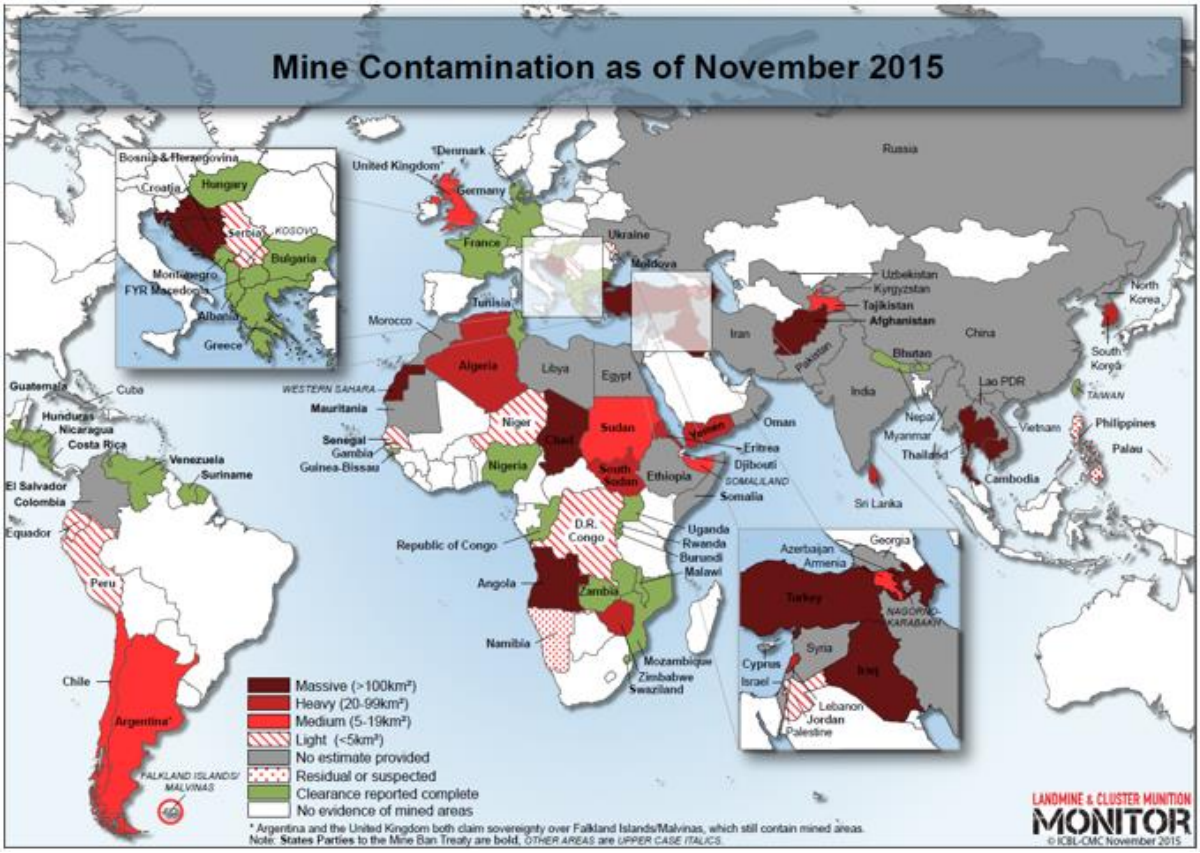

Figure 1-1: World map is indicating landmine contamination per country. Source: ICBL (2015)

Though the use of landmine is currently limited, there are still a number companies and government agencies from countries that remain outside the treaty, producing and exporting 350 types of landmines. China, Russia, the United States, India, and Pakistan hold the biggest stockpiles of landmines. The recent conflicts in Libya (under Gaddafi) and Syria have seen a staggering amount of landmines still being used.

In recent years, the case for a landmine free world has become stronger. The first step in clearing landmines is to identify minefields and detect landmines. Detection and removal of landmines are at present a serious political, economic, environmental and humanitarian challenge. There are

various ongoing efforts within several engineering fields to develop new or improve existing technologies. Each technology has its advantages and disadvantages due to the nature of landmines, the environmental conditions, operational needs and requirements, cost and level of accuracy. It is imperative to study and understand landmines when selecting the best-suited technologies for the correct application.

1.2 History of Landmines

The history of landmines is closely tied to the history of military conflicts that can be dated back to 2,500 years ago. Ancient Chinese and Romans first used traps such as spikes and stakes that were buried or scattered on the ground. The first modern mechanically fused high explosive landmines are said to have been used in the American Civil War in the 1800s. Further improved landmines were created and widely used in World War II. They have since been used in many conflicts, including the Vietnam War, the Korean War, and the first Gulf War; during the Cold War, many states laid long stretches of landmines along their borders *(Croll, 1998)*. By the 20th century landmines and explosives devices became weapons of choice for many armed forces and extremist groups.

1.3 Landmine Types

Explosive devices fall into three categories: Land or sea mines, Unexploded Ordnances (UXO) and Improvised Explosive Devices (IED). All three use high explosive to project blast and often fragmentation from the point of detonation. Landmines are containers of explosive material with detonating mechanisms that are triggered by contact with a person or vehicle. They are designed to incapacitate human targets or damage the vehicles by an explosive blast, fragments or in the case of some antivehicle landmines, a jet of hot metal. When explosive weapons such as bombs, shells, and grenades fail to function as designed, they are often left as Unexploded Ordnances (UXO).

There are numerous identified types of landmines; they are classified into two main categories: **Anti-Personnel Mines (AP) and Anti-Vehicle Mines (AV)**. They differ in their size, shape and buried depth. However, their structures and triggering mechanisms are quite similar. A typical landmine includes a detonator, a booster charge, a main charge and a casing (which can be made of metallic or non-metallic materials). Figure 1.2 shows typical components found in most types of landmine.

AP landmines are commonly divided into three types. Blast landmines are triggered by 5-16 kg newtons of force, designed to destroy a person's foot or leg. Directional fragmentation and bounding where explosion is directed into the air, causing injury to the chest and head. Fragmentation landmines release metal or glass fragments when exploded and can cause injury up to 200 metres away. These landmines are illustrated in Fig. 1.3. Landmines can be buried or surface laid depending on their geometries and targets; they can be scattered randomly or placed strategically in regular or irregular distributions. There is different operational weight (e.g. triggering mechanism) for each type of landmines, therefore, the buried depth may vary according to its intended application.

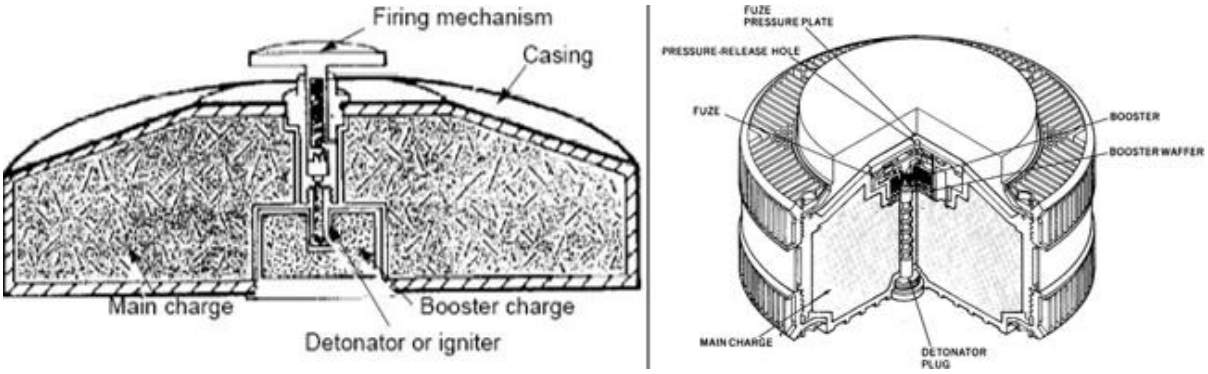

Figure 1-2: Typical Landmine Components. Source: TheCeIotajs (2013)

A landmine can be triggered by pressure, movement, sound, magnetism and vibration; these have to be taken into account when designing suitable detection systems. Some AP landmines have long spikes that stick out of the ground when laid to catch a person's foot as a means of the trigger. Tripwires are also used to reduce the activation force applied by the victim by less than couple of kilogrammes. Landmines are designed to be concealed and tend to use as little metal as possible, making detection by metal detectors very difficult; most AP landmines have plastic casings which make them invisible to metal detectors and have the added advantage of being very inexpensive.

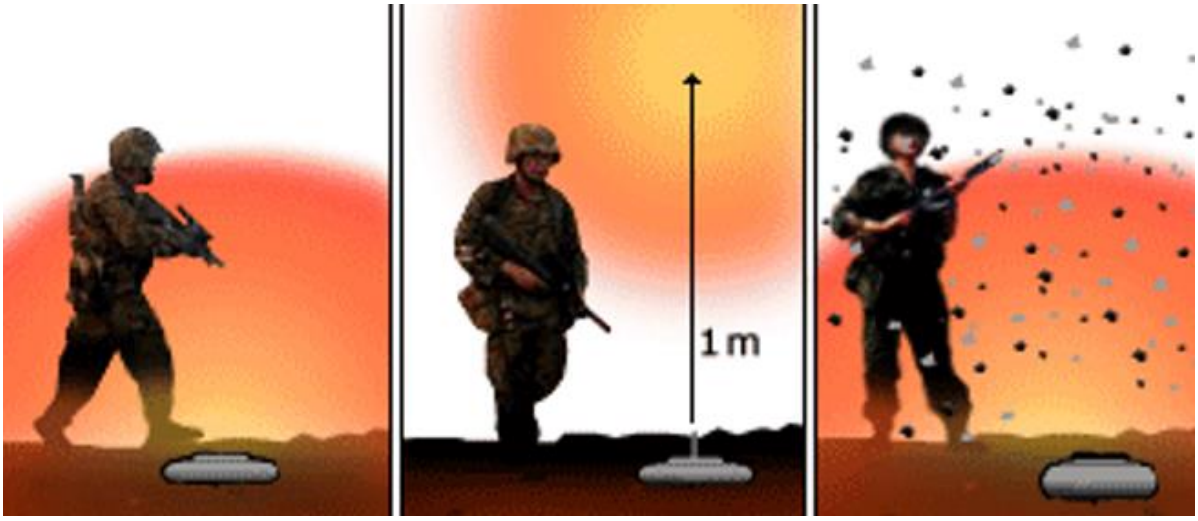

Figure 1-3: Types of Landmine, Blast (Left), Bounding (Middle), and Fragmentation (Right). Source: DFI (2014)

Anti-personnel landmines are the commonest type of landmine and the most difficult to detect because of their small size and often plastic casing. The main difficulty in designing a reliable landmine detection system, therefore, is the consideration of the huge variety of landmines in use. Figure 1.4 - 7 and Tables 1.1 - 4 show some examples of those frequently encountered AP landmines deployed worldwide. They are mostly designed in a rectangular, circular, butterfly or cylindrical shape with variable sizes, as small as 6 cm in length and 2 cm in height.

Figure 1-4: Common Blast AP Mines – Source: cat–uxo (2016)

Name:	**PFM-1**	**PMN-2**	**Type 58**	**VS-50**	**NR-409**
Country:	Russia	Russia	China	Italy	Belgium
Diameter:	12 mm	121 mm	112 mm	90 mm	82 mm
Weight:	75 g	450 g	550 g	117 g	183 mm
Explosive:	37 g	115 g	240 g	44 g	80 g

Table 1-1: Common Blast AP Landmines. Source: cat – uxo (2016)

Figure 1-5: Common Bounding AP Landmines. Source: cat–uxo (2016)

Name:	**V-69**	**Type 69**	**PSM-1**	**PROM-1**	**PP Mi-Sr**
Country:	Italy	China	Bulgaria	Yugoslavia	Czech Rep
Diameter:	130 mm	60 mm	76 mm	75 mm	101 mm
Weight:	3.2kg	1.35 kg	2.7 kg	2.7 kg	3.2 kg
Explosive:	420g	110g	170 g	425 g	360 g

Table 1-2: Common Bounding AP Landmines. Source: cat – uxo (2016)

Figure 1-6: Directional Fragmentation AP Landmines. Source: cat–uxo (2016)

Name:	**MON-50**	**M18A1**	**Hamdy**	**MON-100**	**MON-200**
Country:	Russia	USA	Egypt	Russia	Russia
Diameter:	226 mm	216 mm	218 mm	236 mm	434 mm
Weight:	2 kg	1.6 kg	1.3 kg	5 kg	25 kg
Explosive:	700 g	680 g	471 g	2 kg	12 kg

Table 1-3: Directional Fragmentation AP Landmines. Source: cat–uxo (2016)

Figure 1-7: Fragmentation AP Landmines. Source: cat–uxo (2016)

Name:	**Type-58**	**Type-59**	**POMZ-2**	**P-40**	**NR 413**
Country:	China	China	Russia	Vietnam	Belgium
Diameter:	60 mm	60 mm	60 mm	69 mm	46 mm
Weight:	2.3 kg	1.5 kg	2.3 kg	617 g	640 g
Explosive:	75 g	75 g	75 g	120 g	95 g

Table 1-4: Fragmentation AP Landmines

Most AP landmines are normally designed to injure or maim rather than kill the victims as this will increase the logistical and medical cost of the adversary. They are, therefore, equipped with sharp ribs (e.g. VS-50), fragments (e.g. V-69), long spikes, pellets (e.g. MON-50) and small metal shreds.

Landmines are typically designed in a symmetrical shape and contain curves, and right-angled corners, however, there are a few irregularly shaped landmines. An example of the latter is Soviet PFM-1 pressure activated blast landmine, also known as a butterfly landmine, widely used in Afghanistan. The shape and flexibility of landmines unfortunately, attract children who think PFM-1 is a toy to play with and cause devastating consequences as a result.

Most of the landmines shown in the figures 1.5 – 1.7 are pressure activated and contain plastic casing; wood and glass casings have also been reported. As the casing material decays, the triggering mechanism may shift, and the device often sets itself off or becomes dysfunctional. The high explosive main charge of landmines vary from powdered form such as TNT, RDX, and Composite C to solid plastic form such as Semtex. They can also be in the form of liquid such as Nitroglycerin and Nitromethane.

The second category of landmines is Anti-Vehicle landmines (also known as big killers). AV landmines are larger and more powerful than AP landmines. They contain more metal and explosive charge and are thus easier to be detected. They typically come in squares with round corners or truncated cylinders. The largest dimension of the AV landmines ranges from 15 to 30 cm and a thickness of 5 to 9 cm. The explosive material of AV landmines is typically TNT, Composite B, or RDX. They contain sufficient explosive to destroy a vehicle (e.g. tank) as well as people in or around the vehicle. Also, AV landmines require more weight to operate (e.g. 100 kg) and are found mostly on or at the side of the road surface. Figures 1.8 - 9 show two of the commonest types of AV landmines.

Figure 1-8: Common Blast AV Landmines. Source: cat–uxo (2016)

Name:	**TC-6**	**TM-62M**	**Barmine**	**M19**	**PRB M3**
Country:	Italy	Russia	Britain	USA	Belgium
Diameter:	270 mm	320mm	1.2 m	332 mm	230 mm
Weight:	9.6 kg	10 kg	10.3 kg	12.56 kg	6.8 kg
Explosive:	6 kg	7.5 kg	8.1 kg	9.53 kg	6 kg

Table 1-5: Common Blast AV Landmines

Figure 1-9: Common Shaped Charged AV Landmines. Source: cat–uxo (2016)

Name:	**TMK-2**	**TMRP-6**	**UKA-63**	**TM-72**	**Type 84**
Country:	Russia	Yugoslavia	Hungary	Russia	China
Diameter:	307 mm	290 mm	298 mm	250 mm	114 mm
Weight:	12.5 kg	7.2 kg	9 kg	6 kg	3.125 kg
Explosive:	6 kg	5.1 kg	6 kg	2.5 kg	780 g

Table 1-6: Common Shaped Charged AV Landmines

1.4 Minefields

Landmines may be positioned by several means: they can be buried or surface laid. The preferred, but most labour intensive method is to bury the landmines manually. However, they can also be scattered on the surface by specialised mine-laying vehicles such as helicopters, mine scattering shells or cruise missiles. Thus, landmines may be found in regular patterns or irregular distributions. Minefields can contain both AV and AP landmines to prevent the use of armoured vehicles for rapid AP landmines removal. It is reported that some minefields are specifically booby-trapped to make their clearance more dangerous.

Figure 1-10: Example of Minefields. Source: GICHD & MercoPress (2016)

Mixed AP and AV landmines are found to be either stacked (of the same type) or laid on top of each other (AP over AV) *(Frost, 2006)*. When weather causes soil or coastal erosion, landmines may be moved to new locations. They can be covered by mud or be exposed. Landmines can be encountered in various environmental conditions such as deserts, mountains, jungles, and urban areas. They can also be found lying or buried in debris, burnt-out buildings and metal enclosures which can influence the performance of landmine detectors. Figure 1.10 shows some examples of minefields.

The minefield's soil condition also introduces a challenge; they can be different geographically, either dry or wet and be mixed with other substances. In addition to landmines being found in random land assortments (not necessarily flat), they can be found in a rusty and corroded state. A few examples of AV and AP landmines in various minefields are shown in Figure 1.11.

Figure 1-11: Buried and Surface Laid Landmines. Sources: DRH Norway (2013), Keenan (2008), Hazeltine *& Bull (2013)*

1.5 Technologies for Landmine Detection and Detection Standard

Landmine detection has been an important research subject since the 1990s, and a large amount of effort have been invested worldwide with the aim of improving the detection performance. However, only a few of these technologies have progressed from research to field ready operational systems. The complexity of the environment, minefield conditions and numerous types of landmines place challenges on detection systems. There is an increasing demand to find safer and more practical ways to detect and clear landmines. Apart from the need for improving humanitarian management, there is also need to develop and deploy better equipment *(GICHD, 2006).*

Detection and clearance of landmines fall under two types of demining categories: humanitarian demining and military demining. During a military demining process, the objective is to breach a minefield as fast as possible. The operation involves identifying possible minefield and breaching through this using rollers, ploughs, diggers, rakes and explosive charges to trigger landmiens. In this process, full detection and clearance of landmines are not of concern *(E.M.A and Waller, 2000).* Humanitarian demining, on the other hand, is more difficult and dangerous as it requires 99.6% detection rate (set by the UN) and complete removal of all landmines in the field. In order to re-establish the use of land and restore public confidence, no landmines should be left behind in the area being cleared.

Over the past decades, there has been significant interest in finding suitable technological options. These include acoustic sensors combined with laser technology, improved metal detectors, nuclear

quadrupole resonance detection, X-rays, biological agents (that change colour in the presence of explosives), the controversial use of animals and insects (e.g. rats & dogs), and recently more attention is being paid to using Electromagnetic (EM) wave including Ground Penetrating Radar (GPR). Most of the options above, however, have been proven to be inefficient in providing clearance rates demanded by the local governments and humanitarian communities *(GICHD, 2006).* A landmine detection system should be able to detect landmines regardless of the type of explosive charge, shape or type of casings used. It should further be able to distinguish between landmines and background clutter such as rocks and metal shred using signal processing or imaging techniques. It is also clear that such a system has to function in a wide range of physical environments, climates, operating temperatures and transportation methods. In the following section, various techniques for the detection of landmines are discussed, according to information gathered from the guidebook on detection technologies and systems for humanitarian demining *(GICHD, 2014).*

1.5.1 Manual Method

One of the widely used approaches for locating mines is still hand prodding which involves using prodders (rigid sticks of metal) about 25 cm long. The demining personnel scan and probe the ground at a shallow angle of typically 30 degrees and when encountered with an unusual object, visual inspection is used to determine whether the object is a landmine. Although this method can be highly effective, the process is slow and dangerous. Accidental detonation due to the displacement of landmines is highly likely, and deminers cannot search the ground deep enough to locate all landmines reliably. Figure 1.12 shows deminers using prodders in the minefield.

Figure 1-12: Deminers, searching the ground. Source: GICHD (2014)

1.5.2 Electromagnetic Induction

Electromagnetic induction (EMI) is the principle behind all metal detectors. A metal detector contains a receiver and transmitter coil and operates by emitting into the ground a time-varying magnetic field to induce eddy current in metallic objects nearby. The eddy current generates a detectable secondary magnetic field that can be picked up by the receiver coil. This technology has reached a mature stage and has been around since World War I. Metal detectors can detect extremely small quantities of metal under various soil and can provide relatively fast scans. However, one of the most obvious and serious limitations of such detectors is their restriction in detecting metal only. They are very sensitive to metal fragments, as small as a few millimetres in length. Minefields are often littered with a large number of such metal fragments and other metallic debris. Metal detectors, therefore, have a high rate of false alarms as well as incapability to detect plastic landmines. Figure 1.13 shows a typical metal detector and how it is deployed in a minefield.

Figure 1-13: Metal detector. Source: gettyimages (2016)

1.5.3 X-Rays Backscatter Method

This method involves passing photons through an object and detecting the small amount of reflected radiation which is in proportion to the density and effective atomic number of the material. By scanning beams of X-rays, a 2D or 3D subsurface image can be obtained. However, this technique is limited by poor penetration depth of X-rays through the soil and extremely low amount of backscattered energy. Moreover, the system is complex, bulky and hazardous due to the use of ionising radiation *(Niemann et al., 2002)*.

1.5.4 Neutron and Nuclear Techniques

Neutron Back Scattering (NBS) technique is a well-established method to find hydrogen, nitrogen or carbon in objects. It can be applied in landmine detection by taking advantage of the fact that

explosive material in landmines is abundant in hydrogen. Although a few systems have been proven to be successful, their main drawbacks are the long processing time, limitations due to fundamental physics, and operational limitations such as size, weight and operating power *(Megahid, 1999).*

1.5.5 Biological Methods

Traces of explosive charge and landmines could be detected passively. This eliminates the effect of any other type of backscatter signal from soil, shrapnel, and other fragments in active systems. Trained dogs can sniff out explosives odours with incredible accuracy. The dogs undertake an intense 3-5 month training course where they learn to detect explosive odours commonly found in landmines *(Marshall Legacy, 2005).* Similar performance can be seen in rats using detection by scent, and the training usually takes around nine months; other species used for this purpose includes insects such as bees. According to a research centre in Croatia, Bees have an adequate sense of smell that can quickly detect the scent of explosives *(Rodacy, Bender et al., 2002).* Another example of a living system that responds to explosives materials is the microbial mine detection. A common soil microorganism has been genetically engineered to recognise explosives such as TNT; they are sprayed over fields and upon encounter with explosives they produce a detectable fluorescent protein *(Fischer, Burlage, and Maston, 2000).* Once the fluorescent protein is produced, the bacteria becomes detectable using common fluorescence detection techniques. This technique is still under development. However, the research presents unique opportunities for developing new capabilities through the direct use of trained bio-systems, integration of living and non-living components, or inspiring new design by mimicking biological capabilities. It is expected that controlled bio-systems, biotechnology, and microbial techniques will contribute to the advancement of landmine detection and other application domains.

The major argument against using animals for detection of landmines is the unethical nature of training animals for involvement in warfare. It is unethical because the animals are placed in dangerous situations by force. The counterargument is that some of the animals are already fighting for their survivals in the landmine contaminated areas where they live. They are constantly finding new ways to find and avoid landmines. Figure 1.14 illustrates the use of dogs, rats, and bees in the process of detecting landmines and the genetically modified bacteria that glow upon contact with explosives in landmines.

Figure 1-14: Living examples of landmine detection methods. Dogs (a), Rats (b), Modified bacteria (c), Bees (d). Source: Marshall Legacy (2005), Rodacy, Bender et al. (2002), Fischer et al. (2000)

1.5.6 Acoustic and Ultrasound Techniques

Sound waves have the ability to penetrate earth materials at shallow depths. Most of the energy is reflected back into the air but a small percentage, however, couples into the ground causing vibrations of buried landmines and ground motions. These vibrations can be detected remotely by microwave, ultrasonic and laser doppler vibrometers. Figure 1.5 shows the concept of using a truck mounted system to direct a narrow beam of the acoustic wave and a laser vibrometer as a seismic detector. As illustrated in this figure, acoustic sound waves penetrate the soil surface to generate seismic waves within the soil; waves cause the mine to vibrate and resonate, producing a displacement velocity field at the ground surface above the landmine. This displacement can be measured by a laser vibrometer or UHF radar *(Haupt and Rolt, 2005)*. This technique is still at early stages of development. Although work has been conducted to understand the technique better, there is much to be done for a practical and operational method.

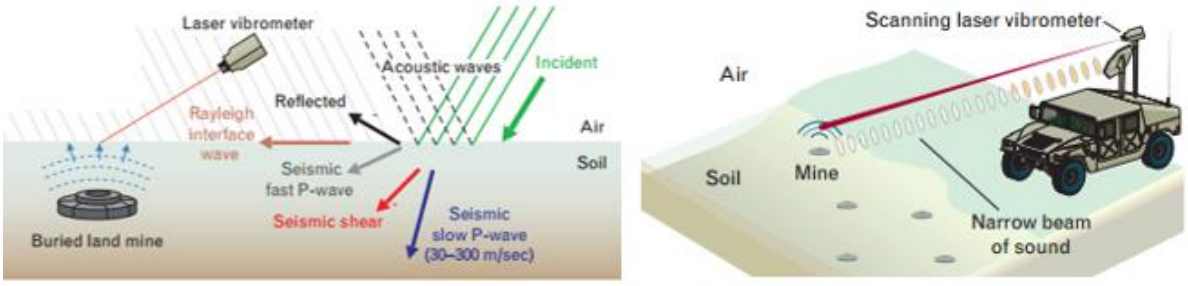

Figure 1-15: Acoustic to Seismic wave coupling (a) and a concept of an operational system (b) – Source: Haupt and Rolt (2005)

1.5.7 Thermal Techniques

The basic principle behind thermal detection of landmines is the change or difference in heat conduction causing a temperature difference on the surface of the soil where the landmines are buried. The contrast in the temperature difference is outlined in surrounding areas when the surface is naturally (e.g. sun) or artificially (local heating) heated and or cooled (dynamic thermography). Thermal detection systems have advantages of being sensitive to bulk materials and employing safe and simple stimulation *(Balsi 2003)*. Figure 1.16 (left) shows the thermal detection by local heating (e.g. lamp, microwave heaters) where the temperature is detected by a thermometer (e.g. infrared sensor). Figure 1.16 (right) shows thermal detection by using passive sources such as sunlight.

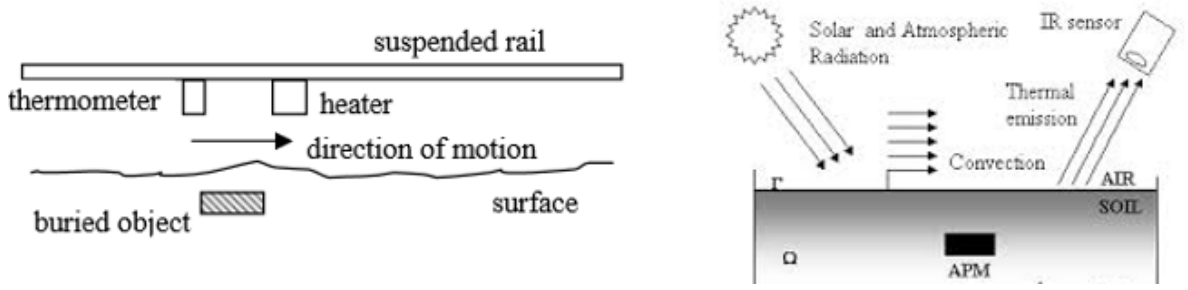

Figure 1-16: Thermal detection concept by an active source (right) and passive source (left). Source: Balsi (2003)

The main drawback of such systems is the time required (e.g., the heating and cooling process) for reliable results. Moreover, temperature contrast tends to be low and noisy, particularly in areas of vegetation. The penetration depth of these systems is limited to about 10 cm *(KA and JP 2000)*.

1.5.8 Ground Penetrating Radar

Ground Penetrating Radar (GPR) is an electromagnetic technique that is applied to various applications from archaeology and geology to engineering, for the detection of buried objects and

soil study. Radar has the potential to penetrate earth materials and detect metal or non-metal buried landmines. This technique is utilised by emitting an electromagnetic wave into the ground rather than into the air as in many radar applications. Buried objects cause reflections of the emitted wave which are then detected by the receiver system. GPR can produce a fuzzy depth image of subsurface by scanning the area of interest. The contrast in electrical properties of the buried objects and the background is the main basis for this detection technique. This technique is well established for a number of applications and has shown promising results. An intensive amount of on-going research has applied GPR techniques in the detection of landmines and explosive materials. This technique is the main focus of the work presented in this thesis.

GPR has an ability to sense the electrical inhomogeneity of metal and non-metal content in the presence of a less conducting surrounding soil. However, other dielectric objects such as rocks, roots, surface roughness and earth material density are considered as clutter and can result in scattering signatures comparable to that of a landmine. The conditions of earth materials and their properties can affect the obtained weak reflections from the case of dielectric landmines. It has already been shown that the received signal is often very weak, which implies that the reflection caused by the buried landmine is very small *(Daniels, 2004)*. Moreover, strong reflections from the air-earth material can often mask the weak returns from shallowly buried landmines. This thesis will illustrate that the bandwidth of the radar system can significantly affect the imaging resolution and thus the ability to detect buried objects. There is a significant potential for GPR techniques. This thesis will address the main parts involved in the study of GPR and will show the recent achievements of electromagnetic modelling to allow the study of various GPR parameters such as antennas, bandwidth, operating frequency, properties of earth materials, signal processing and hardware systems. It will then focus on an antenna design used to acquire experimental GPR data to detect and image target models based on realistic AP and AV landmines.

1.6 Thesis Layout

The broad objective of the research addressed in this thesis is to study and understand the GPR systems in regards to their electromagnetic behaviour to develop new techniques and designs in the field of antennas. This thesis is organised according to the main objectives, and every chapter can be understood as a representation of one aspect of the overall research work. The thesis is presented in nine chapters, and its outline is as follows:

Chapter 2 reviews the fundamental principles of radar in the context of GPR, which is needed for the description of the propagation of waves. Chapter 3 examines the EM properties of ground and target materials which are of great importance to study and model the effects of the propagating medium on the signal delay time, amplitude, and signal shape. These effects must be properly incorporated when dealing with target images, detection, and localisation. Some lossy ground materials and multiple types of targets are used in the modelling of EM behaviour. Chapter 4 is concerned with the dielectric properties of materials. Experimental measurements are presented to identify the electrical properties of a few materials.

Chapter 5 covers the proposed antenna design and the basic principles in the design of antennas for GPR. Chapter 6 discusses the fabrication process concerned with the antenna design and presents the results of experimental measurements of the antenna for verification.

Chapter 7 presents the laboratory and field GPR measurements that are based on the proposed antenna design.

Chapter 8 explains the ethical issues concerning the GPR technologies. If the GPR is to be deployed in demining actions, these ethical considerations have to be taken into account to ensure safe operation. Finally, Chapter 9 gives a conclusion that is drawn from the research presented in this thesis and discusses improvements and future work.

1.7 Novel Aspects

1. Design and fabrication of a new type of UWB horn antenna for GPR applications
2. A novel multi-channel, shared aperture antenna is introduced
3. A novel polarisation diversity technique is introduced
4. Simultaneous multi-channel imaging is introduced
5. Full 3D modelling of GPR environment is performed and studied
6. Realistic 3D models of AP and AV landmines are designed and fabricated
7. Collection of experimental GPR data is gathered based on realistic models of AP and AV landmines

1.8 Publications

Tong, K.F., **Amiri, A.,** Fortuny C.B. (2014). *Reconfigurable antennas for very wide spectrum monitoring*. IEEE International Workshop on Electromagnetics (iWEM).

Ezeoke, M., Tong, K., **Amiri, A.,** Al-Armaghany, A. (2013). *Effects of Electrical and Physical Properties of Barefaced Terrain on Backscatter Response.* Proceedings of the International Conference on Advances in Computing Electronics and Communications *(ACEC).*

Amiri, A., Tong, K.F. (2013). *Frequency Reconfigurable Patch Antenna for Landmine Detection*. International Workshop on Antenna Technology (iWAT).

Amiri, A., Tong, K.F., Chetty, K. (2013). *Reconfigurable Multiband Patch Antenna for Ground Penetrating Radar Applications*. International Conference on Electromagnetics in Advanced Applications, IEEE APCW.

Amiri, A., Tong, K.F., Chetty, K. (2012). Feasibility study of multi-frequency Ground Penetrating Radar for rotary UAV platforms. IET International Conference Radar.

1.9 References

Boutwell, J., and Klare, T. (1999). *Light Weapons and Civil Conflict* – Controlling the tools of Violence. Rowman and Littlefield Publishers, incorporated.

BBC NEWS. (1999). *World Scourge of the landmine*. [Online] Available from: http://news.bbc.co.uk/1/hi/288034.stm [Accessed: 4th November 2015]

Balsi, M. (2003). *A new concept for thermal mine detection by local heating*. Department of Electronic Engineering, "La Sapienza" University via Eudossiana 18 – 00184 Rome, Italy and Inter-University center for Research on Natural and Artificial Cognitive Systems (E.Co.N.A.).

Croll, M. (1998). *The History of Landmines*, Pen & Sword Books Ltd.

Cat–uxo. (2016). *Collective Awareness to UXO*. [Online] Available from: http://www.cat-uxo.com/#/landmines/4565410561

Daniels, D.J. (2007) *Ground Penetrating Radar*. 2nd Ed. IET Radar, Sonar, Navigation and Avionics Series 15.

Daniels, D.J. (2004) *Ground Penetrating Radar*. 1st Ed. IET Radar, Sonar, Navigation and Avionics Series 15.

DFI. (2014). *Army camp in Uri under attack, several personnel killed*. [Online] Available from: http://defenceforumindia.com/forum/threads/army-camp-in-uri-under-attack-several-personnel-killed.65612/page-13.

DRH Norway. (2013). *Landmines*. [Online] Available from: http://drhnorway.altervista.org/?p=1206

Frost, M. (2006).*Landmine*. [Online] Available from: http://www.martinfrost.ws/htmlfiles/may2006/landmine.html

Fischer, R., Burlage, R., and Maston, M. (2000). *UXO and Mine Detection Using Laser Induced Fluorescence Imagery and Genetically Engineered Microbes.* Army AL&T July-August, pp. 10–12.

GICHD. (2006). *Guidebook on Detection Technologies and Systems for Humanitarian Demining*. [Online] Available from: http://www.gichd.org/fileadmin/GICHD-resources/rec-documents/Guidebook_Detection_2006.pdf [Accessed: 1st May 2015]

GICHD. (2014). *Guidebook on Detection Technologies and Systems for Humanitarian Demining*. [Online] Available from: http://www.gichd.org/fileadmin/GICHD-resources/rec-documents/Guidebook_Detection_2006.pdf [Accessed: 12th November 2015]

Gettyimages. (2016). Best of News. [Online] Available from: http://www.gettyimages.co.uk/detail/news-photo/sri-lankan-soldier-uses-a-metal-detector-in-search-of-news-photo/155241399

Hussein E.M.A, and Waller, E.D. (2000). *Landmine Detection: The Problem and the Challenge*, Applied Radiation and Isotopes, Vol 53 pp 557 – 563.

Haupt, R.W., and Rolt, K.D. (2005). *Standoff Acoustic Laser Technique to Locate Buried Landmines*. [Online] Available from: https://www.ll.mit.edu/publications/journal/pdf/vol15_no1/15_1standoff.pdf

Hazeltine, B., and Bull, C. (2003). *Field Guide to Appropriate Technology. Academic Press. p. 853.* ISBN 978-0-12-335185-2.

ICBL. (2015). *International to campaign ban landmines*. [Online] Available from: http://www.icbl.org/en-gb/home.aspx [Accessed: 20th June 2015]

KA, M., and JP, L. (2000). *Current and emerging technologies for use in a hand-held mine detector*. The. Royal Military College of Canada, [Online] Available from: http://www.rmc.ca/academic/gradrech/minedetector.pdf.

Megahid, R.M. (1999). *LANDMINE DETECTION BY NUCLEAR TECHNIQUES.* 2nd Conference on Nuclear and Particle Physics, 13 - 17 Nov. Reactor Physics Department, Nuclear Research Centre, Atomic Energy Authority, Cairo, Egypt.

MercoPress. (2016). *Falklands Islands' minefield priority areas are named as bidders visit***.** http://en.mercopress.com/2014/09/12/falklands-islands-minefield-priority-areas-are-named-as-bidders-visit

Marshall Legacy. (2005). *Dogs for the Detection of Landmines.* [Online] Available from:

http://www.marshall-legacy.org [Accessed: 10th November 2015]

Niemann W., Olesinski S., Thiele T. (2000). *Detection of buried landmines with X-ray backscatter technology*. 8th ECNDT Proceedings, European Conference on Nondestructive Testing. Barcelona (Spain).

Rodacy, P. J., Bender, S. F., Bromenshenk, J. J., Henderson, C. B., and Bender, G. (2002). *The Training and Deployment of Honeybees to detect explosives and Other Agents of Harm*. Proc. of SPIE Vol. 4724 − Detection and Remediation Technologies for Mines and Minelike Targets VII, pp. 474–481, 2002. 8.

Keenan, S. (2008). *The landmine victim problem*. [Online] Available from: http://www-pub.naz.edu:9000/~skeenan1/images/

TheCeļotājs. (2013).*"Latvia" Former Soviet Union Military Bases.* [Online] Available from: http://sovietbases.thecelotajs.com/Ordnance-Pressure-Fuzes.php

Vietnam Veterans of America Foundation. (2007). *Anti-personnel Land Mines – the eternal sentinels.* [Online] Available from: http://www.thirdworldtraveler.com/Life_Death_third World/landmines.html

Chapter 2

Ground Penetrating Radar

2.1 Introduction

The term radar was coined in 1940 by the United States Navy as an acronym for Radio Detection And Ranging *(Translation Bureau, 2013)*. However, the technique was first patented by a German inventor Christian Hulsmeyer in 1904, following the pioneering work by James Clerk Maxwell in 1855, Heinrich Hertz in 1886 and Alexander Popov in 1895 *(Hulsmeyer, 1904)*. Radar is considered as an electromagnetic sensor for the detection and location of reflecting objects. A radar system radiates an electromagnetic wave from an antenna into the free space. When the radiated wave illuminates an object, three occurrences usually take place. 1) Reflection, 2) Absorption of the radiated wave by the object and 3) Refraction of the wave into the object in case of non-metallic materials. The proportion of reflected wave depends on the wavelength of the radiated signal, shape, size and material composition of the object. The direction of the reflected wave depends mainly on the shape of the object. Although the first ever radar systems were developed for ship anti-collisions, it was not until the beginning of World War II that radar technology became practically useful and attained the importance that holds nowadays. Radar systems are used in various applications from ship anti-collisions, weather systems, and astronomy to medical applications and beyond *(Tait, 2005).*

Ground Penetrating Radar (GPR) also known as ground probing radar, subsurface radar or georadar took its development in parallel from the early days of radar in 1910. GPR is a high resolution and a non-invasive electromagnetic technique that provides the possibility of detecting and locating buried objects. It is now a well-accepted geophysical technique and has reached a high level of maturity. The basic form of GPR measurements deploys a transmitter and a receiver in a fixed geometry, which are moved over the ground surface to detect reflections from the contents of the ground in a non-invasive manner as shown in Fig. 2.1 (a). In some cases, effects on energy transmitted through the ground material are of interest and this method is invasive (Fig. 2.1 (b)). GPR operates by sending out an electromagnetic wave into the ground through the antennas. The radiated electromagnetic wave is reflected back from buried objects and different interfaces with contrasting electrical properties. The first and the strongest reflection occurs at the air and soil interface. The intensity of any reflections after the air and soil interface depends mainly

on the dielectric properties (relative permittivity, relative permeability and conductivity) of materials being intercepted. Moreover, the shape and size of the target, the conditions of the ground material (e.g. wet or dry), the ground clearance of the antennas from the air/soil interface and the penetration depth also have an effect on the intensity of the reflected signal.

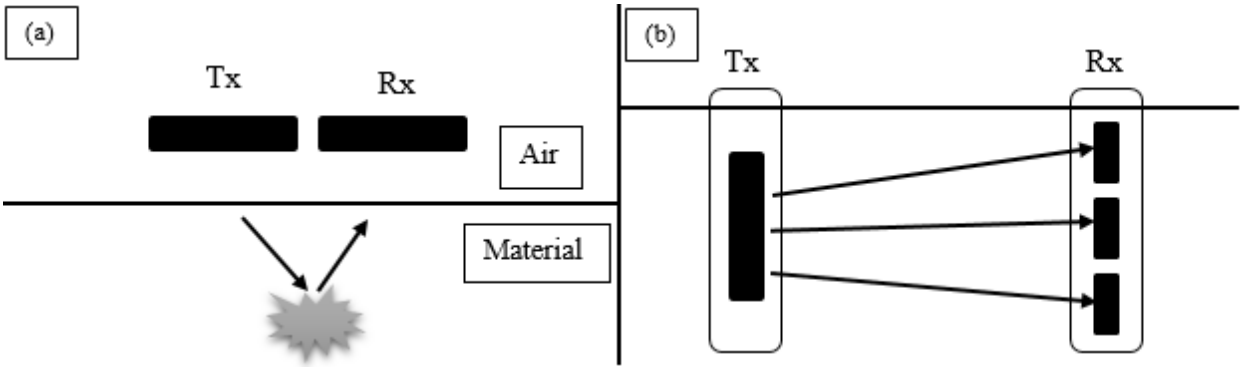

Figure 2-1: Two Modes of GPR Measurements – non-invasive (a), invasive (b)

The conductivity of material effects the penetration depth of the GPR due to the absorption of the radar signals in the medium. Thus, wet ground materials such as soil with high moisture content decrease the penetration depth. On the other hand, relative permeability is considered as one since most ground materials lack magnetic content. In contrast, relative permittivity which corresponds to the dielectric constant of materials provides useful information in distinguishing between the levels of contrast in the reflected wave. Figure 2.2 illustrates a block diagram of a generic GPR system and the main factors affecting its performance.

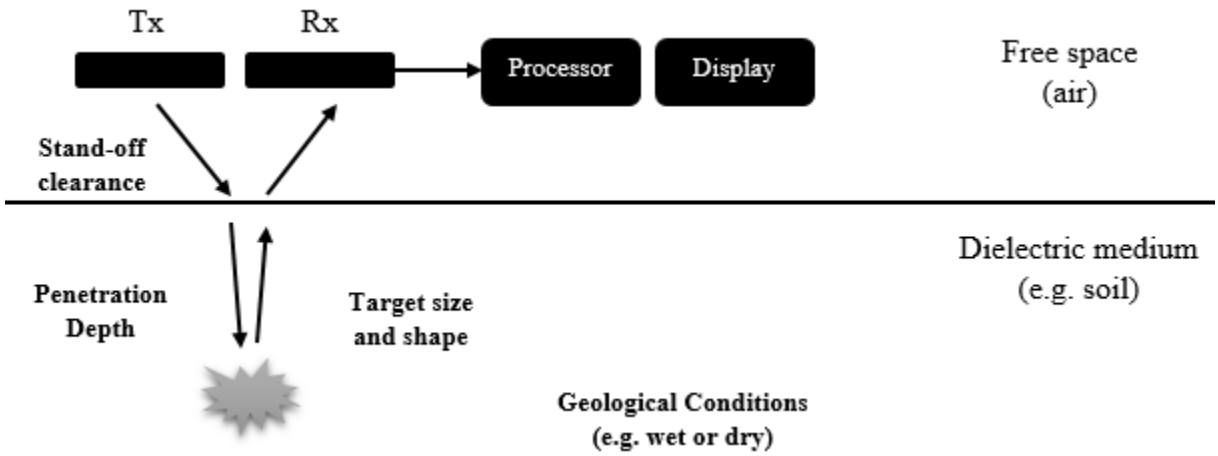

Figure 2-2: Block diagram of a generic GPR system and typical factors affecting its performance

The two-way travel signal sent and received by the GPR system is a time-dependent geophysical technique that can provide a good three-dimensional subsurface image. Accurate depth estimation is possible for many common subsurface objects. A typical GPR system consists of a signal generator that provides the source of the energy in the form of amplitude, frequency, phase modulated waveform and noise signal. The transmission and reception of the signal are performed by one or multiple antennas. The antennas are usually identical and are selected to meet the characteristics of the generated signal. The receiver has to pose an adequate dynamic range for the path loss that the signal encounters. As shown in Fig 2.2, the performance of GPR depends on the surface and subsurface conditions and other specifications such as bandwidth, operating frequency and mean radiated power depend on the depth of investigation, path loss, resolution and target dimension. The ability at which GPR can detect objects deep in the ground depends on its wavelength, generally longer the wavelength, the lesser path loss and hence deeper penetration. However, this comes at a cost of resolution. The quality of an image obtained from the detected object can be improved by operating at higher frequencies. The dielectric properties of the ground are frequency dependent. Therefore, the image obtained at different operating frequencies tells a different story of the same medium *(Conyers, 2004)*.

2.2 GPR Systems

In general, the transmitting and the receiving GPR systems can exist at the same location, which is either called a quasi-monostatic radar if the distance between the transmitter and receiver is equal to zero or referred as a monostatic radar if a single antenna performs both transmit and receive operations. If the transmitter and receiver have separate locations the system is called bistatic, *(Willis and Griffiths, 2007)*. If a radar system involves one or more transmitting platforms and multiple receiving platforms, it is referred to as multistatic radar. The different concepts of the spatial distribution of transmitter and receiver fulfil different requirements. More receivers may aid in providing different information about the target. Radars can also be classified according to their waveforms. A continuous wave (CW) type transmits continuously. Moreover, the signal can be frequency modulated (FMCW) or create the resulting signal as a combination of monochromatic steps through a certain band of frequencies, referred as stepped frequency continuous wave (SFCW). When the transmitted waveform is pulsed in the time domain, the system is called pulsed radar. Moreover, one can distinguish passive radars from active radars, by

if the system has its own transmitter *(Griffiths and Baker, 2005)*. Five main types of GPR systems are summarised below.

Conventional GPR systems operate in the time domain (impulse radars). However, more use has been made of frequency domain radars in recent years as they can provide greater dynamic range than time domain radars. All types of GPR systems have the same objective, and that is to measure the amplitude and the travelling time of the excited signal. The specification of a particular type of system can be laid out by examining the various factors which influence the detectivity and resolution. An acceptable Signal to Clutter ratio (SCR), Signal to Noise Ratio (SNR), spatial and depth resolutions of the target have to be considered to operate successfully.

An impulse radar transmits a narrow pulse (in nanoseconds range), associated with a spectrum of signals, with a large peak power at a constant pulse repetition frequency (PRF). This spectrum should be wide, to measure the target signature at high resolution. The time-delayed received waveform is then sampled, using rapid A/D converters to deal with the wide instantaneous bandwidth. Improvements in the signal to noise ratio (SNR) can be achieved by averaging the reflection profiles *(Tait, 2005)*

Stepped frequency, pulsed stepped frequency and stepped frequency continuous wave radars (SFCW) are a variation of the concept where the signal is stepped uniformly in frequency across the desired band. The advantage of these systems is the reduction of the instantaneous bandwidth and sampling rate requirements, as well as the possibility of skipping frequencies that might be corrupted due to external interfering frequency sources. Signal to noise ratio improvement is achieved by dwelling on each frequency and integrating them. A/D conversion rates do not need to be as rapid as impulse systems. In SFCW systems, the data is recorded in the frequency domain. At each frequency, amplitude and phase of the target are sampled and acquired. The received signal is transformed into the time domain using Inverse Discrete Fourier Transform (IDFT) to obtain a synthesised pulse. Direct coupling of transmitting and receiving signals lead to some dynamic range problems for these systems *(Mazzaro et al., 2013)*. The main advantage of the Stepped frequency continuous wave radars is that they can have a higher average radiated power for transmission.

Frequency modulated continuous wave radar (FMCW) is a short range measuring radar which its operating frequency changes during the measurement. That is the transmission signal is modulated in frequency. The frequency deviation of the received signal will increase with distance from the

transmitter. Such deviation will reduce the effect of the doppler signal. Echoes from a target are then mixed with the transmitted signal to produce a beat signal which will give the distance from the target after demodulation. The limitations of these systems are poor side-lobe suppression and FM range modulation *(Daniels, 2007)*.

2.3 Visualisation of GPR Data

The design of GPR determines the operation environment and the type of targets to be detected. It poses a challenge to creating robust algorithms for detection and imaging. A common image of buried targets generated by the GPR data is radargram. It is constructed from a collection of radar traces one after another in a 2D plot (signal strength vs. time delay). This plot does not represent the geometrical representation because of the ratio of signal wavelength to the target physical dimensions. There are three types of scan that are applied to the appropriate dimensional format of the data gathered *(Daniels, 2004)*. These are listed below and shown in Figure 2.3.

- A-scan - a single waveform recorded with antennas at a given fixed position (it is related to the depth in the propagation direction)
- B-scan - set of A-scans traces with antennas moving in a line along the x or y-axes
- C-scan - multiple B-scans traces with antennas moving over a grid in xy-plane

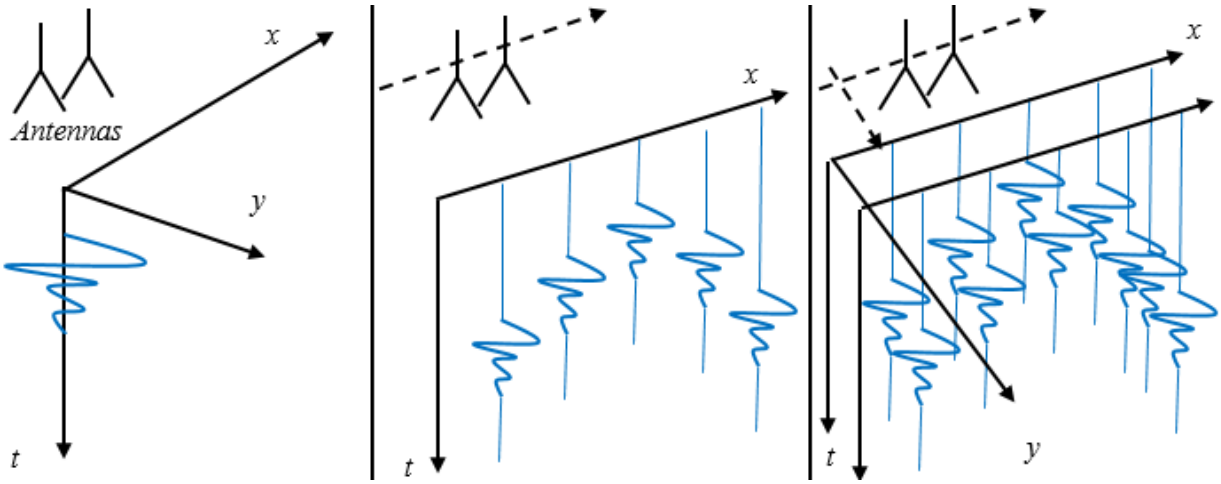

Figure 2-3: GPR Scan Methods - A-Scan (left), B-Scan (middle), C-Scan (right)

2.4 GPR Data Acquisition Modes

The imaging technique for the GPR is based on the movement of the antennas and the mode of the radar data acquisition. There are four modes where the transmit and receive antennas are surveyed above the target. If the transmitter and receiver antennas are moved simultaneously on a linear track with a fixed height above the target, then the measured travel time against the distance the antennas have travelled can be displayed in a radargram and this mode is called common offset (CO). This technique is also known as Synthetic Aperture Radar (SAR) where a long antenna aperture is synthesised by moving a smaller antenna aperture linearly or circularly. This mode can be used to improve the azimuth or plan resolution in the image formation.

In a common source point mode (CSP), also known as wide-angle reflection and refraction (WARR) sounding, the transmitter is kept at a fixed location, and the receiver is moved away at increasing offset. If the moving receivers are replaced with transmitters and a fixed receiving point, then the data is gathered in a common receiver point mode (CRP). Common Midpoint (CM) mode is where the transmitter and receiver antennas are moved away at increasing offset so that the midpoint between them stays at a fixed location *(Jol, 2009)*. These modes are illustrated in Fig 2.4 (transmitter and receiver antennas are indicated by blue and orange colours respectively).

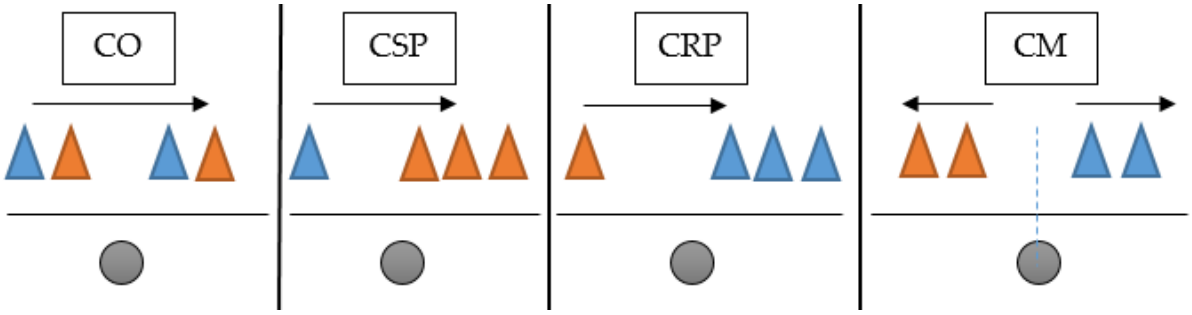

Figure 2-4: GPR Measurement Configurations

The imaging technique regarding different modes influences the quality of a GPR image. Different operating modes are considered regarding a particular application and where multiple antennas are needed, it is in the favour of the operator if the antennas are small and light weight. The target geometry and ground topography also influence the type of scanning mode. If the material properties are uniform and the target is planar in nature and features smooth surfaces with curves (e.g. pipes, cables) then CO, CSP and CRP scanning modes are suitable where the direction of the scanning is aligned with the target. The limitation of all four modes discussed above arises when

the target exhibits edges, curves and 3D geometry (e.g. irregular shaped landmines). These targets tend to scatter the incoming signal in all directions. If the GPR system aims to improve the image quality of these types of targets, then it has to employ multiple antennas with 3D scanning capabilities *(Gaffney and Gater 2003)*.

2.5 System Design

2.5.1 Transmitted Waveform

The waveform that the GPR system transmits may be modulated in both amplitude and frequency with time. As different types of waveforms have been mentioned, all are based on the signal defined by Eq. 2.1.

$$s\,(t) = a(t)\cos[\omega_0 t + \theta\,(t) + \varphi_0] \qquad (2.1)$$

where $a(t)$ represents the amplitude modulated envelope of the transmitted signal, $\theta\,(t)$ is a phase term due to frequency modulation, ω_0 is the frequency in radians per second and $\varphi_0$is treated as a certain phase constant *(Peebles, 1998)*.

2.5.2 The Radar Equation

The radar equation provides the ability to assess the performance of a radar such as radar signal and sampling, radar subsystems including, transmitter, receivers, antennas, etc., radar target and radar environment such as losses (which will be explained in the next section), attenuation and so on. The parameters of a radar system are optimised iteratively to fulfil the desired performance while a trade-off about all other demands including cost and complexity have to be considered. The reflection of the buried target in GPR may vary depending on whether the system is monostatic, bistatic or multistatic. According to Skolnik (2008), flat targets at monostatic configuration (e.g. incident angle $\theta = 0$) produce highest return signals. For the case of the monostatic configuration, where one antenna is used for both transmission and reception, the power received can be estimated by the Eq. 2.2.

$$P_r = \frac{P_t\, D^2(\theta_t\, \varphi_t)\, \lambda^2}{(4\pi)^3\, d^2 L_t\, L_{rad}^2\, L_{ch}^2} \qquad (2.2)$$

P_t represents the average peak power transmitted into the ground. This power will be reduced by mismatch and losses that are discussed later in this chapter. L_t is the power loss from the transmitter

to the antenna, L_{ch} is the channel loss along the propagation path and L_{rad} is the radiation loss of the antenna. $D\ (\theta_t\ \varphi_t)$ is related to the directivity of the radiated power in regards to the direction of the target in spherical coordinates similarly for the directivity of the received power from the same target considering the same antenna is used for transmission and reception. d is the two way distance to the target and λ is the wavelength at the centre frequency. This link budget was used to evaluate adequately transmitted power and expected received power from the target. Chapter 3 addresses the signal level and a typical transmitted power and received power in a GPR environment.

2.5.3 Losses

The penetration depth of a GPR is primarily governed by the total path loss and the three main contributions to this are the material loss, the spreading loss and the target reflection loss. This is illustrated in Fig 2.5. The total path loss is the addition of all the losses starting from the point of excitation of the signal (e.g. antennas) to the point where the signal is absorbed and no longer detectable. The first set of losses come from antenna loss (the antenna efficiency) and antenna mismatch loss (the antenna to transmitter matching). The spreading loss occurs within the distance from the antennas to the first interface and depending on whether the antennas are in near field or far field, this loss is calculated differently. The interception of the signal by the ground material, the physical dimensions and shape of the target, all influence the return signal back in the direction of the receiver. The material properties of the target also introduce attenuation loss.

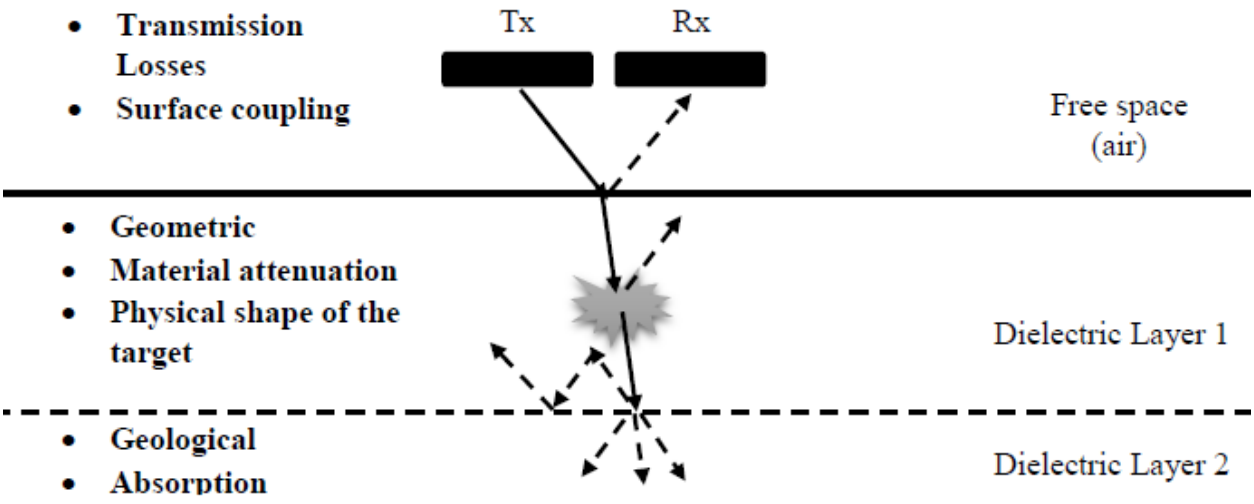

Figure 2-5: Total losses encountered by GPR signals

2.5.4 Range Measurement and Velocity of Propagation

The basic and most important task of a GPR system is to determine the distance between the radar and the target. The speed of the propagating signals in a dielectric medium depends on the dielectric constant of the material. The velocity at which signals propagate through the medium gets slower (with increasing dielectric constant), and if this can be measured or derived, then an absolute measurement of depth or thickness can be evaluated. For homogeneous and isotropic materials, the relative propagation velocity in metres per second can be calculated from

$$v_r = \frac{c}{\sqrt{\varepsilon_r}} \quad ms^{-1} \qquad (2.1)$$

and the depth is derived from

$$d = v_r \frac{t}{2} \quad m \qquad (2.2)$$

where ε_r is the relative permittivity of the medium and t is the transit time to and from the target. To determine the relative permittivity, laboratory experiments can be performed (will be explained in chapter 4) to estimate its value. However, in most practical trial situations the relative permittivity needs to be measured in situ.

2.5.5 Clutter

The clutter that affects the GPR performance can be regarded as those signals that are unrelated to the target but occur in the same sample time window. The received signal by the GPR usually consists of 1) Coupling signal included by transmitting and receiving antennas, 2) Strong reflection by ground surface, 3) Stochastic EM interference either from GPR system itself or the environment, 4) Reflection by subsurface targets. 5) Dispersion or reflection by underground inhomogeneity. Clutter from the GPR antennas can be caused by the breakthrough between transmit and receive antennas (if separate antennas are used), antenna self-clutter (e.g. ringing) as well as multiple reflections between the antenna aperture and the ground surface.

Often higher frequencies are used to detect a small object or structural changes in the ground. GPR becomes more sensitive to the natural heterogeneity of the soil when a higher frequency is used.

Soil heterogeneity scatters electromagnetic waves, and the scattered waves are in part observed as unwanted reflections that are often referred to as clutter. Data containing a great amount of clutter are difficult to analyse and interpret because clutter disturbs reflections from objects of interest.

How to effectively reduce the clutter has been a demanding area of research. There are various methods, including background subtraction *(Mayordomo, 2008)*, wavelets-transform (*Ni et al., 2010*), similarity measurement methods *(Haizhong and Xiaojian, 1997)* and Kalman-filer based techniques *(Luo and Fang, 2005)*. The experimental results from Chapter 7 will show how multi-band and multi-channel imaging can be used to minimise clutter to some extent.

2.5.6 Depth Resolution

There are some applications of GPR where the target of interest is a single interface such as road layer thickness deep in the ground. Under such circumstances, it is possible to determine the depth sufficiently by measuring the elapsed time between the received reflection and a reference time which is usually the reflection from the first interface. However, when a lot of features may be present as well as multiple interfaces within the ground close to the first interface, multiple returns at different times and of varying amplitude will be produced. The addition of targets also increases the complexity of the return signals. The ability of the radar to distinguish two targets with similar ranges is called range resolution (also known as vertical or depth resolution). Two targets can be resolved if the envelopes of their transient returned signals are clearly separated in time. The signal bandwidth determines the resolution. The smallest time interval that the radar can resolve is the inverse of the bandwidth which gives a range resolution in Eq. 2.4 *(Eaves and Reedy, 1987)*. In the case of landmines buried close to the surface, it is important that the GPR system has an adequate range resolution to be able to distinguish the landmine from the surface interface as well as closely buried objects. Fig. 2.6 illustrates a few return pulses from a target buried in the ground and the ability to resolve the return signals from the target and the ground interface. It can be seen that they are clearly separated using 5 GHz of bandwidth (a), overlapped using 2 GHz of bandwidth (b) and coincident using 500 MHz bandwidth (c).

$$\tau = \frac{1}{BW(f_{max} - f_{min})} \qquad (2.3)$$

$$R_{res} = \frac{1.39c}{2BW\sqrt{\varepsilon_r}} \qquad (2.4)$$

where, BW is the operating bandwidth, f_{max} is the upper frequency range, f_{min} is the lower frequency range, c is the speed of light and ε_r is the relative permittivity of the medium.

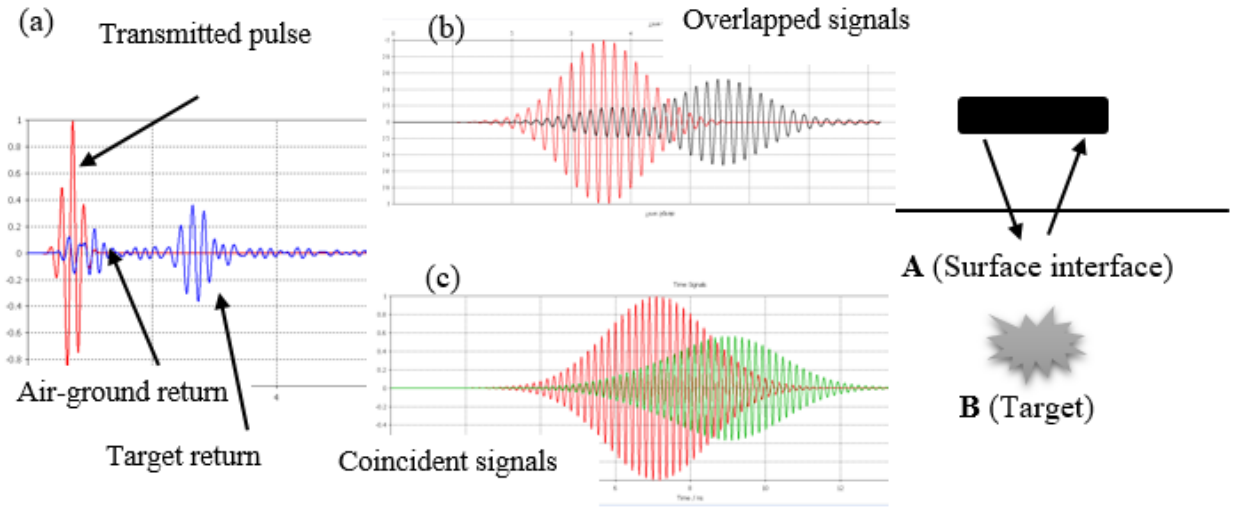

Figure 2-6: GPR range resolution – Resolved signals (a), Overlapped signals (b), Coincident signals (c)

2.5.7 Lateral Resolution

The lateral resolution (also known as plan resolution) is the ability of the radar to distinguish between multiple targets closely spaced at the same depth. These are the object features on a line perpendicular to the direction of radiation. It is different from range resolution as shown in Fig. 2.7 in regards to a GPR system. In the case of landmines, particularly in AV landmines, some of them exhibit distinctive geometrical features. Therefore, the GPR system should have an adequate lateral resolution for detecting these small features. Also, landmines can be found near other objects close to each other at the same depth. Therefore, high lateral resolution can help in separating them in the obtained image. Lateral resolution depends on the distance of the illuminating signal to the target, velocity and the pulse width and can be expressed as Eq. 2.5 *(Annan, 2005)*.

$$L_{res} = \sqrt{\frac{d\lambda_c}{2}} \qquad (2.5)$$

where d is the distance to the target and λ_c is the wavelength of the centre frequency. The footprint of the illuminating signal by the antennas ultimately influences the lateral resolution.

The area under the antenna and on the surface of the ground that is directly related to the size and position of the aperture of the antenna.

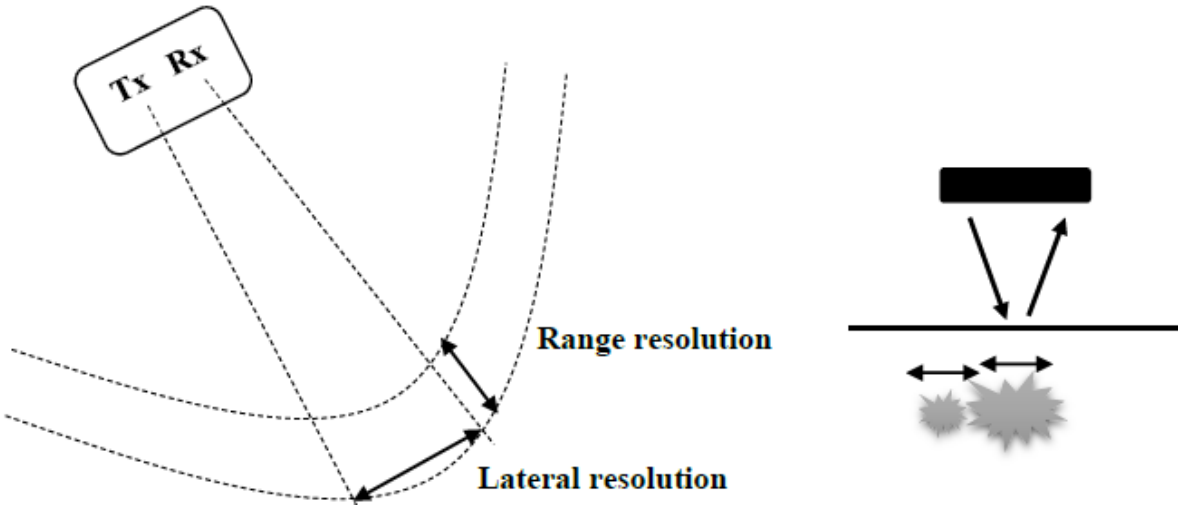

Figure 2-7: GPR lateral resolution

Another parameter that influences the footprint and consequently the lateral resolution is the radiation pattern and beamwidth of the antenna. Different radiation patterns can result in different signal returns of target features. Figure 2.8 presents the simulated E-field distribution of a) dipole antenna and b) horn antenna placed directly above a dry sandy soil with a metallic circular disc target buried at 2 cm. Both antennas are placed at a height of 3 cm above the ground (same direction of polarisation), and E-field distribution is monitored at 5.5 GHz and 180 ° phase.

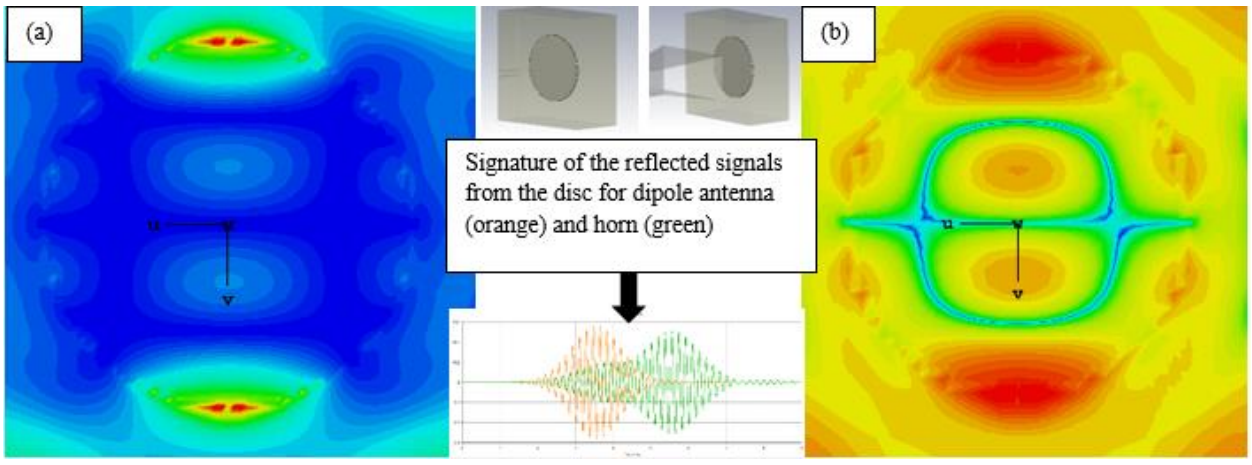

Figure 2-8: E-field distribution of a dipole (a) and a Horn antenna (b) inside a sandy soil material with a buried metallic disc

The E-field distribution of both antennas in E – plane shows the main peaks from the edges and the centre part of the disc. However both images differ in a) the intensity of the peaks and b) smaller additional patterns. The intensity of the peaks from the image with horn antenna shows that better coupling and gain can be achieved. In addition, there are smaller patterns with lower intensity that don't appear in the distribution of the E-field from the dipole antenna. This is further shown by the signature of the reflected signals back towards the antenna. The green signal from the horn shows that additional peaks appear later in time. This means although the main distribution on the circular target is similar for both antennas, other patterns can be seen from different radiation pattern. The E-field distribution from the horn antenna shows the edges of the target with strong indication in the direction of the E-field of the horn antenna. This can be used to estimate the dimensions of the target from the range profile of the received signal (will be further explained in Chapter 7). The dipole antenna is producing a slightly different pattern on the side of the disc. This difference in the shape of the image obtained from multiple radiation patterns and characteristics can add additional information about the target, enhancing the overall understanding of the imaged scene.

2.5.8 System Consideration

To employ a suitable GPR system for the desired application, it is imperative to understand the limitations of each system and how they influence the performance of the GPR system. Figure 2.9 illustrates a general design consideration that needs to be taken into account when selecting the type of radar system. Two key factors determine the detectability of the small returns from the buried objects. The adequate dynamic range in the receiver range and the signal integrity and shape when propagating from the antennas. Antennas tend to produce a ringing effect, especially with impulse systems, producing a noisy transmitted signal. Careful antenna design has to be employed to reduce the ringing effects. The type of radar system deployed for the purpose of this thesis is a SFCW and is discussed further in Chapter 7. Antenna design is a crucial part of the GPR system since it has to be designed in a way to reduce losses and preserve the signal integrity. Because of the short range of the target and lossy propagation media, antennas have to operate well in the near field to maximise the surface coupling. The total path loss considerably influences the maximum range of the GPR. The properties of the ground such as soil type and water content, affect the path loss (which will be discussed in Chapter 3) and the path loss may not always be a linear function of depth. To overcome some of the path losses that are related to the wavelength, lower operating

frequency signal can be used. But this will reduce the operating bandwidth which is directly proportional to the resolution. Additionally, antenna size increases as the frequency decreases (Explained in Chapter 5). This engineering trade-off between resolution and operating frequency poses a challenge for the performance of the GPR systems.

Figure 2-9: GPR System Design Considerations

2.6 Summary

The majority of current GPR systems operate from a stand-off distance from the ground. They are mostly based on the time domain impulse design. Although time domain radars are at a mature stage, there are alternative design options that can be considered. These are, stepped-frequency or synthesised-impulse as well as frequency modulated (FMCW). Low frequency is desirable to detect targets buried deep in the ground. However, to distinguish and resolve small features and ground layers, higher frequency signal and wider bandwidth should be used to achieve an adequate range resolution. This introduces various design options in the type of radar system used with currently available electronics. In the time domain, the pulse length dictates the overall bandwidth available. A long pulse is desirable for deep penetration in the ground. However, for short range precision, a short pulse length is needed. Extremely short pulse length may prove to be challenging regarding RF electronics and also signal processing. Frequency domain radars may prove to be an attractive alternative for wide bandwidth operation.

2.7 References

Conyers, L. B. (2004). *Ground-penetrating Radar for Archaeology*. Walnut Creek, CA. United States: AltaMira Press Ltd.

Clark, A.J. (1996). *Seeing Beneath the Soil*. Prospecting Methods in Archaeology. London, United Kingdom: B.T. Batsford Ltd.

Daniels, D.J. (2004). *Ground Penetrating Radar*. 1st Ed. IET Radar, Sonar, Navigation and Avionics Series 15.

Griffiths, H.D and Baker, C.J. (2005). *Measurement and analysis of ambiguity functions of passive radar transmissions*. University College London.

Gaffney, C. and Gater, J. (2003). *Revealing the Buried Past: Geophysics for Archaeologists*. Stroud, United Kingdom. Tempus.

Hulsmeyer, C. (1904). *Verfarhen um entfernte metalische Geogenstandemittels electrische Wallen einem Beobachter zu melden*. German Patent Office. No. 16554.

Jol, H.M. (2009). *Ground Penetrating Radar: Theory and Applications*. 1st Ed. Elsevier Science.

Luo, Y. and Fang, G.Y. (2005). *GPR clutter reduction and buried target detection by improved Kalman filter technique*. Department of Electronic Eng., Tsinghua Univ., Beijing, China. International Conference on Machine Learning and Cybernetics.

Mazzaro, G., Phelan B., Sherbondy K., Koenig F., (2013). *Introduction to Stepped-Frequency Radar*. US Army RDECOM.

Mayordomo, A.M. (2008). *Optical background subtraction in GPR for humanitarian demining.* IRCTR, Delft University of Technology, Mekelweg 4, 2628 CD, the Netherlands. Radar Conference, EuRAD.

Ni, S.H., Huang Y.H., Lo K.F., Lin, D.C. (2010). *Buried pipe detection by ground penetrating using discrete wavelet transform*. ScienceDirect, Computers and Geotechnics, Volume 37.

Peebles, P. (1998). *Radar Principles*. New York, Jon Wiley.

Tait, P. (2005). *Introduction to radar target recognition*. IEE Radar, Sonar and Navigation Series.

Translation Bureau (2013). Radar definition. Public Works and Government Services Canada.

Willis, N.J. and Griffiths, H.D. (2007) *Advances in Bistatic Radar*. IEEE Aerospace and Electronic Systems Magazine, Volume 23, Issue 7.

Chapter 3

3D Electromagnetic Simulation of Ground Penetrating Radar

3.1 Introduction

The advance of electromagnetic simulation software in combination with using computer technology allows researchers to study electrically large problems, such as a complete GPR environment in details. In general, electromagnetic simulations are very helpful for achieving an in-depth understanding of the underlying physical concepts, because it is possible to study the effect of different parameters of the GPR system systematically.

The modelling of wave propagation in different material layers requires a 3D full-wave simulation and the correct manipulation of the electromagnetic properties. GPR geometry can be studied from a simple single frequency evaluation of path losses to complete 3D time domain descriptions of each physical layer of GPR and its environment. There are several methods of modelling techniques such as single frequency models, time domain models, ray tracing, integral techniques and discrete element methods. Recent studies have extensively explored the use of Finite Difference Time Domain (FDTD) and the Finite Integration Technique (FIT) which are proven to be popular techniques and can be computed by several commercial EM simulation software packages listed below, able to run on most desktop computers with reasonable efficiency:

- Microwave Studio (CST) - FDTD and Hybrid Techniques
- HFSS (Ansoft) - Finite Element (FEM)
- FEKO (EMSS) - Method of Moments (MoM) and Hybrid Techniques

CST is a general purpose EM simulator based on hybrid solvers such as FIT and FDTD. This numerical method provides a universal spatial discretisation scheme applicable to various electromagnetic problems ranging from static field calculations to high-frequency applications in time or frequency domain. In FDTD, Maxwell's equations are solved by computing the electric field components in a volume of space at a given instant in time. Then the magnetic field components in the same spatial volume are solved at the next instant in time, and the process is repeated until the desired transient EM behaviour in the model is fully resolved. The strength of

FDTD modelling is its ability to calculate the response of the system over a wide range of frequencies from a single simulation. It is well suited for modelling complex inhomogeneous media and applying absorbing boundaries to truncate the grid for simulating an infinite region (*CST 2012*). Figure 3.1 shows how the EM components in the CST calculation domain is formulated and consequently the Electric and Magnetic fields are visualised.

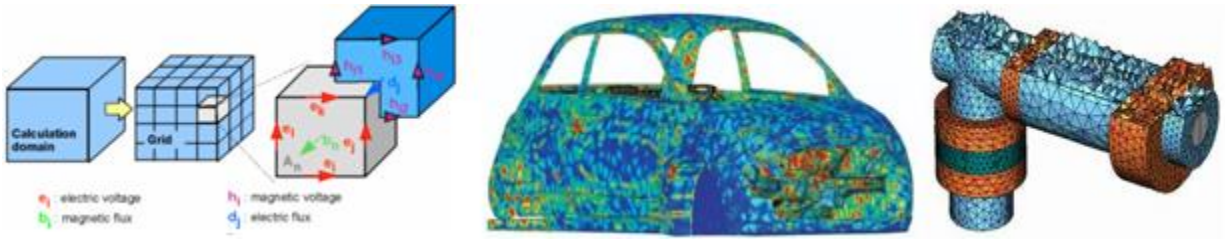

Figure 3-1: CST Cell Computation. Source: Weiland, Timm and Munteanu (2008)

There are three different types of solvers available for calculating high-frequency EM field problems in CST, transient (T-solver), frequency (F-solver) and eigenmode solvers (E-solver). The work being carried in this thesis has been computed mostly using T-solver with occasional validation of some results (e.g. S parameters) in F-solver. Transient solver provides a simulation method suitable for situations with open boundaries or relatively large dimensions. It allows calculation of a structure's behaviour in a wide frequency range in just a single computation run. Electric and magnetic field monitors are only available in T-solver. Boundary conditions are set around the calculation cell to decide the behaviour of incident waves as they propagate through, symmetry planes may be defined to reduce the calculation runtime.

3.2 Definition of Material Properties and Waveguide Ports

In CST, several different material properties are offered for a realistic modelling of practical simulation problems. Some of the common materials available are PEC (Perfect Electrical Conductor) and Vacuum (free space). However, any material can be created using the electromagnetic definition functionality of CST where the measured electromagnetic properties (see Chapter 4) can be imported and defined.

Waveguide ports are used to model experimental conditions of signal excitation with 50 ohms characteristics. Ideal or lossy waveguide ports can be implemented, and their properties can be configured to suit the simulation model.

3.3 Modelling of Realistic Soil Material

A propagation path in GPR is defined as mostly natural earth materials (sand, soil, etc.) or man-made materials (e.g. concrete) that lie within the EM wave path of the GPR system. They cause a measurable effect on the path loss. Therefore, electrical properties such as dielectric constant of these materials are very important parameters for detection and imaging *(Andrusenko, Burbank and Ward, 2009)*. Also, the electrical properties, physical shape and roughness of these materials and their composition also influence the propagation effects. Water content is not the only factor affecting the attenuation of electromagnetic waves. It has also been demonstrated that the textures of the soil and the bulk density are also key factors that can have a noticeable effect on electromagnetic waves *(Hallikainen et al. and Dobson et al., 1985)*. Multipath and reflection are other effects contributing to the distortion of the electromagnetic waves. Multipath effects are accumulated if the material is heterogeneous. To assess the behaviour of electromagnetic waves inside a lossy medium and the time domain signature, a conceptually simple model can be used to gain insights into the effects of the delay time, optimum centre frequency of operation, signal amplitude level and pulse shape. One of the key parameters to investigate when examining the behaviour of earth materials on the electromagnetic waves is the propagation of electric fields at various operating frequencies. Dielectric properties of real earth materials (Explained in Chapter 4) have been used to model the environment as well as a simple inhomogeneous texture for the structure of the environment. Figure 3.2 illustrates the layout of the model. Waveguide ports are implemented to provide transmission and reception of the propagating signals inside a dielectric medium. E-field probes can capture the signals reflected back from the surface of the material to investigate the scattering properties and signal level.

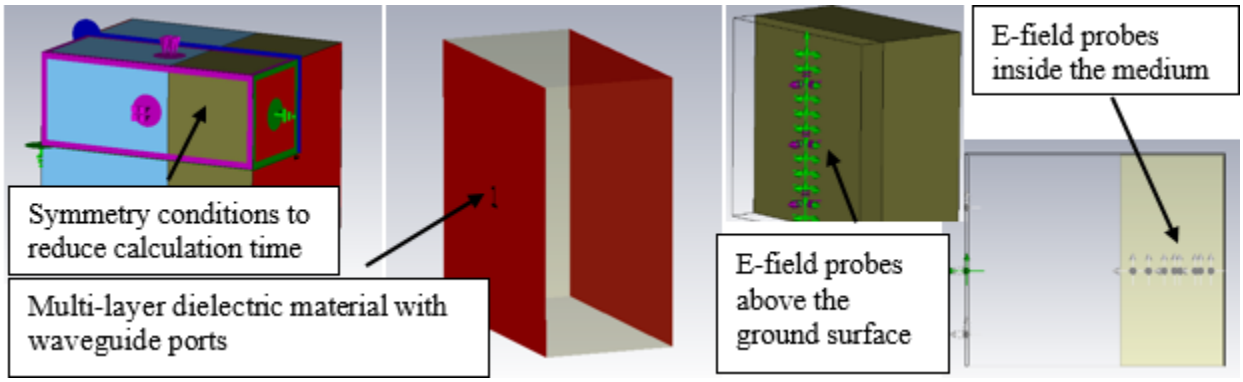

Figure 3-2: Model of a homogenous material

Figure 3.3 shows the A-scan waveform of the transmitted (red) and received pulses (green) in the time domain from (a) dry sandy soil, (b) wet sandy soil and (c) concrete. The scattered signal is received at a distance of 20 cm from the top of the interface. The highest amplitude of the return signal belongs to the wet sandy soil (almost half of the transmitted amplitude).

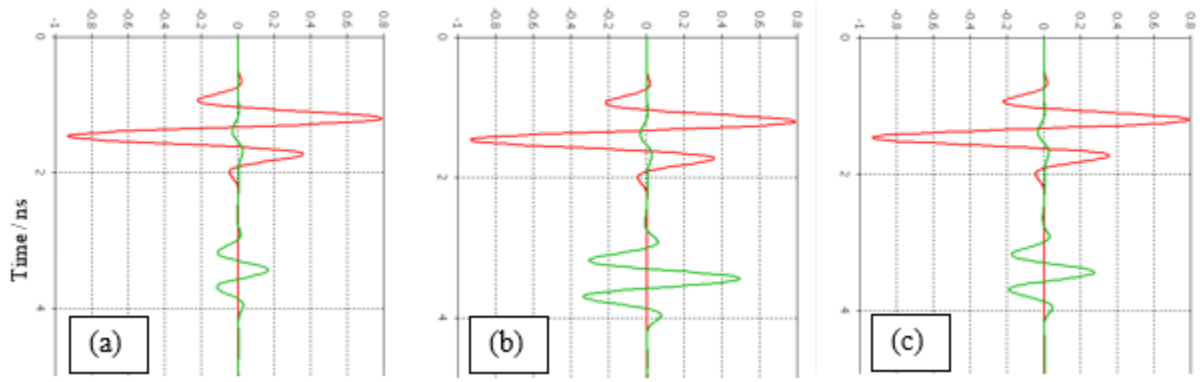

Figure 3-3: A-scan waveforms of Dry sandy soil(a), Wet sandy soil (b), Concrete (c)

3.3.1 Attenuation

The loss of the soil is often measured as a propagation loss in decibels per metre, and it is dependent on the conductivity of the soil and the frequency of operation. However, most numerical models such as the one mentioned by Daniels (2007) assumes a far-field environment. In the case of short ranges and near-field environment appropriate model has to be applied. To characterise the soil material and extract the effective material properties, a homogeneous block of the material was excited by a signal from a waveguide port using a transient solver. Another waveguide port terminated the model, and the desired mode patterns were imposed by using appropriate boundary conditions. As shown in Fig. 3.2, the boundary conditions for the model impose a transverse electromagnetic condition. This method acts as placing the material inside an enclosed transmission line (e.g. rectangular waveguide, explained in Chapter 4). The attenuation is computed by investigating the amplitude of the signal through the material. Figure 3.4 shows the attenuation of dry and wet sandy soil for a different depth of the material at 1.7 GHz centre frequency. The one-way attenuation is relative to 1 V of input power through the material. As the depth of the material is increased from 5 cm to 30 cm, the attenuation for the wet sandy soil increases drastically.

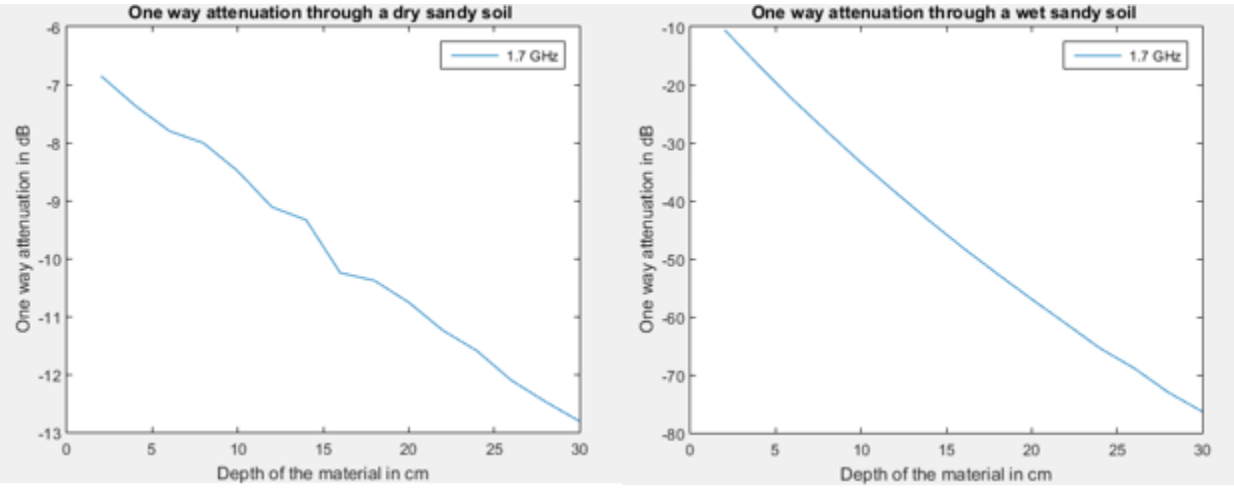

Figure 3-4: Attenuation through dry sandy soil (left) and wet sandy soil (right)

3.3.2 Spectrum

The impact of material attenuation on signal characteristics can be seen from the following simulation. A Gaussian impulse is a typically radiated signal from a GPR and transmitting this through a lossy material is equivalent to passing through a low pass filter. The effect on the spectrum of the signal resulting from a Fourier transform of the received signal through the material is shown in Fig. 3.5.

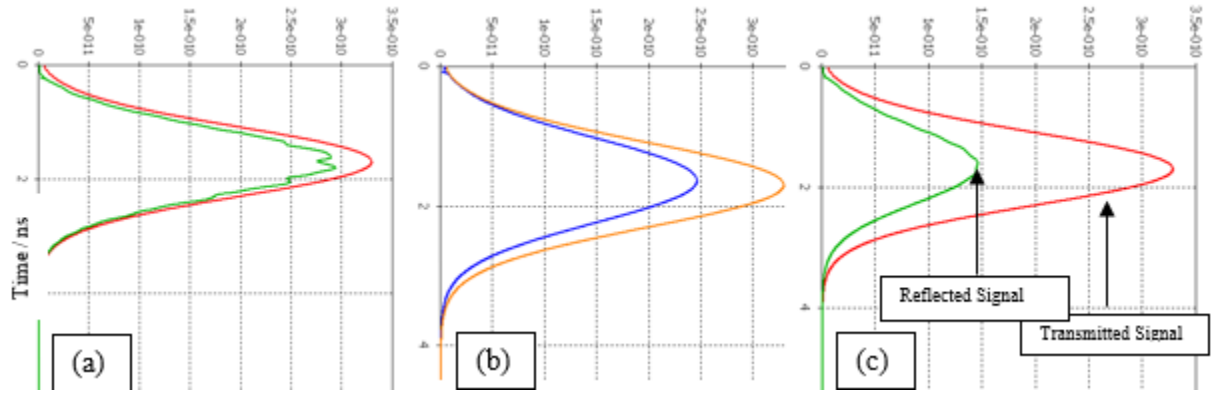

Figure 3-5: Spectrum of transmitted and received signals after passing through, Dry sandy soil (a), Wet sandy soil (b), concrete (c)

It can be seen that the peak of the spectrum is shifted to lower frequencies, and the level of higher frequencies components is reduced (higher attenuation in wet sandy soil). This is not as severe in the case of dry sandy soil (a) and concrete (c) however, the shape of the peak of the signal through the dry sandy soil is relatively distorted.

3.3.3 Signal Level

The limiting factor of detectability is the level of the noise floor of the radar receiver. Therefore, the received voltage from the buried landmine must be significantly greater than the noise level generated by the radar system. A simulation scenario can be set to investigate the level of the return signal from a plastic object at various buried range and target size. In the simulation setup, the illuminating signal is originated from a horn antenna placed at 5 cm above the ground. The medium in which the signal propagates is a dry sandy soil, and the buried target varies its buried depth and dimensions. The return signal level in dBm for a transmitted pulse of 30 dBm peak magnitude is shown in Fig. 3.6.

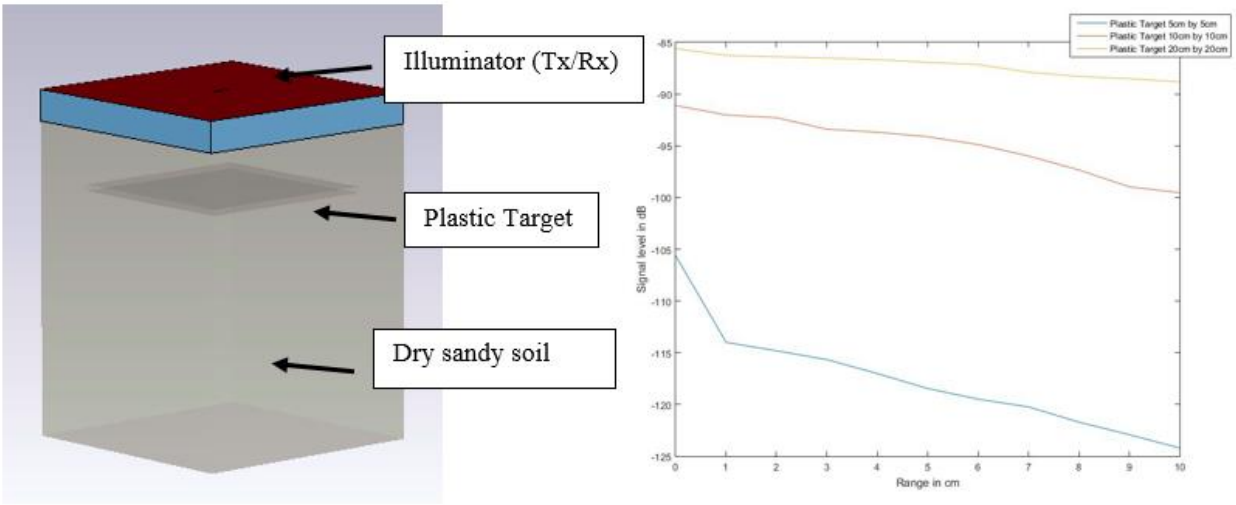

Figure 3-6: Signal amplitude against range

Three different dimensions of a plastic target are investigated, 5 cm by 5 cm (blue), 10 cm by 10 cm (brown) and 20 cm by 20 cm (yellow). From the values of attenuation indicated above, it can be seen that for a given signal detection threshold the maximum signal level decreases rapidly with increasing depth and decreasing dimensions. As shown, to detect a plastic target of dimensions 5 cm by 5 cm at a buried depth of 10 cm, the noise floor of the radar system must be below -125 dBm.

3.3.4 Multilayer Environment

Models of the structure of earth materials can range from a single layer to multiple layers as well as homogeneous to heterogeneous textures. In a realistic environment where landmines are found, the contents of the ground may include several layers of earth materials. Due to climatic and

weather conditions, the ground may also preserve some water content which can change dramatically within the course of days or years. This variability in groundwater content around the landmine can strongly affect the landmine detection. Figure 3.7 shows a model of a multilayer ground structure with the parameters summarised in Table 3.1. The output of the model can be used to assess the A-scan waveform. The A-scans simulations given in Fig. 3.8-3.11 show the effect of changing the bandwidth of operation on the resultant waveform. As expected, the A-scan waveforms show the improvement in resolution in going to higher bandwidth and the consequent reduction in signal amplitude in the high-frequency part of the bandwidth

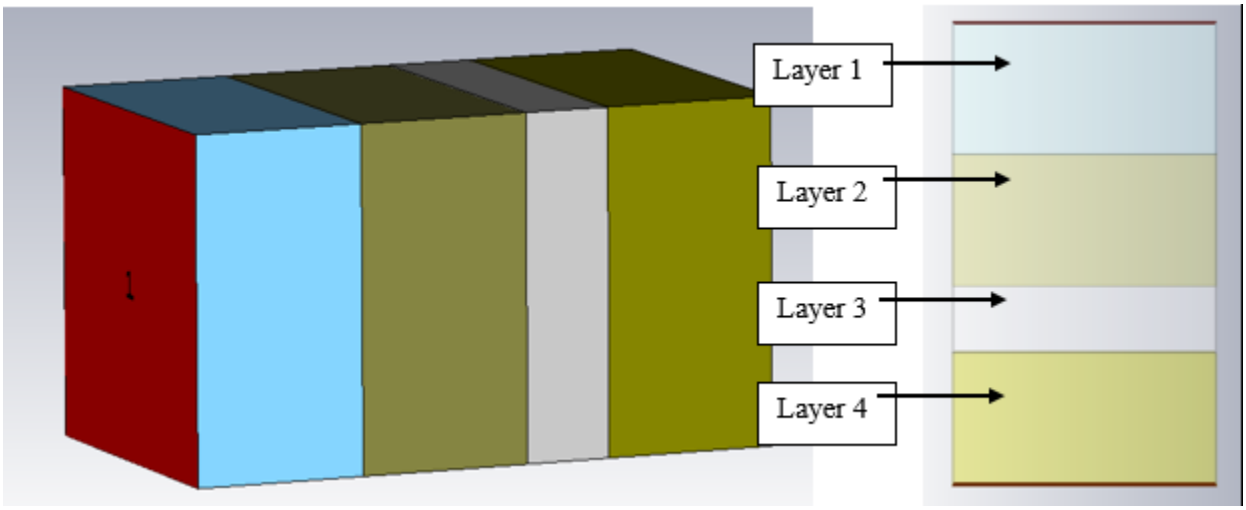

Figure 3-7: Layout of a multilayer ground

Layer	Range, m	Dielectric constant	Loss tangent	Material
1	0.2	1	0	air
2	0.2	2.53	0.0036	dry sandy soil
3	0.1	13	0.06	concrete
4	0.2	4.5	0.29	wet sandy soil

Table 3-1: Layer characteristics

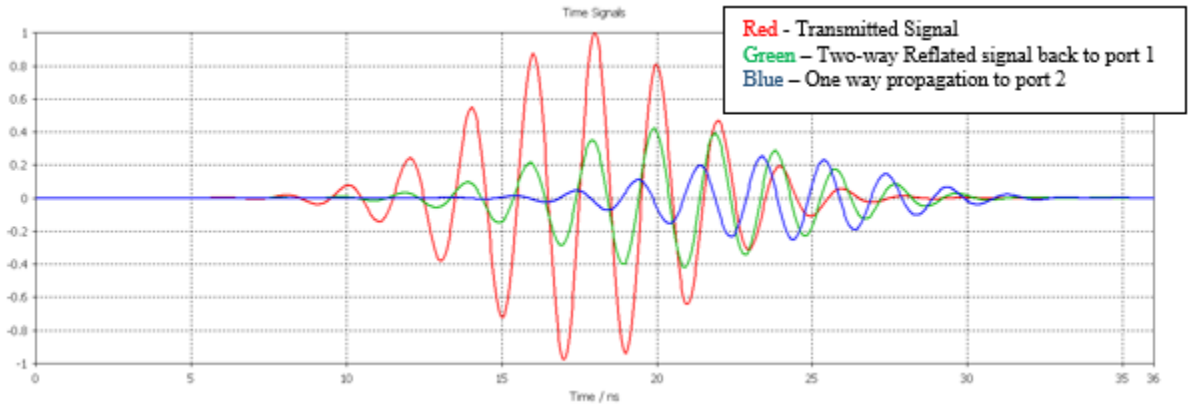

Figure 3-8: Simulation of A-scan from a multilayer environment using 500 MHz centre frequency (200 MHz bandwidth)

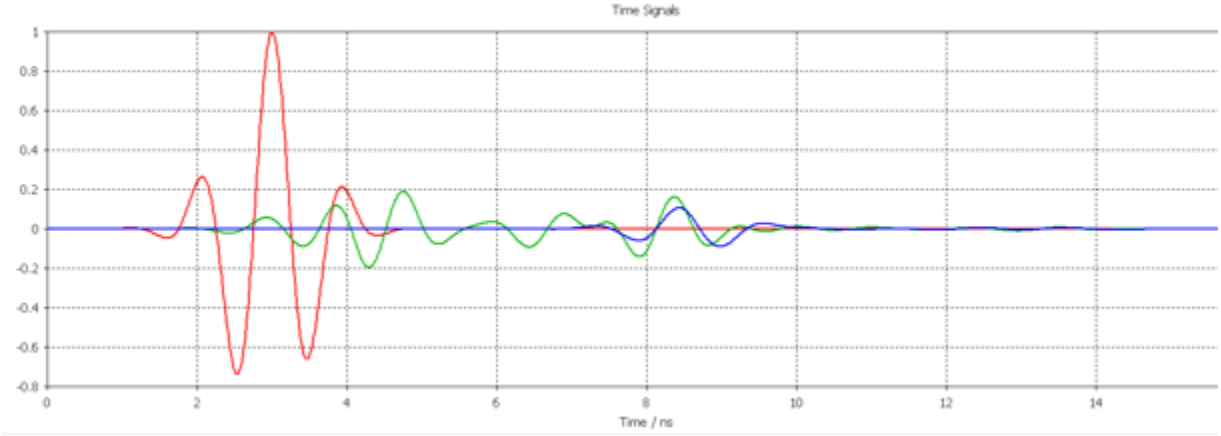

Figure 3-9: Simulation of A-scan from a multilayer environment using 1 GHz centre frequency (1.2 GHz bandwidth)

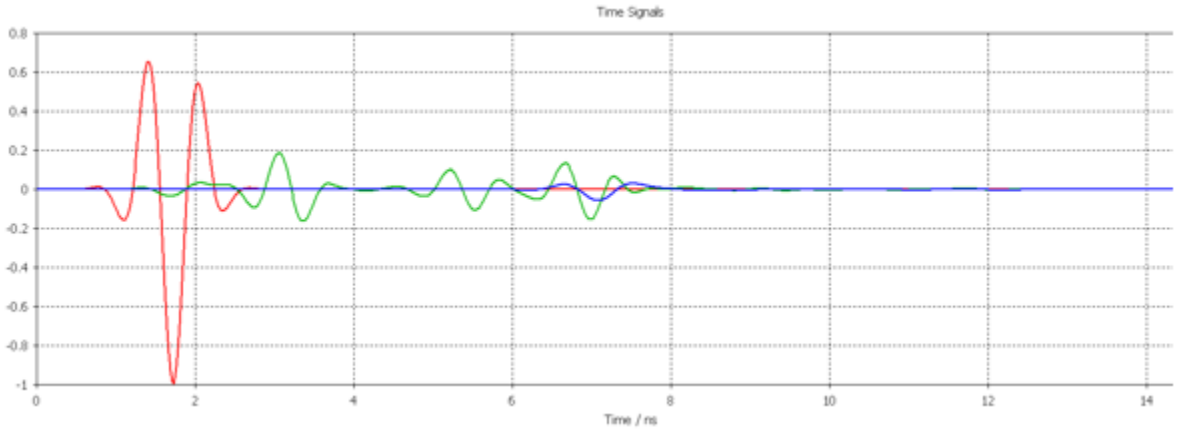

Figure 3-10: Simulation of A-scan from a multilayer environment using 1.45 GHz centre frequency (2.1 GHz bandwidth)

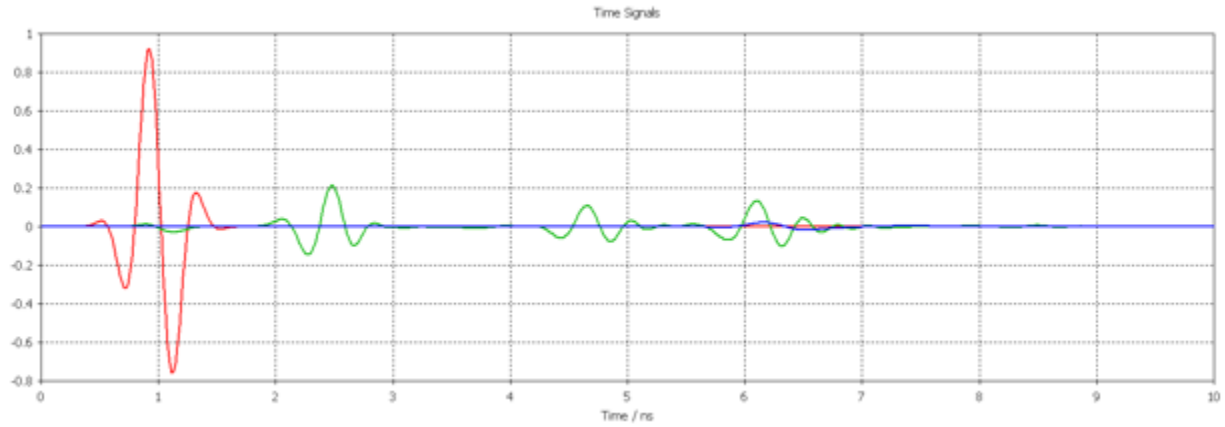

Figure 3-11: Simulation of A-scan from a multilayer environment using 2.2 GHz centre frequency (3.6 GHz bandwidth)

The red signal is the transmitted Gaussian pulse at a given bandwidth, into the medium and the green signal is the reflected signal back towards port 1. Therefore, it is the two-way travel signal, and the peaks correspond to each interface inside the medium. The blue signal is the signal that has travelled through the medium and arrived at port 2 which is located on the opposite side of port 1. This represents the attenuation that the signal undergoes as it travels through the each interface.

3.3.5 Model of Antenna Radiation and Buried Target Interaction

In GPR environments, the image quality from the buried target is often influenced by the near-field radiation pattern and interaction of antennas (e.g. coupling or induction effects). In this section, simulation of field propagation in a typical GPR system is investigated as shown in Fig. 3.12. The transmitter and receiver operated above the ground and a dielectric medium surrounds the buried target. The objective is to study a) the radiation pattern or the electric field distribution that the illuminator imposes on the medium and the buried target. This is compared to a plane wave and a standard horn antenna as the illuminator. Fig. 3.12 shows the electric field strength on the vertical plane cutting the antenna and ground geometry for a single frame. The various reflections and field propagation from the antenna and inside the medium can be seen. From the figure, the strong field region on and inside the horn is evident. The buried object is also visible at a lower intensity of the fields. The main reflection caused by the air-ground interface can clearly be seen coming back towards the antenna structure. Also, a weaker reflection coming from the buried object is starting to form and follows the interface reflection in time. Furthermore, the other wave phenomena can be observed such as the free space loss and the wave speed reduction inside

the lossy medium. It has to be noted that correct boundary conditions have to be used to retrieve the true value of return signal from the target. In a realistic GPR system if the return signals that bounce back from the air-soil interface and the aperture of the antenna, is larger than the return signal from the plastic target, then the detectability of the target will be reduced.

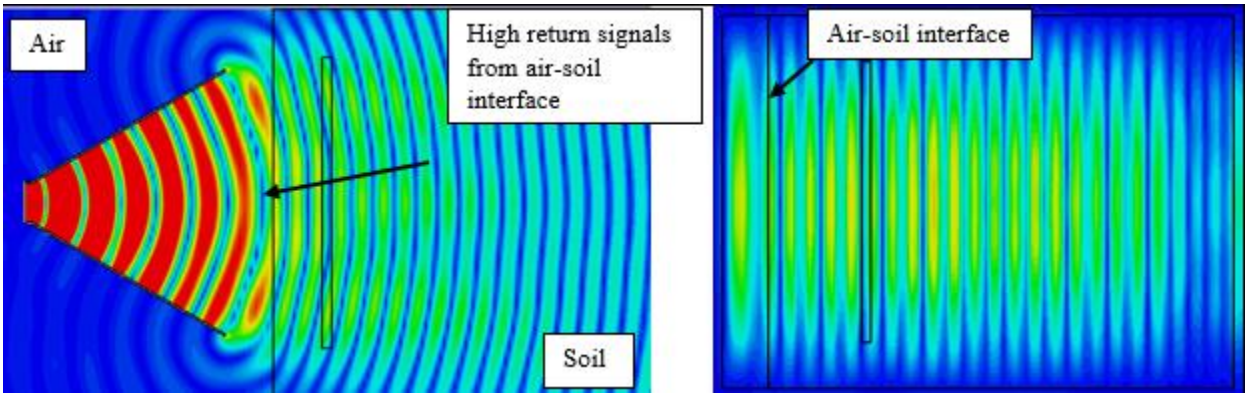

Figure 3-12: Electric field distribution in a vertical cut plane for a standard horn (left) and plane wave (right)

3.4 Modelling of Realistic Target Objects

The aim of the GPR application described here is to detect target objects such as landmines which have been buried in the ground. To simulate a complete GPR, the electromagnetic models of such targets have to be designed and utilised. The most basic models of landmines can be regarded as simple cylindrical or rectangular shapes with specified dimensions to gain insight into their initial characteristics. The complexity of the geometrical shape of the landmines can be extended and using the detailed literature available, complex models of landmines can be taken into account.

In an attempt to create a realistic model of landmines, detailed measurements and examination were performed at the Imperial War Museum and National War Museum where access to real landmines was granted. Following models described here are exact and accurate to an acceptable level for GPR investigation.

3.4.1 Modelling of Typical AP Landmines

A few common AP landmines shown in Chapter 1 were selected and modelled. The material for the casing of the mines is plastic which has a dielectric constant between 2 and 3 (Explained in Chapter 4). Figure 3.13 shows the modelled AP landmines. Before examining the interaction of EM waves with the buried landmines in a full GPR environment, it is necessary to understand their behaviour in a free space environment. Figure 3.14 illustrates the simulation model that was used

to study the model landmines with plastic material. The dielectric constant (ε_r) of the plastic part of the main body was assumed to be 2 for all the models. The dielectric constant ε_r for the activator of the VS-50 model was assumed to be 6. The illuminator is a plane wave vertically polarised, and the receivers are defined as E-field probes (green arrows) scattered linearly (1 cm spacing) along the landmine model. The receiver probes were set to monitor the return signal in all the directions (e.g. x, y, z). As well as return signals, RCS measurements were also taken in the model shown by the purple RCS probes.

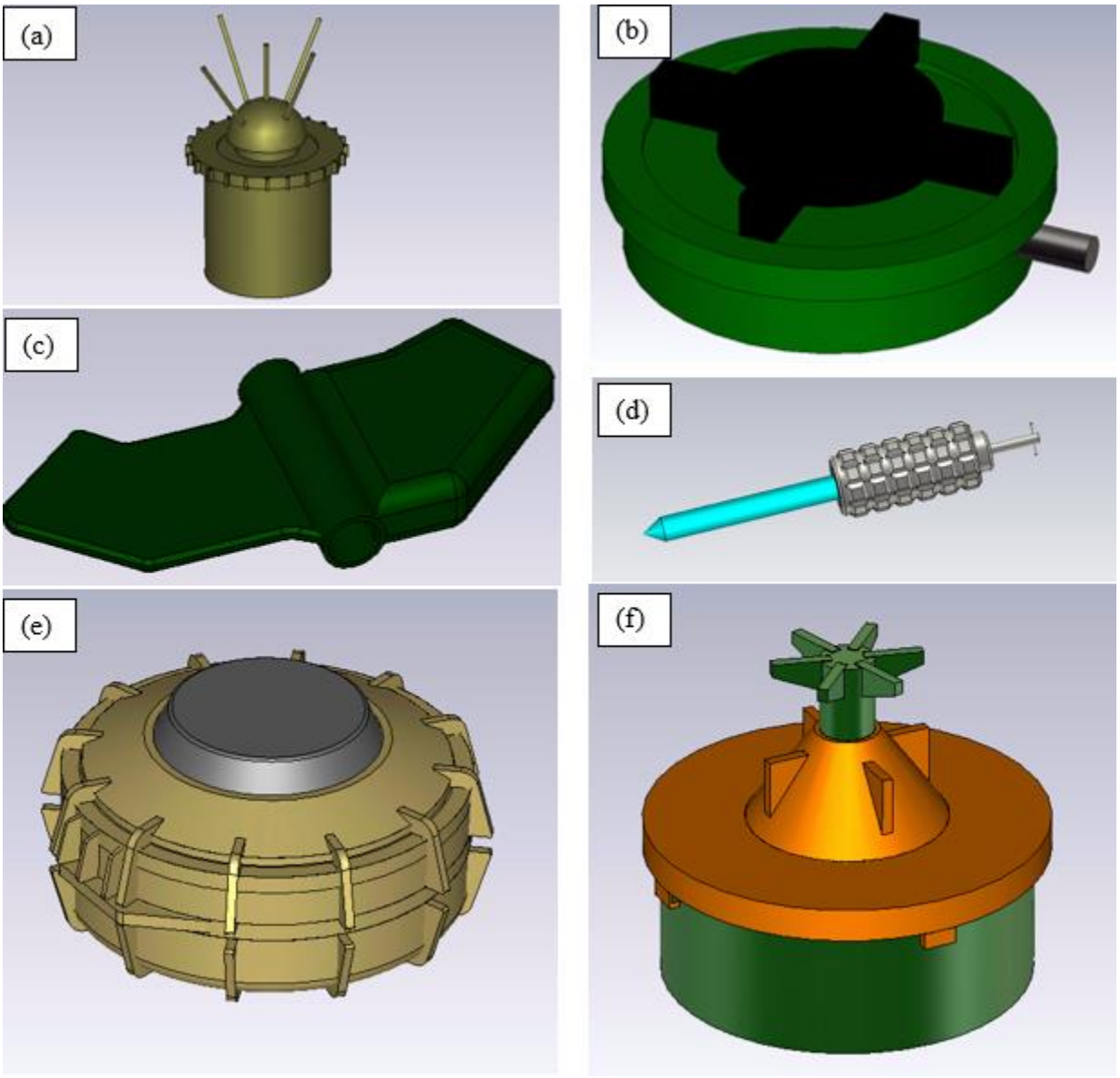

Figure 3-13: 3D CAD models of AP landmines. VS-69 Valmara (a), PMN-2 (b), PFM (butterfly) (c), Type-58 (d), VS050 (e), PMA2 (f)

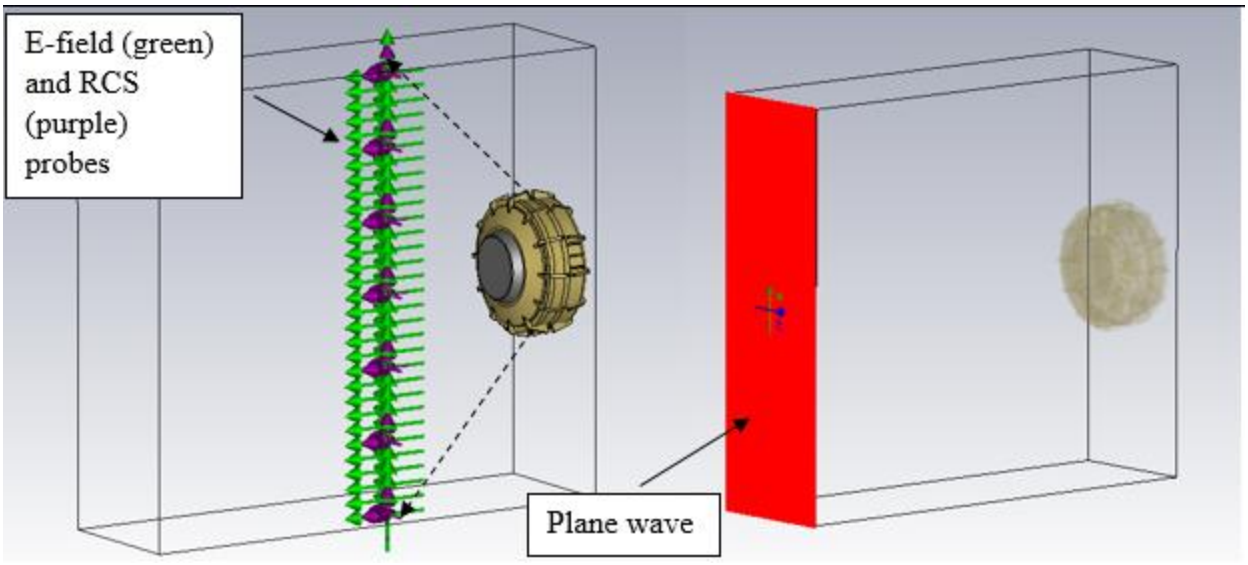

Figure 3-14: Simulation setup of landmine models in free space

Scattering of an electromagnetic wave results from the difference of dielectric constant of the landmine compared with the host material that it is buried in. The RCS and the radiation characteristics of cylindrical landmines are well understood as described by Skolnik (*2008*). AP landmines may have a number of scattering centres, each with their angular radiation pattern and in the case of plastic landmines, the internal structure of the landmine may generate additional scattering. Most plastic landmines can be considered as multiple layered dielectric cylinders, of which each interface causes a reflection. However, only a high bandwidth signal would be able to resolve theses interfaces. As shown in Fig. 3.14, the models of landmines are studied regarding their scattering properties, from the angle of incident equal to the angle of reflection as well as other angles as indicated by the black arrows in the figure. Figures 3.15 and 3.16 show the A-scan responses (amplitude vs. time) of the landmines in free space from boresight direction and a standoff clearance of 20 cm. Other aspects of the radar cross section of landmines are concerned with the relative contributions of specular reflections, diffraction off discontinuities, travelling wave including direct illumination running wave, creeping wave on metal, trapped guided wave on dielectric as well as the contribution due to resonant scattering. There are all a combination of discontinues that allow the echo to build up *(Desai, 2001)*.

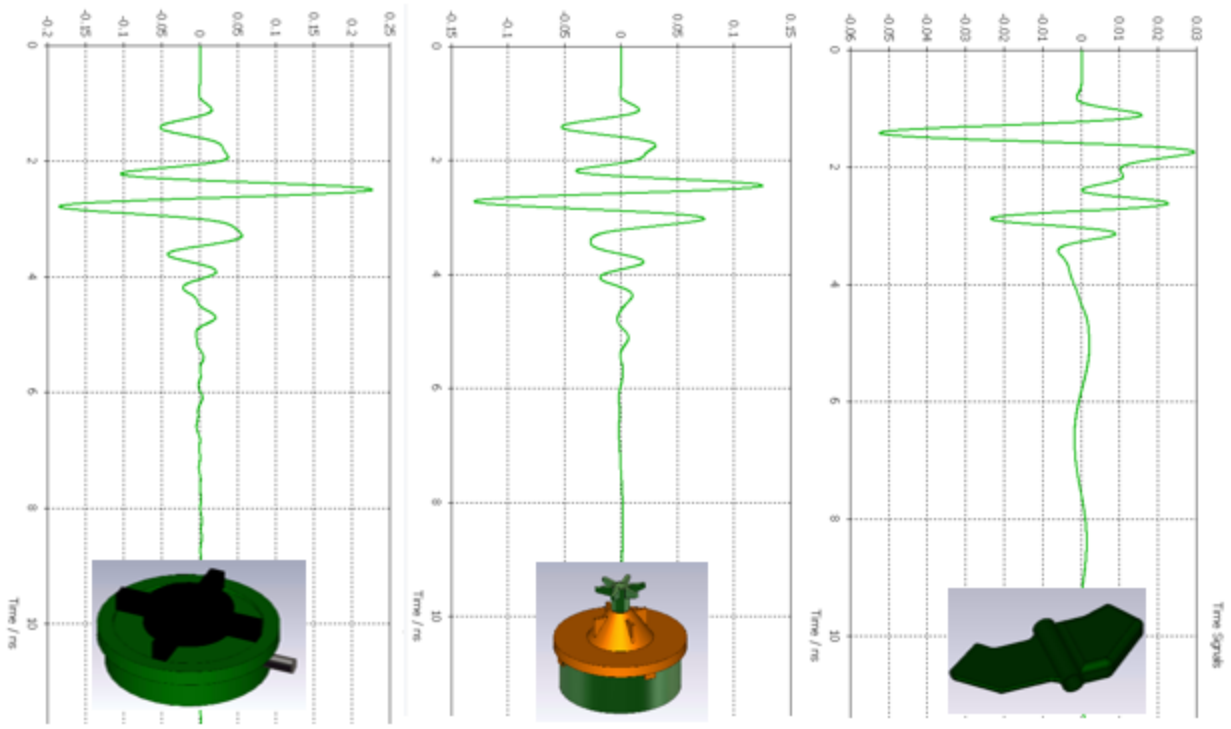

Figure 3-15: PMN-2 (left), PMA-2 (middle), PFM-1(butterfly) (right)

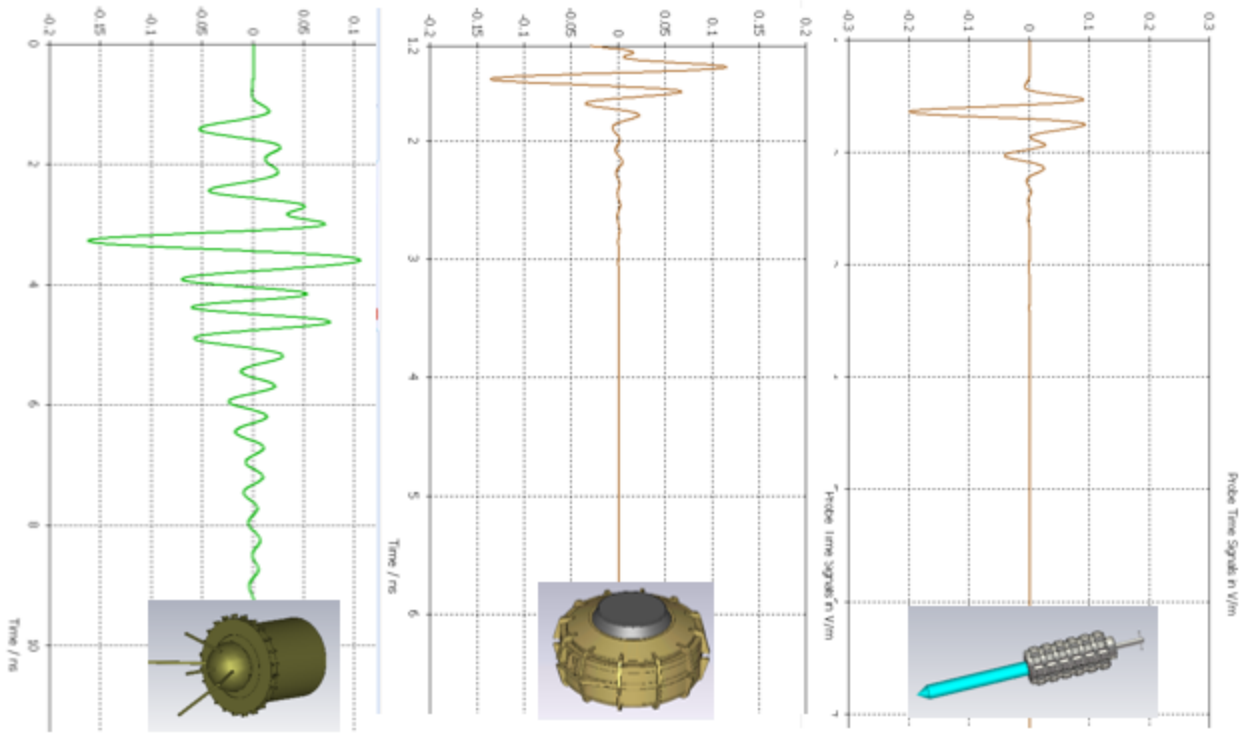

Figure 3-16: Valmara-69 (left), VS-50 (middle), Type 58 (right)

In addition to A-scan information, simulation can be used to study other aspects of the scattering properties of 3D targets. As described in Fig. 3.14, the data from linearly scattered E-fields can be analysed and an image of the target can be reconstructed using appropriate processing. Figure 3.17 shows a B-scan image from a VS-50 landmine in free space and for a comparison, a flat metal target is also presented.

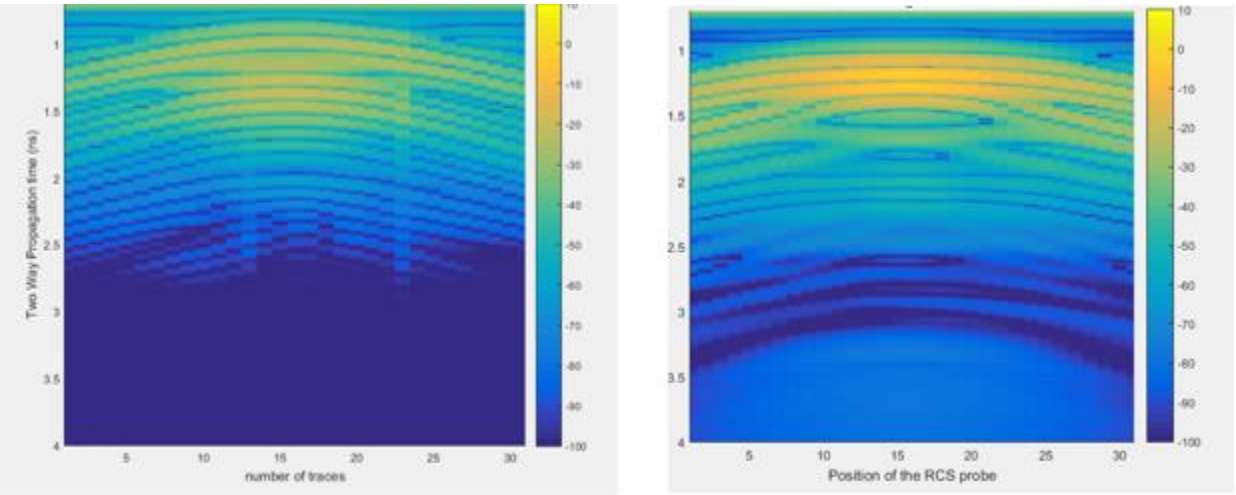

Figure 3-17: B-scan simulation of a VS-50 (left) and a flat metal target (right)

The image for the VS-50 and other landmine models appear as a hyperbolic image or a curve of maximum convexity, compared to a relatively flat image of a flat metal target. A hyperbolic curve is the fundamental indication of small and complex objects. Almost all targets except spherical targets at extremely high frequencies are dependent on operating frequency *(Microwaves 101, 2015)*. By looking at the RCS along the target with an angle defined by the points where the RCS is measured, this effect can be investigated for a VS-50 and a flat target. In Fig. 3.18, RCS patterns are shown for a range of frequencies on the x-axis for a number of points along the target dimension. It can be seen that for the VS-50 the maximum RCS appears when the target is facing the RCS probe directly above it as expected. However only a few frequencies show strong reflection from the target; these are indicated around 4 and 7 GHz. In comparison to a flat target, much higher reflectivity is shown at all frequencies and positions, with a maximum when the flat target is facing the radar. This suggests that for small plastic targets of the same nature as the VS-50, frequencies above 3 GHz show a good reflectivity. However, lower frequencies show more reflection from larger metallic targets over a wider angle.

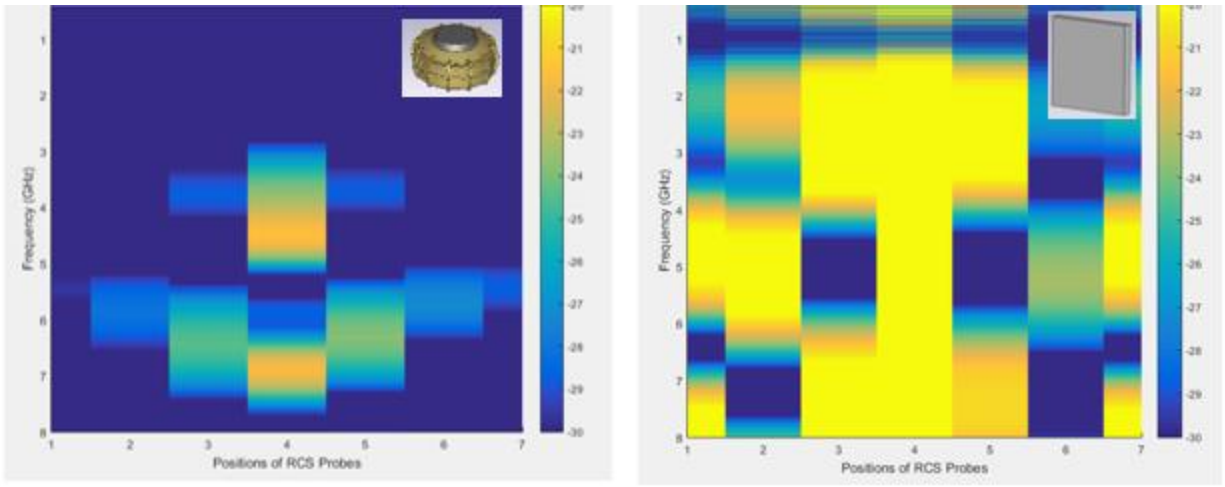

Figure 3-18: RCS pattern of a VS-50 AP landmine (left) and a flat metal (right)

For the butterfly type landmine, RCS patterns only show strong reflections at frequencies above 5 GHz over a narrow angle. However for a Type 58 stick landmine, lower frequencies show a better pattern over a larger angle. The pattern of the RCS also shows a general trend in geometrical shape of the target over a particular frequency range. For instance in Fig. 3.18 the hyperbolic curve of the VS-50 can be seen over a frequency range of 5 to 8 GHz. In Figure 3.19, stronger and asymmetric distribution seem to appear over the frequency range of 1 to 3 GHz for Type 58 landmine.

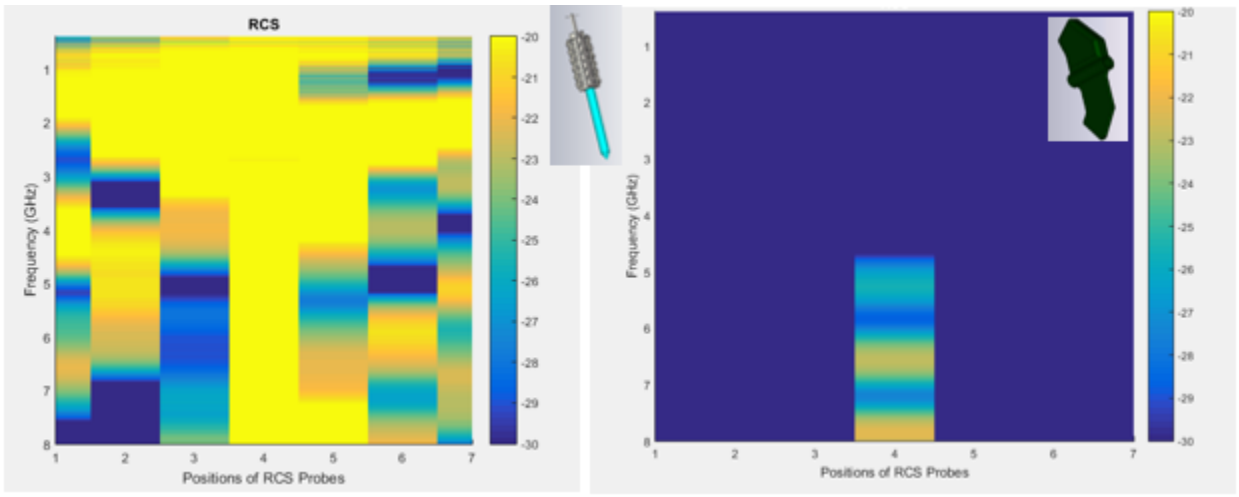

Figure 3-19: RCS pattern of Type 58 (left) and a butterfly landmine (right) AP landmine

3.4.2 Modelling of Typical AV Landmines

AV landmines are larger in size and are made of metal. Four common AV landmines described in Chapter 1 are modelled. The material for the casing of the landmines is assumed as Perfect Electrical Conductor (PEC). Figure 3.20 shows the modelled AV landmines. Similar analysis was performed to assess the scattering properties of AV landmines. Due to the large structure of these landmines, the RCS patterns shown in Fig. 3.21 suggest a larger reflectivity over a wide angle and frequency range. The circular pattern and the rectangular pattern of both AV landmines can also be seen. The signal level in Fig. 3.21 suggests that flat linear targets reflect more of the signal towards radar as opposed to targets such as TMRP-6 with complex features.

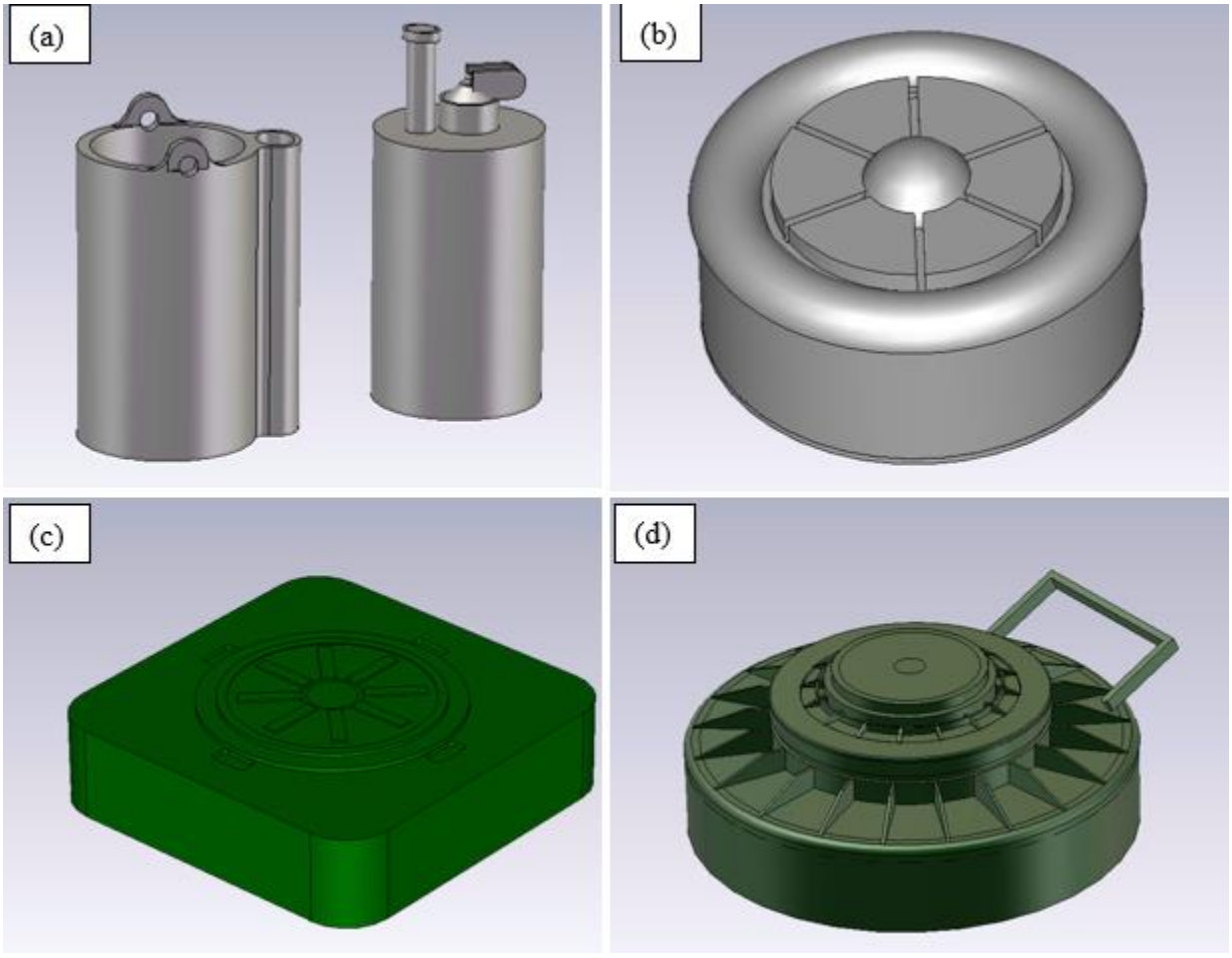

Figure 3-20: 3D CAD models of AV landmines - MK2 (a), AV like test model (b), M19 (c), TMRP-6), (d)

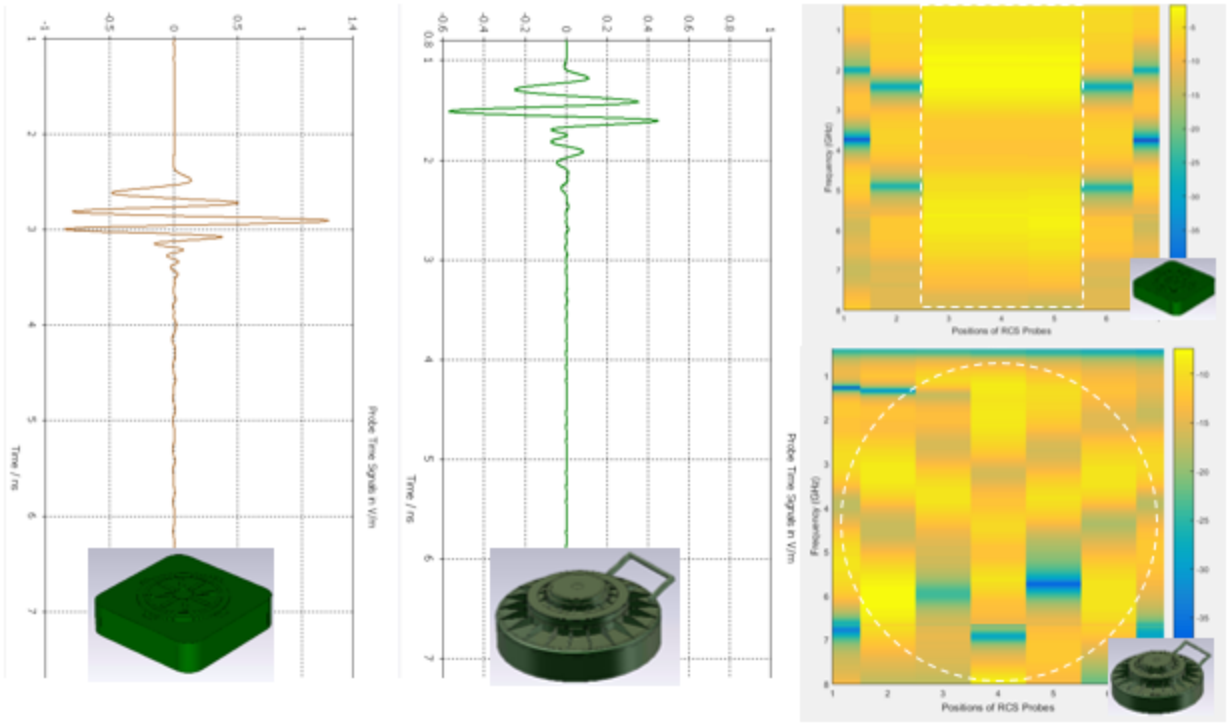

Figure 3-21: RCS pattern of AVM19 (left) and TMRP-6 (right) AV landmines

3.5 Multi-Frequency and Configuration in GPR Simulation

From the simulation results, it has been found that illuminating signals in the different frequency bands and with different radiation patterns on the target result in different target scattering, hence different acquired images. This is well demonstrated by a GPR simulation setup where the scenario is a TMRP-6 AV landmine buried 2 cm in the dry sandy soil as shown in Fig. 3.22. The illuminator is a novel antenna design that is described in Chapter 5. The surrounding environment is enclosed by wood and natural rubber (similar setup to the experimental environment described in Chapter 7) to reduce multipath and reflection from the bottom of the box. The antenna is moved over the target in a linear manner from 0 cm to 72 cm, and the data is recorded at every 1.5 cm step. First, the antenna is operating at 0.5 to 5.5 GHz and is vertically polarised. Correct timing and sampling settings are used in the simulation setup to capture each return waveform in time domain. The acquired data is then prepared and processed to reconstruct a B-scan image. Figure 3.23 (left) shows the B-scan of the TMRP-6 AV landmine. And on the right, the outline of the target can be visualised. The strongest feature of the target highlighted by the reflecting signals appears to be the main part of the target which is the activator. Different scattering phenomena can also be observed such as the spreading of the signals from the positions outside the physical dimension of

the target. Also, reflections from the bottom of the target can also be seen. If the top of the target is measured as 6.9 ns for the two-way travel time on the y-axis, and the bottom of the target is measured as 7.5 ns, then the corresponding distance can be calculated. Taking into account the dielectric constant of the dry sandy soil, this distance is 11.3 cm which is very close to the actual height of the target (e.g. 11cm).

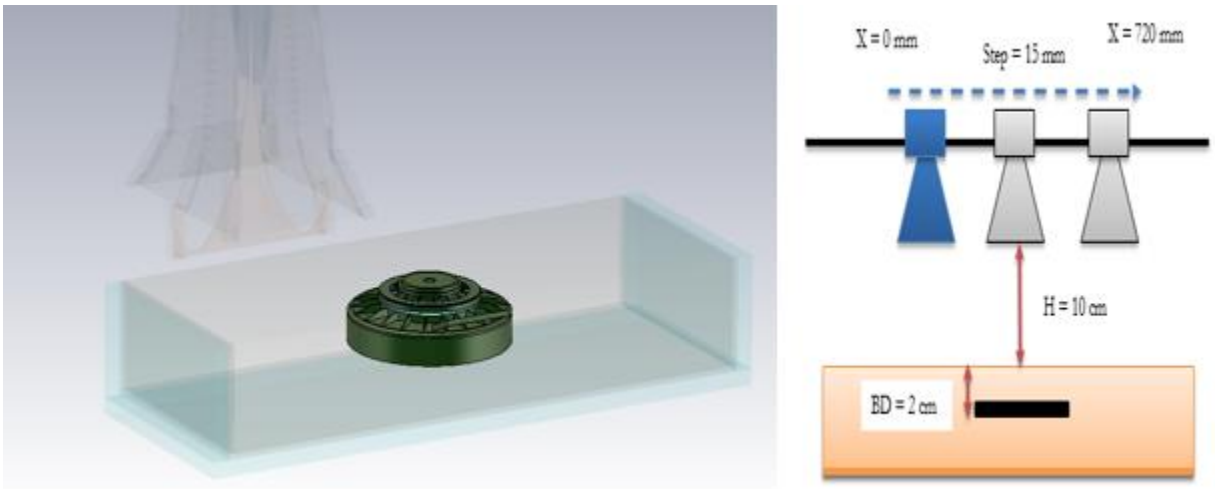

Figure 3-22: Full GPR simulation for a buried TMRP-6 AV landmine

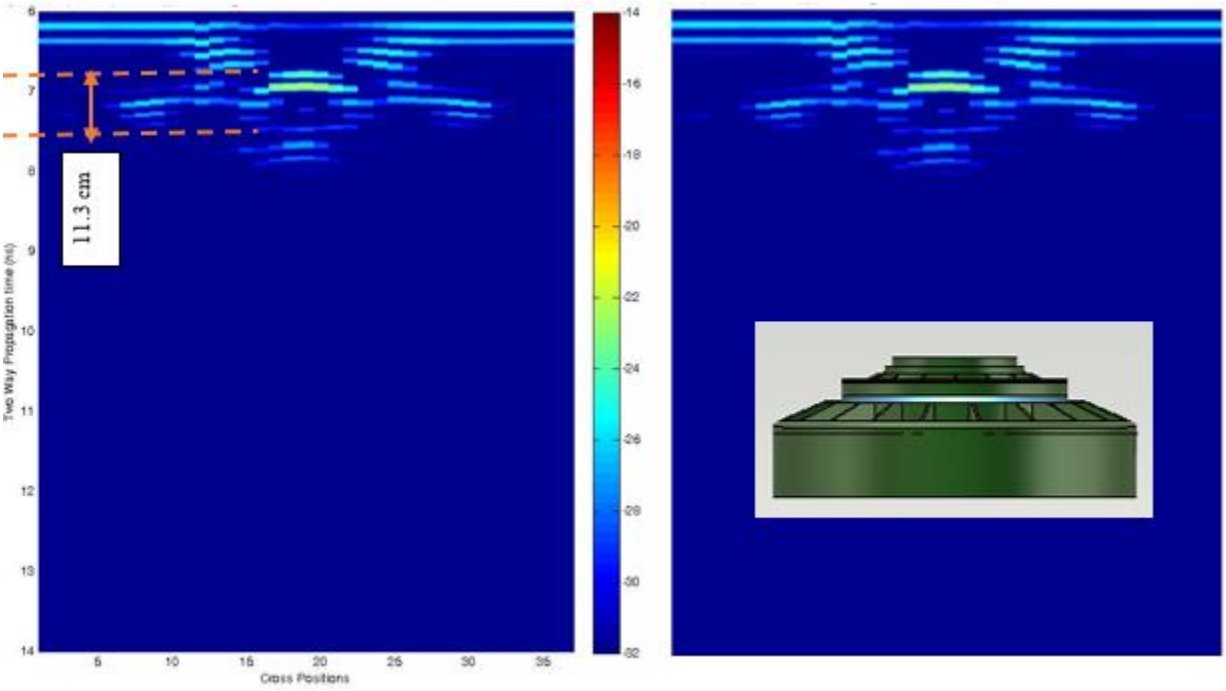

Figure 3-23: B-scan simulation of a GPR model for a TMRP-6 landmine from 0.5 to 6 GHz

The antenna is now switched to a frequency band of 3 to 6 GHz and is horizontally polarised. As described in Chapter 5, this particular antenna operates from a pair of sub-antennas. Therefore, different configurations can be used to acquire the data from the same aperture of the overall antenna structure. Figure 3.24 (left) shows the acquisition of the data (transmit and receive) from one of the antennas. And on the right, the pair is used in a bistatic mode, where one antenna is used as a transmitter while the other as a receiver. This antenna pair has a radiation pattern different to the 0.5 to 5.5 GHz band as well as different radiation characteristics such as time domain response etc. Figure 3.25 illustrates the B-scan of the TMRP-6 in a monostatic (left) and a bistatic (right) mode. In the monostatic mode, the image suggests, the main features having strongest reflections are the edges of the target. And in the bistatic mode, the top part of the target is strongly highlighted. In contrast to the 0.5 to 5.5 GHz, this shows better signal quality for top and edges of the target, however, height information is lost. It can be concluded that the combination of both antennas can be used to enhance the reflectivity of a particular feature and hence improving the quality of the image.

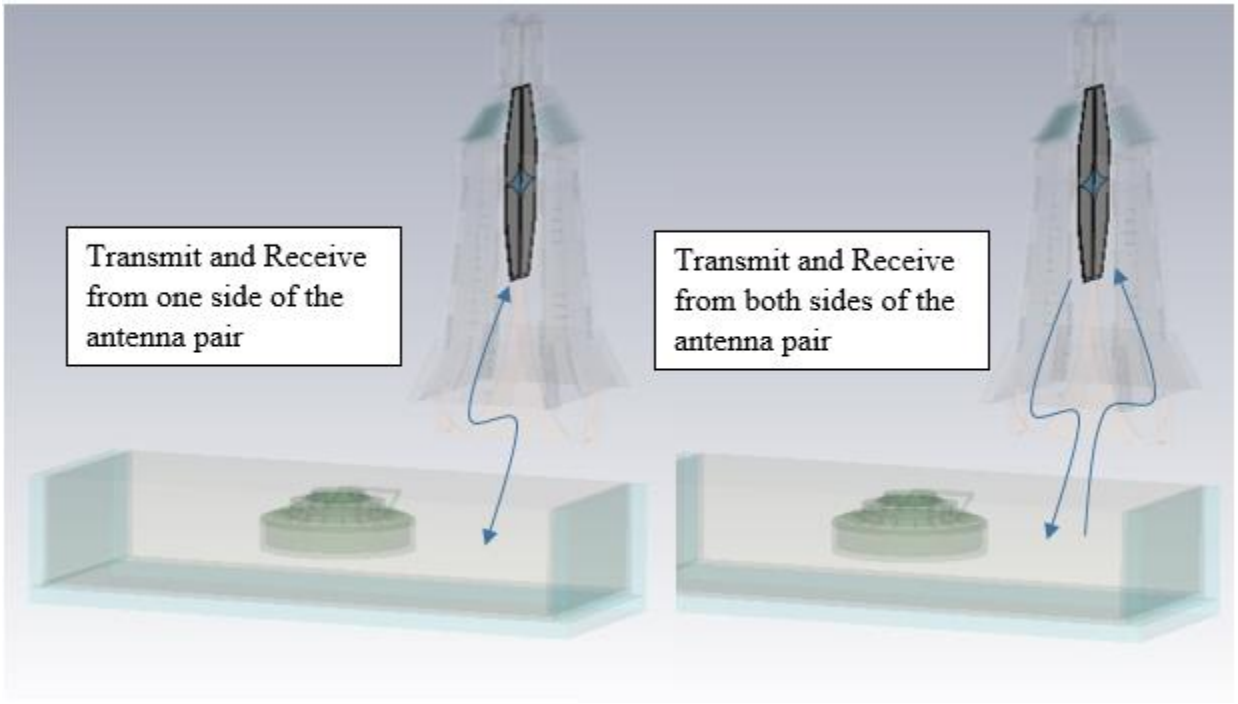

Figure 3-24: Simulation setup of a GPR model for a TMRP-6 landmine from 3-6 GHz in a monostatic (left) and a bistatic (right) mode

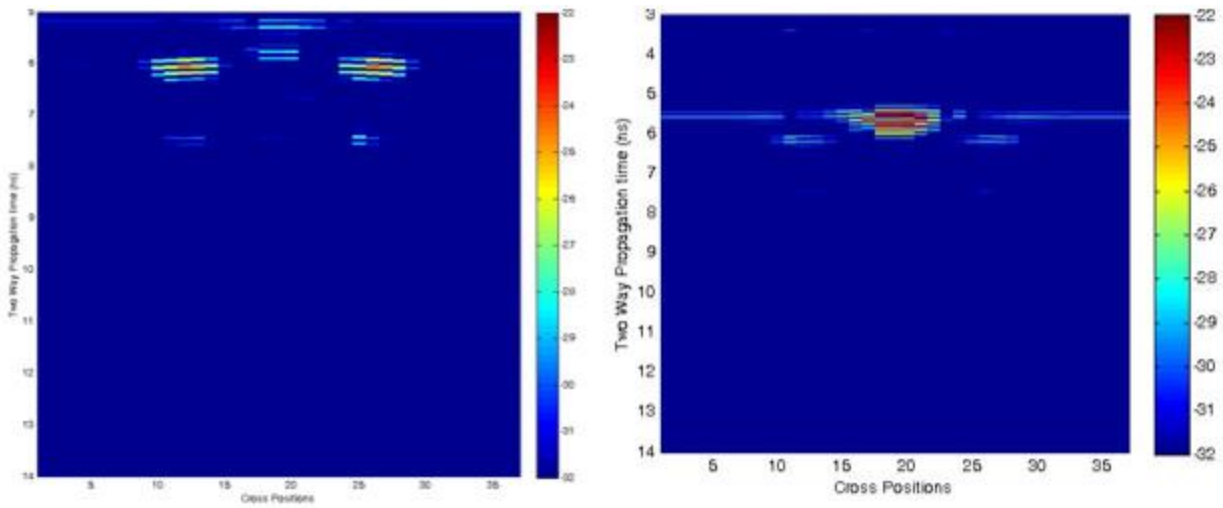

Figure 3-25: B-scan simulation of a GPR model for a TMRP-6 landmine from 3-6 GHz in a monostatic (left) and a bistatic (right) mode

3.6 Summary

There are many different modelling methods including ray tracing, MoM, FIT and FDTD techniques. However, FIT has become one of the most common in the past few years, particularly with access to inexpensive computational resources. CST Microwave Studio has been used to provide an effective modelling tool and gain useful insight into the basic capability of a particular GPR system performance. Full three-dimensional modelling has been performed in the consideration of time domain signatures of multiple reflecting layers and realistic models of landmines. This chapter has provided an initial insight into the range of approaches that have been taken to predicting the reflected signals and EM fields from buried targets. Also, an estimate of the expected reflecting power level from plastic landmines have been investigated. Realistic soil model has been used to study the attenuation level it introduces in the propagation path. The key parameters of the radar including operating frequency and bandwidth have also been discussed. It is found that to be able to distinguish layers close in down range, pulses of the order of 1 ns (or less) are needed for an adequate bandwidth. However, as shown, higher frequencies suffer great attenuation. Therefore, lower frequencies can be used to probe deeper with minimum attenuation. The flexibility of using both cases provide the ability to operate in various environmental conditions.

3.7 References

Andrusenko, J., Burbank, J., Ward, J. (2009). *Modelling and Simulation for RF Propagation*. APL. The John Hopkins University.

CST (2012). *CST Studio Suite Manual 2012*. Computer Simulation Technology. [Online] Available from: https://www.cst.com/Content/Media/cst-studio-suite-2012-brochure-low.pdf

Daniels D.J. (2004). *Ground Penetrating Radar*. 1st Ed. IET Radar, Sonar, Navigation an Avionics Series 15.

Desai, A.S., Wilkinson, A.J., and Inggs, M.R. (2001). *GPR SAR simulation and image reconstruction*. IEEE International IGARSS '01, Geoscience and Remote Sensing Symposium.

Microwaves101 (2015). *Radar Cross Section (RCS)*. [Online] Available from: http://www.microwaves101.com/encyclopedia/Navy%20handbook/4.11%20Radar%20Cross-Section%20(RCS).pdf

Skolnik, M. (2008). *Radar Handbook.* 3rd Edition. The McGraw-Hill Companies.

Weiland, T., Timm, M., Munteanu, I. (2008). *A Practical Guide to 3-D Simulation*. IEEE Microwave Magazine, Volume 9, Issue 6.

Chapter 4

Measurements of Dielectric Properties of Material

4.1 Introduction

A significant amount of literature exists on dielectric properties of earth materials and man-made objects. It has been proven experimentally that most materials within the subsurface of the earth have a great impact on electromagnetic radiation *(Hippel, 1995 and Loor, 1983)*. The attenuation of electromagnetic waves rises with frequency, and at a given frequency, wet (e.g. moisturised) materials introduce a higher loss than dry ones. This is because at high frequency any material behaves as dielectric and the displacement current dominates the conducting current *(Santamarina, 2001 and Olhoeft, 1981)*. From this generalisation, it is important to understand the characteristics of materials in which the EM waves propagate. The velocity of propagation and attenuation of different materials need to be investigated for the GPR to be useful in a particular application. In low electrical loss materials, where conductivity is zero, signals would penetrate to great depth. In practice earth materials are comprised of many other materials or compounds, for example, dry sand can be a mixture of soil grains and air each having slightly different electrical properties.

The dielectric properties of the material that are important in GPR applications are mainly permittivity and permeability. Resistivity is another material property which is of importance in other sensing techniques such as Electrical Resistivity Tomography (ERT). The permittivity and permeability of material are not constant. They change with frequency, temperature, orientation of the material under test, mixture of the material filling, pressure, and molecular structure of the material. They determine the electromagnetic wave reflectivity and velocity. The material is said to be dielectric if it can store energy when an external electric field is applied. Permittivity describes the interaction of a material with an electric field E and is a complex quantity *(Hippel, 1954)*.

$$k = \frac{\varepsilon}{\varepsilon_0} = \varepsilon_r = \varepsilon_r' - j\varepsilon_r'' \qquad (4.1)$$

The dielectric constant (k) is equivalent to relative permittivity (ε_r) or the absolute permittivity (ε) relative to the permittivity of free space (ε_0) which is $8.854 \times 10^{-12}\, m^{-3}kg^{-1}S^4A^2$. The real part of permittivity (ε_r') is a measure of how much energy from an external electric field is stored in a material. The imaginary part of permittivity ($\varepsilon_r^{"}$) is called the loss factor and is a measure of how dissipative or lossy a material is to an external electric field. The imaginary part of permittivity ($\varepsilon_r^{"}$) is always greater than zero and is usually much smaller than (ε_r'). The loss factor includes the effects of both dielectric loss and conductivity.

When complex permittivity is drawn as a simple vector diagram shown in Fig. 4.1, the real and imaginary components are 90° out of phase. The vector sum forms an angle δ with the real axis (ε_r'). The ratio of the energy lost to the energy stored is the definition of the overall loss of a material.

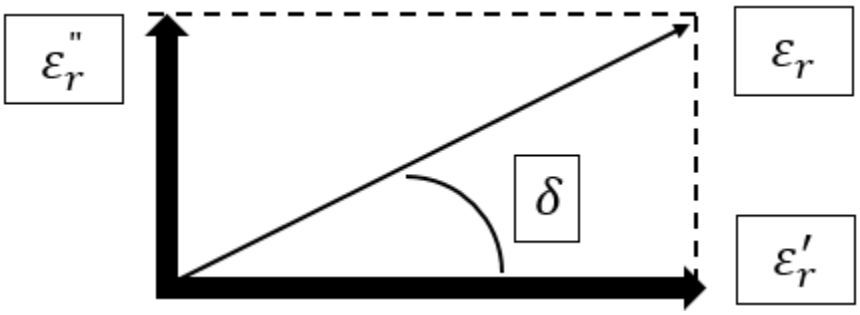

Figure 4-1: Loss tangent vector diagram

The loss tangent (tan δ) is defined as the ratio (or angle in a complex plane) of the lossy reaction (resistive) to the electric field E in the curl equation to the lossless reaction (reactive) or from the diagram is the ratio of the imaginary part of the dielectric constant to the real part. It is also known as dissipation factor (D) and is shown in Eq. 4.2 *(Rohde & Schwarz, 2006).*

$$tan\ \delta = \frac{\varepsilon_r^{"}}{\varepsilon_r'} \qquad (4.2)$$

Permeability describes the interaction of a material with a magnetic field. The complex permeability (μ) consists of a real part (μ') that represents the energy storage term and an imaginary

part ($\mu^{"}$) that represents the energy loss term. Relative permittivity μ_r is the permittivity relative to free space. This is shown in Eq. 4.3.

$$\mu_r = \frac{\mu}{\mu_0} = \mu_r' - j\,\mu_r^{"} \qquad (4.3)$$

where $\mu_0 = 4\pi \times 10^{-7}$ H/m is the free space permeability

Most of the materials for GPR applications are nonmagnetic making the permeability close to the permeability of free space $\mu' = 1$. The velocity of propagation is mainly governed by the dielectric properties of the materials and their water content so it decreases with increasing relative permittivity. The wavelength (in meters) within the material also decreases as the velocity of propagation decreases in accordance with Eq.4.4.

$$v_r = \frac{c}{\sqrt{\varepsilon_r}} \qquad (4.4)$$

When an electromagnetic wave interacts with a material of different electrical properties, discontinuity happens, and this causes the waves to reflect or scatter. The Fresnel reflection theory and Snell's law both quantify how the amplitude and direction of the electromagnetic fields vary across an interface between two materials. Figure 4.2 shows a two-layer medium in which the intrinsic impedance of the layers determine the transmitted and reflected energies. Equation 4.5 shows the relation between the dielectric constant of the material in each layer and the reflection coefficient, assuming the medium is a non-conducting and homogenous material. This relation is represented in Fig. 4.3. In this range, dielectric constant measurement using the reflection coefficient will be more sensitive and hence precise. Conversely, for high dielectric constants (for example between 70 and 90) there will be little change of the reflection coefficient and the measurement will have more uncertainty. The reflection coefficient has a positive value when $\varepsilon_r 2$ (from layer 2) > $\varepsilon_r 1$ (Layer 1, e.g. air).

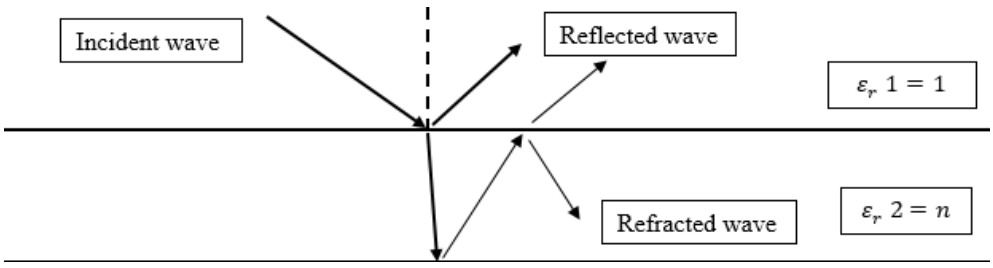

Figure 4-2: Multi-layer dielectric ground

$$r = \frac{\sqrt{\varepsilon_r\,2} - \sqrt{\varepsilon_r\,1}}{\sqrt{\varepsilon_r\,2} + \sqrt{\varepsilon_r\,1}} \qquad (4.5)$$

where $\varepsilon_r 1$ and $\varepsilon_r 2$ correspond to the dielectric constant in layer 1 and 2, respectively.

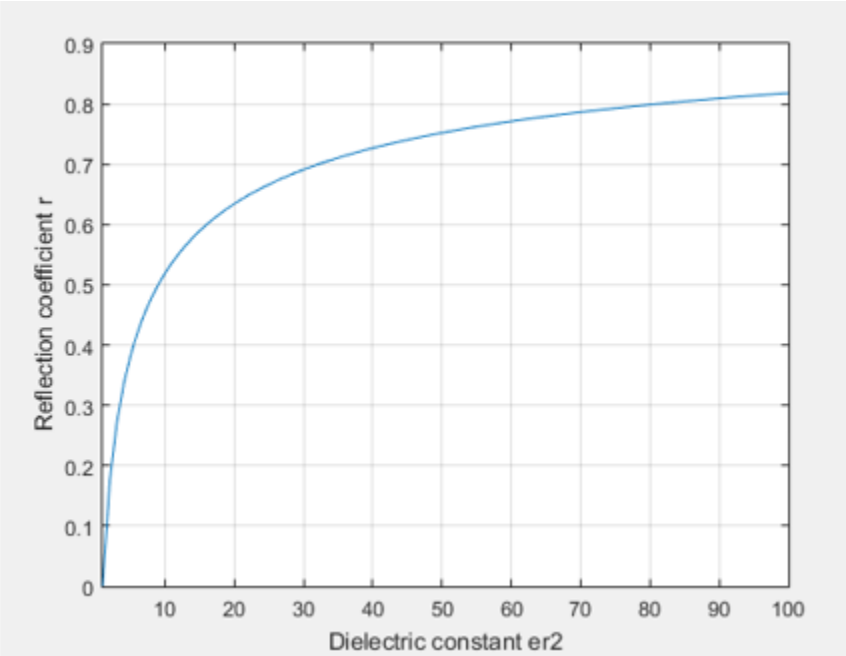

Figure 4-3: Reflection coefficient versus dielectric constant

It can be seen that the amplitude of the reflected signal can be affected by the dielectric constant of the host material (layer 2). Higher dielectric constant from materials such as water or wet sand tends to reflect most of the energy back towards the radar and lets a small amount of the signal to propagate into the material. Although the operating frequency influences this generalisation, because the dielectric constant is very much frequency dependent. For example, dry sandy soil can have a dielectric constant of around 2.5 at high frequencies (e.g. 8 GHz) but will have a lower dielectric constant of around 2 at lower frequencies (e.g. 1 GHz) as seen later in the chapter.

4.2 Laboratory Measurements of Dielectric Materials

It is well understood that the dielectric properties of materials vary with frequency. Numerous methods have been employed to create a suitable measuring technique best suited to the particular frequency range. In general, at lower frequencies, a parallel plate capacitor or an impedance bridge method can be used. In higher frequencies, it is reported that resonant cavity, waveguide and transmission line methods are best suited *(Agilent, 2006)*. For GPR applications, it is imperative to understand and be able to measure complex dielectric properties of the ground materials at

desired frequencies. This is of great importance especially in GPR signal processing and antenna design. For example, to be able to estimate accurately the depth of a target, the dielectric constant of the ground material has to be known.

There is a wealth of information available about the dielectric constant of various materials. However, they tend to vary from one site to another, their conditions and sample size. Many techniques have been developed to measure these complex properties such as techniques in time domain or frequency domain with one port or multiple ports. Every technique is limited to specific application regarding the frequencies and materials. Some of the common methods described by Rohde & Schwarz dielectric measurements *(2006)* are summarised below:

- Parallel Plate: (sometimes called capacitance method), uses a parallel plate capacitor, with the material sandwiched in between. This method uses an impedance analyser. It is typically used at the lower frequencies, below 1 GHz.

- Coaxial probe: This method uses an open-ended coaxial probe, usually with a network analyzer. It is the easiest method to use for liquids, or soft semi-solids, although very flat hard solids can be measured as well. Many instruments offer probes in the RF to microwave frequency range, 200 MHz to 50 GHz.

- Resonant Cavity: This method uses a resonant cavity for the sample holder, and a network analyzer to measure the resonant frequency and Q of the cavity, both empty and with the sample present. From this, permittivity can be calculated. This method has the best loss factor resolution.

- Transmission/Reflection Line: This method involves placing a sample in a section of the waveguide or coaxial line and measuring the two ports complex scattering parameters with a Vector Network Analyser (VNA). Coaxial lines and waveguides are commonly used to measure samples with medium to high loss.

- Free Space: This method allows measurements under high temperature or hostile environment and operates in wideband frequencies. The measurements are performed by placing the sample holder midway between two antennas (usually horn antennas). The

material is then placed on the sample holder between the antennas, and the measurements are taken.

With the advance of new technologies, the techniques can be employed with a software program that measures the complex reflection and transmission coefficients with a VNA and converts the data into the complex dielectric property parameter. The outcome of these techniques mainly depends on the following:

- Frequency of interest
- Expected value
- Required measurement accuracy
- Material properties (e.g. homogeneous, isotropic)
- Form of material (e.g. liquid, powder, solid, sheet)
- Sample size restrictions
- Destructive or non-destructive
- Contacting or non-contacting
- Temperature

4.2.1 Coaxial Probe Dielectric Measurement

In this section, measurements of dielectric constant using coaxial probe technique are discussed and presented. This technique involves resting an open-ended coaxial probe against a sample of material and the reflection coefficient is measured. The measured reflection coefficient is then be used to determine the permittivity. Calibration of the probe for acquiring accurate readings is important. This is to ensure that the reflection coefficient measurements are referenced to the aperture plane. The calibration process usually is to calibrate the system by connecting the probe to three material of air (open circuit), metallic shorting block, (short circuit) and deionised water. It is important to make a good contact between the probe and the material to avoid any air gaps. The sample size under the test has to be thick enough in all directions to avoid the reflections from the boundaries of the sample holder. Common practice is a quarter wavelength of the frequency of interest.

The most well-known product that provides this measurement technique is the Keysight 85070E dielectric kit. The system comes with a software package that converts the reflection coefficient

readings into dielectric properties values. Figure 4.4 shows the dielectric kit and the measurement equipment. The measurement setup consists of a Vector Network Analyser (VNA) E5071C operating from 9 kHz to 8.5 GHz, the high-temperature coaxial probe with the shorting block and deionised water for the calibration process.

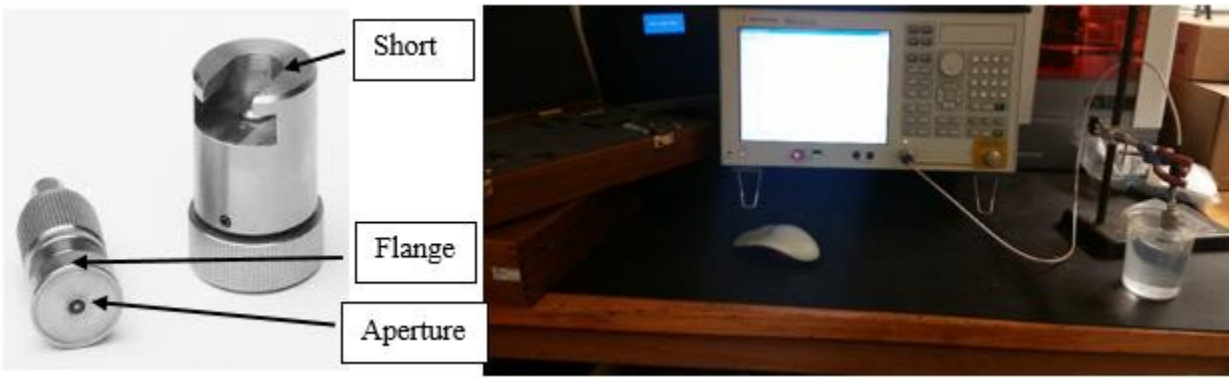

Figure 4-4: Coaxial probe dielectric kit and measurement setup – (left) Dielectric Probe Kit (Source – Agilent, 2006), (right) Dielectric Measurement Setup

For the measurement, first, the frequency operation of interest is entered, followed by the calibration process. A flexible and a good quality cable is then connected to the probe. The calibration accuracy can be furthered increased by calibrating the cable separately (using, short, open and load) before the calibration of the overall cable and the probe. The open-ended coaxial probe is a cut off section of a transmission line. The material is measured by inserting the probe into a liquid or touching it to the flat face of a solid (or powder) material. The fields at the probe end "fringe" into the material and change as they come into contact with the material. This is shown in Fig. 4.5.

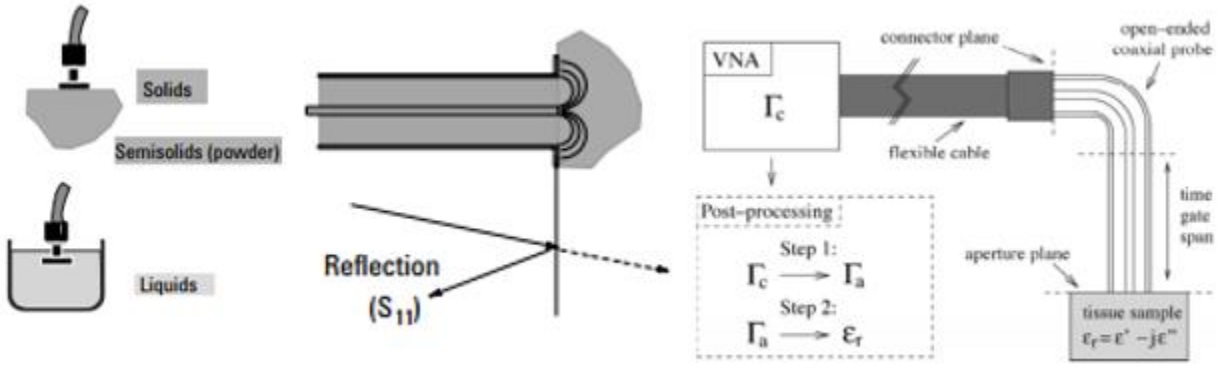

Figure 4-5: Coaxial probe method. Sources: Agilent, (2006) and Rohde & Schwarz, (2006)

The sources of error can be reduced by a) cable stability, b) minimising air gaps and c) sample thickness. It is important to allow enough time for the cable (that connects the probe to the network analyser) to stabilise before making a measurement and to be sure that the cable is not flexed between calibration and measurement. The quality of the cable also influences the results. For solid materials, an air gap between the probe and sample can be a significant source of error unless the sample face is machined to be at least as flat as the probe face. For liquid samples air bubbles on the tip of the probe can act in the same way as an air gap in a solid sample. When inserting the probe into liquid or powdered material, it can be inserted at an angle and then back to a flat surface inside the material to minimise the build-up of bubbles or air gaps. The sample holder in this measurement consisted of an air foam placed on a block of Radar Absorbent Material (RAM) and the thickness of the sample material was ensured to be more than a quarter wavelength at the frequency of interest. Figure 4.6 shows a few materials under tests such as dry sandy soil (a), loamy soil (b) and beach sand (c).

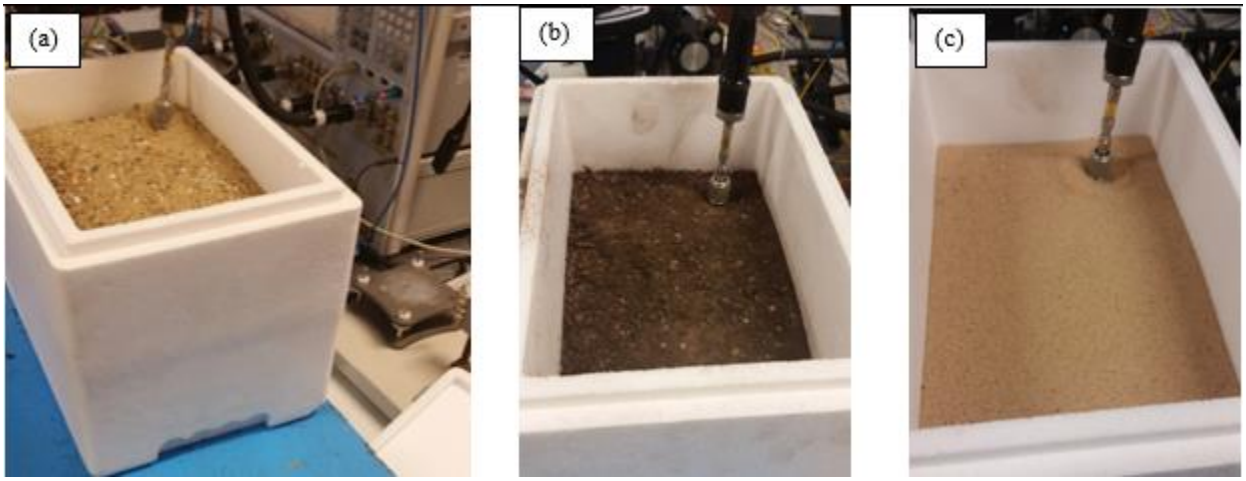

Figure 4-6: Dielectric measurement for a) dry sandy soil, b) loamy soil, c) beach sand

An example dielectric constant measurement is shown in Fig. 4.7 and Table 4.1 presents the dielectric properties in the frequency range of 0.4 GHz to 8.5 GHz for a list of materials that were of interest for the purpose of GPR work undertaken. As can be seen from Fig. 4.7 there is fluctuations in the reading of the values, and this directly relates to the sources of the errors that could be present in the measurements system. Lower frequencies show a huge drop towards 1, and this indicates the possible presence of air gaps and instability of the probe. The airs gaps are mainly introduced by the ratio of the size of the probe to the sand grains. The outer connector of the probe

has a radius of less than 5 mm which means that it may not be able to resolve the surface with large grains of the material. However, the results show a reasonable quality of measurement for the dielectric constant of the material.

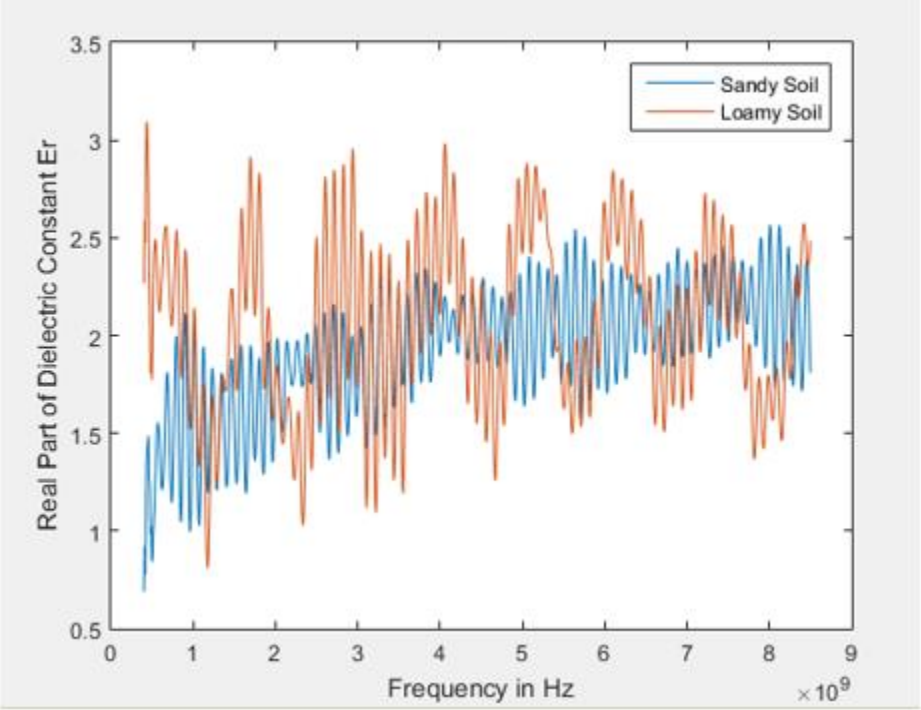

Figure 4-7: Dielectric constant of Sandy soil and Loamy soil

The average value of the dielectric constant for the dry sandy soil appears to lie around 2.1 and for loamy soil just below 2. However, values up to 3 for dry sandy soil and 2.5 for loamy soil can be seen at different frequencies.

Material	**Loss tangent,** $tan\delta$	**Relative permittivity,** ε_r	**Propagation velocity,** v_r (ms^{-1})
Air	0	1	3×10^8
Sandy soil – sharp (dry)	0.0036	2.53	1.9×10^8
Sandy soil – normal (dry)	0.0029	2.1	2.1×10^8
Sandy soil – normal (wet)	0.29	13	8.3×10^7
Rogers RO435 substrate	0.0037	3.48	1.6×10^8
Wood	0.1	1.22	2.5×10^8
Dried peanuts	0.08	3	1.7×10^8
Paraffin Wax	0.02	2	2.1×10^8
Concrete	0.0111	4.5	1.4×10^8
ABS Plastic - 3D printing material	0.07	2.5	1.8×10^8
Paper	0.0053	3.0	1.7×10^8

Table 4-1: Dielectric properties of various materials

The values for the dielectric constant of various materials reported in Table 4.1 were measured by the open-ended coaxial technique mentioned earlier in the chapter. The accuracy of the values was dependent on the sample size and texture.

For GPR applications, the most important microwave characteristics of earth materials are the relative dielectric constant and attenuation. The values of the dielectric constant can be used to estimate the depth of the target in GPR signal processing of the acquired data. This is only an estimation and has to be considered carefully since the values of the dielectric properties can change due to the variations often encountered by the measurement technique and sample conditions.

4.3 Summary

A laboratory open-ended coaxial probe technique was used to measure the dielectric constant of the materials of interest in the context of GPR. The values of the dielectric constant were found out to be mainly dependent on the sample size, shape, and operating frequency. Nevertheless, the values were in good agreement with the ones reported in the literature. To assess the performance of the GPR, values of the dielectric constant should be taken into account. However, the actual performance of the radar can vary due to the wide variations often encountered in local material conditions. For example, the laboratory dry sandy soil (sharp sand) which was used for the GPR measurements were found to have a dielectric constant of 2.5. In contrast, when GPR field measurements were performed in a different environment (e.g. Cranfield University sand pit), the

dry sandy soil under test was found to have a dielectric constant of 2.1. Not only is the range but also resolution in depth affected by the attenuation of the material. Initial calibration or separate measurements are needed to predict the dielectric properties of the material under test for each environmental conditions.

4.4 References

Agilent Application Note. (2006). *Agilent Basics of Measuring the Dielectric Properties of Materials*. Agilent Technologies, USA.

Loor, G. P. (1983). *The Dielectric Properties of Wet Materials.* IEEE Transactions on Geoscience and Remote Sensing, Volume 21, Issue 3.

Hippel, A.R. (1954). *Dielectric Materials and Applications.* MIT Press, Cambridge, MA, USA.

Olhoeft, G.R. (1981). *Electrical properties of rocks in Touloukian*. *Physical Properties of Rocks and Minerals*, Vol. II, MGraw-Hill, New York 1981, p.548.

Rohde & Schwarz. (2006). *Measurement of dielectric material properties*, Application Note, [Online] available from: https://www.rohde-schwarz.com/uk/applications/measurement-of-dielectric-material-properties-application-note_56280-15697.html

Santamarina, J.C. (2001). *Soils and Waves: Particulate Materials Behaviour, Characterisation, and Process Monitoring*. John Wiley and Sons, Sussex, England.

Chapter 5

Antenna Design for GPR

5.1 Introduction

It has already been discussed that an antenna is a piece of crucial hardware for GPR system. The radiation characteristics of the antenna affect the performance of the GPR in regards to the quality of the image and the corresponding resolution of the imaging system. Important parameters of the antenna are the bandwidth of operating frequencies, radiation pattern and radiation efficiency. The propagation medium for the electromagnetic waves contains lossy and inhomogeneous dielectric materials. This imposes frequency dependent attenuation. Low frequencies propagate through the medium with minimum attenuation. The need to obtain high range resolution and lateral resolution requires the antenna to operate at high frequencies with ultra-wide-bandwidth (UWB). To obtain higher bandwidth, higher frequencies should be used. The requirement for wide bandwidth and the high attenuation in upper frequency are mutually conflicting and hence usually a design compromise is adopted where antenna operates at a wide range of frequencies. This chapter addresses the design and development of a new type of antenna that supports a good GPR performance and provides the ability to operate at multiple frequency bands with different characteristics using the same aperture. The proposed antenna behaviour is predicted using a 3D field simulation (CST), prior to fabrication.

In general, when designing any GPR imaging system with desired performance such as ability to detect, image and characterise the target, the following requirements are considered regarding the antenna design *(Daniels, 2007and Jol, 2009)*:

- Adequate aperture size operating over a wide frequency range – this provides the ability to resolve target features spatially in both cross-range and down-range
- Sensitivity to magnitude, phase and polarisation of the scattered signals – The antennas may be designed with dual polarisation or circular polarisation to take advantage of polarimetric techniques for image enhancement.
- Good radiation and transmission performances – the footprint of the antenna contributes to the level of clutter

- Adequate gain, good radiation pattern and phase response across operating band – to avoid signal distortion.
- Low cross coupling levels between multiple channels (antenna inputs)
- Low ringing effects.

5.1.1 Antenna Parameters

An antenna is a device or a system, which is responsible for the region of transition between guided and free space (normally air) propagation. For GPR, it is desirable to have most of the radiation from the antenna coupled into the dielectric medium; therefore, boresight (directive) antennas are efficient in doing so. There are two regions for the waves to interact with the medium, near-field (close to the antenna) and far-field. If the GPR is to operate in the near-field, the radiation and coupling performance (input impedance) affect the antenna design to a considerable extent. In far-field operation, antenna efficiency is more of concern *(Lacko and Clark, 2003)*.

Other antenna parameters that can affect the system include the phase centre location (although this can be calibrated for in signal processing), the gain and the radiation efficiency. Moreover, the polarisation, the corresponding polarisation diversity and different effects of self-clutter, which are known as ring-down or reverberation, have to be taken into account. Such ring-down events, which occur due to an impedance mismatch at the aperture of the antenna, could be misinterpreted as multiple reflections *(Radzevicius, Guy and Daniels, 2000)* and, therefore, have to be avoided in the antenna design process. The following subsections describe the basic parameters of the antenna and the considerations that have been taken into account in regards to GPR.

5.1.1.1 Energy Transfers from the Antennas

It is important to understand the detection capability of GPR antennas operating at near-field or far-field regions. If we consider a small electric dipole radiator with a radiation pattern similar to a doughnut, the total field, radiated field, induction field and quasi-stationary field are all equal in field strength at distance equal to the ratio of wavelength to 2π, which is the boundary between the near-field (less than 1) and far-field (greater than 1). The approximate field boundaries are shown in Fig. 5.1. *(Kraus and Marhefka, 2002)*:

- Electromagnetically short antennas – for antennas shorter than half of the radiating wavelength, the near-field is $r \ll \lambda$ and the far-field is $r \gg 2\lambda$

- Electromagnetically long antennas – for antennas physically larger than half of the radiating wavelength, the near and far fields are defined in Eq 5.1 and 5.2.

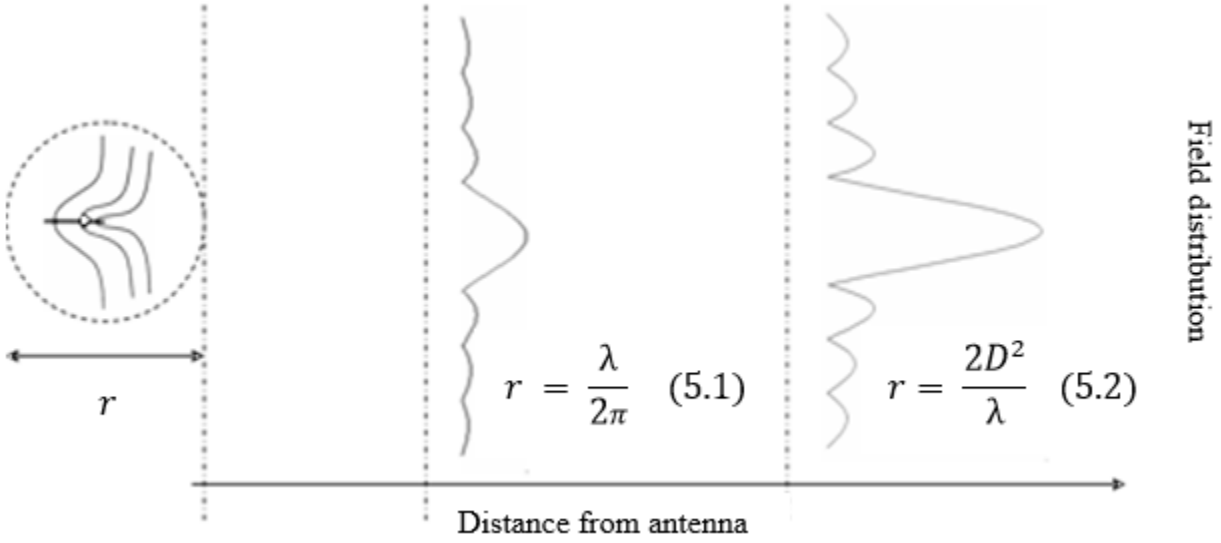

Figure 5-1: Antenna field regions. Source: Ihf (2006)

Any consideration of the signal detected in GPR receiver should therefore fully account for the physical proximity of the antenna and the target. In the case of electromagnetically short antennas and a radiating frequency centred at 0.5 GHz, it can be seen that targets closer than 1.2 m will have increased field contributions, whereas radar radiating shorter wavelengths will lose out on the increased field contributions because it moves into the far-field zone and becomes dependent on the largest dimension of the antenna aperture (D).

5.1.1.2 Directivity and Gain

An antenna gain is a key performance factor, which combines the antenna's directivity and electrical efficiency. In GPR to achieve an acceptable plan resolution (along track resolution), a high gain antenna is required. The directivity of an antenna refers to the degree of sharpness of its beam. This requires the antenna dimensions greater than the wavelength of the lowest operating frequency. To avoid a large antenna dimension, a high carrier frequency should be used. The gain of an antenna is defined as follows:

$$G = {}^{4\pi}/_{\lambda^2} A_{eff} \qquad (5.3)$$

where A_{eff} is the antenna effective aperture and λ is the wavelength of the operating frequency. Directivity is similar to gain but, resistive losses are not included. In Chapter 3, the signal level was investigated for different dimensions of the buried target, therefore, depending on the penetration depth and target size, a rough level of gain for the antenna can be estimated.

5.1.1.3 Bandwidth

An antenna is only effective over a certain frequency range where the radiated energy is of low return loss or, in other words, the Input Voltage Standing Wave Ratio (VSWR) is less than 2. To achieve a good depth resolution, large bandwidth should be used. The GPR bandwidth, sometimes called antenna fractional bandwidth is defined by the following expression in percentage:

$$BW = \left[\frac{2\,(f_{max} - f_{min})}{f_{max} + f_{min}}\right] \times 100 \qquad (5.4)$$

where f_{max} and f_{min} are the higher and lower limits of the frequency range within which some specified fraction (90 – 99 %) of the total signal energy lies *(DARPA, 1990)*. Nearly all GPR systems are required to operate at a fractional bandwidth of higher than 100% for the reasons described in Chapter 3.

5.1.1.4 Polarisation

The polarisation of an antenna is the orientation of the transmitted or received electric fields. The most common forms of polarisation are linear, elliptical and circular. A further consideration in the design of an antenna for GPR is the shape of the target. For instance, when the target is a planar surface then linear polarisation is adequate. However, if the target has a mixture of edges and curves, the backscattered fields experience a characteristic polarisation independent of the state of the polarisation of the incident waves. Therefore, dual or circular polarised (e.g. rotating the polarisation vector in space) antennas can provide better information.

5.1.1.5 Phase Centre

The phase centre of an antenna is considered to be the point from which the electromagnetic radiation spreads spherically outward, with the phase of the signal being equal at any point on the sphere. The importance of the phase centre is related to the characteristics of the radiation field. For instance, some antennas such as log periodic or spiral, the physical position of the source of radiation at a particular frequency will vary along either the length of the antenna or the position

of the antenna. This may introduce signal dispersion particularly in spiral antennas *(Drabowitch et al., 2005)*. In the case of waveguide antennas such as horns, the phase centre depends on the aperture distribution and the taper of the horn, and the resultant far-field pattern is affected by the variation of phase centre. The GPR antennas should have the same phase centre for all used frequencies in order not to change the pulse shape. For dispersive antennas, frequency domain radar systems (e.g. SFCW) are usually used, where the dispersion can be corrected by suitable post-processing of measured data. The phase centre can be estimated by far-field or near-field techniques as well as 3D simulation techniques. To estimate the phase centre of the antenna described in this chapter, a calibration technique was performed by measuring the reflections coming from a metal plate for heights varying between $5 < h < 18$ cm above the ground.

5.1.1.6 Radiation Pattern

The radiation pattern of an antenna is related to the gain versus angle in θ (azimuth) and φ (elevation) planes. From radiation pattern, mainlobe gain, beamwidth, sidelobes and backlobes can be visualised. For downward-looking GPR systems, boresight radiation pattern is required with minimal side lobes and back lobes.

5.1.1.7 Antenna Time Sidelobes and Ringing

Ground penetrating radar systems often operate at short ranges from the ground. Therefore, the rate of decay of energy stored within the antenna is a key factor in the contribution of self-clutter to the complete radar system. The time sidelobes or the impulse response of the antenna can obscure the targets close in range. Control of the range sidelobes in any GPR system is an essential issue for the GPR system performance.

5.1.1.8 Antenna Footprint

The antenna radiation pattern and signal processing govern the azimuth and elevation resolutions of the GPR system. In low attenuation media, the resolution obtained by the horizontal scanning technique is degraded, but employing Synthetic Aperture Radar (SAR) techniques increases the plan resolution. However, in high attenuation media, SAR techniques may not be as useful as it is restricted by the ‘window’ placed across the SAR aperture. The plan resolution of a GPR system is important when there is a need to distinguish multiple targets close to each other at the same depth. The effect of radiation footprint on the ground also needs to be considered, as the distance

of the antenna from the ground is related to the 3 dB footprint and this affects the image resolution as well as increasing the level of ground clutter. Figure 5.2 (b) and equation 5.5 show the conical spreading of radar energy propagating through the medium (with dielectric constant ε_r) and the footprint that it imposes on and below the ground *(Conyers, 2004)*:

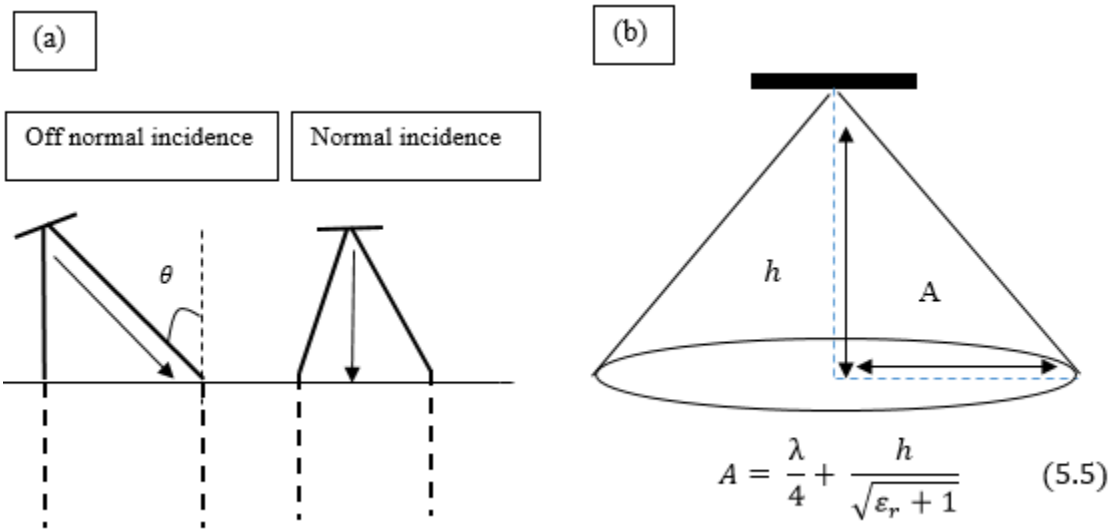

Figure 5-2: Antenna footprint at different angle of incident (a) and antenna footprint estimation (b)

Moreover, the reflection at the air-soil interface usually appears much stronger than the reflection of the target object itself. In *(Magg and Nitsch, 1998)* the successful implementation of a Brewster angle configuration has been reported which eliminates the air-surface reflection by applying a certain inclination angle to transmitting and receiving antenna (Fig. 5.2, a). Unfortunately, the size of the GPR system increases significantly, because the inclination angle of the antennas demands a certain distance between them which increases with higher permittivities of the soil. Moreover, it is very difficult to apply such a setup if the dielectric properties of the soil medium are not constant or completely unknown as it is the case for most field measurements.

5.1.1.9 Antenna Mainlobes, Sidelobes and Backlobes

Mainlobe of the antenna is the lobe that contains the maximum signal strength. The radiation pattern of most antennas shows a pattern of lobes at various angles in the polar coordinate system. In directional antennas where the requirement is to emit the waves in one direction, the lobe in that direction is designed to have the highest field strength than the others (e.g. mainlobe). The other lobes at other angles are called sidelobes. These are known as unwanted radiation in undesired

directions. The lobe that occurs in the opposite direction from the main lobe is called the backlobe. The maximum level of the sidelobe/backlobe and their radiation patterns are often dictated by the requirements of the application or regulatory bodies. In GPR depending on the mode of operation, the side lobes and back lobes are regulated. For instance, in the case of bistatic operation, reduced sidelobes are important to avoid saturation of the receiver and Direct Signal Interference (DSI) from the air and soil interface. Backlobes are often minimised to avoid the reflections that could build up from the structures behind the antenna such as mounts and moving platforms.

5.1.1.10 Antenna Efficiency

Antenna efficiency of an antenna relates to the fact that all antennas suffer from ohmic losses. This is regarded as the power delivered to the antenna and the power radiated or dissipated within the antenna. A lossless antenna would be an antenna with an antenna efficiency of 0 dB (e.g. 100%). Figure 5.3 shows an input signal (red) injected into a lumped dipole (a) and a pin fed circular patch antenna (b). The reflection to the point of excitation from the antenna aperture is shown in green. A good efficiency antenna (a) has most of the power present at the antenna's input radiated away (less reflection). A low-efficiency antenna (b) has most of the power absorbed as losses within antenna or reflected back to its point of excitation due to impedance mismatch. For GPR, the antenna needs to have a high efficiency so it can introduce maximum power into the ground.

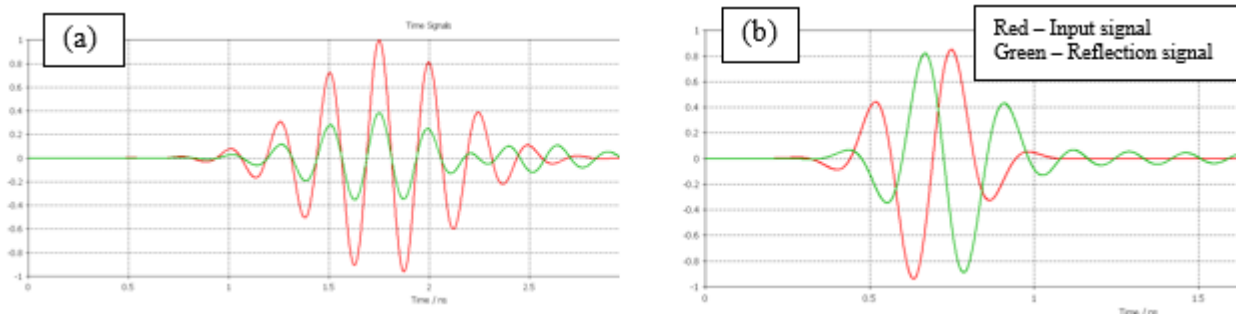

Figure 5-3: Antenna efficiency of two antenna examples, lumped dipole (a) and circular patch antenna (b)

5.1.2 GPR Antennas and Configurations

GPR antennas are designed according to the type of radar system used. If the radar system is a time domain that applies an impulse to the antenna, there is a requirement for linear phase response across the operating band. Unless using a matched filter to reduce the effect of the frequency-dependent radiation characteristics of the antenna, only a limited number of antennas can be used in time domain radars *(Daniels, 2007)*. When the radar system is frequency modulated (e.g.

FMCW) or synthesised (e.g. SFCW), the requirements for linear phase response from the antenna can be relaxed. The configuration and number of antennas used also add another level of complexity of the antenna design. In the case of bistatic operation where separate transmitter and receiver antennas are used, the cross coupling level between them is a critical parameter. Figure 5.4 shows three types of antenna arrangements and their main advantages.

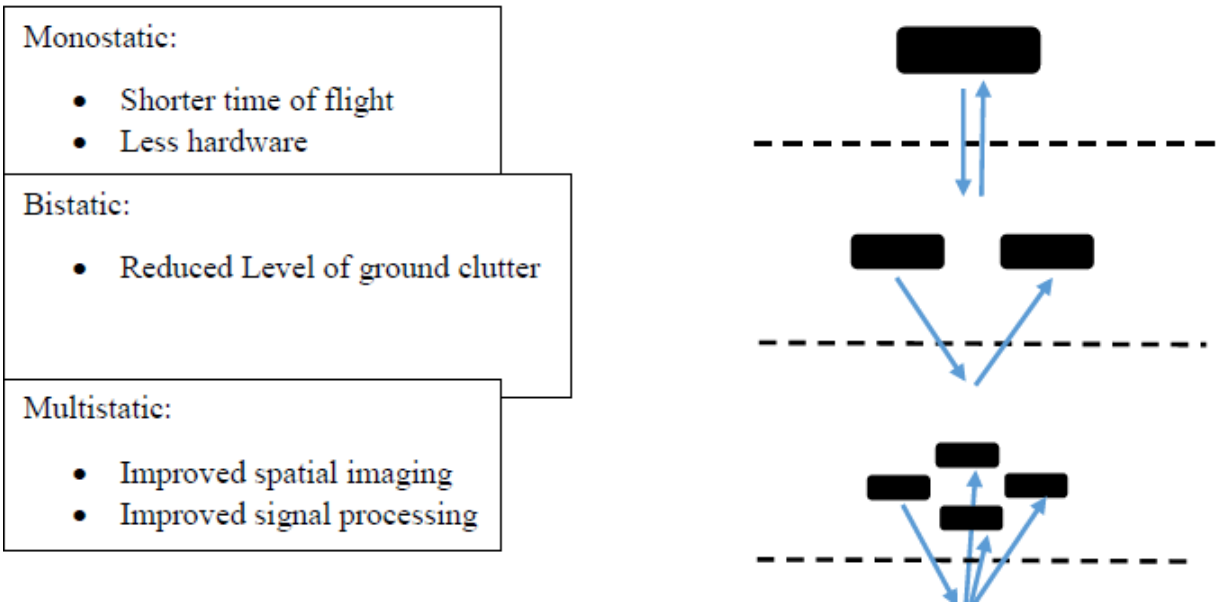

Figure 5-4: Antenna arrangements

Most GPR antennas operate within short ranges of the ground interface; therefore, it is important to appreciate the effect of the ground material near the antennas. As discussed in earlier chapters, the ground material, in general, is regarded as a lossy dielectric medium and can play a significant role in the low-frequency performance of the antenna. Two approaches are taken when considering the dielectric medium in the antenna design, first is to take into account the ground material in the antenna model and optimise its performance accordingly. The aim is to reduce the interaction of the antenna with the interface and maximise the power coupled into the ground. In this case, the two key factors are the current distribution and the radiation pattern. Although this method provides a better overall performance, it suffers from two main practical problems for many applications. The first problem arises with the mechanical damage of the antenna due to an insufficient spacing between the interface and the antenna. The second problem is the specific performance of the antenna in regards to a particular material. For example, if the antenna is designed to couple well into sandy soil, it may not perform as well in other materials such as loamy soil or ice. The second approach in the design is to consider several materials of interest and

optimise other parameters such as the distance from the antenna to the ground. As the antenna spacing is increased, the antenna field patterns are modified by a reduction in the effect of the reactive field. The other parameter is the use of multiple frequencies of illumination. Since the dielectric medium imposes frequency dependent attenuation, frequency diversity can be used to overcome the fluctuations in the dielectric constant of the medium.

In contrast to conventional microwave antenna systems, which are designed for the transmission or reception of high-frequency electromagnetic waves in nearly homogenous free-space conditions, GPR antennas have to cope with various inhomogeneous media. Figure 5.5 shows the two-way propagation path of the signal to and from the antenna. The main boundaries where the signal enters different media is the antenna aperture to air and air to ground. These interfaces have different impedances, and if there is any mismatch between them, the signal is reflected back and can be regarded as a source of high return signals. Reduction of these high return signals can increase the amplitude of the weak target return signal. In contrast to conventional microwave antenna systems, which are designed for the transmission or reception of high-frequency electromagnetic waves in nearly homogenous free-space conditions, GPR antennas have to cope with various inhomogeneous media. Figure 5.5 shows the two-way propagation path of the signal to and from the antenna. The main boundaries where the signal enters different media are the antenna aperture to air and air to ground. These interfaces have different impedances, and if there is any mismatch between them, the signal is reflected back and can be regarded as a source of high return signals. Reduction of these high return signals can increase the amplitude of the weak target return signal.

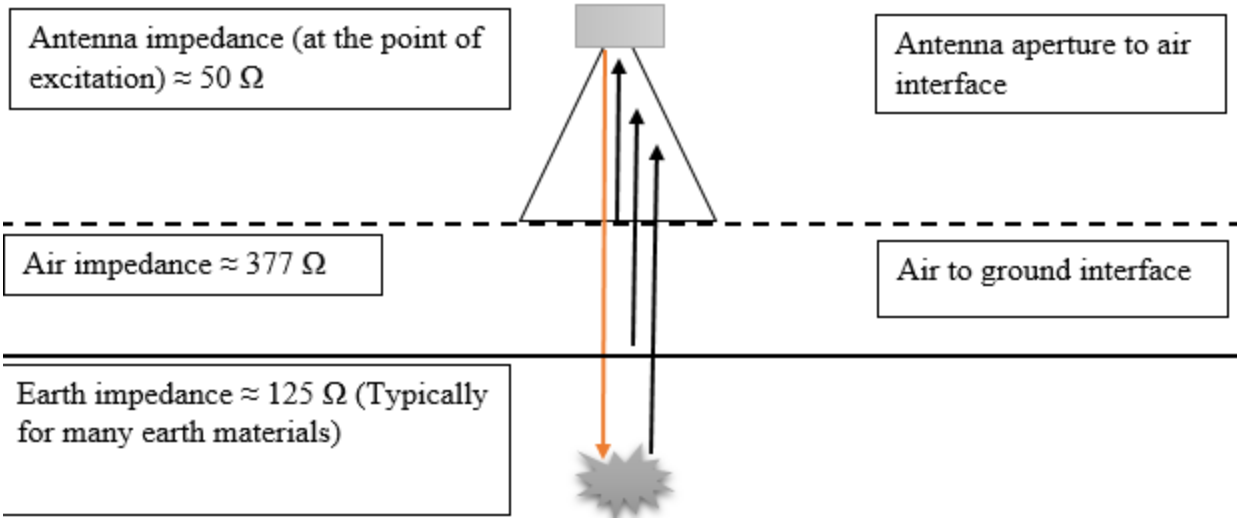

Figure 5-5: Antenna signal path and its main boundaries

Ideally, a well-designed GPR antenna should, a) have a stable antenna characteristic for a wide variety of acquisition conditions, b) radiate a consistent broadband pulse, and c) be characterised by relatively high transmitter efficiency. For efficiency, the antenna should be minimally resistive. Un-damped antennas, however, tend to be distinguished by multiple reflections from the antenna ends (aperture). This results in ringing in the emitted and received signals that interfere with the weak return signal coming from the target buried in shallow subsurfaces. Table 5.1 summarises classification of antennas that are employed for GPR applications. The ticks correspond to their advantages and the squares correspond to their main drawbacks.

Wire type antennas	Aperture type antennas
• Single or Cross Dipoles • Monopoles • Biconical • Loop • Helical	• TEM Horn and open waveguide • Reflector • Slot • Microstrip • Logarithmic or Archimedean Spiral
✓ Linearly polarised ✓ Element antennas (simple structures) ▪ Narrowband ▪ Low efficiency ▪ Low directivity ▪ Low gain	✓ Linear, Dual and Circularly polarised ✓ Antenna array ✓ Ultra-Wide-Band ✓ Highly directive ✓ High gain ▪ Complex structures ▪ Relatively high fabrication cost

Table 5-1: Classification of antennas for GPR Applications

5.1.3 Antenna Characteristics and UWB Requirements

For UWB GPR systems, the frequency-dependent characteristics of the antennas and the frequency-dependent behaviour of the ground material have to be considered. UWB GPR systems can also be realised in an impulse-based technology, and therefore, the time-domain effects and properties have to be known as well *(Shlivinski, 1997)*. The antenna's behaviour, including frequency dependency, can be described by the linear system theory. The characteristics can either be expressed by a time domain impulse response or by the frequency domain transfer function. The dispersion of the antenna can be examined by regarding the analytic impulse response which is calculated by Hilbert transform, and it is a measure of similarity of two waveforms as a function of a time-lag applied to one of them. The Hilbert transform f can be thought of as the convolution of $f(t)$ with the function $g\ (t)$. Cross-correlation of "1" means perfect signal transmission.

$$cross - correlation = \int_{-\infty}^{\infty} f(\tau).g(t+\tau)d\tau \qquad (5.7)$$

The envelope of the impulse response localises the distribution of energy versus time and is hence a direct measure of the dispersion of an antenna. A typical example of measured antenna behaviour is shown in Fig. 5.6 (left) for a given polarisation and direction. The measured antenna

response is usually performed by transmitting and receiving from and to, two identical antennas. In 3D field simulations, the receiving point can be defined by an E-field monitor at the direction of the mainlobe and also at the sidelobes. This is shown in Fig. 5.6 (right).

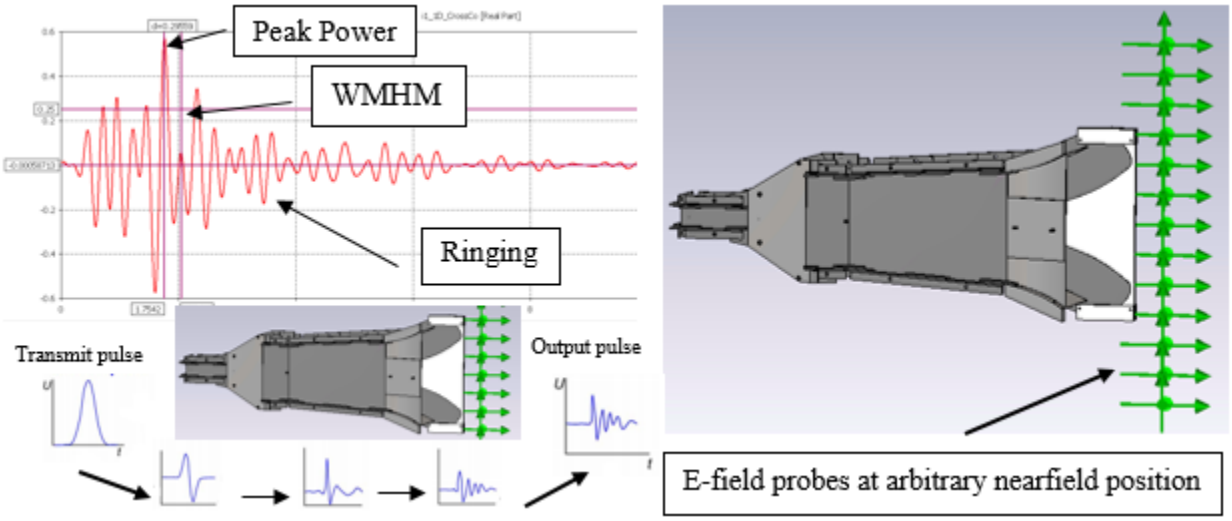

Figure 5-6: Antenna response and setup to perform antenna analysis

The peak value is a measure of the maximal value of the strongest peak of the antenna's time domain transient response envelope. A high peak value is desirable. Envelope width describes the broadening of the radiated antenna's response and is defined as the width of the magnitude of the cross-correlation at half maximum (WMHM). The envelope width should not exceed a few nanoseconds to ensure high resolution in GPR applications. The ringing of a UWB antenna is undesirable and usually caused by resonances due to energy storage or multiple reflections in the antenna. It results in oscillations of the radiated pulse after the main peak. The duration of the ringing is defined as the time until the envelope has fallen from the peak value below a certain lower bound which depends on the level of weak return signals from the targets in GPR. In order to increase the detectability of the weak return signals, a small level of ringing is desirable. The energy contained in ringing is of no use at all, and it lowers the main peak value. Ringing can be reduced by absorbing materials and resistive antenna termination. Group delay is a measure of the transit time of a signal through a device versus frequency and is shown in Eq. 5.6. The variations in group delay cause signal distortion. Constant and low group delay (typically below 3 ns) means good signal transmission *(Wiesbeck, 2009)*.

$$group\ delay = -\frac{\Delta\emptyset}{\Delta\omega} \qquad (5.6)$$

where ω is the angular frequency in radians per unit time, and $\emptyset$ is the total phase shift in radians.

5.1.4 Antenna Multiband Feed

In Chapter 3, it was discussed that the source of illumination from different types of antennas can produce a different footprint and hence scattering patterns from the ground and the buried targets. To increase the GPR antenna versatility and adaptation, this thesis addresses a proposed antenna whereby, additional bands with different antenna characteristics are introduced. The design can be classified as reconfigurable antennas where different bands or sub antenna elements can be accessed by reconfiguring the structure of the antenna. Conventional GPR antennas are designed for a single band. The antenna parameters such as centre frequency of operation, radiation pattern, polarisation and gain are fixed. In GPR applications, the environment and the nature of the targets may differ from one scenario to another. Therefore, antennas with multiple characteristics can improve in understanding the target scene by adapting to the surrounding environment. Control over operating frequency band, beam pointing direction, polarisation, antenna gain, and so forth can provide multiple stories of the same scene, all providing additional information and hence improving the quality and understanding the GPR images. A single multifunctional antenna can replace a number of single-function antennas. Thereby overall size, cost, and complexity of a system can be reduced.

In recent years much attention has been focused on the design of reconfigurable and multifunctional antennas for many different applications, for example, cellular radio systems, multi-frequency radar systems, satellite communication, airborne systems and smart weapon protection.

There are three design approaches for achieving frequency or polarisation diversity and summarised as below:

- Antennas integrated with electronic switches, mechanical actuators, tunable materials for reconfigurability in terms of circuital characteristics and radiation properties
- UWB or multiband antennas integrated with tunable filters
- Reconfigurable/multiband antennas where the same aperture is utilised for different individual radiators.

From previous research work, it was found out that it is quite challenging to achieve acceptable UWB performance in regards to GPR, for different configurations in microstrip and planar antennas. Another limitation of microstrip antennas is concerned with their low gains. Although their gain can be increased by introducing ground planes or other techniques, this will have an effect on the UWB requirements. The shared aperture antenna is an alternative approach. In this approach, the idea is to share the physical area of the antenna aperture between different individual radiators. Here interleaved radiators with separate feed are used. This concept can be utilised for multi-frequency, multi-function, and multi-polarisation applications. The advantage of shared aperture antenna is the possibility to perform multiple tasks, achieve multiple beam widths, avoid amplitude tapering, and so forth. The main challenges related to shared aperture antenna is to design individual elements which satisfies their requirements and placing the elements while avoiding any physical overlapping.

Travelling-wave antennas were chosen as a starting point for the antenna design that this thesis addresses. Traveling-wave antenna is a class of antenna that use a travelling wave on a guiding structure as the main radiating mechanism. Their distinguishing feature is that the RF current that generates the radio waves travels through the antenna in one direction. This is in contrast to a resonant antenna, such as the monopole or dipole, in which the antenna acts as a resonator, with radio currents travelling in both directions, bouncing back and forth between the ends of the antenna. An advantage of travelling wave antennas is that since they are non-resonant, and they often have a wider bandwidth than resonant antennas. These type of antennas are directive and can achieve high gain *(Walter, 1990)*. They often result in 3D structures, therefore, can allow expansion and further design options in regards to a multi-element and feed concept. In practice, the choice of the antenna structure is dictated by (a) the desired operating frequency band, (b) the amount of the power to be transferred, and (c) the amount of transmission losses that can be tolerated. Waveguide and horn antennas are a type of travelling-wave antennas, and they have been chosen as the basis of the antenna design described in the section.

5.2 Antenna Design

5.2.1 Waveguide Analysis

Travelling wave antennas support a forward travelling TEM wave. In general, such antennas consist of a pair of conductors either flat, cylindrical or conical in cross section, forming a V structure in which radiation propagates along the axis of the V. The V structure can be modified for various antenna characteristics but all are variants of the basic TEM structure as shown in Fig. 5.7. The two advantages of these antennas are their high gain/directivity and broadband behaviour. A pyramidal horn is a rectangular waveguide with a flare out at the end. This causes the antenna to have a higher directivity than a normal waveguide. The general form of a pyramidal horn has the following design.

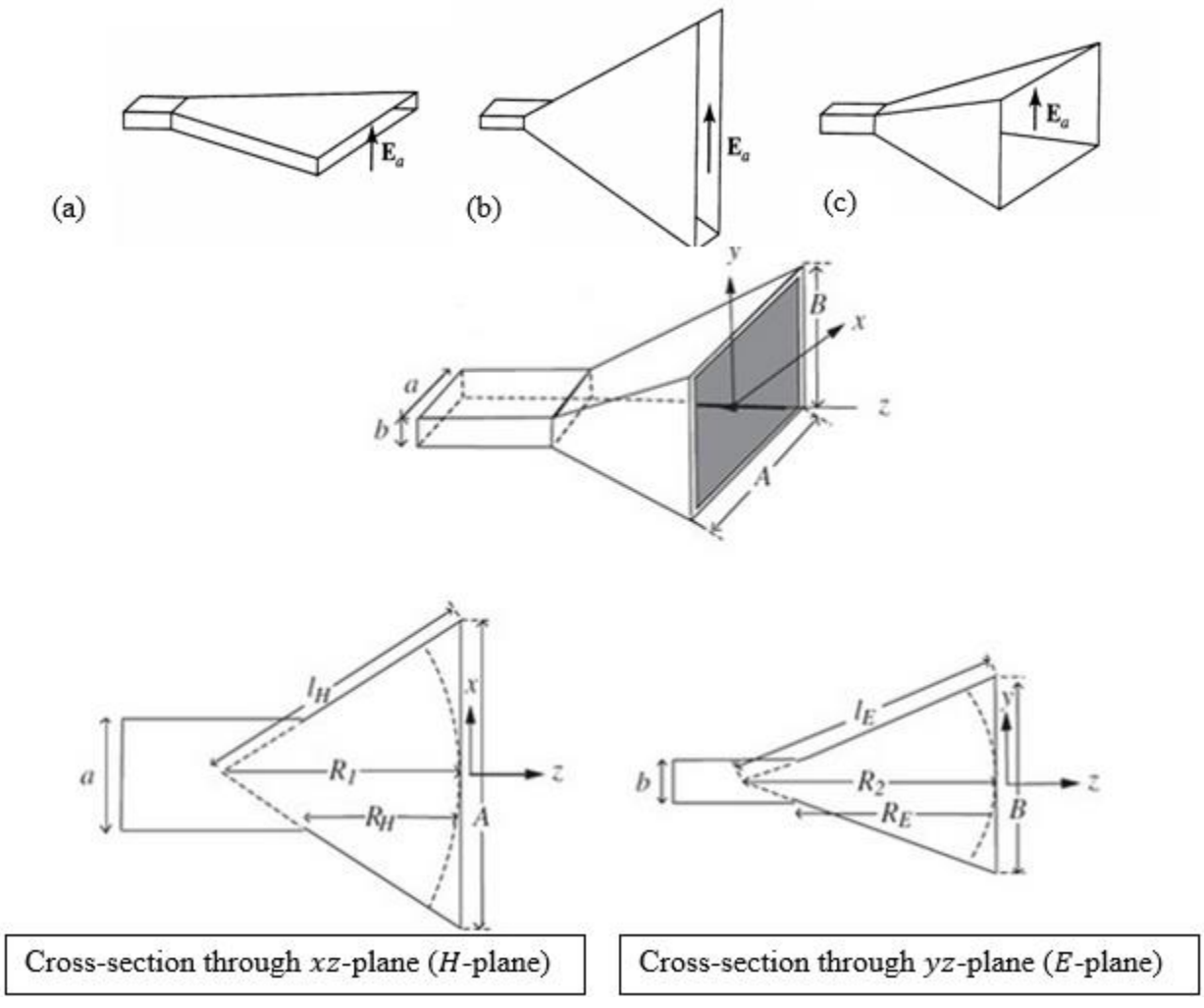

Figure 5-7: Three types of rectangular horn antennas. H-plane sectoral horn (a), E-plane sectoral horn (b), Pyramidal horn (c). Sources: Huang (2008) and Drabowitch, et al., (2005)

To design a horn shown in Fig. 5.7, first the principal dimensions have to be calculated. If we assume $R_E = R_H$ then in the H-plane, the dimensions are linked by Eq. 5.7 & 5.8 and in the E-plane, the Eq. 5.9 & 5.10.

H-plane:

$$l_H^2 = R_1^2 + (A/2^2) \tag{5.7}$$

$$R_H = (A - a)\sqrt{(l_H/A)^2 - 0.25} \tag{5.8}$$

E-plane:

$$l_E^2 = R_2^2 + (B/2^2) \tag{5.9}$$

$$R_E = (B - a)\sqrt{(l_E/B)^2 - 0.25} \tag{5.10}$$

Therefore

$$\frac{R_1}{R_H} = \frac{\frac{A}{2}}{\frac{A}{2} - \frac{a}{2}} = \frac{A}{A - a} \tag{5.11}$$

$$\frac{R_2}{R_E} = \frac{\frac{B}{2}}{\frac{B}{2} - \frac{b}{2}} = \frac{B}{B - b} \tag{5.12}$$

The directivity for a standard horn is:

$$D = \frac{4\pi}{\lambda^2}\, \varepsilon_{ap}\, AB \tag{5.13}$$

(where the aperture efficiency ε_{ap} is typically 0.51)

In the case of a hollow rectangular waveguide with conducting walls, we may assume that the lengths a, b of the inner sides satisfy $b < a$ .The guide is typically filled with air, but any other dielectric material can be used. The simplest and the dominant propagation mode is the TE_{10} mode and depends only on the x or y coordinates (of the longest side). Figure 5.8 shows three cases where the sides a and b differ and the corresponding E-field direction. In (a), the longest size is in the direction y, (b) has its longest size in the direction x and in (c) both sides are equal.

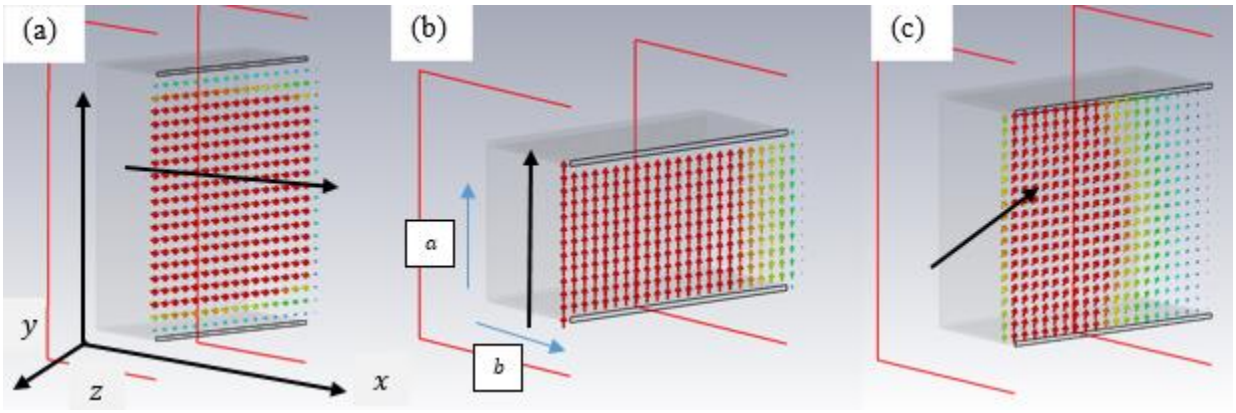

Figure 5-8: E-field distribution in a rectangular waveguide

Equation 5.14 determines the lower cut-off frequency in Hz for a particular mode in a rectangular waveguide. The length of the waveguide in the z direction has no bearing on the cut-off frequency. For TE_{10} mode (since it has the lowest attenuation of all modes) either m or n can be zero, but not both.

$$(f_c)_{mn} = \frac{1}{2\pi\sqrt{\mu_0\varepsilon_0}} \sqrt{\frac{m\pi^2}{a} + \frac{n\pi^2}{b}} \qquad (5.14)$$

where, a = Inside width in metres, (longest dimension)

b = Inside height in metres (shortest dimension)

m = Number of ½ wavelength variations of fields in the "a" direction

n = Number of ½ wavelength variations of fields in the "b" direction

ε_0 = Permittivity ($8.854187817 \times 10^{-12}\ F.m^{-1}$ for free space)

μ_0 = Permeability ($4\pi \times 10^{-7}\ N/A^2$ for free space)

Equation 5.14 provides a good starting point to calculate the dimensions a and b for a given frequency of interest. A model rectangular waveguide was constructed and the dimension a (longer side) was varied to investigate a sufficient length for a frequency of 500 MHz. Figure 5.9 shows the transmission loss (dB) between the two ends of the waveguide (S_{21}) against frequency (GHz) for various dimensions of the waveguide in cm (W x H x L). It can be seen that to have a high power transfer for a frequency of 500 MHz the size a has to be of the order of 30 cm (blue) or longer.

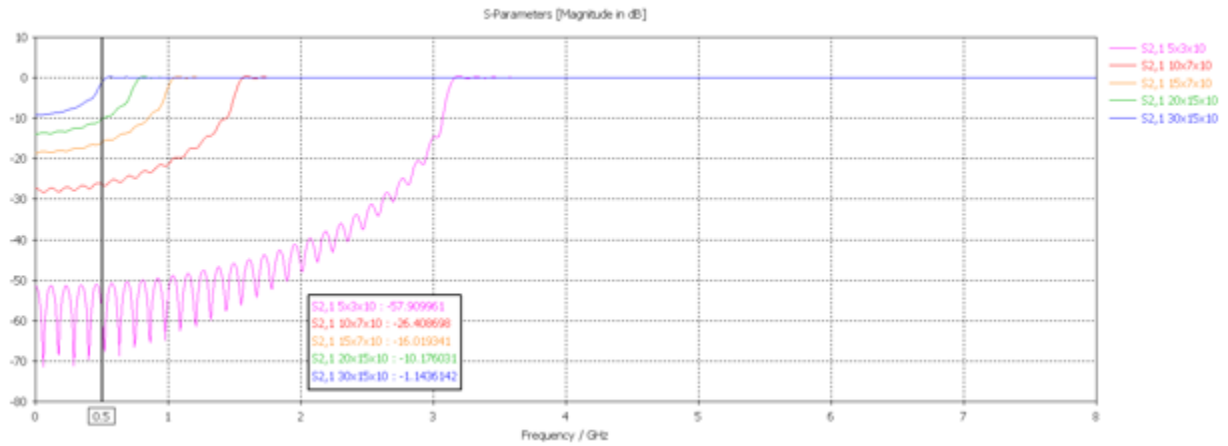

Figure 5-9: Varied size of a in a rectangular waveguide and its effect on 500 MHz frequency

With fixed dimensions of a and b, one can determine the amount of power transmitted along the waveguide, as well as the transmission losses. For a waveguide with conducting walls, the transmission losses are due to (a) primarily ohmic losses in the conductors and (b) the dielectric medium filling, the space between the conductors and in which the fields propagate. Figure 5.10 (a) shows the ratio of the voltage loss (relative to an input of 1V) for a rectangular waveguide of 5x3 cm dimensions whose length is varied from 1 to 21 cm. The material used for constructing the waveguide in CST is assumed to be PEC, however for fabrication purposes, copper or aluminium is considered. Regarding the power loss from the conductor thickness of the structure, one has to keep in mind the skin depth factor of the material. As frequencies increase, conduction begins to move from an equal distribution through the conductor cross section toward existence almost exclusively near the surface. Depending on the conductor bulk resistivity (δ), at sufficiently high frequencies all the surface current is flowing within a very small thickness at the surface. Furthermore, the current concentrates nearest to the surface that abuts the highest relative dielectric constant *(Kraus and Marhefka, 2002)*. Lower bulk resistivities result in shallower skin depths. To

ensure this effect is minimised, the wall thickness of the structure should be thicker than the skin depth of the material at the frequency of interest. The skin depth of a conductor in metres is described in Eq. 5.15.

$$\delta = \sqrt{\frac{\rho}{\pi f \mu_0}} \qquad (5.15)$$

where,

μ_0 = Permeability ($4\pi \times 10^{-7}\ N/A^2$ for free space)

ρ = resistivity (Ω*m)

However, as the thickness of the structure is increased, some ohmic losses due to the increased resistivity of the material are introduced. This effect is shown in Fig.5.10 (b) where the thickness of the wall is varied from 1 (red) to 5 mm (purple) and the transmission losses between the two ends of the waveguide are recorded.

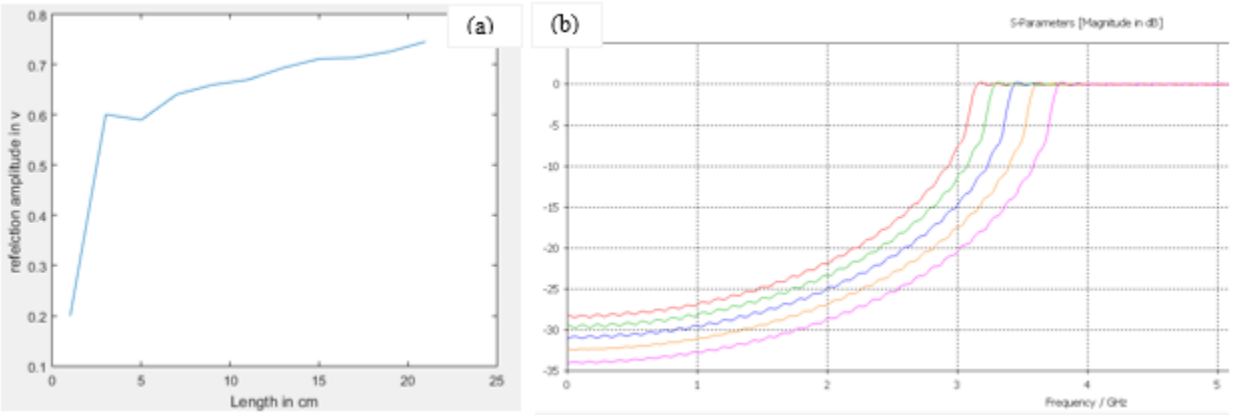

Figure 5-10: The effect of varied length (a) and wall thickness (b) on the transferred power in a rectangular waveguide

5.2.2 Standard Waveguide to Double-Ridged Horn Transition for 500 MHz – 5.5 GHz

The standard rectangular waveguides and horn antennas acting like band-pass filters have limited bandwidth. It can be seen from Fig 5.9 that to operate at low frequencies, the dimensions have to get longer. This may not be feasible for some applications. To extend the maximum practical bandwidth of these waveguides, ridges are introduced in the flare section of the waveguide to air

transition. The idea of using ridges in waveguides was adopted in horn antennas by Walton and Sundberg *(1964)* and completed by Kerr *(1973)* in early 1970 when they suggested the use of a feed horn launcher whose dimensions were found experimentally. This is commonly done in waveguides to increase the cutoff frequency of the second propagating mode (TE_{11}) and thus expands the single-mode range before higher order modes occur *(Hopfer, 1955 and Jarvis, 2000)*. A detailed investigation on ultra-wide bandwidth pyramidal double-ridge horn antenna is reported by Bruns et al *(2003)*. A common multi-octave bandwidth technique is to use a tapered ridge in the horn aperture, to serve as an impedance transition between the ridged waveguide feed and free-space. A double-ridge is used for single linear polarisation and a quad-ridge for dual linear or circular polarisation. The design objective is to taper the ridges to make a smooth transition from the input (usually a coaxial transition to the ridged guide) to the aperture to achieve a good aperture match. Capacitive effects caused by ridges in waveguides or horns help lower the cutoff frequency of the dominant mode TE_{10} and broaden the single mode bandwidth. Radiation pattern distortion arises in high frequency band in conventional ridged horn antennas, caused by greater phase error at the antenna aperture when frequency gets higher. To overcome the problem to some extent, a dielectric sheet is loaded between the ridges in the horn to reduce the phase error at the aperture which helps improve the antenna's radiation patterns in the high frequency band.

In the following, based on the standard double-ridged rectangular waveguide, a new double ridged waveguide with integrated absorbers including a 50 Ω coaxial feed input is proposed. Accordingly, a waveguide transition structure for the single-mode, the TE_{10} mode, with relatively low return loss performance and a new design for reducing the ringing of the aperture by employing an exponential taper on both the flare and the ridges, is presented. The double-ridged antenna is divided into three parts: a double-ridged rectangular waveguide, a cavity back, and the exponentially tapered part. In the next sections, design details for each part will be described.

5.2.3 Design of the Double-Ridged Rectangular Waveguide

The double-ridged rectangular waveguide and a cavity back are the two main parts of the coax to waveguide transition. For single-mode operation, an increase of the bandwidth between the TE_{10} and the TE_{11} modes can be obtained by loading the waveguide with ridges along the direction of the E-fields. A very small gap separates the ridges. The narrow spacing of the ridges ultimately determines the lowest frequency for a given geometry, closer spacing of ridges enables a wider bandwidth.

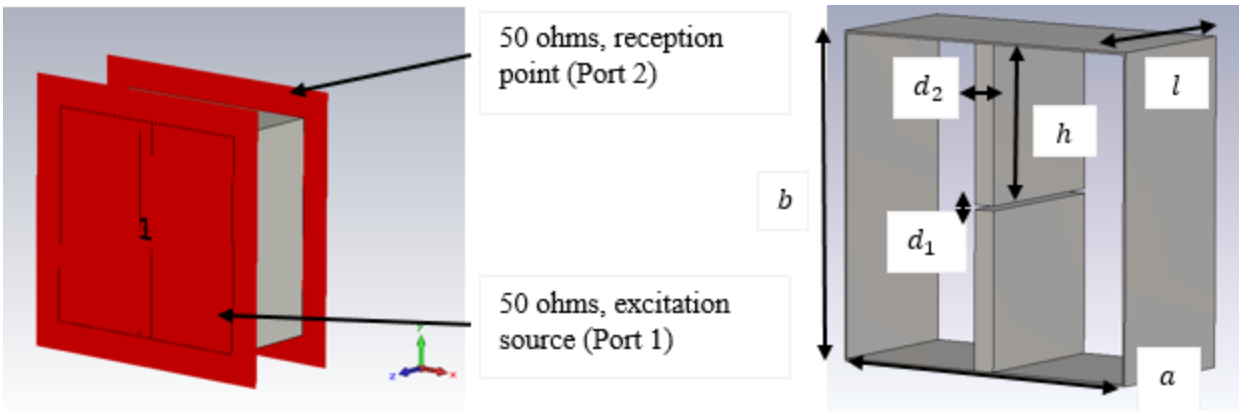

Figure 5-11: Double ridged rectangular waveguide design

In the first step, as shown in Fig. 5.11, a two port rectangular waveguide for single-mode (i.e., TE_{10} mode) is excited in the frequency range of 0-8 GHz. The height and width of the designed ridges and distance between the ridges are h = 74 mm, d_2 = 10 mm, d_1 = 2 mm, respectively which are loaded in the rectangular waveguide.

The dimensions and overall length of the rectangular waveguide were optimised. To allow flexibility and accommodation of other designs regarding multi-frequency and polarisation designs, the dimensions a and b are set to 15.1 cm and l to 7.3 cm. The S_{21} parameters of the TE_{10} mode in the waveguide verses the frequency are presented in Fig. 5.12 it can be seen that at 500 MHz the return loss is at 0 dB and comparing to a non-ridged waveguide at longer dimensions (Fig. 5.9 green line), this has improved by a factor of 10 dB. The characteristic impedance of the fundamental propagation mode (i.e., TE_{10}) versus frequency is presented in Fig. 5.13. It is obvious from this figure that the characteristic impedance varies between 54 Ω and 51 Ω.

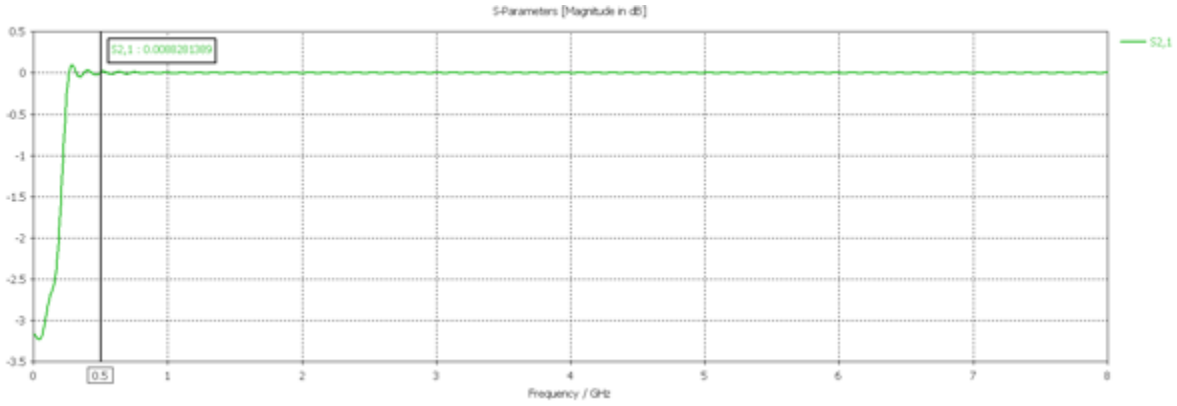

Figure 5-12: S21 parameter of the propagation mode TE10 versus frequency

Therefore, there is a good impedance matching between the point of excitation and a double-ridged rectangular waveguide for single-mode operation over the entire frequency band of 0.5–8 GHz.

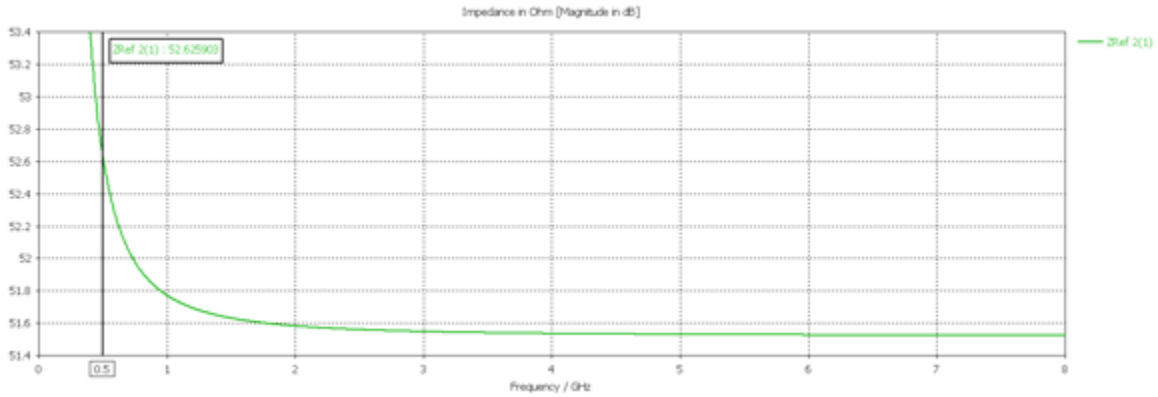

Figure 5-13: Characteristic impedance of the fundamental propagation mode (TE10) versus frequency

5.2.3.1 Coaxial to Double-Ridged Rectangular Waveguide Transition

The double-ridge waveguide consists of a pair of ridges symmetrically placed at the centre of the rectangular waveguide, parallel to the sidewall. In double-ridged horn antennas, the waveguide section interconnects the horn section with the feed section. The excitation method for double-ridged horn antennas is commonly achieved by using a coaxial connector. Therefore, it is necessary to use a transition between the coaxial probe and the double-ridged rectangular waveguide. The transition between the coaxial probe and the double-ridged waveguide is important to the performance of the antenna. The principal goal is to obtain low levels of VSWR throughout the transformation of the TEM-mode in the coaxial section to the TE-mode in the waveguide. Figure 5.14 (a) shows the general structure of the waveguide section with the coaxial line inserted into one of the ridges. The excitation source as port 1 in the previous design step is replaced by a shortening wall also known as the cavity back. The cavity back on the waveguide helps maintain a low S11 at the lower frequencies of operation. To achieve a low S11, the effect of the cavity back length C_l, the initial distance between ridges in the rectangular waveguide, probe spacing from the ridged edge P_s , the tapering and chamfering the back end of the ridges, and the coaxial probe offset were all studied and optimised. A standard rectangular cavity back design is shown in Fig. 5.14 (b). A model SMA connector and a coaxial line is introduced in the waveguide (Fig. 5.14 c and d) and regarded as the source of the excitation signal (port 1). The input impedance of 50 ohms is matched from the source of the excitation signal to the coaxial connector.

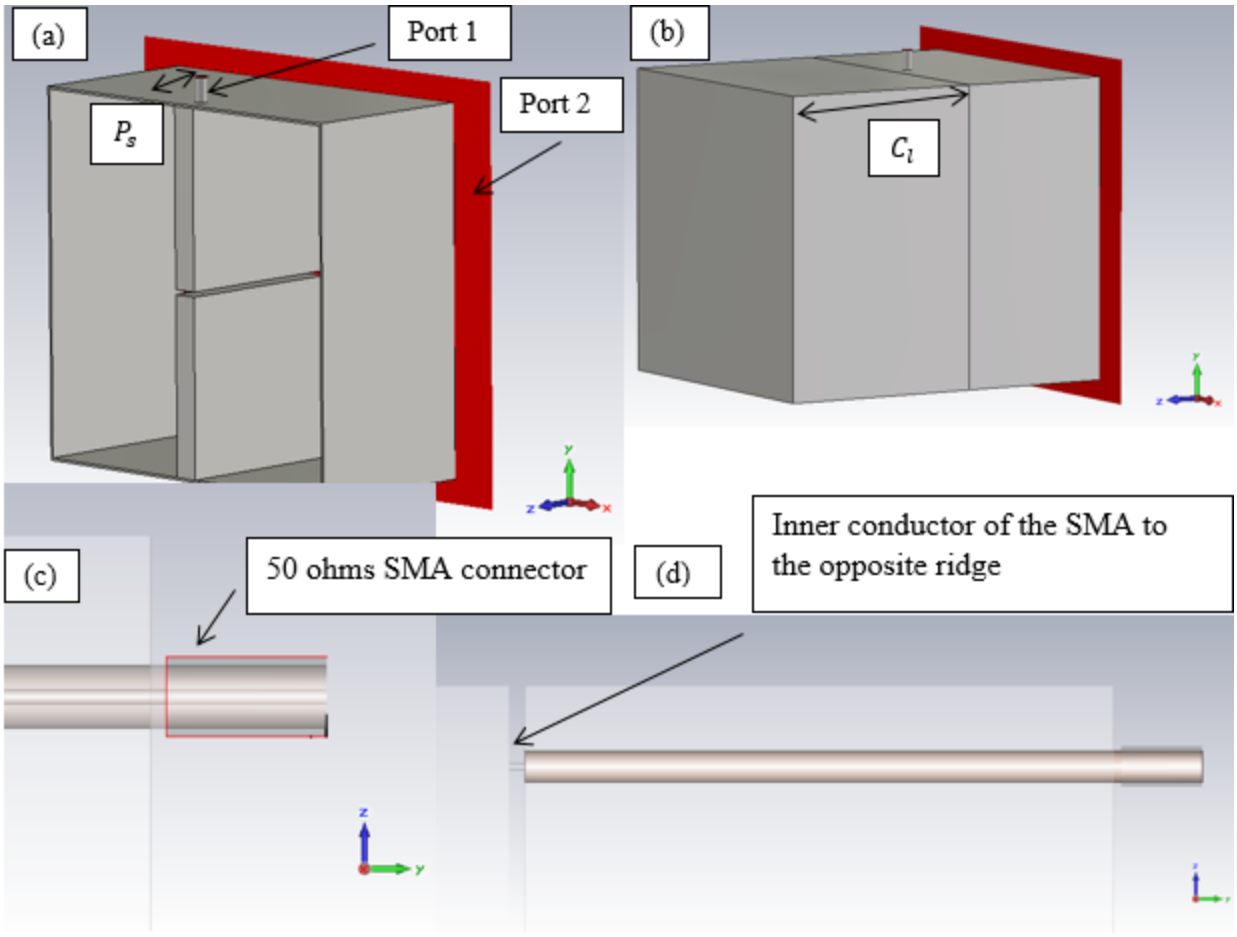

Figure 5-14: Coaxial line to double ridge transition

From the optimisation process, it was found that the probe spacing from the ridged edge, P_s affects the gain of the waveguide (from S_{21}) and shaping of the main lobe at high frequencies when incorporated with the horn section. Numerous simulations have been done to optimise the transitional performance using parameter optimiser approach to cover the 0.5 to 5.5 GHz frequency band. It is very common to use a cavity back to obtain a much lower return loss in coaxial to double-ridged waveguide transitions. It was found that the VSWR of the waveguide is critically dependent on the shape and dimensions of the cavity back.

Figure 5.15 illustrates the E-field at 2.5 GHz (a) & 5 GHz (b) and surface current distribution at 2.5 GHz (c) inside the waveguide structure. It can be seen there is a backward radiation from the double ridges towards the shortening wall. The reflection back towards the double ridges introduces phase error and distorts the propagation of the signal between the double ridges. This is more severe at higher frequencies.

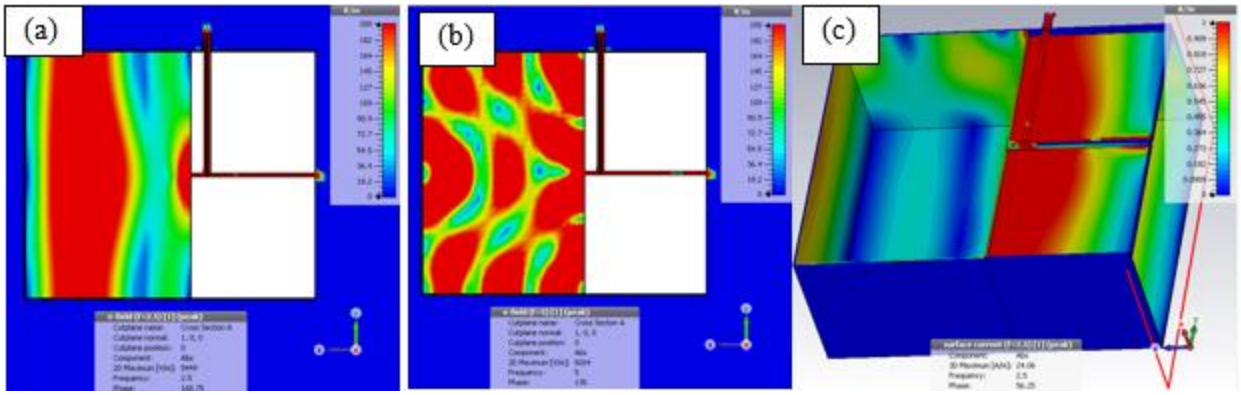

Figure 5-15: E-field distribution inside a cavity backed double-ridged rectangular waveguide at 2.5 GHz (a), 5 GHz (b), and surface current distribution at 2.5 GHz (c).

To improve the performance of the waveguide, a new design for the cavity back is proposed and realised. As shown in Fig. 5.15 (c), the backward surface current travels along the edge of the ridges and the shortening walls. To stop this, a serration technique is employed where the walls surrounding the ridges are loaded with slots to minimise and absorb the travelling surface current. The serrated space in the walls is then filled with high quality Radar Absorbent Material (RAM). This design is integrated into a pyramidal shaped cavity with an extended shortening wall to furfur reduce the unwanted reflection. The free space RAM (ECCOSORB FGM 125) is considered and simulated according to the specification provided by the Laird Technology. Figure 5.16 shows the basic principles of the RAM and the design that has been employed. When a wave is illuminated onto RAM, part of the incident wave is reflected off the medium, and part is transmitted through the medium. Both reflected and transmitted waves are modified in amplitude and phase based on the material properties. Attenuation through the material is achieved by the dielectric, conductive losses and magnetic losses. If the surface of one side of the RAM is covered by a ground plane, then the transmitted wave will undergo a second reflection through the material back towards front face. When primary reflection and secondary reflection are identical in magnitude and 180 degrees out of phase, reflection minimum occurs. Magnitude cancellation occurs when the thickness of the material is around a quarter of a wavelength.

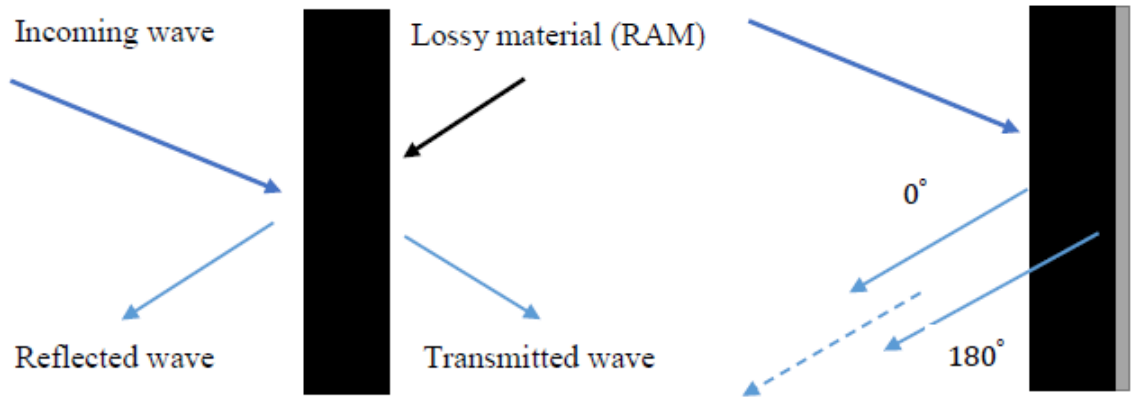

Figure 5-16: Radar Absorbent Material (RAM) principle

The quarter of a wavelength for the frequency of 500 MHz yields to thick RAM, of the order of a few centimetres. This increases the cost of the RAM as well as occupying larger space in the structure. To overcome this issue, the angle of the RAM inside the serrated walls in the direction of the incident wave is modified so the E-fields experience multiple reflections inside the walls. Figure 5.17 (a) shows the overall design of the cavity back with integrated RAM and serrated walls. Figure 5.17 (b) illustrates the propagation paths of the backward radiation and how it is influenced by the angle of the serrated walls.

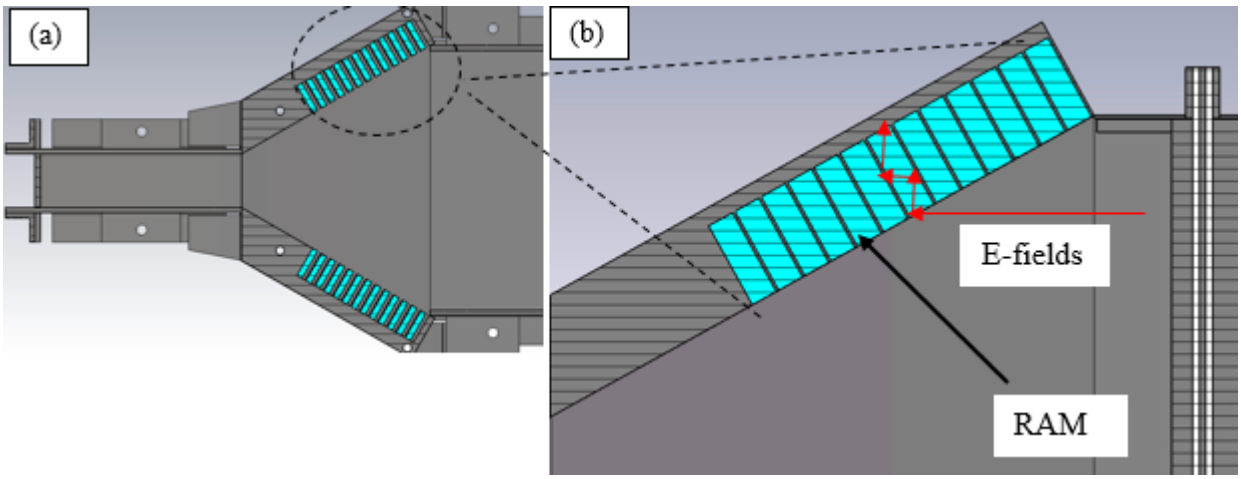

Figure 5-17: Design of the serrated walls in the cavity back

The cavity dimensions which are obtained by optimising its parameters such as the flare angle, the size of the inner and outer height of the cavity, the width and the length of the cavity. The parameters of the serration and its overall design have also been optimised towards a good trade-off between performance and the complexity of the structure (e.g. fabrication cost). The dimensions are shown in Fig. 5.18.

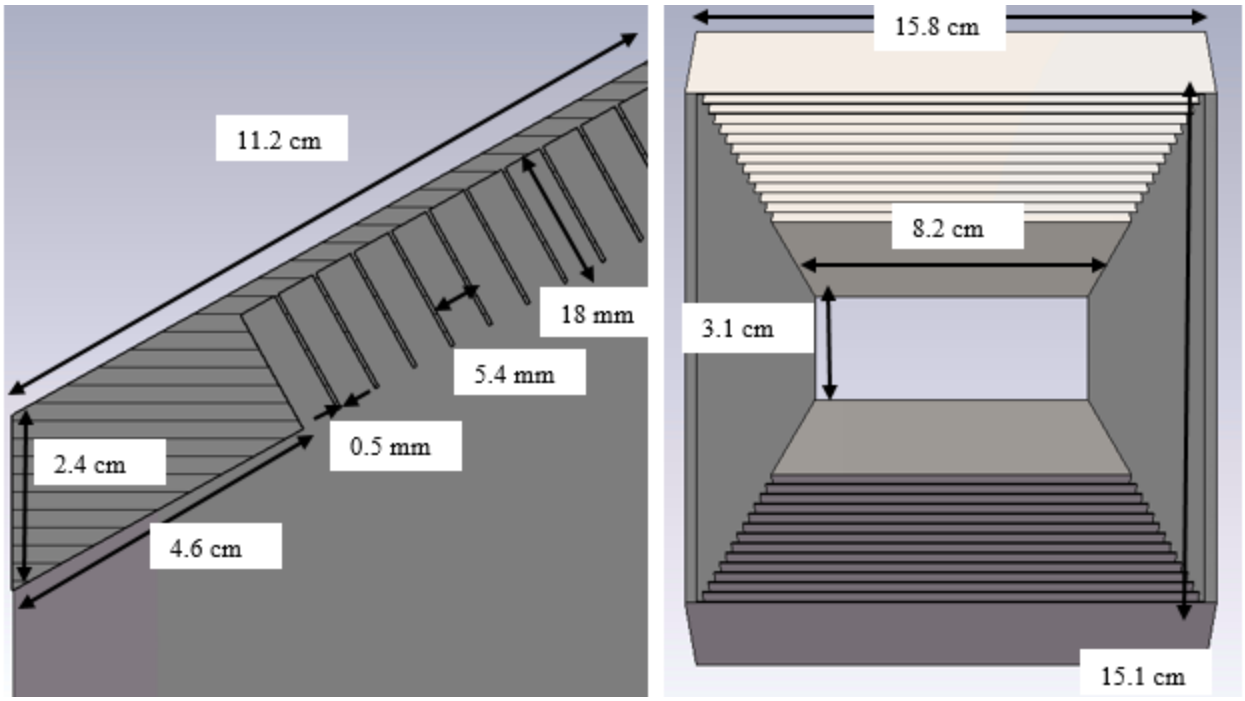

Figure 5-18: Dimensions of the cavity back geometry

Figure 5.19, shows the effect of the modified design to reduce the backward radiation. As it can be seen, the E-field distributions towards the end of the cavity inside the modified waveguide structure (b) are considerably less compared to the standard cavity back design (a). The tapered conical structure with integrated RAM and serrated walls, show a good performance in absorbing the waves and reduction of the unwanted radiation towards the coaxial probes and the horn antenna. Therefore, this improves the impedance matching of the whole antenna structure.

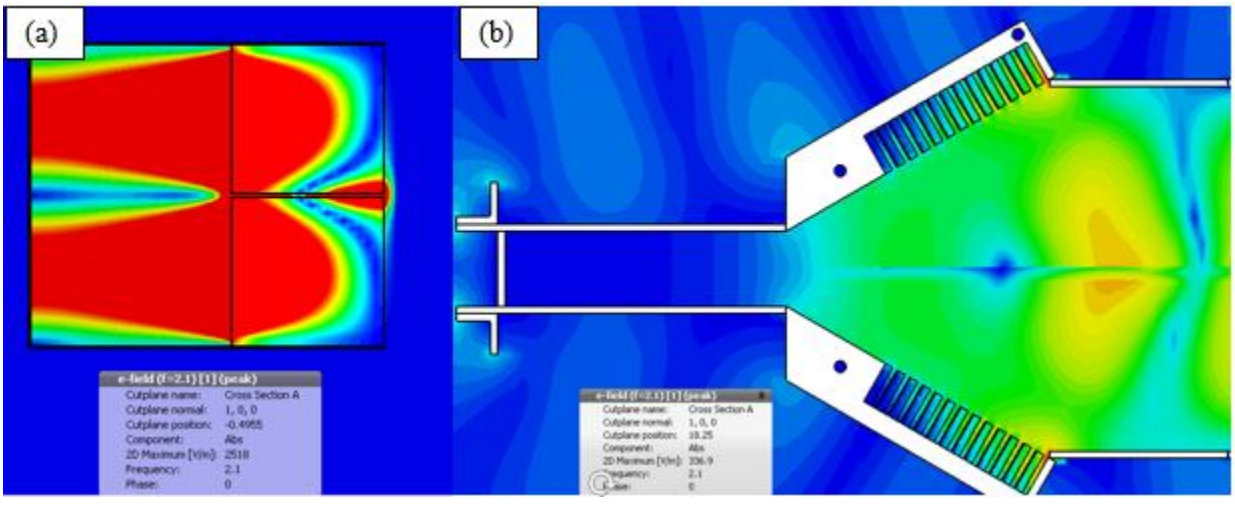

Figure 5-19: Standard cavity back design (a), proposed cavity back design (b) in order to reduce unwanted radiations

5.2.3.2 Design of the Exponential Tapered Ridges and Horn Structure

In order to transform the rectangular waveguide to an antenna, the double ridges have to take a smooth transition to create an aperture. The design of the transition of the ridges is the most significant part of the antenna design. The impedance of the waveguide is 50 Ω while the impedance of the air is approximately 377 Ω. Therefore, the ridges are exponentially tapered to the aperture of the antenna to achieve a good impedance matching. The impedance variation in the tapered part is defined in Eq. 5.16.

$$z\,(y) = z_0\, e^{ky}\,, \quad (0 \le y \le L) \qquad (5.16)$$

where y is the distance from the waveguide aperture and L is the axial length of the antenna opening. The k is calculated by the Eq. 5.17 which has been reported by Bruns *(2007)*.

$$k = \frac{1}{L}\ln\left(\frac{Z_L}{Z_0}\right) \qquad (5.17)$$

Z_0 and Z_L are the characteristics impedances of double ridged rectangular waveguide and free space, respectively. As discussed by Eq. 5.7 – 5.13, the initial dimensions of the horn antenna can be calculated. Figure 5.20 shows the arms of the tapered ridges with enclosed walls to form an aperture.

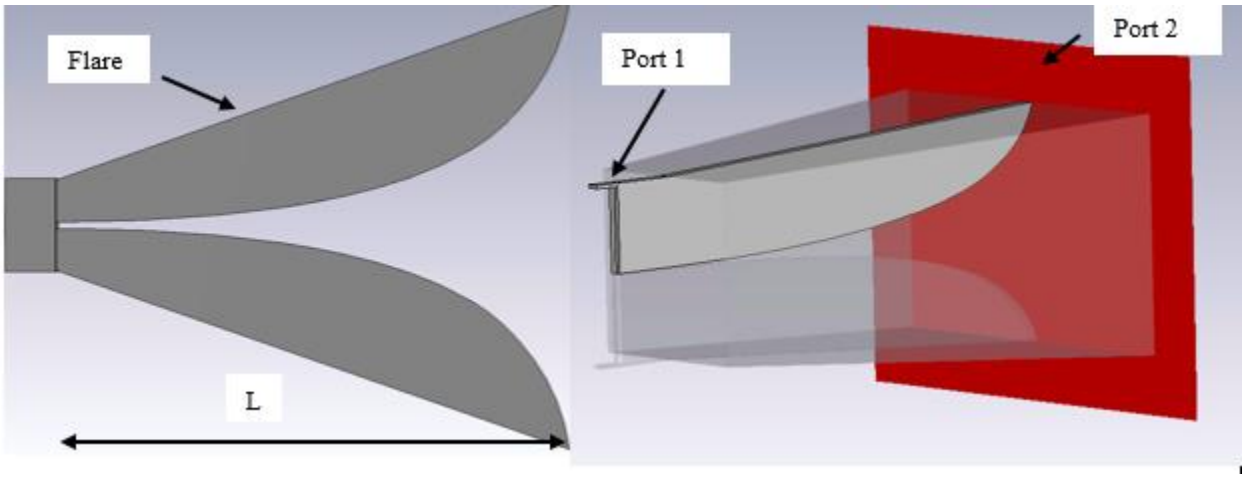

Figure 5-20: Tapered ridges and the antenna aperture

In order to study the effect of the parameters of the ridges and the aperture on the characteristics of the antenna, port 2 is placed at the end of the antenna where the reflection of the signal and impedance of the structure can be monitored. The main parameters that influence the return loss of the antenna are the narrow spacing of the ridges, the length of the taper, which should be at least four times the wavelength at the lowest frequency, the flare length, the length of the cavity and the aperture of the horn. The initial dimensions for the spacing of the ridges were set as 2 mm, the flare length of 32 cm, cavity length of 7.5 cm and an aperture of 28 cm (height) by 40 cm (width). Figure 5.21 shows the VSWR and the reflection from the open aperture to the point of excitation. As it can be seen the VSWR of the antenna is quite high across the band, in particular, the frequencies of 2 GHz and 4 GHz. This effect can also be seen in the ports reflection plot where the overall amplitude reflected back to the excitation point is quite large and suffers from ringing.

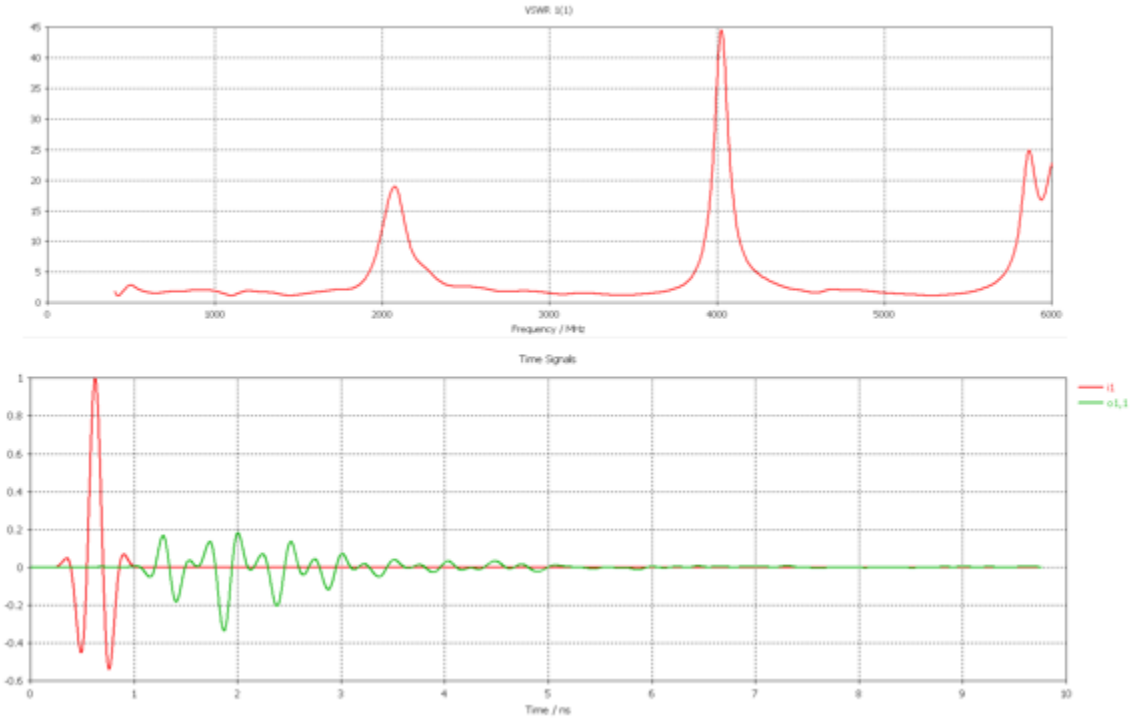

Figure 5-21: VSWR (top) and the port reflection (bottom) for the initial design of the horn antenna

The ringing effect is caused by multiple reflections of the signal from discontinues or open structures of the antenna. Multiple E-field and H-field monitors can be defined at various frequencies to investigate the locations of these effects visually. It was found out that the flat end edges of the ridges are responsible for high signal returns at high frequencies while the flare and

the curvature of the ridges at the end are responsible for low frequencies. These are illustrated in Fig. 5.22.

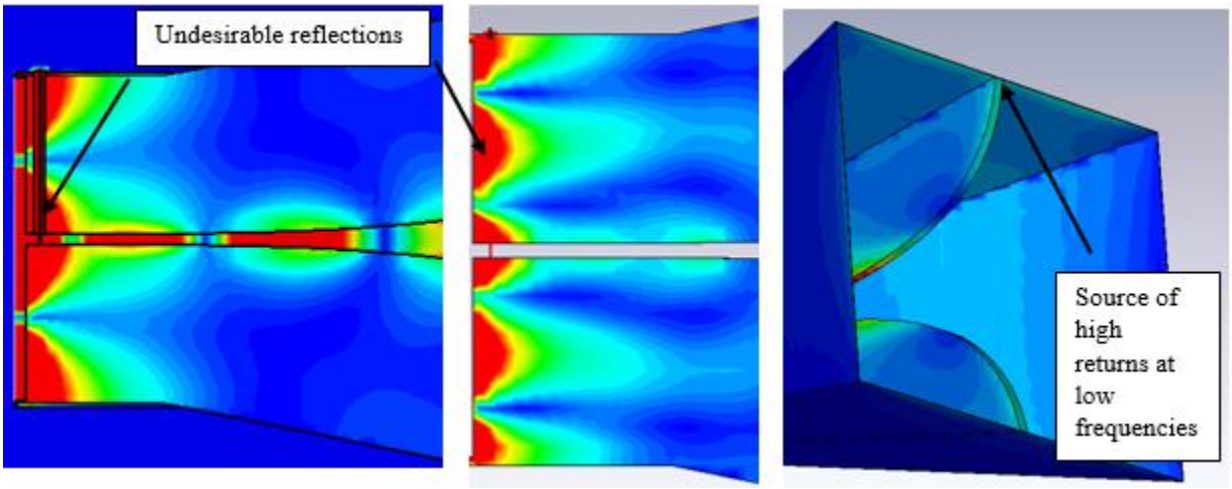

Figure 5-22: Surface current distribution at 2 GHz (left), 4 GHz (middle) and 0.5 GHz (right)

To further improve the performance of the antenna, three parts of the ridges were modified. These are the edges of the ridge, the end curvature of the ridges at the aperture and the flare profile. In the first step, a new design has been applied to the edges of the ridge. The aim is to minimise the reflection of surface current that builds up around the discontinuities of the structure. Figure 5.23 shows how the flat and right-angle profile of a standard ridge is transformed into a new profile where a shorter ridge is introduced near the coaxial input and the flat edge is chamfered to create a curvature. The parameters of the design were studied and having considered the fabrication accuracy and cost; the optimised dimensions are shown below.

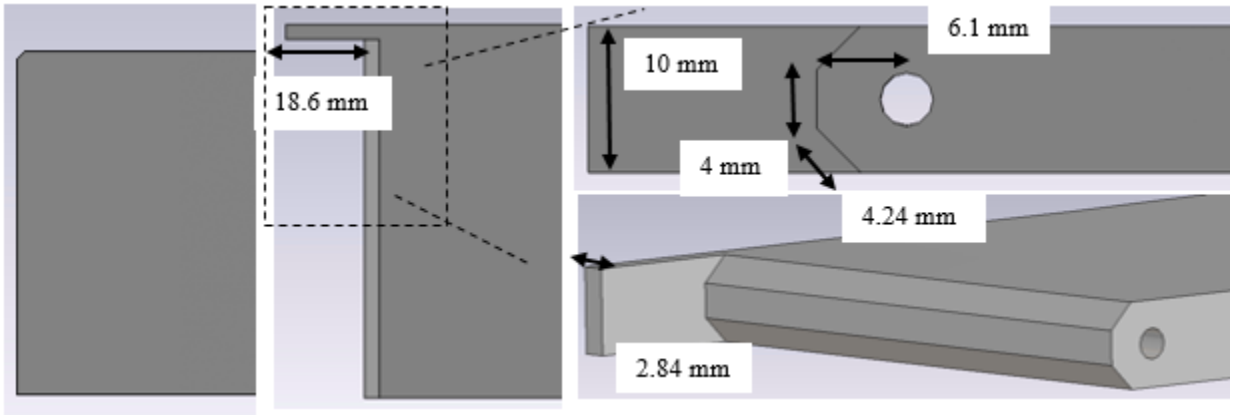

Figure 5-23: New design of the ridges back end

In general, the TEM horn antenna has a linearly tapered structure or an exponentially tapered structure. A linearly tapered structure issued more frequently because it is easy to construct. On the other hand, an exponentially tapered structure delivers a smaller input reflection coefficient over a narrower frequency bandwidth (*Ameri et al., 2011*). As illustrated in Fig. 5.22 lower frequencies contribute to high reflections at the antenna aperture in standard linearly tapered horn structures. In this work, a modified horn structure with an exponentially tapered walls and ridges have been proposed.

It was found out that the longer the axial length of the horn, the better performance at lower frequencies. However, this increases the overall length of the antenna. To minimise the reflections at the aperture and preserve the axial length of the horn, additional means for matching has been considered. As shown in Fig. 5.24, the walls of the horn have been tapered to create a curvature at the antenna aperture. The optimum radius of the curvature was found to be R = 35 cm, and its angle φ = 20°.

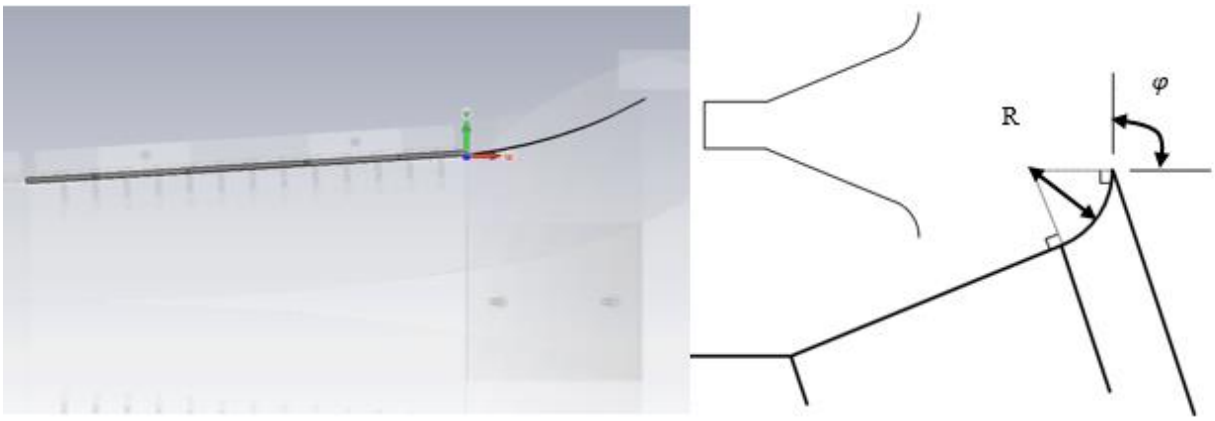

Figure 5-24: Modified aperture matched design

The flared profile is influenced by a curvature of a rounding radius R and a rounding end angle φ at the aperture. By optimsing these two parameters it was found out that as well as affecting the return loss of the antenna, increasing the rounding radius decreases the ripple in the E-plane radiation pattern. Increasing the rounding end-angle much beyond about 90 ° (i.e. parallel to the aperture) did not significantly affect the radiation pattern nor the return loss. However, larger angle introduced slight improvement in reducing the ringing effects. Further modification to the aperture matched structure is proposed. A curved (exponentially tapered) profile is introduced in the ridges to match the antenna aperture. The curvature of the ridges is rolled over the outer aperture to create

a continues path. Therefore, the surface current at low frequencies travel on a profile with reduced discontinues and this helps to reduce the unwanted reflections at the aperture. The dimensions of the outer and inner lengths of the profile are shown in Fig. 5.25.

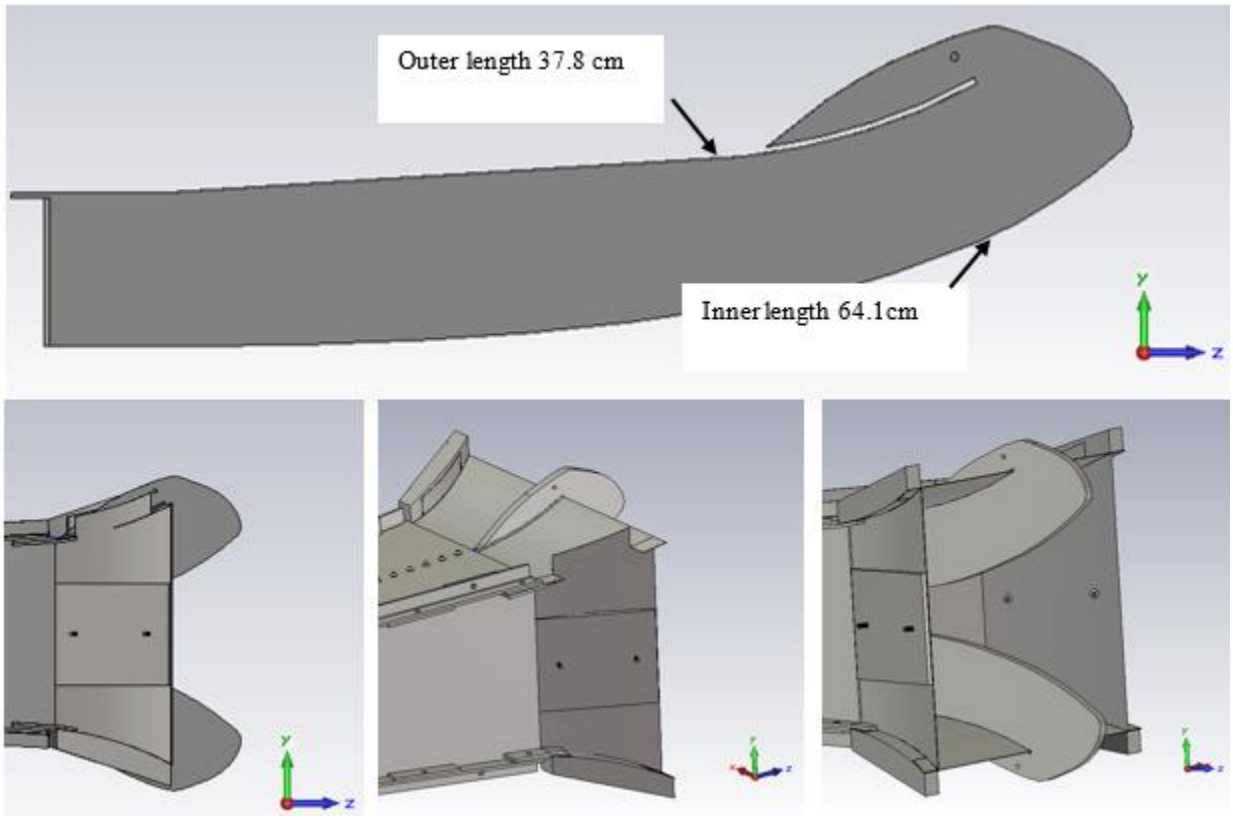

Figure 5-25: The flare and ridge tapering and the overall dimensions

An appropriately designed aperture-matched horn provides superior E-plane patterns, input impedance and frequency characteristics compared to conventional horns. Moreover, uniform patterns across a wide beamwidth with low back lobes, low VSWR can be achieved. In Fig. 5.26, the E-field distributions in H-plane shows strong undesirable side fields highlighted by the arrows for standard horn (a). These fields are reduced in the modified horn (b) and the main distribution of the E-fields are concentrated in the boresight. Figure 5.26 (c) shows the input reflections which is mainly from the antenna aperture. The return signal level from the modified horn structure (blue) is evidently lower than the signal level from the standard horn (green).

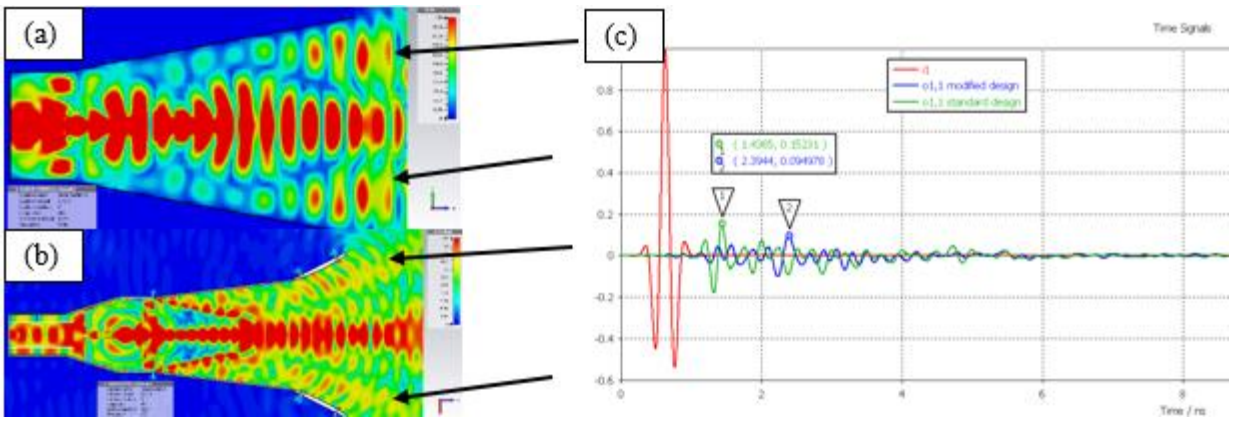

Figure 5-26: E-field distributions in H-plane at 5 GHz for standard horn (a) and modified horn (b) and the input port reflections (c)

To further support the E-fields between the ridges as well as reducing lower frequency operation of the horn while keeping the same axial length, a dielectric sheet is introduced. In this technique, the space between the ridges is partially filled with dielectric material. This is mainly incorporated in the design to decrease the lower cut-off frequency and by doing so increasing the bandwidth for the same dimensions *(Yarovoy, 2002 and Turk, 2007).* At the coaxial feeding line inside the ridge spacing, a dielectric material homogenously filled up the gap between the ridges. The best trade-off between a reasonable S11 and the maximum extension of the operating frequency without disturbing the higher frequencies has been obtained for dielectric materials with permittivity of 2 (PTFE). The thickness of the material and the shape of its aperture mostly influence the radiation pattern of higher frequencies since it acts as a lens. The optimum thickness of 8 mm and a flat aperture aligned with the ridges have been designed, and they are illustrated in Fig. 5.27.

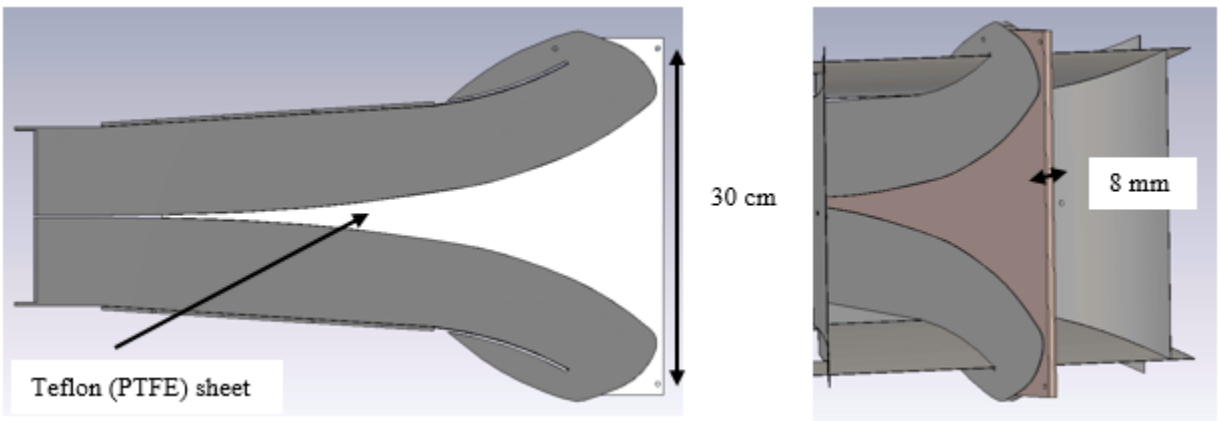

Figure 5-27: Dielectric filling of the ridges

Figure 5.28 presents the surface current distribution of the ridges and the improvement in minimising them by the new design modification can be seen. The new design has forced most of the current to flow around the taper of the ridges and comparing to Fig. 5.22 it has reduced the unwanted surface current from the edges of the ridge. The current distribution at 500 MHz shows reduced surface current around the curvature of the ridges. The surface current is further minimised as it travels along the profile of the ridges.

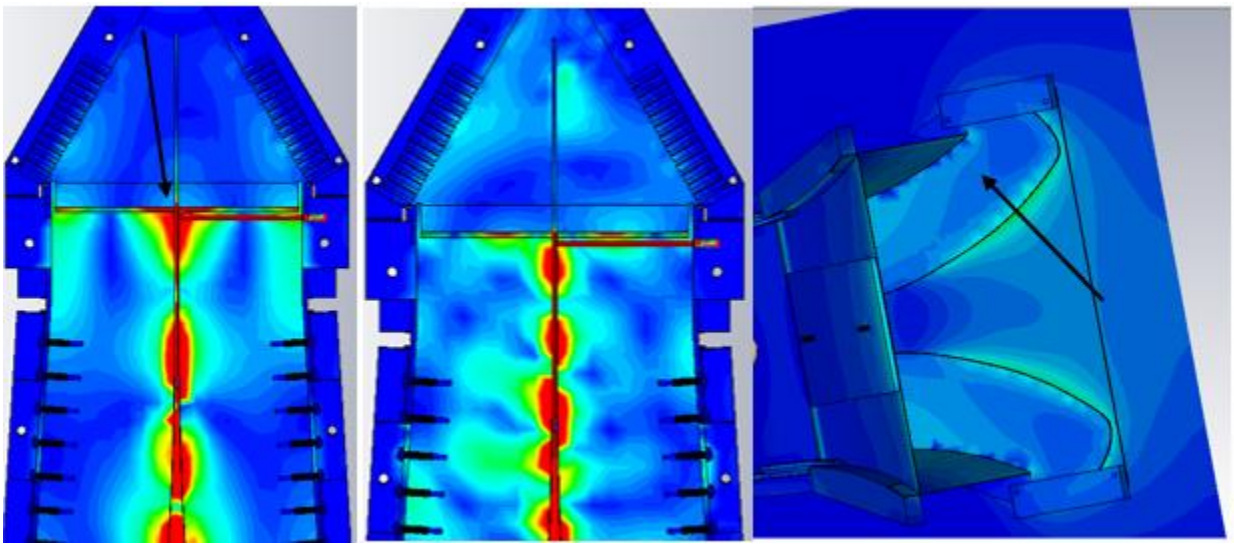

Figure 5-28: Surface current distribution of the ridges at 2 GHz (left), 4 GHz (middle) and 0.5 GHz (right) after improvement

The input reflection of the whole antenna structure is presented in Fig. 5.29. The maximum level of the return signal is around 0.095 V for an input signal of 1 V. This suggests that only around 10% of the energy is reflected back towards the coaxial input. The maximum reflected signal is recorded at 2.36 ns, and as it can be seen, the return signal has a steady and reduced ringing effect after 4 ns.

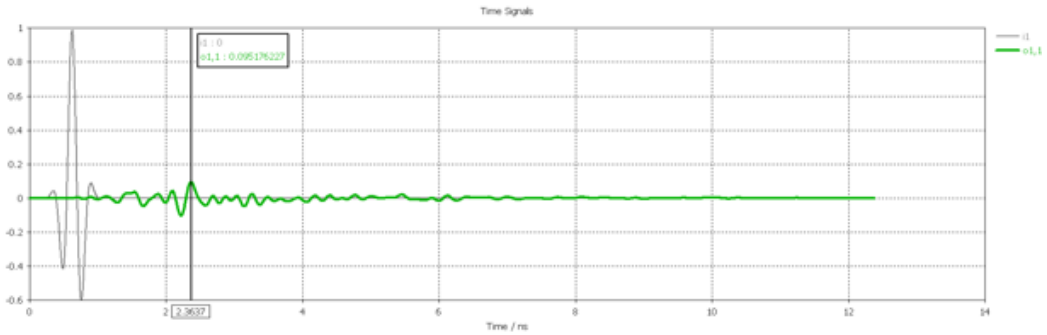

Figure 5-29: Return signal from the antenna aperture for an input signal of 1 V

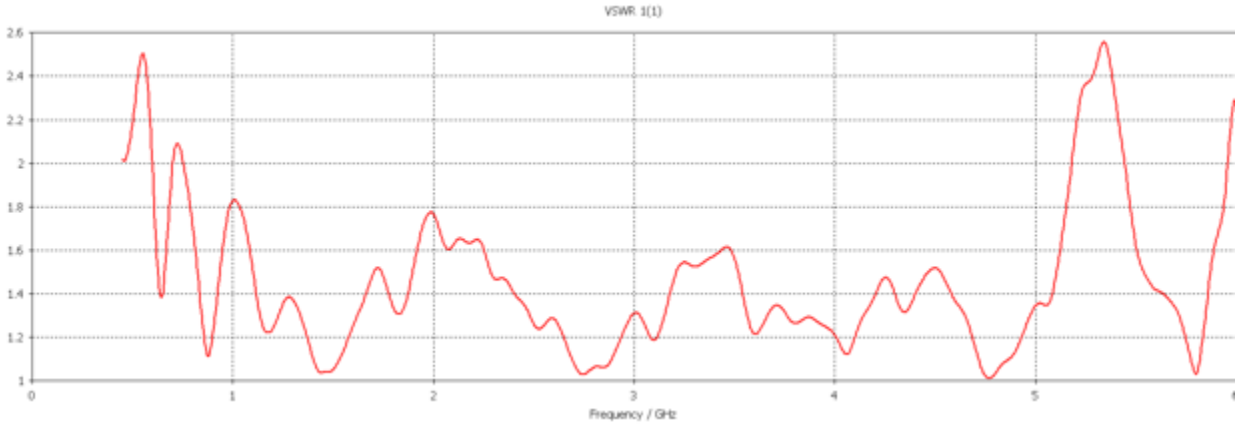

Figure 5-30: VSWR of the overall antenna structure for the designed frequency band of 0.5 – 5.5 GHz

Figure 5.30 shows the VSWR of the antenna structure. The maximum VSWR in the designed frequency band of 0.5 – 5.5 GHz is found to be less than 2.4.

The effect of the dielectric loading of the ridges on lower frequencies has been presented in Fig. 5.28 the VSWR of the antenna with a dielectric filling of the ridges have been lowered for the lower frequency as well as increasing, the lower cut-off frequency of 500MHz to around 450 MHz. This comes at a cost of increasing the VSWR slightly for higher frequencies. The trade-off can be compromised by varying the thickness of the filling. The thick dielectric filling is found to introduce ripples in high-frequency E-field distribution as well as increasing the sidelobe levels unless the aperture is curvature shaped.

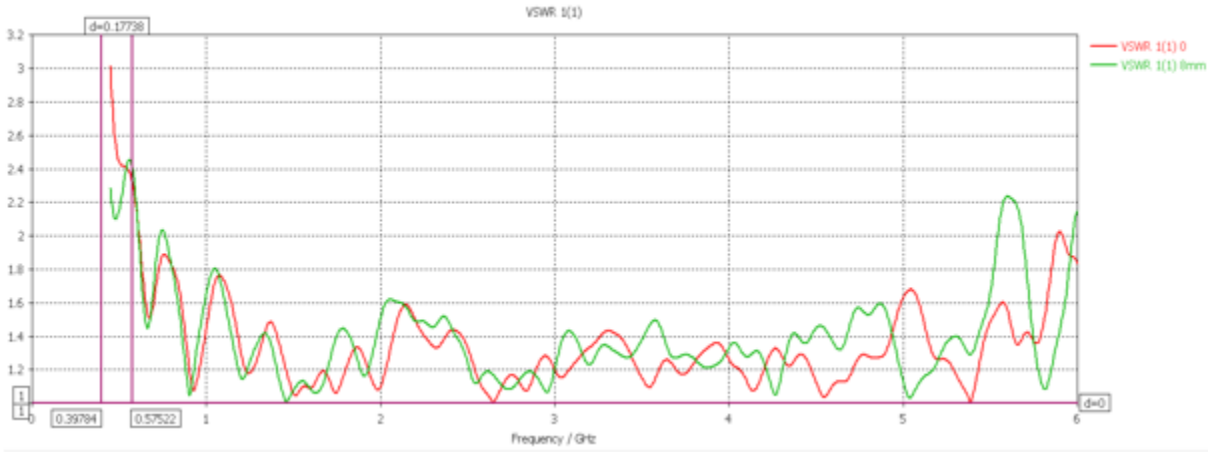

Figure 5-31: The VSWR of the antenna with (green) and without (red) the dielectric filling of the ridges

5.2.4 Thin-Ridged Antenna for 2.7 – 6 GHz (Horizontal Polarisation)

To accommodate multiple channels (e.g. multiple frequency bands) within the same antenna structure, the second pair of ridges can be inserted perpendicular to the previous ones to make a quad ridge structure. This technique also introduces a horizontal polarisation. However, having an additional pair of ridges would add to the complexity and fabrication cost of the antenna structure. In this work, a new design is proposed where thinner ridges are introduced instead. The modified design is based on antipodal Vivaldi antennas.

Vivaldi shaped antennas are variations of tapered slot antennas that are characterised by two exponential flare shape arms. The flare radiates at different points along its length for different frequencies, determined by the flare width. The conventional flare design has theoretically unlimited bandwidth. In practice, the bandwidth is limited by the physical dimensions of the antenna. The antenna can be constructed on a PCB where both arms of the antenna are stacked on top of each other with the substrate in between, and a number of variations exist. The conventional form of antipodal Vivaldi antenna is fed from a tapered microstrip to symmetric double-sided stripline transition. A further development of the antipodal Vivaldi antenna is the balanced antipodal Vivaldi (*Langley et al., 1993*) that uses a stripline to balanced slot line transition.

Since the aim of the antenna design described here is to provide a horizontal polarisation and a boresight radiation using the same overall antenna aperture, it needs to be carefully placed within the horn structure. The horizontal polarisation can be realised by placing the antipodal Vivaldi antenna on the H-plane inside the horn structure. This is illustrated in Fig. 5.32 (a). In order to propagate the E-fields from the point that they are created (Vivaldi's mouth) to the point where they are radiated (Overall antenna's aperture), the overall antenna structure is used as a waveguide. Another word, the antenna is placed as if the half of the overall antenna structure created a waveguide as shown in Fig. 5.32 (b). Therefore, the E-fields propagate in a right angle path and radiated at the antenna aperture as shown in Fig. 5.32 (c). Because the outer wall of the horn structure is tapered, the radiation pattern for this antenna is slightly distributed off the boresight. However, this can be compensated for if another pair of the same antenna design is placed on the opposite side.

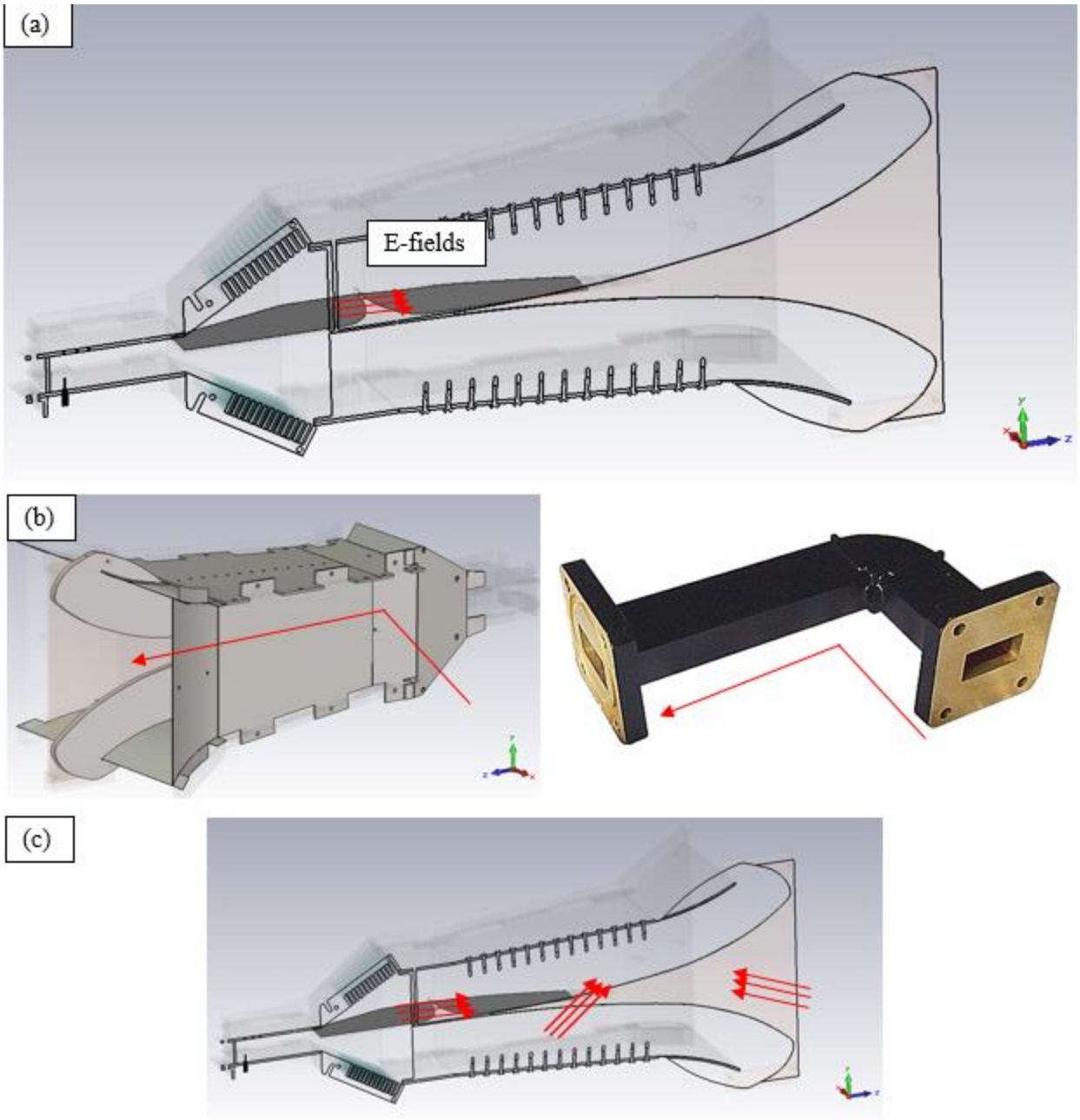

Figure 5-32: Thin ridge antenna design structure (a), its concept of propagation in waveguides (b) the propagated E-fields (c)

The antenna is first designed in free space but optimised and characterised when placed inside the horn structure. Figure 5.33 (a) shows the antenna geometry and its dimensions. The antenna is designed on RO435 substrate with ε_r = 3.48 and height, h = 1.6 mm. The tapered radiation structure (inner mouth), follows the design procedure as described in Eq. 5.16 and 5.17. The width at the start of the flare defines the upper frequency and the width at the mouth of the flare defines

the lower frequency. At a wavelength λ, the antenna radiates from a point on the exponential flare defined by

$$z\,(y) = \frac{\lambda}{4} \qquad (5.18)$$

In practice, the antenna does not radiate from a single point for a given frequency, but from a small section along the curve of the flare. The requirement for constant alignment of the E-fields is that the length of this section is in direct proportion to the wavelength. Thus, in the Fig. 5.33 the optimised total length L_1 of the inner flare for both arms of the antenna is 22 cm. To design the width of the antenna W, following equation was used (*Greenberg et al.,2003*) :

$$W_1 = \frac{c}{2\,f_{low}} \times \sqrt{\frac{2}{\varepsilon_r + 1}} \qquad (5.19)$$

The optimised width W_1, is 8 cm and W_2 is 3.3 cm which is formulated by the following equation to achieve a 50 ohms characteristics impedance in microstrip structures (*Technick, 1997*):

$$Z_0 = \frac{87}{\sqrt{\varepsilon_r + 1.41}}\; Ln\left(5.98\frac{H}{0.8\,W_2 + T}\right) \qquad (5.20)$$

where H is the height of the substrate and T is the height of the microstrip. To improve the impedance matching and radiation characteristics, both arms of the antenna are placed on the same side of the substrate separated by the dimensions shown in Fig. 5.32 (b). The shape of the substrate is then cut out to match the internal structure of the horn. The rigidity of the chosen substrate allows stable and secure placement inside the horn structure with an added support that is described in Chapter 6.

To minimise the reflections from the open end of the antenna arms. A smooth and graduate transition from the point of excitation (50 ohms) to higher impedance is needed. However, this results in a slightly larger microstrip profile. To overcome this issue, resistive and capacitive termination technique is used whereby, a combination of resistors and capacitors in series and parallel were designed to absorb the energy at the end of the structure.

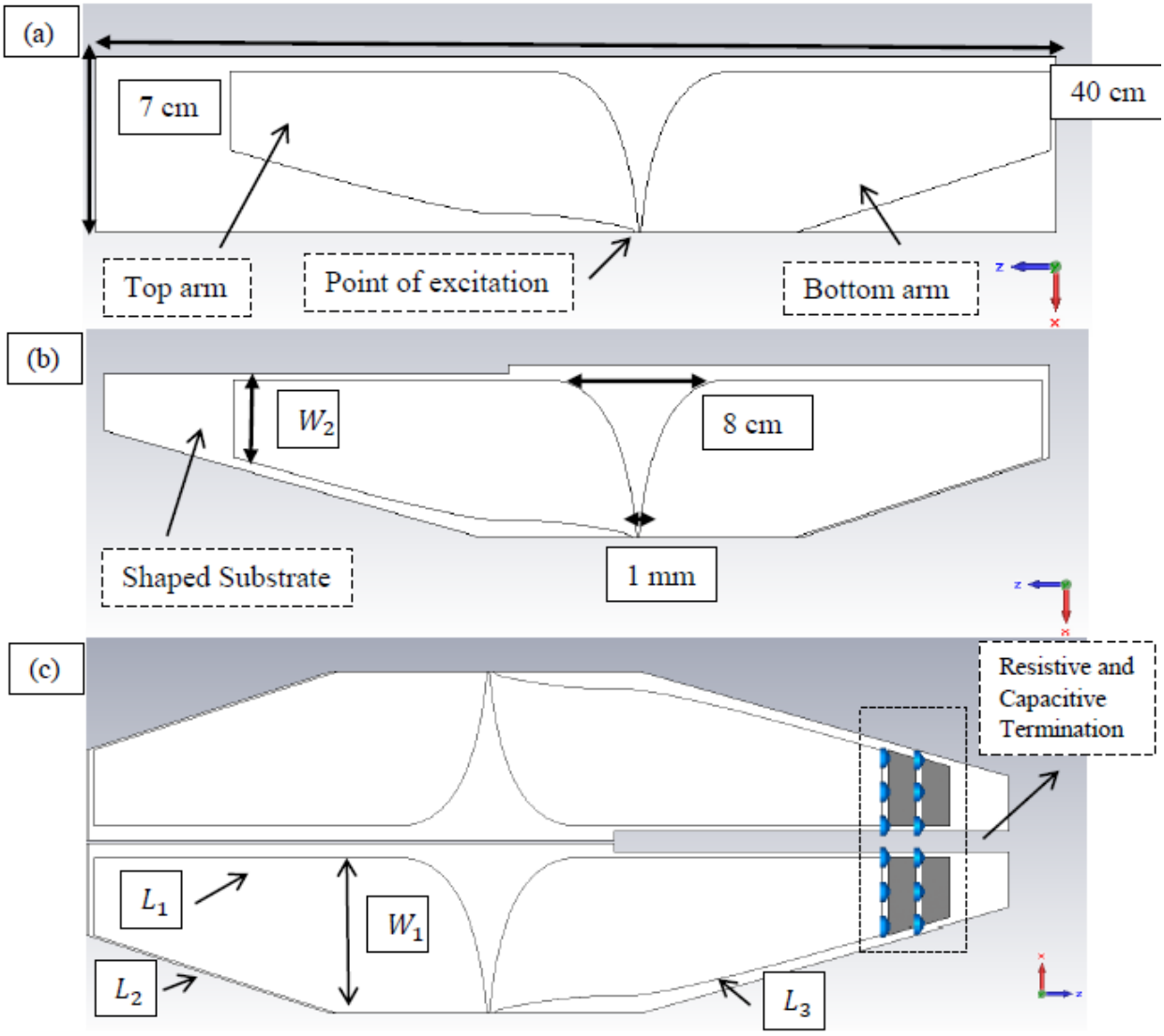

Figure 5-33: Thin ridge antenna geometry and dimensions

The characteristic impedance of the microstrip profile at the end of the top arm with the width W_2, is around 48 ohms. In order to step this up gradually to a higher impedance, a RC circuit was designed and simulated in CST Design Studio. Figure 5.34 shows the RC circuit and its realisation in microstrip structures. A trade-off between the number of resistors and the efficiency was taken into account. The grounded shunt capacitors are the vertical gap capacitance between the microstrip and the substrate with an assumption that the substrate is grounded on the other side. A 3 mm gap between microstrip traces was calculated in order to realise the equivalent capacitance. This gap length is ideal regarding the length of SMD resistors. The first row of resistors has the

value of 50 Ω while the resistors in the second row are 100 Ω. The resulting impedance that increments from each stage of the circuit is shown in the figure.

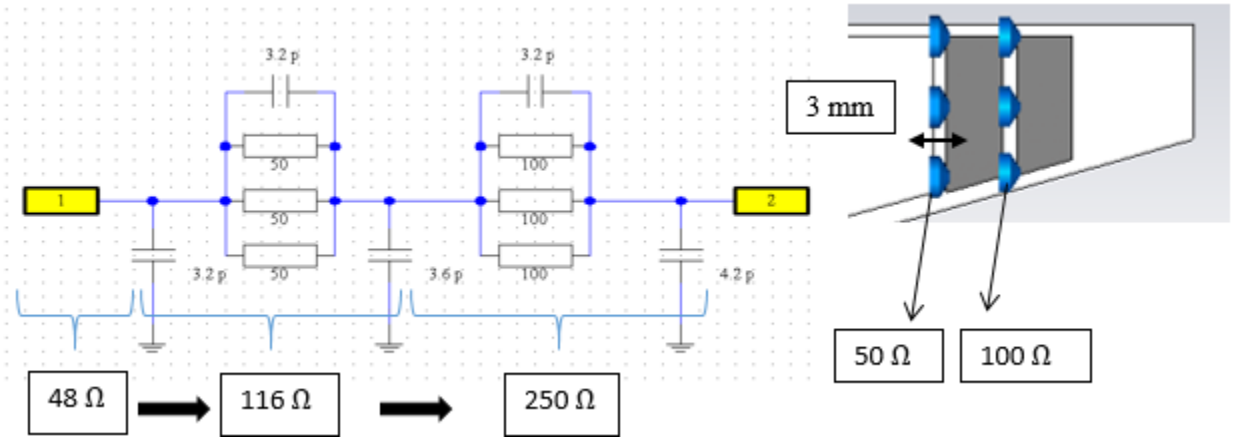

Figure 5-34: RC termination of thin ridge antenna, equivalent circuit (right), its realisation (b)

Figure 5.35 shows how the antennas are placed within the horn structure. Two pairs of the antennas have been considered. They can be excited simultaneously with a phase difference of 180 degrees for a better radiation pattern, or they can be excited separately and independent of each other with a diversity in the radiation pattern. This is illustrated in the form E-field distributions in Fig. 5.36. The E-fields on the *H* - plane at 4 GHz for both the antenna pair 1 and 2 are presented. As suggested the E-fields are propagating between the inner wall (the double ridge) and outer wall (the horn flare). There is a small amount of energy coupled from antenna pair 1 to 2 and vice versa, which subsequently helps to pull the radiation pattern of each pair towards the boresight. The coupling between the pair is presented in Fig. 5.37.

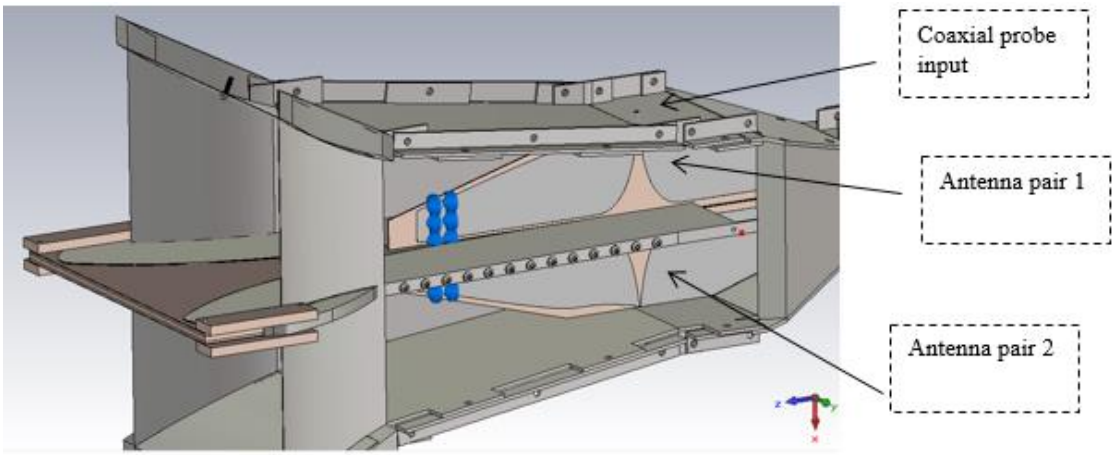

Figure 5-35: Thin ridge antenna within the horn structure

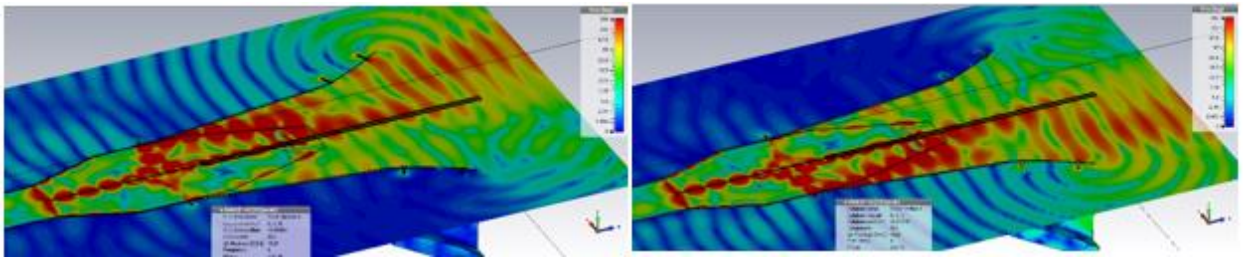

Figure 5-36: The E-field distribution on the H – plane at 4 GHz, for antenna pair 1 and 2

Figure 5.37 (a) shows the isolation between the two antenna pair as S23 between the ports they are excited. The S_{23} (port 2 and 3) shows isolation of around – 20 dB for frequency range of 2.5 to 6 GHz. This is further illustrated in Fig. 5.37 (b), where the signal from port 3 to 2, e.g. O_{23} for an input signal of i_2 = 1 V, shows a maximum level of around 0.02 V.

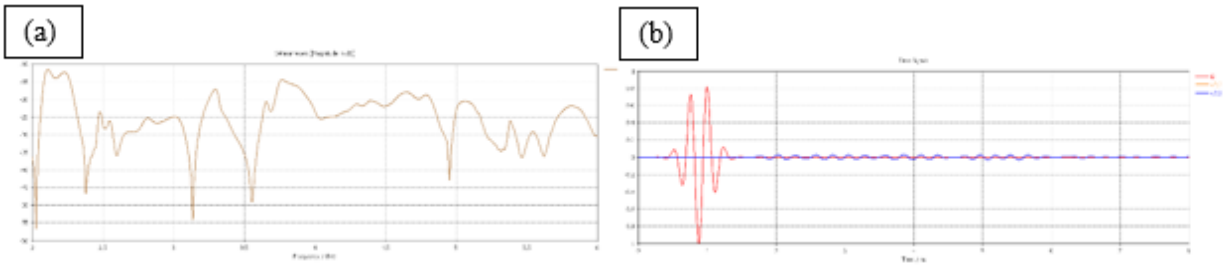

Figure 5-37: The isolation (a) and coupling port signal (b) between the antenna pair 1 and 2

The VSWR of both antenna pair 1 and 2 are presented in Fig. 5.38. The operating band that corresponds to VSWR of below 2 can be defined from around 2.7 to 6 GHz. There is a negligible difference in performance between each pair. The input port return reflection signals with and without the RC termination is presented Fig. 5.35 (b). The main peak of the reflected pulse is below 0.2 V, and the ringing is dampened after 3 ns.

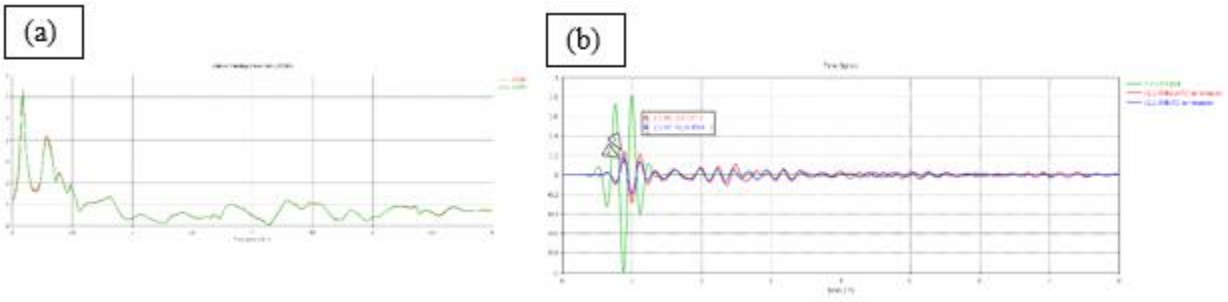

Figure 5-38: The E-field distribution of the second band antenna design

5.2.5 Extended Cavity Back Waveguide for 3.5 – 7.5 GHz

Another channel to accommodate additional frequency band is designed and discussed. The aim is to add another antenna element in the same structure that can operate at different frequency band. Since the horn structure supports forward travelling waves, the extended wall of the cavity back of the main rectangular waveguide can be used as a smaller rectangular waveguide. The design parameters for the waveguide follows the same principles as discussed before and require optimisation to obtain good performance. Figure 5.39 shows the extended cavity back that have been optimised for a rectangular waveguide operating in the frequency band from 3.5 GHz to 7.5 GHz. The dimensions if the waveguide are as follow: width, W = 8 cm, height, H = 3 cm and length, L = 11.5 cm.

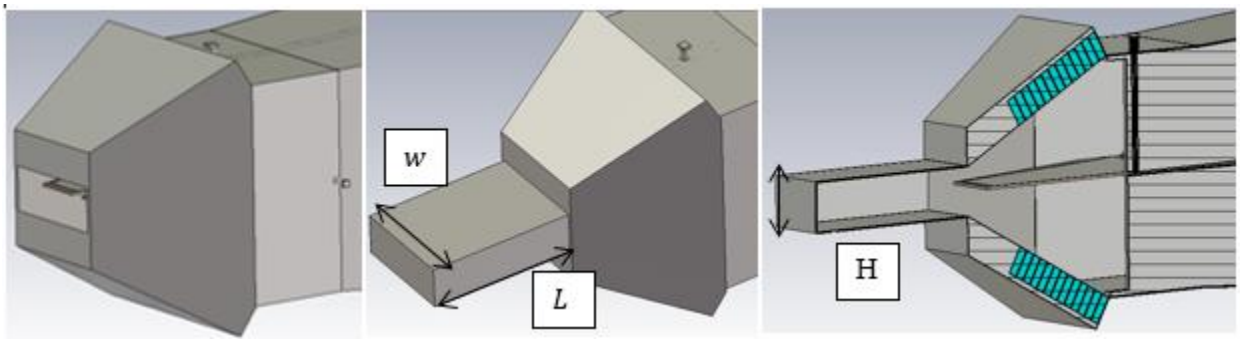

Figure 5-39: Extended cavity back rectangular waveguide design

Coaxial probe to monopole transition is used to excite and create the field patterns for the TE_{10} mode in a rectangular waveguide. Coaxially fed monopole in a rectangular waveguide has been widely used in microwave devices including coaxial-line-to-waveguide transition. The inner conductor of the coaxial cable behaves like a dipole antenna and it creates a maximum electric field in the middle of the cross section. The monopole is placed vertically in order to excite vertically polarised E-fields. The geometry and dimensions of the monopole antenna are shown in Fig. 5.40. The monopole length is based on λ, at lower frequency of operation and its offset from the closed wall influences the input impedance.

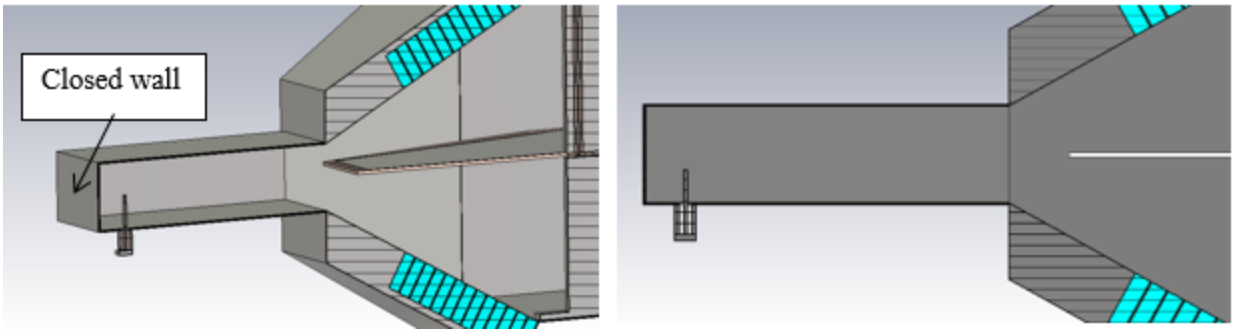

Figure 5-40: Monopole to rectangular waveguide transition antenna

The coaxial connector is mounted on the centre line of the waveguide broad wall with its bare centre pin extending into the guide. One end of the guide is short-circuited about 1/8 of the waveguide wavelength *(Wade, 2006)*, from the pin to make an open cavity. The other end is open and far enough from the pin to suppress higher order modes. The operation of the transition can be understood by considering a CW signal entering the coaxial port with the waveguide port terminated in a matched load. The maximum of the TE_{10} electric field pattern is polarised in the plane of the broad wall centre line, thus the extension of the centre conductor couples strongly to the TE_{10} mode by acting as a short capacitive monopole. Higher-order waveguide modes are cut off but contribute to the probe's reactance. The short-circuit guide with length about 1/8 of the guide wavelength produces an inductive reactance in parallel with the probe's capacitive reactance and is used to tune the total input reactance to zero *(Ramo, Whinnery & Van Duzer, 1994)*, *(Pozar, 2005)*. The input impedance is controlled by changing the probe length, the pin offset from the closed wall can be adjusted to compensate for the change in the pin reactance. The probe reactance is dependent on its length and diameter, and the short-circuit guide reactance on its length. These three dimensions are adjusted to minimise the total input reactance and get a resistive impedance match between the coaxial and waveguide ports *(Keam & Williamson, 1994)*. The impedance bandwidth of a bare probe can be increased by increasing the probe diameter. And in some cases, it can be further enhanced by covering the pin with a dielectric material. The optimised length of the probe is 10.5 mm and it has a 20 mm offset from the closed wall. The diameter of the pin is 1 mm and is covered with TEFLON material of 3 mm diameter. The simulated VSWR of the antenna is presented in Fig. 5.41 and it can be seen that the band from 3.1 GHz to 7.5 GHz is just below 2.

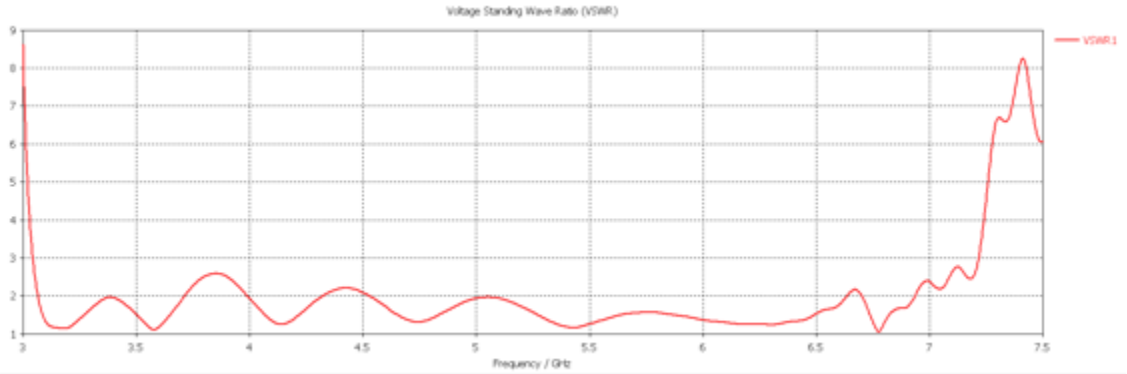

Figure 5-41: VSWR of the coaxial to waveguide transition antenna

The ringing of the antenna in the port reflections is presented in Fig 5.42. Although open-end coaxial probes are not in favour of low ringing, the design in its simplest form has reasonable levels of ringing where the maximum peak is around 0.2 V (for a 1 V input power), and the signal is dampened around 10 ns.

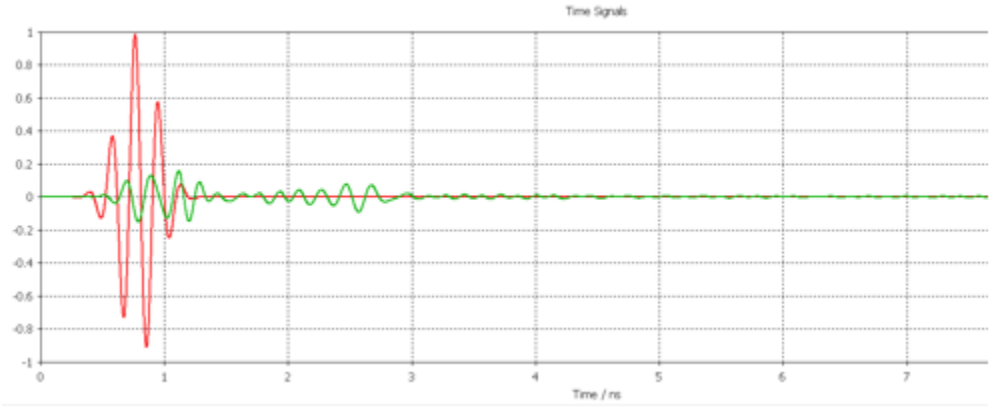

Figure 5-42: Ringing and ports reflection of the coaxial to monopole waveguide antenna

5.3 Overall Antenna Structure

The final antenna structure is shown in Fig. 5.43. The antenna has 4 ports, and each port corresponds to a particular channel with a different frequency band, polarisation and radiation pattern. The overall dimensions of the antenna is L = 77 cm , W = 33 cm, and H = 30 cm . In order to fabricate the antenna, the outer structure of antenna was redesigned to ensure mechanical validity. The mechanical design of the antenna structure and its performance are discussed in Chapter 6. The functionally of the antenna is summarised in Table 5.2.

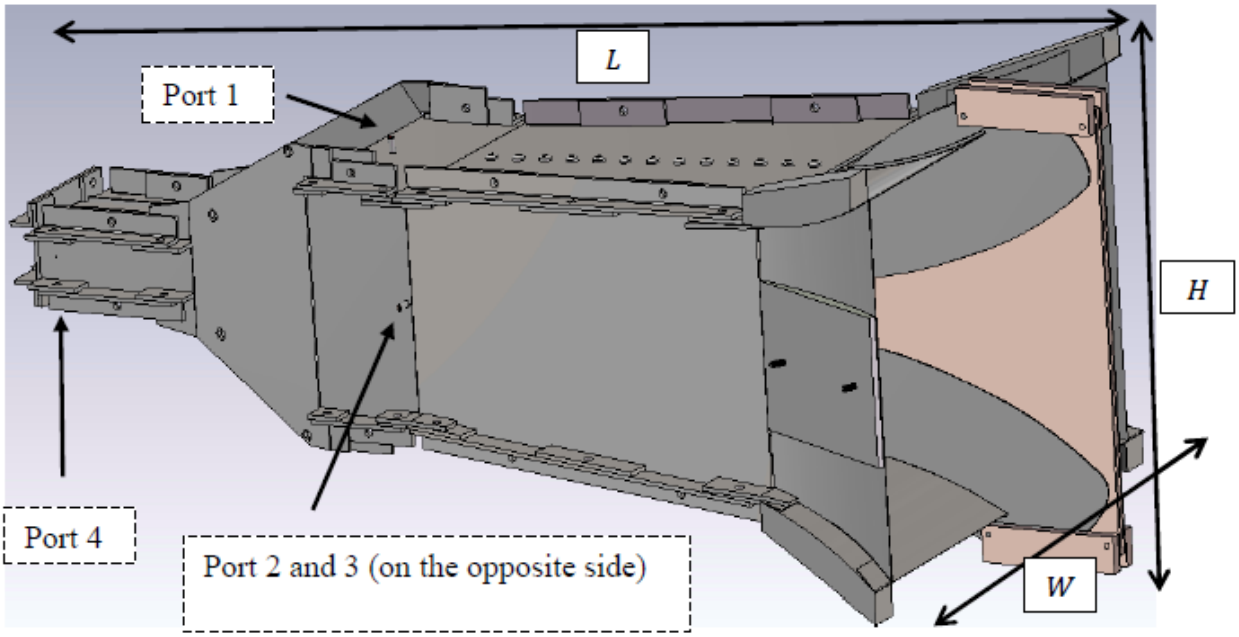

Figure 5-43: Overall Antenna Structure

Port number	**Operating frequency**	**Polarisation**	**Radiation pattern beamwidth (at centre frequency)**
1	0.5 – 5.5 GHz	Vertical	26 °
2	2.5 – 6 GHz	Horizontal	22.7° , 10.6 ° (combined)
3	2.5 – 6 GHz	Horizontal	22.9 °, 10.6 ° (combined)
4	3.5 – 7.5 GHz	Vertical	41 °

Table 5-2: Multi-Functionality of the Antenna Design

5.4 Summary

Ultra-wideband antennas are an essential part of GPR systems as well as ultra-wideband radar and communications systems. The fractional bandwidth of the GPR antennas is usually greater than 100 % and provides very high range resolution. Only a selected type of antennas can be used in GPR systems. Depending on the type of radar system, whether time or frequency domain, these antennas are carefully designed. The aim of the antenna design is to provide an acceptable GPR performance; this is measured by the quality of their signal integrity, adequate gain, adequate efficiency and directivity.

The nature of the ground and landmine targets play an important role on the characteristic of the EM wave illuminated. Different operating frequency, polarisation and radiation patterns can result in a different image acquired from the target scene. Therefore, multi-functional antennas that can provide this diversity may result in the transfer of useful developments.

In this work, a multi-functional antenna is introduced and designed. The antenna can provide diversity in operating frequency band, polarisation and radiation pattern beamwidth using the same antenna structure. In the development of the antenna structure, new design techniques have been undertaken and investigated. A new cavity back for the rectangular waveguide in horn antennas have been designed that provide reduced unwanted reflections towards to coaxial probe input and hence enhancing the performance of the horn antenna. To further minimise the reflections from the open end aperture of horn antennas, a new modified aperture matched structure have been introduced. To overcome the complexity of conventional methods to operate at different polarisation in horn antennas, a new technique has been introduced that can provide horizontal polarisation as well as the ability to add additional operating channel to the antenna.

The overall antenna design provides 4 channels that can be operated simultaneously or independently. Each channel can provide different characteristics and their performances in GPR have been discussed in Chapter 7.

5.5 References

Ameri, A., Kompa, G., Bangert, A. (2011). *Study About TEM Horn Size Reduction for Ultra-Wideband Radar Application*. German Microwave Conference (GeMiC), Darmstadt, pg 1-4.

Bruns, C., Leuchtmann, P., Vahldieck, R. (2003). *Analysis and simulation of a 1–18 GHz broadband double-ridged horn antenna*. IEEE Transaction on Electromagnetic Compatibility, Vol. 45, 55–59

Conyers, L. (2004). *Ground Penetrating Radar for Archaeology* (Geophysical Methods for Archaeology)

Drabowitch, S., Papeirnik, A., Griffiths, H.D., Encinas, J., Smith, B.L. (2005). *Modern Antennas*. 2nd Edition, Springer

DARPA/OSD. (1990*). Ultra-Wideband Radar Review Panel, Assessment of UltraWideband (UWB) Technology*. Arlington: DARPA.

Greenberg, M. C., Virga, K.L., Hammond, C. L. (2003). *Performance characteristic of the dual exponentially tapered slot antenna (DETSA) for wireless communications applications*. IEEE Trans. Vol. 42, No. 2, 305–312, Mar. 2003.

Hopfer, S. (1955). *The design of ridged waveguides*. IRE Trans. Microwave Theory Tech. Vol. 3, 20–29

Ihf. (2006). *Research topic antennas*. [Online] Available from: http://www.ihf.uni-stuttgart.de/forschung/forschungsgebiete/nahfeld/index.html

Jarvis, D. A., Rao, T.C. (2000). *Design of double-ridged rectangular wave guide of arbitrary aspect ratio and ridge height*. IEE Proc. Microw. Antenna Propagat. Vol. 147, 31–34

Kraus, J.D, Marhefka R.J. (2002). *Antennas: For All Applications*. 3rd Ed. McGraw-Hill

Kerr, J. L. (1973). *Short axial length broad-band horns*. IEEE Trans.Antennas Propagat. Vol. 21, 710–714

Keam, RB, Williamson, AG. (1994). *Broadband design of coaxial line/rectangular waveguide probe transition.* IEE Proceedings – Microwaves, Antennas and Propagation, vol 141, no 1, February 1994, pp 53-58.

Langley, J.D.S., Hall, P.S., Newham, P. (1993). *Novel Ultrawide-Bandwidth Vivaldi Antenna With Low CrosspolarisationI*. Electron. Lett. Vol. 29, No.23.

Lacko, P. R., Clark, W. W., Sherbondy, K., Ralston, J. M. (2003). *Studies of Ground Penetrating Radar Antennas*. 2nd International Workshop on Advanced GPR, pp. 24–29, Delft, Netherlands

Magg, M., Nitsch, J. (1998). *Mine Detection with Microwaves*. RTO Lecture Series: Advanced Pattern Recognition Techniques

Pozar, D.M. (2005). *Microwave Engineering*, 3rd Edition, Wiley

Ramo, S., Whinnery JR., Duzer T.V. (1994). *Fields and Waves in Communication Electronics.* 3rd Edition, Wiley, Section 8.11, Excitation and reception of waves in guides.

Radzevicius, S. J., Guy, E. D., Daniels, J. J. (2000). *Pitfalls in GPR Data Interpretation: Differentiating Stratigraphy and Buried Objects from Periodic Antenna and Target Effects.* Geophysical Research Letters, vol. 27, pp.

Shlivinski A., Heyman E., Kastner R.B. (1997). *Antenna characterization in the time domain*. IEEE Trans. Antennas Propag, vol. 45, pp. 1140–1149.

Turk S., Sahinkaya D.A. (2007). *Partial Dielectric Loaded TEM Horn Design for Ultra-Wideband Ground Penetrating Impulse Radar Systems*. Ultra-Wideband Short-Pulse Electromagnetics Series 7, chapter 34, Springer, Berlin.

Technick. (1997). *PCB Impedance and Capacitance Calculator*. [Online] Available from: http://www.technick.net/public/code/cp_dpage.php?aiocp_dp=util_pcb_imp_microstrip

Walton, K. L., Sundberg, V. C. (1964). *Broadband ridged horn design*. Microwave J. 96–101

Walter, C.H. (1990). *Travelling Wave Antennas*, McGraw-Hill, 1965, Dover, 1970, reprinted by Peninsula Publishing, Los Altos, California.

Wade, P. (2006). *Rectangular waveguide to coax transition design*. [Online] Available from: http://www.w1ghz.org/QEX/Rectangular_Waveguide_to_Coax_Transition_Design.pdf

Yarovoy G., Schukin A. D., Kaploun I. V., Ligthart L. P. (2002). *The dielectric wedge antenna*. IEEE Trans. on Antennas and Propagation, vol. 50, no. 10, 1460- 1472.

Chapter 6

Antenna Fabrication and Verification

6.1 Design Process and Fabrication

A systematic approach for the design, fabrication, and testing of the antenna was performed in five stages. The complete design and fabrication processes are schematically illustrated in Fig. 6.1. As shown, there are five main stages in the proposed approach, namely simulation, mechanical design, mechanical verification prototyping, antenna fabrication and antenna measurements. The design and fabrication process started with the numerical simulations using CST Microwave Studio. After acceptable simulation results had been obtained, the design was further modified to take into account the mechanical assembly of the design in real life. This includes flanges, supporting wedges and screw heads. The CAD design of the antenna then was converted into an appropriate Computer Numerical Control (CNC) file for manufacturing. The first prototype was made out of wood and plastic to ensure reliable assembly of the design.

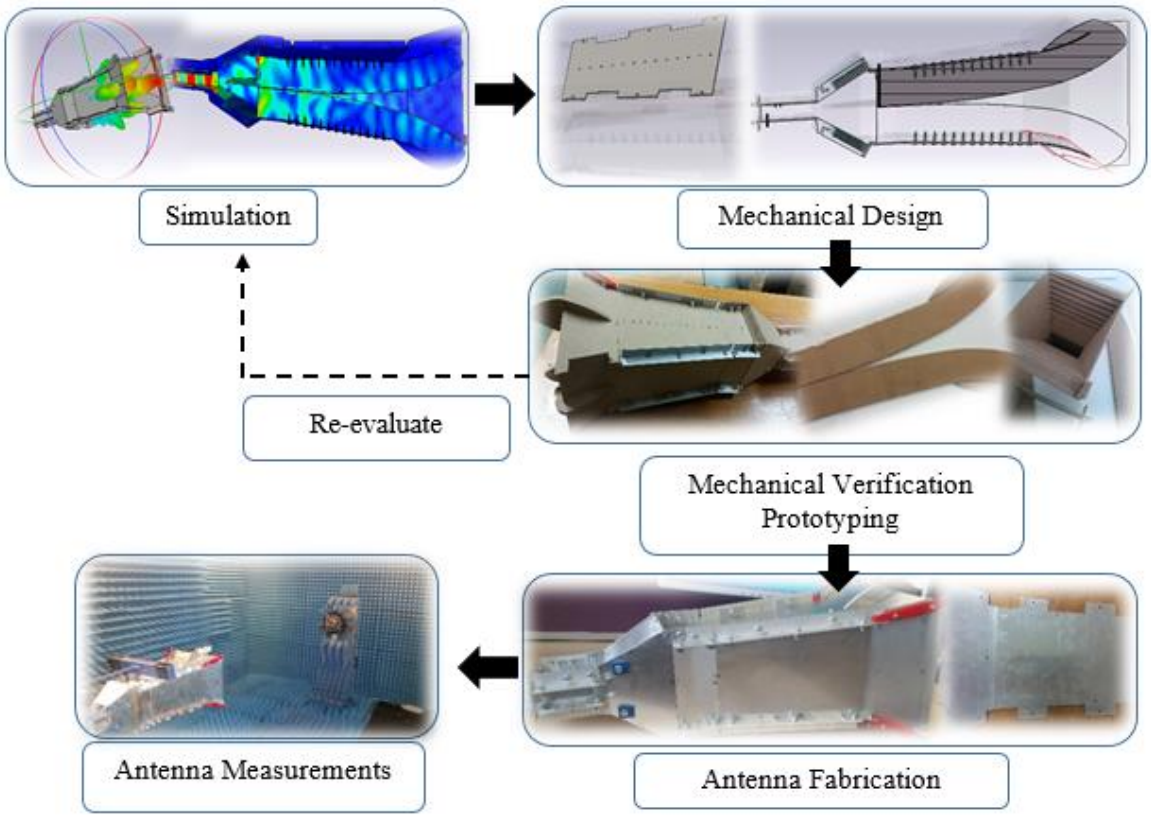

Figure 6-1: Design and fabrication processes of the prototype antenna

After the prototype design had been constructed, the modifications and improvements were noted and realised by altering the initial design in simulation stage. The performance of the antenna was also re-evaluated at this stage to ensure the new changes did not introduce any anomalies. Once the final requirements were met, the design was fabricated and assembled. The optional fabrication conditions, such as the material, manufacturing type, feed structure, electrical conductivity and complexity of the fabricated pieces were investigated. The final stage involves measuring the antenna parameters such as resonant frequency, gain, and far-field radiation patterns.

6.1.1 Mechanical Design and Construction

Various fabrication processes were considered to realise the complex structure of the antenna. Additive Manufacturing (AM) is now a new trend to synthesize a 3D object. AM technology can vary from one technique to another, and the most common ones include Stereolithographic (SLA), Selective Laser Sintering (SLS), Fused Deposition Modelling (FDM), Direct Metal Laser Sintering (DMLS) and 3D printing. In 3D printing, successive 2D layers of material of choice are formed upon one another under computer control to create an object. DMLS, metal laser cutting and milling, 3D printing and waterjet cutting techniques were used to prepare various parts of the antenna.

As shown in Fig. 6.1 before the fabrication of the antenna, the design has to be revised. In order to fabricate the design practically, mechanical considerations have to be taken into account. This involves dividing the design into pieces that can be assembled after fabrication. One of the concerns with fabricating horn antennas is the quality of welding the pieces together. Any discontinuity on the surface of the pieces will cause reflections of propagating signal. To minimise this, large parts of the design were fabricated in one piece; this includes the double ridges and the conducting walls. Figure 6.2 shows the aperture matched conducting walls and how it is slotted inside the double ridges. The double ridge is then secured and maintains a good connection to the conducting walls by consecutive screws placed along the ridge. To join the pieces together, an interlocking mechanism is used where two pieces form a right angle with a minimum gap from the inside and are screwed and held together from the outside. Figure 6.3 shows how the rectangular waveguide is formed. The top and bottom pieces of the rectangular waveguide is cut together with the conducting walls and it is bent to form the correct profile. The side pieces of the rectangular waveguide and conducting walls are cut separately and are joined.

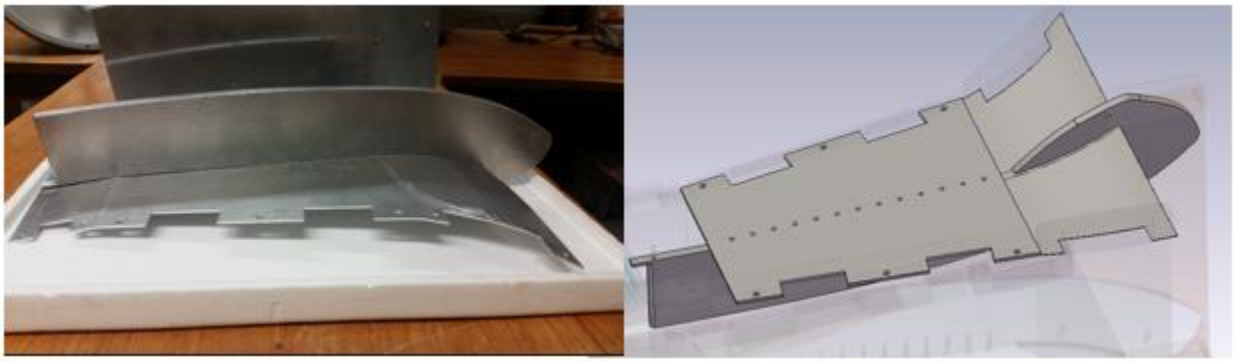

Figure 6-2: Fabricated conducting walls and Double Ridges of the Horn Antenna

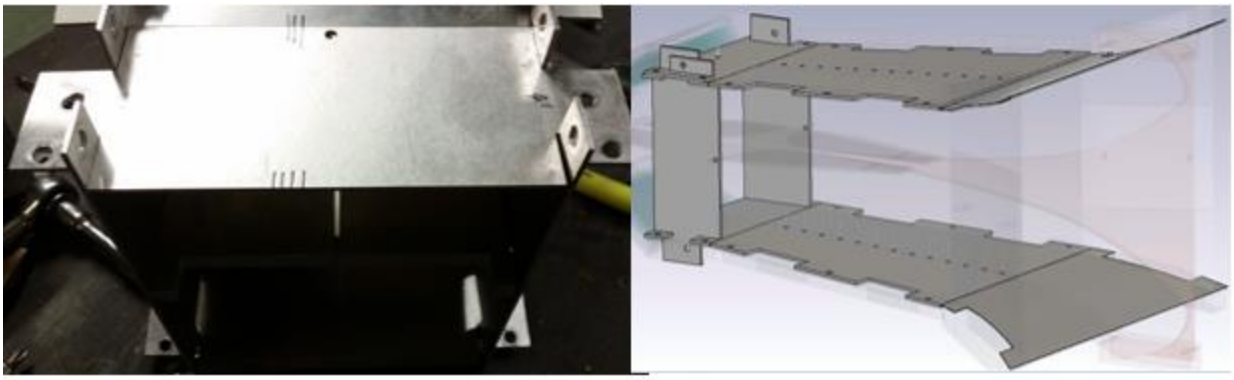

Figure 6-3: The interlocking mechanism to join the pieces together

The next step is to construct the feed for the double ridges. Since the height of the ridges is 7.1 cm, no off-the-shelf SMA coaxial connector was available to feed the ridges. Instead, a semi-rigid coaxial cable was used to make a 50 Ω connection line. The dimensions of the dielectric and inner conducting pin were re-entered in the simulation design to ensure the integrity of the performance is maintained. The holes inside the ridges were made by special drilling machines in the workshop to obtain a relatively smooth surface. Figure 6.4 shows how the feeding mechanism is implemented inside the double ridges.

Figure 6-4: Feeding mechanism of the double ridges

The inner pin of the feed was particularly decided to be inserted deeper into the opposite arm of the double ridges to keep a stable connection and preserve the symmetry of the structure. The third step in the fabrication process is to prepare and attach the Band 2 antenna (thin dielectric ridges) since the structure has to be open to access and place them inside. The thin ridges are fabricated on a Rogers substrate and cut in a way that can be placed inside the horn structure perpendicular to the double ridges. Figure 6.5 shows the PCBs and how they are mounted inside the structure. The side walls of the rectangular waveguide have been modified with a dielectric support to hold the PCBs in place. The SMD resistors and standard 50 Ω SMA connectors are added on, the substrate and the copper surface cleaned and dried before being fixed inside the structure.

Figure 6-5:

The design of the back cavity structure is realised by laser cutting and milling techniques. Before closing the cavity back structure, the RAMs are introduced and kept in place with an adhesive material. The RAMs are cut according to the dimensions of each serrated walls inside the cavity. Figure 6.6 illustrates the cavity back and how it is connected to the rest of the horn structure.

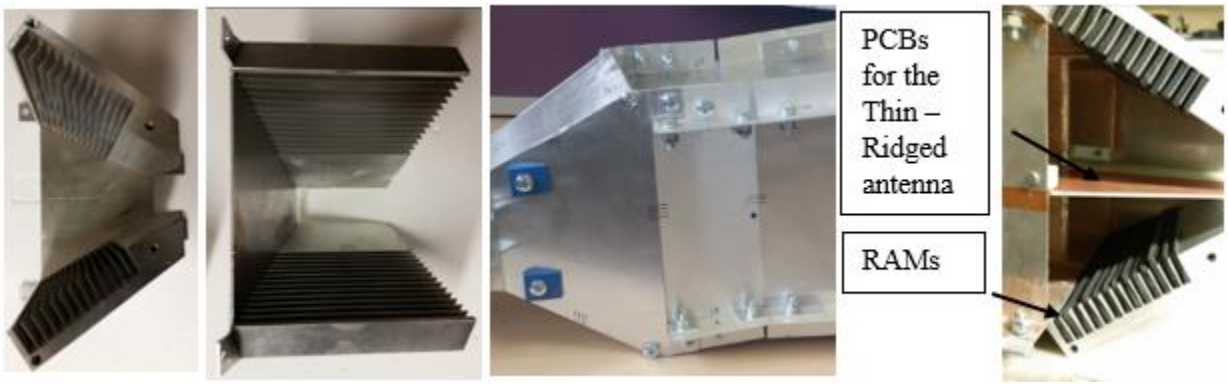

Figure 6-6: The back cavity structure

The smaller rectangular waveguide is connected to complete the back of the horn structure. The waveguide is formed by the same mechanism as the larger waveguide, and the coaxial SMA connector is screwed on. Figure 6.7 shows the cavity back the smaller rectangular waveguide assembled and how it is fed from an extended dielectric coaxial SMA connector.

Figure 6-7: Smaller rectangular waveguide

To complete the horn structure, the dielectric filling of the double ridges are prepared. The profile of the dielectric shape resembles the inner mouth of the ridges and is cut accordingly. The sheet is 8 mm thick TEFLON (PTFE) material and is cut with a drill bit of 3 mm in diameter. Fig. 6.8 shows the profile of the dielectric filling sheet and how it is secured in place with two clamps that were designed and cut to keep the sheet in place from both sides. This is to ensure the gap between the sheet and the ridges is minimised.

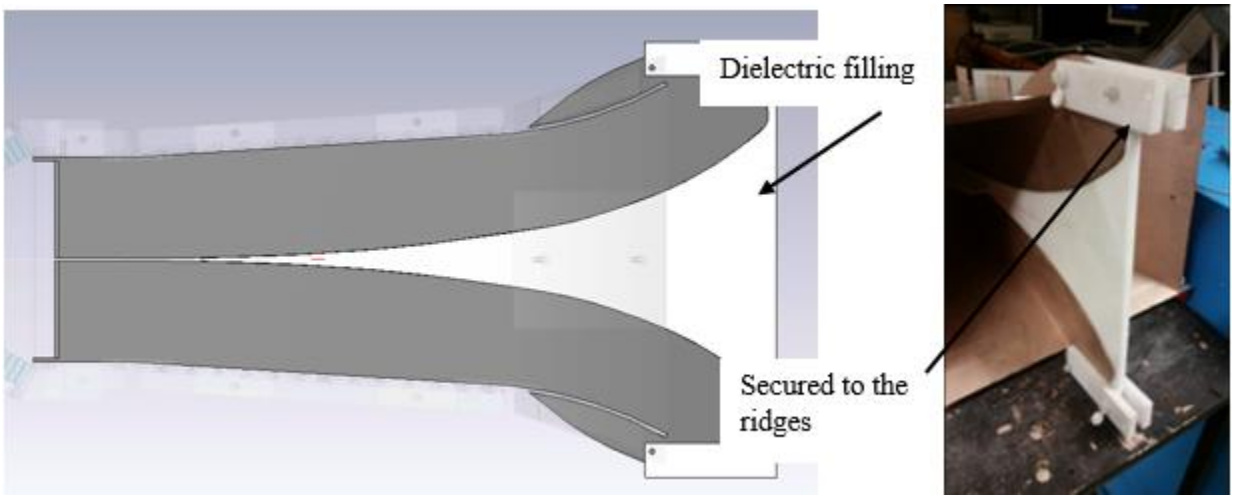

Figure 6-8: Dielectric filling of the double ridges

To reduce signal leakage and increase the conductivity of the structure, all intersections, the surface of the conducting walls and double ridges were covered with CuPro-Cote Paint. This is a copper particle conductivity in a water based paint and has a surface resistivity of less than 1 Ω/sq at 1 mm dry film thickness. Copper paint offers a good trade-off between cost and performance as opposed to silver paint and gold plating (*Willis, 2012*). It is reported by Willis (2012) that increase in a number of layers of copper paint will increase the gain of the horn structure at certain frequencies. It is suggested that the structure is painted 1-2 skin depths thick to minimise the losses in the structure. The skin depth is calculated at several frequencies across all three bands, and the antenna was covered in 3 layers of paint. All the intersections were also covered by copper tape from the outside as well as paint from the inside. Figure 6.9 shows the complete structure. The aperture matched walls were supported and secured by 3D printed blocks (from ABS plastic material) that are screwed on the structure outside.

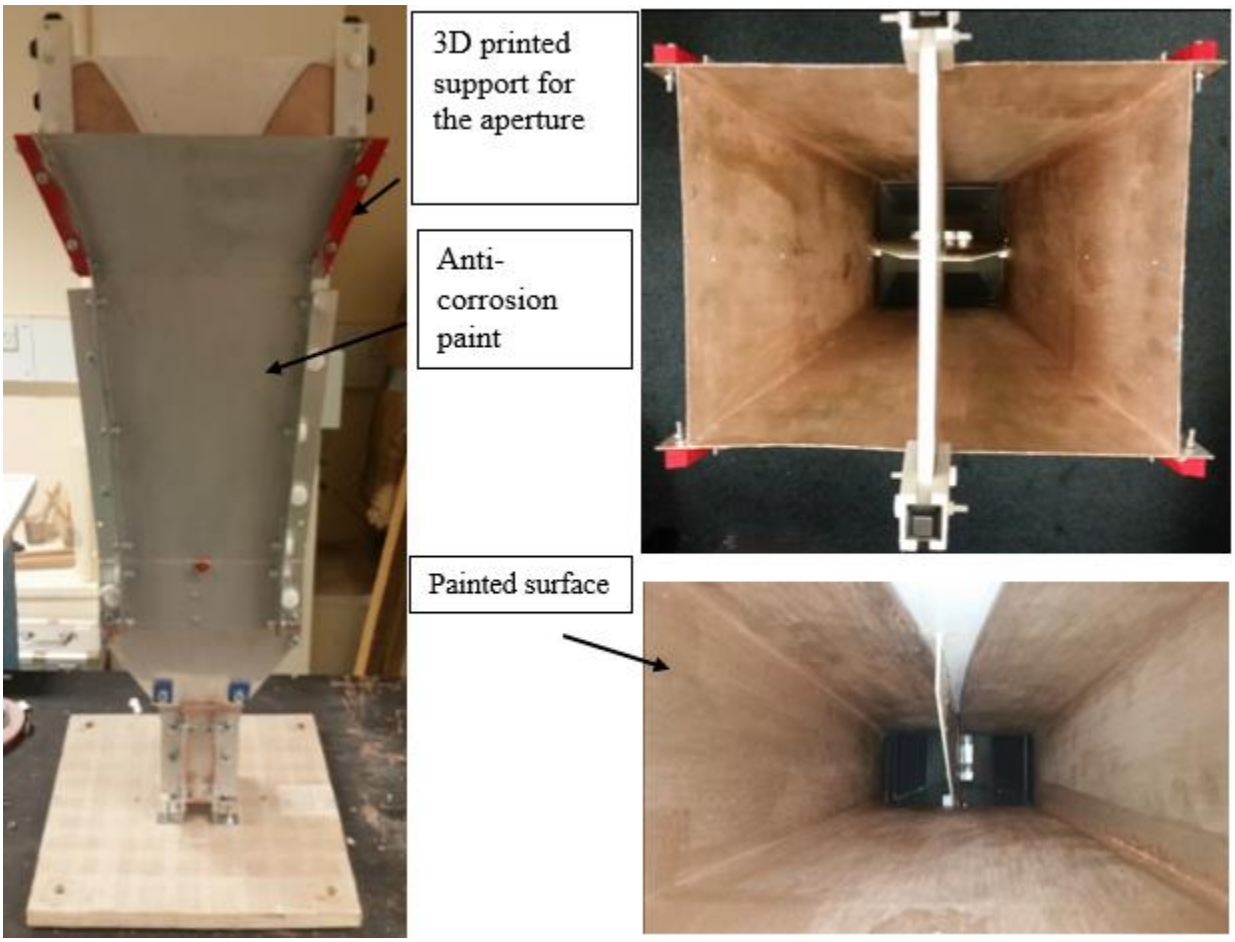

Figure 6-9: The complete fabricated horn structure

6.2 Antenna Measurements

During the process of fabrication, electrical conductivity tests and measurements were performed to check the behaviour of the structure step by step. However accurate measurements are necessary to establish the actual performance of the antenna. This in combination with the simulation results will also help in understanding the fabrication tolerances and errors. In this section methods and techniques that were used to measure the antenna are discussed and presented.

6.2.1 Basic Concepts

The most common antenna measurement is to measure its radiation properties such as radiation pattern and gain. There is a wide range of antenna parameters that can be measured. For radiation pattern, it was decided that a 1-D cut as a function of azimuth, at a single polarisation, is adequate. A typical configuration of the measurement of radiation properties is shown in Fig. 6.10.

Figure 6-10: Typical configuration for the measurement of the radiation properties of an antenna

The procedure consists of placing a transmitting source at a location with respect to the position of the Antenna Under Test (AUT) and get some samples of the pattern. The patterns of the antenna can be measured in transmit or receive mode. Here, receiving mode is taken into account (assuming reciprocity principle). It is not practical to measure the pattern in 3D due to the limitation of the turning table in the chamber. Therefore, only a number of 2D patterns are measured. For azimuth measurements, the elevation is fixed while varying azimuth. The mounting structure and the turn-table have to be suitable to accommodate the procedure. To ensure the sharpness of the measured patterns, only one direct signal path should ideally exist between the source antenna and AUT. This can either be achieved in a reflection-free environment like in an anechoic chamber or, in free space. A suitable outdoor environment or large anechoic chamber will result in better measurement

since there will be a better approximation to a plane wave. However, this requires suitable cables and equipment.

In applying reciprocity principle to the AUT, a few important conditions were taken into account to ensure the validity of the principle. The first step is to make sure the signal in the terminals of the interchanged antennas is of the same frequency range. Hence, suitable source antenna that covers the AUT frequency band was used. The second step is to make sure the power flow is the same either way.

Another consideration for the antenna measurement is the near-field and far-field setup. The conventional setup for most applications requires the antenna to be in far-field, and this setup offers several advantages and disadvantages. These are summarised below *(Kraus and Marhefka 2002)*:

- ✓ The measured field pattern is valid for any distance within the far-field region.
- ✓ The result is not very sensitive to the changes in the location of the phase of the antennas, and therefore, the AUT rotation angle does not cause significant measurements errors.
- ✓ Coupling and multiple reflections between the antennas are reduced.
- o Large distance between the antennas is needed leading to large antenna ranges
- o It can lead to atmospheric attenuation

Considering the field boundary regions, the distance from the source antenna to AUT can be calculated. The largest dimension of the physical aperture of the fabricated antenna is 0.38 m. Therefore, to satisfy the far-field conditions, the distance between the source and the AUT has to be 7.7 m at 8 GHz and 4.8 m at 0.5 GHz. It was decided that it was not feasible to gather and prepare the right equipment including a suitable turntable and measuring devices for far-field setup in an outdoor environment. Instead, the measurements were taken in an anechoic chamber at University College London (installed by MI Technologies, Atlanta, USA, May 2005). The chamber is designed for 2 GHz to 40 GHz spherical near-field measurements. However, it did offer an adequate environment and setup for the measurements discussed here. Figure 6.11 shows the chamber and the station that is used to acquire data and control the turntables. The source antennas that were used to measure the radiation pattern of the AUT were a QH800 quad-ridge antenna that operates from 0.8 to 12 GHz and Log Periodic (LP) antenna that operates from 0.4 to 1 GHz. The acquisition equipment to measure the data is based on a ZNB40 10 MHz to 40 GHz VNA from Rohde & Schwarz. The radiation pattern results in azimuth for centre frequency, lower

cut-off frequency and higher cut-off frequency of the band in each antenna channel are presented in the following sections.

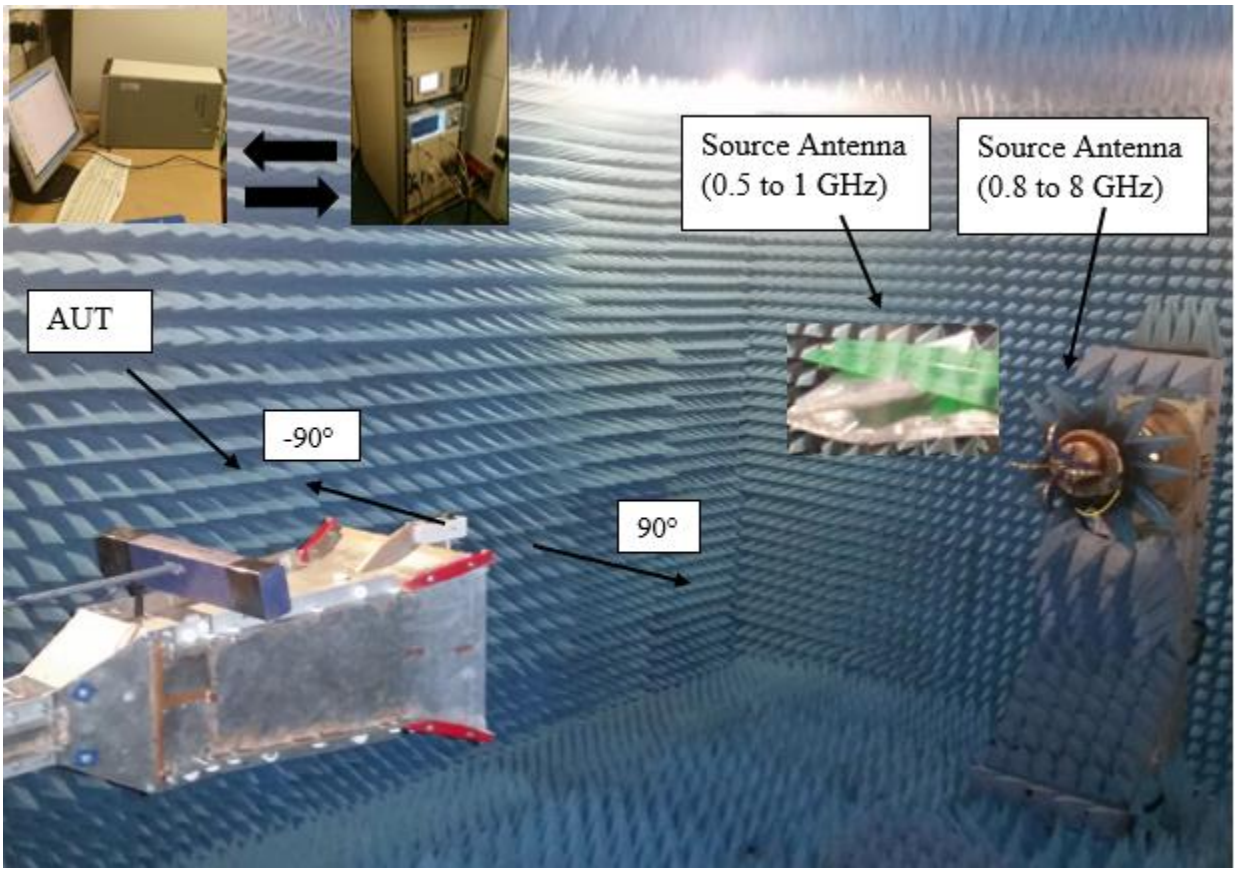

Figure 6-11: An anechoic chamber and measurement setup at UCL

6.2.2 Radiation Pattern Results for 500 MHz – 5.5 GHz Antenna

The radiation pattern was recorded at 1 degree of increment from -90 to 90 scanning angles. Due to the metallic structure of the turntable where the AUT was mounted, angles beyond 90 degrees did not present desirable results. The mount is rotated in azimuth in a forward direction, and the data is recorded. Figure 6.12 shows the normalised radiation pattern for experimental (in blue) and simulation (in red) in comparison. There is a slight agreement for the radiation patterns at 0.5 GHz however the experimental result doesn't seem to be quite symmetrical. This could be because the floor of the chamber is not fully covered by RAMs which could give rise to a different level of ground reflections. At 3 GHz the radiation patterns are in good agreement. However, the experimental results show a lower level of sidelobes at around 50°. The radiation pattern for 5.5 GHz seems to have a slightly different pattern of sidelobes. However, the mainlobe within 20°

show a similar pattern. The 3D radiation pattern of all three frequencies is also presented in the figure.

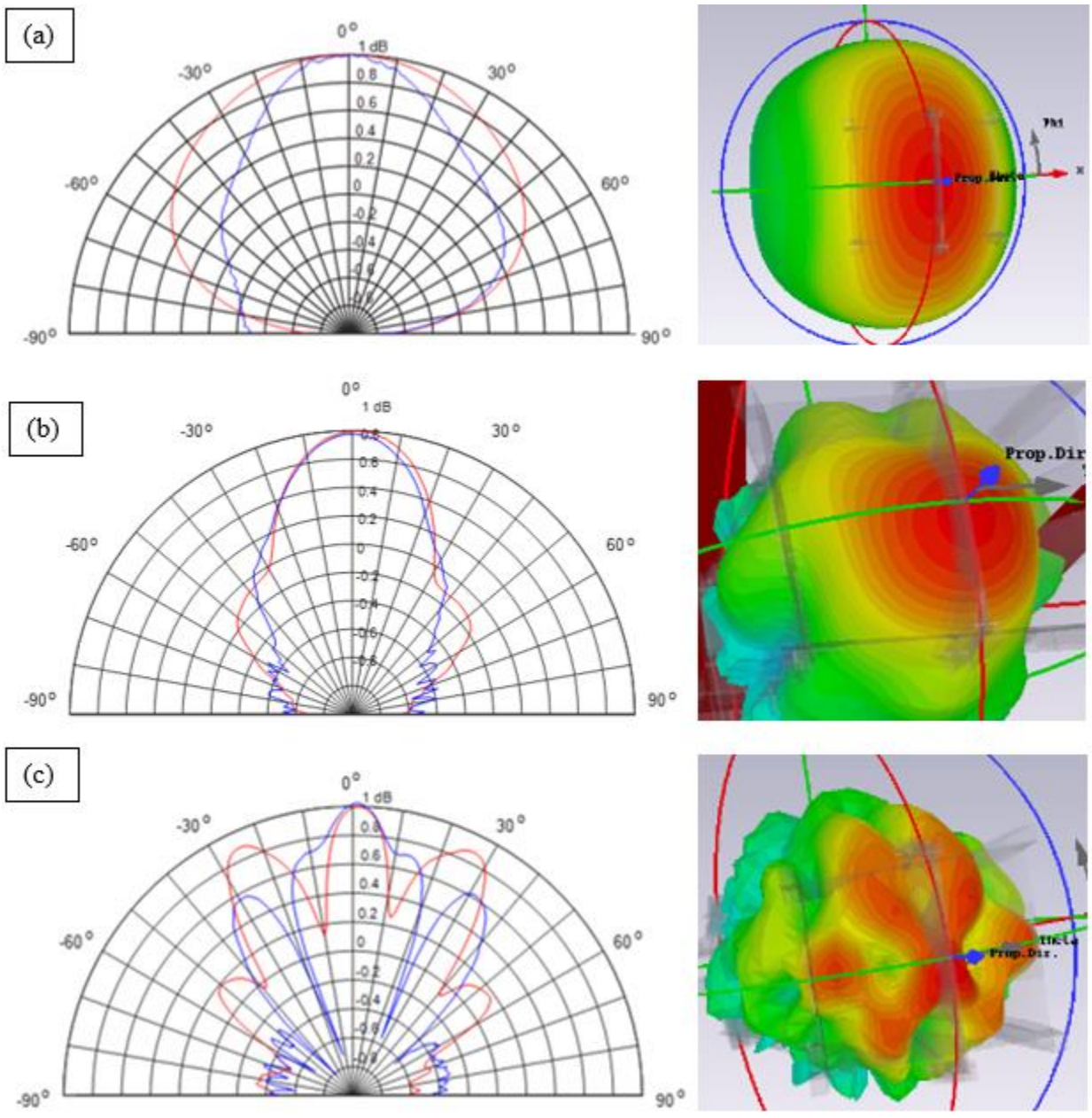

Figure 6-12: : Experimental (in blue) and Simulation (in red) radiation patterns for 0.5 GHz (a), 3 GHz (b) and 5.5 GHz (c) for the band 0.5 to 5.5 GHz antenna

6.2.3 Radiation Pattern Results for 3 to 6 GHz Antenna

As the performance of both pairs of antennas is quite similar, the radiation patterns for one pair (left-hand side of the antenna with the aperture pointing towards the source antenna) is shown in Fig. 6.13. The radiation patterns for 3 and 4.25 GHz are both located on the boresight, and they show similar behaviour. The mainlobe of the radiation pattern for 6 GHz is distributed off the boresight, but the experimental and simulation results show similar patterns.

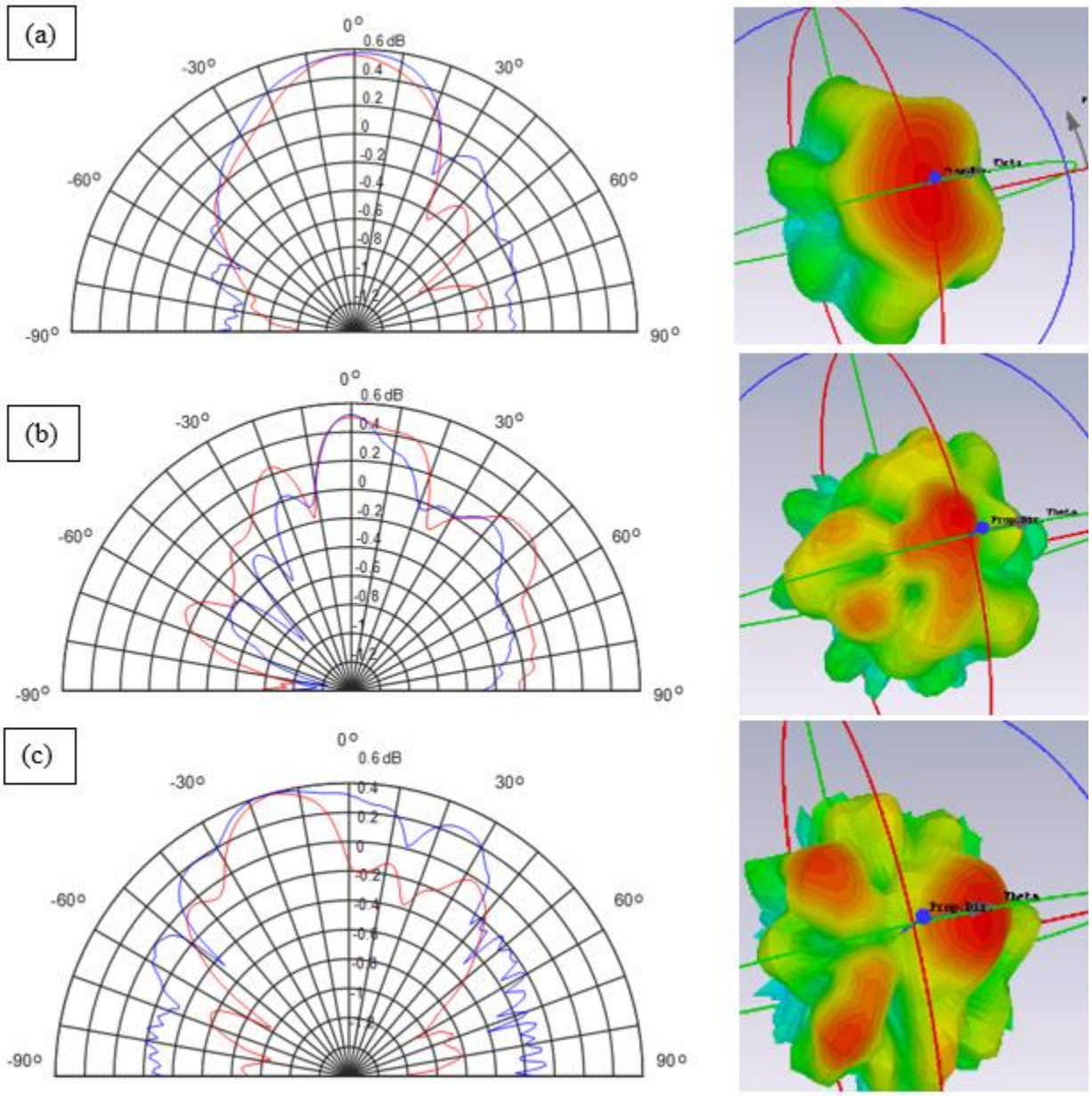

Figure 6-13: Experimental (in blue) and Simulation (in red) radiation patterns for 3 GHz (a), 4.25 GHz (b) and 6 GHz (c) for the band 3 to 6 GHz antenna

6.2.4 Radiation Pattern Results for 3.5 to 7.5 GHz Antenna

The radiation patterns for the third band is presented in Fig. 6.14. The experimental and simulation patterns are in good agreement with small differences between them. The radiation pattern for all three frequencies shows a wide beamwidth and constant pattern.

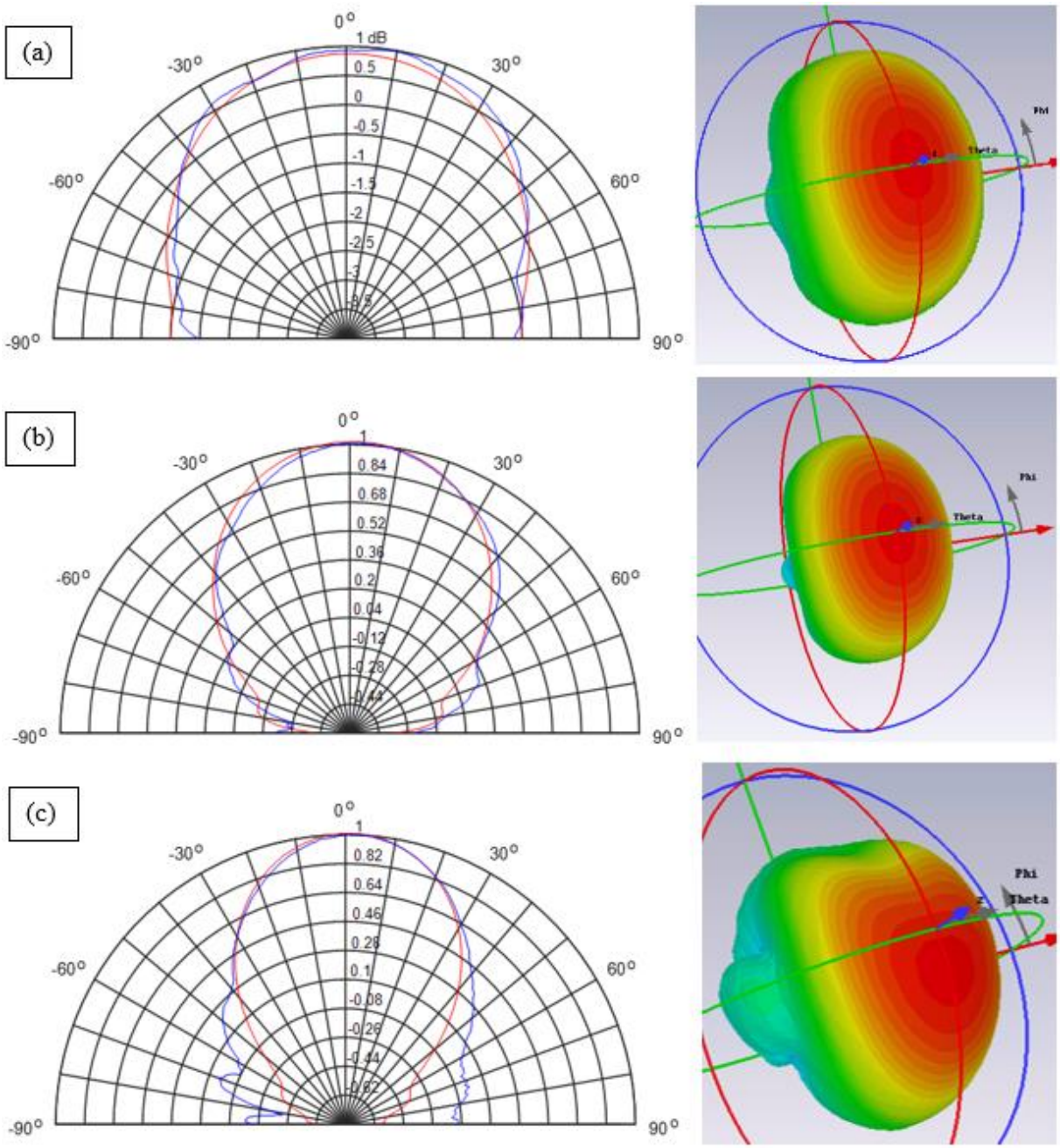

Figure 6-14: Experimental (in blue) and Simulation (in red) radiation patterns for 3.5 GHz (a), 5.5 GHz (b) and 7.5 GHz (c) for the band 3.5 to 7.5 GHz antenna

6.2.5 Gain Measurements

There are several methods to measure the gain of the AUT. Absolute method and comparison method are the two basic gain measurement methods. The measurement setup for each method requires either a two antenna measurement or a three antenna measurement. In all cases, the received power is recorded (e.g. s_{21}) and with the known reference antenna gain the gain of the unknown antenna can be determined. Considering the measurement setup illustrated in Fig. 6.15, the Friis transmission principle that establishes the power received by the AUT and known antenna in dBs can be defined and is shown in Eq. 6.1-6.3.

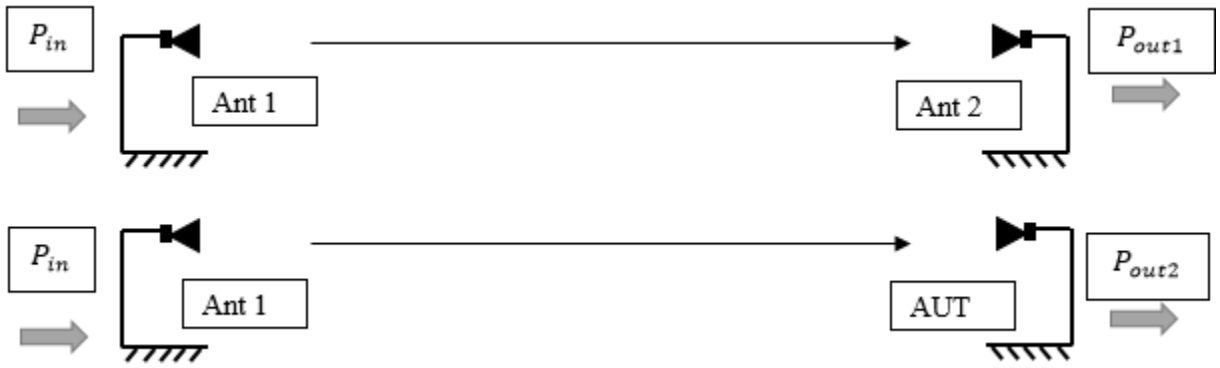

Figure 6-15: Gain measurement setup

$$P_{out1} = P_{in} + G_{ANT1} + G_{ANT2} - Pathloss \quad (6.1)$$

$$P_{out2} = P_{in} + G_{ANT1} + G_{AUT} - Pathloss \quad (6.2)$$

$$P_{out1} - P_{out2} = G_{ANT2} + G_{AUT} \quad (6.3)$$

For the measurement setup, it is important to make sure the polarisation of the antennas is matched, and the mainlobe peaks are aligned with the line of measurement. The power flow in each setup is recorded and Eq. 6.1 is subtracted from Eq. 6.2 leaving the only unknown parameter as the gain of the AUT. This assumes the gain of a reference antenna is known for a particular frequency. Since there was no availability of another pair of antennas that cover the same frequency range of the AUT (0.5 – 8 GHz), two Log Periodic antennas were used. Overall, three measurements were conducted using a particular pair of antennas as shown in Fig. 6.16. Using the equations described above and the specifications of the known antenna, the gain of the AUT for each band is determined.

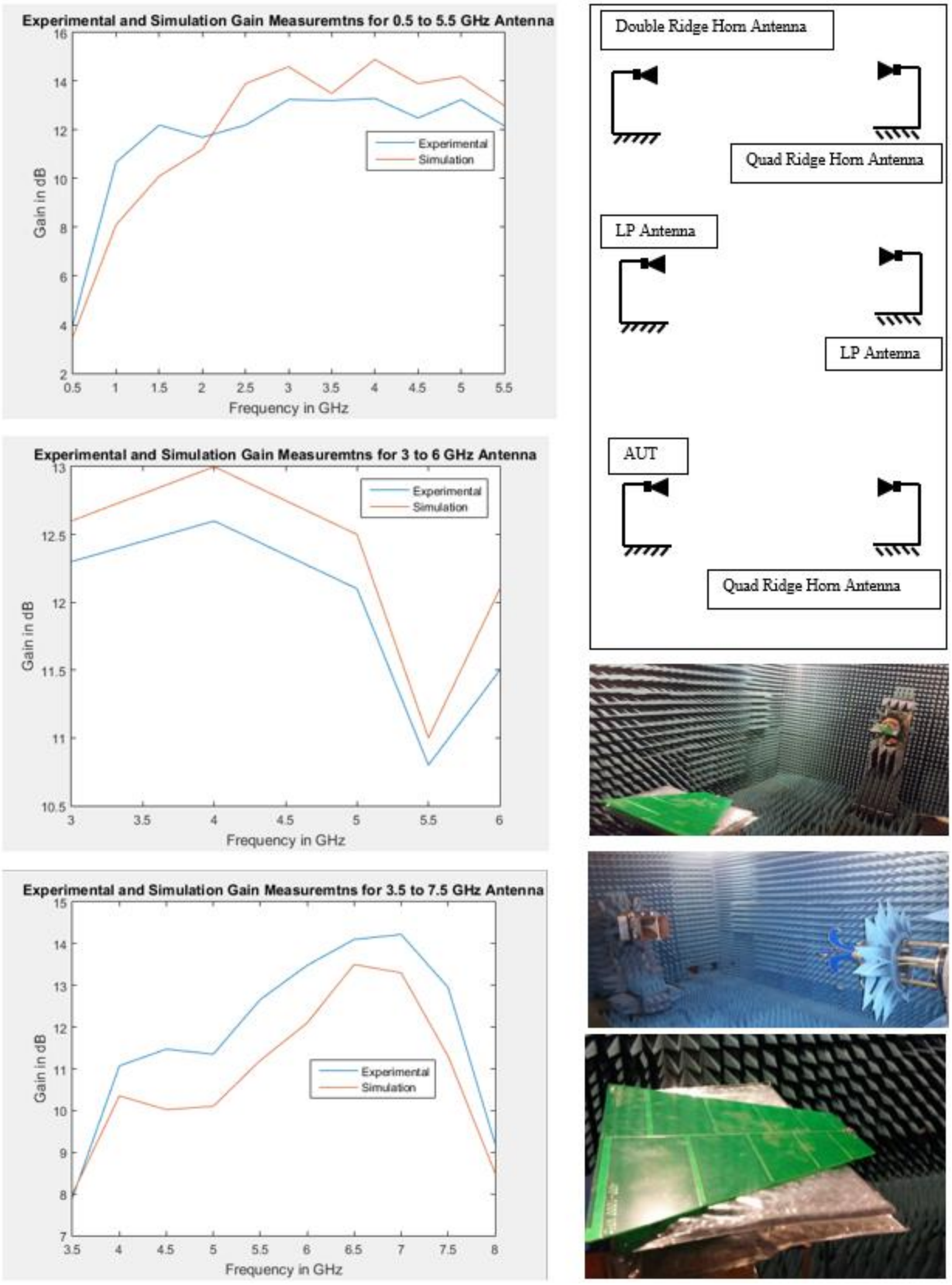

Figure 6-16: Gain measurement setup and the results for 0.5-5.5 GHz (top), 3-6 GHz (middle) and 3.5-7.5 GHz (bottom)

The measured gain of the antenna at boresight presents a relatively constant level across the 0.5 to 5.5 GHz band as well as a good similarity between the measured and simulated results. Although frequencies below 2 GHz show slightly higher gain that simulated ones by about 1 dB. The main reason for this could be the build-up of ground reflections and multipath in the measurement environment. The measured gain for the 3 to 6 GHz shows a dip towards the high frequencies as expected since it suffers from the main beam splitting up and also it is generally at a lower level compared to simulated results. The main reason for this could be the fact that for this particular band the main beam is slightly off the boresight and hence it is not aligned with the source antenna. The gain for band 3.5 to 7.5 GHz shows a good agreement as well as a higher level than the simulated results. The difference could be from the fact that the simulated results were performed at lower mesh settings to provide an acceptable simulation time at high frequencies and large structure. Lower mesh settings result in a poorer quality of results at a cost of simulation runtime.

6.2.6 S11 and Mutual Coupling

The measured and simulated return loss of the antenna are presented in Fig. 6.17. In the 0.5 – 5.5 GHz band, a good similarity can be seen up to 2.5 GHz. For higher frequencies a discrepancy between the measured (in blue) and simulated (in orange) results occurs, that might result from the losses or inaccuracies in the fabrication. However return loss of around -10 dB can be seen for all frequencies across the band. The band from 3 to 6 GHz show a good agreement between the measured and simulated results. The third band from 3.5 to 7.5 GHz also presents similar results. However, the measured one suffers from some levels of fluctuations as well as a slight shift of its lower cut-off frequency. The measured results seem to have shifted by about 200 MHz to the right which could be due to the physical length and fabrication inaccuracy of the coaxial probe inside the small rectangular waveguide.

When considering data acquisition from the antenna at multiple ports (bands) simultaneously as described in Chapter 7, it is important to check the coupling between each band. This is presented in Fig. 6.18 where the coupling between a pair of the band shows an isolation of around -20 dB. The allocations of the bands for the figure are, Band 1 (0.5 – 5.5 GHz), Band 2 (3 – 6 GHz) and Band 3 (3.5 to 7.5 GHz). The coupling between each pair of the band when they are operating can be seen.

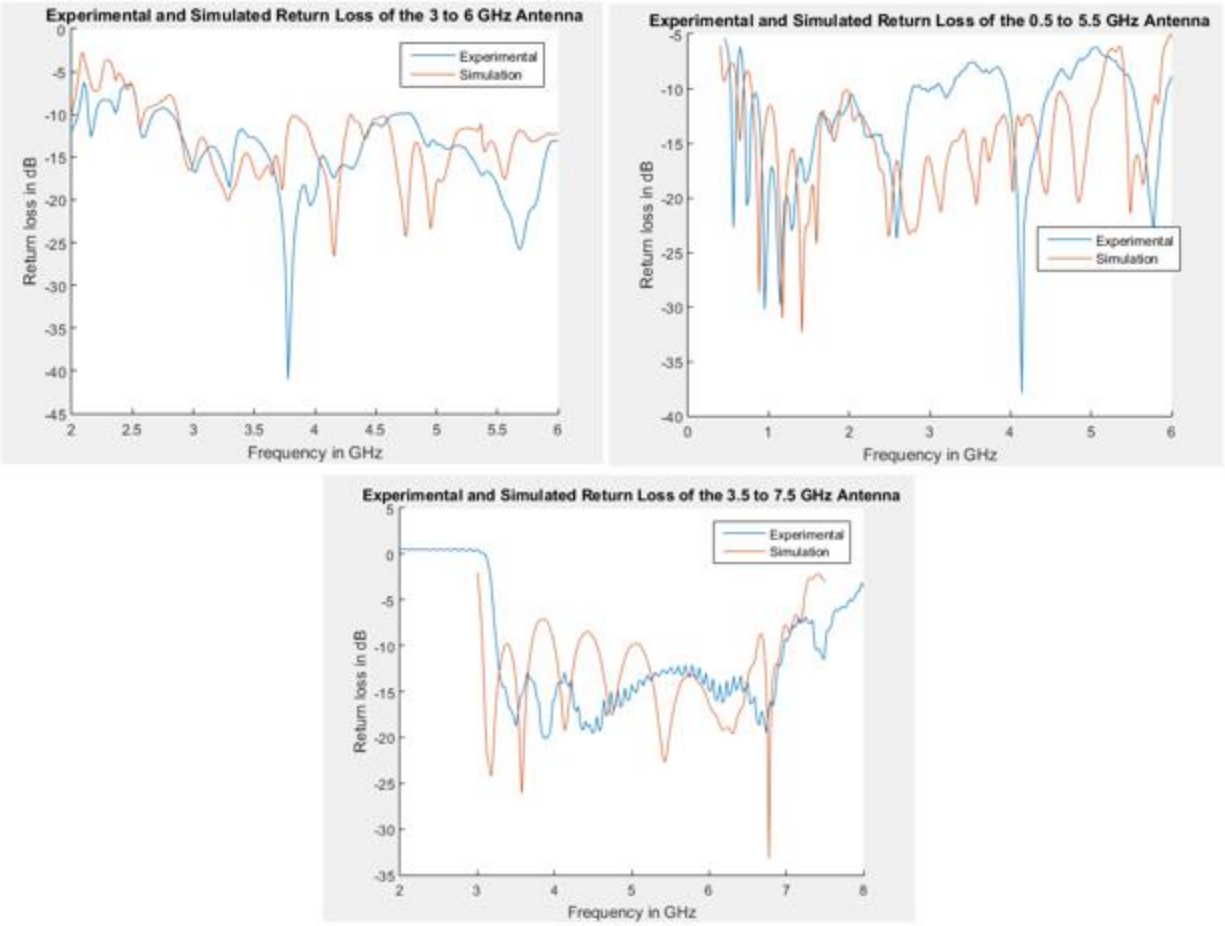

Figure 6-17: Return Loss of all three bands for Experimental and Simulated measurements

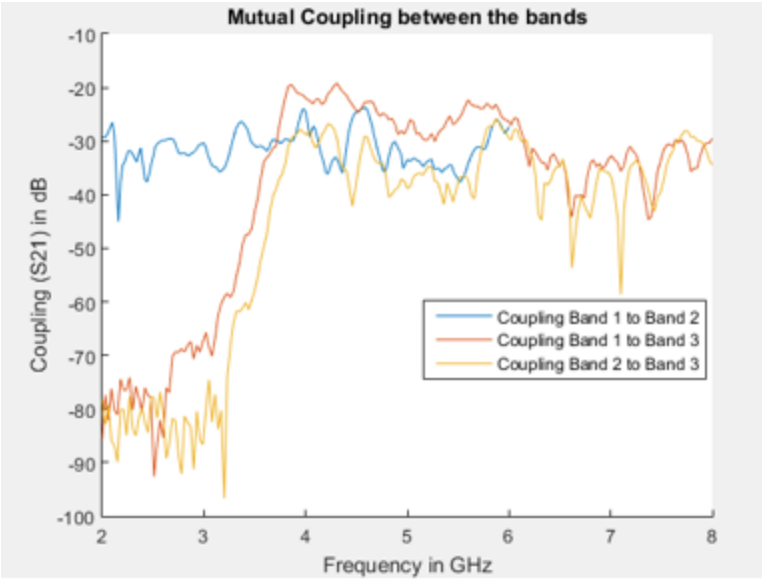

Figure 6-18: Coupling between the operating bands, Band 1 to Band 2 (Blue), Band 1 to Band 3 (Red) and Band 2 to Band 3 (Yellow)

6.3 Summary

The proposed antenna design has been fabricated, measured and verified. The fabrication process consisted of simulation, mechanical design, and verification, fabrication and measurements. The trade-off between the complexity, fabrication accuracy and cost were the main considerations from early stages of the design. As shown, all parts of the antenna were fabricated, and the overall antenna structure was realised. The antenna was then measured regarding its radiation pattern, gain, return loss and coupling. The experimental results were compared with the simulated ones, and the overall comparison shows a good agreement between the two. There is a slight discrepancy in the radiation pattern and return loss of the antenna between the experimental and simulated results. The main cause for this could be the fabrication inaccuracies and the anechoic chamber setting. The fabrication inaccuracies include the smoothness of the antenna surface and the discontinuities on the interior structure.

6.4 References

Kraus, J.D, Marhefka R.J. (2002). *Antennas: For All Applications*. Third Edition. McGraw-Hill.

Willis B.J. (2012). *Compact Form Fitting Small Antennas Using Three-dimensional Rapid Prototyping*. [Online] Available from: http://content.lib.utah.edu/utils/getfile/collection/etd3/id/660/filename/697.pdf

Chapter 7

Experimental Data Collection System

7.2 GPR System

The main equipment, which is used to obtain the data from the proposed antenna hardware, is a Vector Network Analyser (VNA). Since the configuration of the GPR system is intended for near-field operation, the earth material and the antenna become part of a passive transmission line where the signal propagates. As discussed, the most fundamental concepts of GPR network analysis involves reflected and transmitted waves travelling along transmission lines. GPR analysis is concerned with the accurate measurement of the ratios of the reflected signal to the incident signal, and the transmitted signal to the incident signal. VNAs are well suitable for this kind of measurement. A complete characterisation of the medium can be obtained by measuring phase as well as magnitude. VNAs provide excellent wideband capabilities; they can have a large dynamic range, highly sensitive to weak signals and a good time and amplitude stability.

A vector network analyser consists of a signal source, a receiver, and display. The source launches a signal at a single frequency to the device under test. The receiver is tuned to that frequency and detects the reflected and transmitted signals from the device. The measured response produces the magnitude and phase data at that frequency. The source is then stepped to the next frequency, and the measurement is repeated. It displays the reflection and transmission measurement response as a function of frequency. This is known as the Step Frequency Continuous Wave technique (SFCW). Instead of transmitting a very short pulse (impulse technique) directly in the time domain as is common in conventional UWB GPR systems, SFCW radars synthesise the impulse in the frequency domain. Since a time-domain impulse corresponds to a wide-bandwidth spectrum, SFCW radar should ideally transmit all frequency components contained in the impulse. In practice, the SFCW radar transmits a series of discrete tones covering the radar bandwidth. The number of transmitted frequencies determines the quality of the synthesised impulse. Under the conventional sampling theorem, a sampling rate of at least twice the maximum frequency component is mandatory for an exact time-domain signal reconstruction. The required number of samples is equal to the sampling rate multiplied by the signal duration. In comparison to time-domain methods, the SFCW method has an advantage of low transmit power requirement because the energy is spread out in time, wider dynamic range, higher mean power, lower noise figure and

the possibility of shaping the power spectral density. This means that the user has an option of changing the level of the sidelobes just by changing the "windowing" function. SFCW opens a lot of opportunities in regards to signal processing for single or multi-frequencies, time-frequency analysis and polarimetric processing *(Nicolaescu, 2003)*. Another advantage of SFCW and VNAs is their low power transmission and high sensitivity to weak signals. Low power transmission in GPR is desired to avoid nonlinear effects of the sandy soil or moist earth materials involved, which is a serious problem in the high peak power time-domain method. Additionally, it is not an easy task to build a high-speed sampler or digitizer with UWB capability in the time domain. Here, the frequency domain method of the SFCW radar is chosen since it can offer an implementable solution for rapid lab and field measurements.

The GPR system for the experiments performed here consists of a Rohde & Schwarz FSH8 VNA and an Agilent (Now Keysight) E5071C VNA. They are controlled by an Ethernet cable and a laptop. The lab measurement setup and equipment are shown in Fig. 7.1.

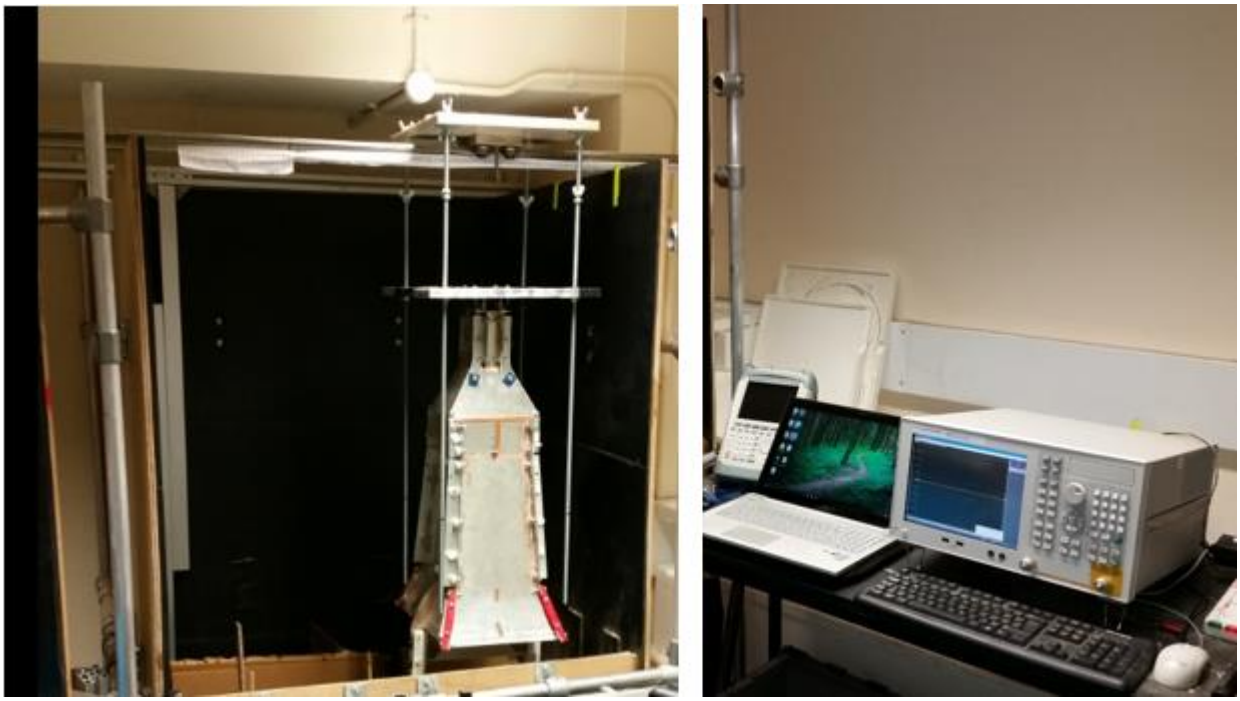

Figure 7-1: GPR Setup and equipment

Since the model VNAs can only generate a single tone, two VNAs were used to acquire data from the multi-port antenna at different bands. An indoor lab test facility consisting of a sandbox (This will be discussed later in the chapter) with various earth materials was designed and constructed. The dimensions of the sandbox are 1 metre wide, 1 metre long and 2 metres deep. The

measurement grid covers the area bounded by x = -20 to 60 cm. The proposed antenna was used to transmit and receive from a monostatic position and was mounted on a moving platform, placed above the ground surface. The height of the antenna from the ground is adjustable and various heights from 0 cm to 30 cm can be achieved. The GPR data according to the acquisition mode (A-scan or B-scan) are recorded. SFCW radar is sensitive to range-doppler coupling. The ambiguity function of the radar can be analysed in order to evaluate the effect of doppler due to antenna motion. However, this can be neglected in the case where discrete steps are used to record the data, as the antenna moves to a stationary position and the data is recorded. The antenna is then moved to the next point and so on. The moving platform and the antenna mount is designed in a way to reduce the effect of any undesirable movement of the antenna while moving along the track. The antenna and the cables are ensured to stay in position at every step along the track to minimise the phase error that could be introduced.

7.2 VNA Radar Parameters

The main parameters of a radar system are the unambiguous range, range resolution, dynamic range and output power. The unambiguous range, R_{max} of an SFCW radar is given by Eq. 7.1.

$$R_{max} = \frac{v}{2\Delta f} \qquad (7.1)$$

where v is the propagation velocity in the medium and Δf is the frequency step. The depth and lateral resolution of the radar can be calculated by equations 2.5-2.6. The depth resolution mainly depends on the bandwidth B and with N the number of frequency steps the total bandwidth is as follows:

$$BW = (N-1).\Delta f \qquad (7.2)$$

Figure 7.2 illustrates the architecture of the VNA in a near-field system. An oscillator generates a stepped frequency signal, which is amplified and transmitted via a dedicated antenna system. The signal reflected from the target is received and fed to a mixer via a low noise amplifier, where it is mixed with the coupled part of the basic signal which was transmitted. The phase shift between both signals produces a DC output; the phase is shifted from zero by an angle proportional to the target range. This phase shift is measured by converting this signal from frequency domain to time

domain using an IFFT (Inverse Fast Fourier Transformation). The radar range profile can be obtained by IFFT of the complex signals achieved for a set of frequencies.

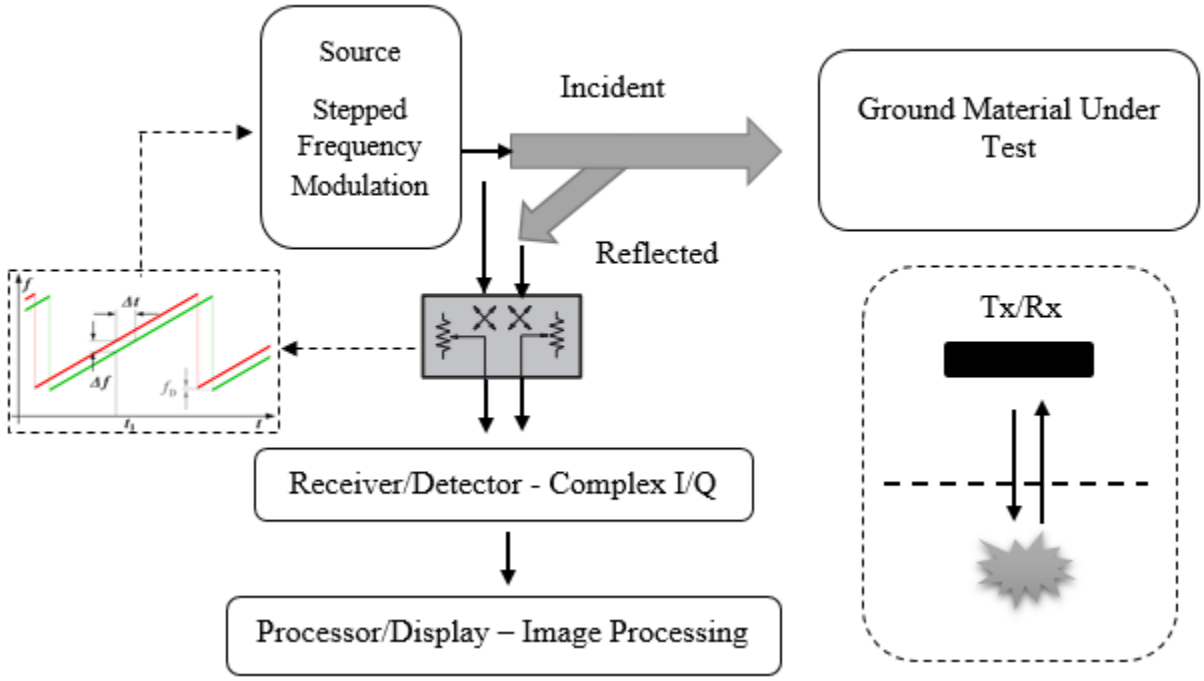

Figure 7-2: VNA Diagram as a SFCW Radar

The main specifications of the two VNAs used for the experiments are summarised in Table 7.1. Both VNAs provide a good performance over the frequency band of interest. They offer an average noise level of less than -120 dBm. The R&S VNA has a fixed number of frequency steps (e.g. N = 635) and a maximum RBW (Range Bandwidth) of 3 MHz. The Keysight VNA offers a higher N but lower RBW. The R&S VNA is rugged, compact and specially designed for use in the field. It is light and reliable. In regards to radar measurements, some of the key parameters of the VNA that could influence the performance of the measurements were considered and are discussed next.

Parameters	Rohde & Schwarz FSH8	Keysight E5071C
Frequency range	9 kHz to 8 GHz	9 kHz to 8.5 GHz
Number of Ports	2	2
Number of Sampling Points (*N*)	635	1601
Bandwidth (Range resolution)	1 Hz to 3 MHz	10 Hz to 1.5 MHz
Dynamic Range	60 to 90 dB	72 to 117 dB
Output Level with 0 dB attenuation	-10 dBm	-10 dBm
Average Noise level	-96 to -155 dBm	-97 to -120 dBm

Table 7-1: FSH8 and E5071C VNAs Specifications

7.2.1 The Effect of Phase Error

There are various sources of phase error, and these can degrade the accuracy of the measurements. Phase noise might limit the resolution of the radar. The radar's transmitter is based on frequency sources with a limited stability over time. Therefore, the transmitted and obviously also the received signal are distorted due to cumulative phase noise. Here cumulative phase noise is the phase change accumulated over the time delay between transmission and reception of the signal. The electrical path length of the incident and reflected signal can introduce phase error if not enough number of sampling points are used. High *N* (number of VNA sampling points) is desirable. However, the time it takes to sweep across the band will increase with an increase in *N*. Figure 7.3 shows the effect of having different sampling points on the range profile (A-scan) of a PMN-2 AP landmine buried 4 cm under the sandy soil. The two differences are the slight increase in the amplitude of the peaks from the profile with higher sampling points as well as a shift in range. The true range of the target is closer to the one indicated with the higher sampling point; this shift is around 2 cm.

For each experiment, the VNAs were turned on a few hours before the measurements were taken. This is to ensure the thermal stability of the components of the VNA at room temperature.

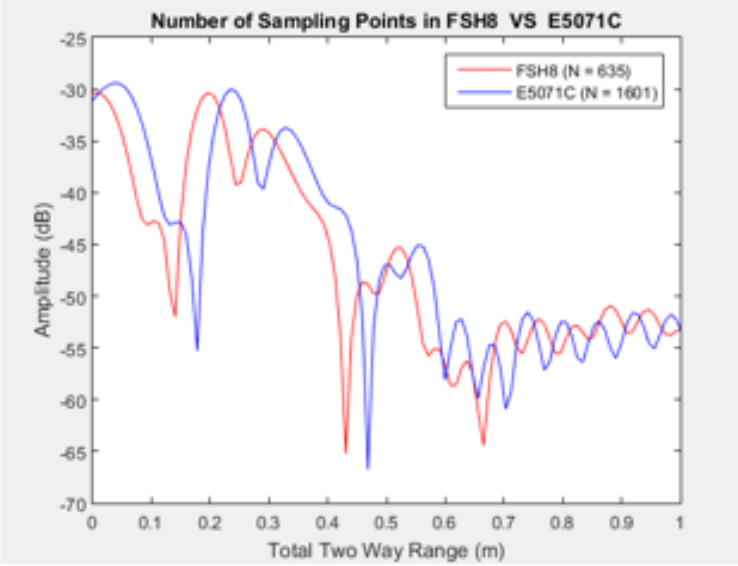

Figure 7-3: Number of sampling points N on the range profile of A-scan measurement

7.2.2 Attenuation and Reference Level

VNAs are designed to measure different types of RF signals with the greatest dynamic range possible. One way to maximise the dynamic range over a broad range of signals is to use attenuation to adjust the signal level to the ideal amplitude for a given signal. VNAs are designed to have a broad range of reference or attenuation levels, specified in decibels (dB). The VNA's reference level was set to a power level that is slightly higher than the expected maximum power. The attenuation is set to 0 dB and 10 dB, and the effect is seen in Fig. 7.4. Less attenuation (in blue) shows higher levels of return signals as well as cleaner signature later in time. However, the peak for the soil interface and buried target have broadened compared to the A-scan profile with 10 dB attenuation. Attenuation or gain is applied as close to the RF front end (e.g. antenna) as possible to maintain a constant signal level at the receiver and to achieve maximum dynamic range on the signal being analysed.

Figure 7-4: Effect of RF attenuation on the A-scan profile applied to the VNA front end

7.2.3 Dynamic Range

Dynamic range describes the maximum and minimum signal amplitudes that you can measure simultaneously. The only factor that determines the maximum signal level is the attenuation applied to the signal, but many different factors determine the minimum signal level. These factors include noise introduced by the amplifier, spurs, and harmonics, or carrier signal leakage (also known as Local Oscillator leakage). More specifically, dynamic range is the ratio of the largest signal that can be measured relative to the power of the greatest distortion, noise, or spur. Dynamic range is specified in decibels, with a larger range as more desirable *(Agilent, 2000)*.

Spurs and noise can be introduced almost anywhere in the RF signal chain. The nonlinear characteristics of earth materials often result in distortion products, each of which can produce spurs in the frequency domain. Dynamic range is an important specification for low-amplitude measurements. The specification is even more essential when measuring a low-power signal level (peak from the landmines) next to a high-power signal (air to soil interface especially in the high-frequency band). The dynamic range of the VNA determines the minimum signal that it can view next to a high-power signal because the reference level of the VNA cannot be set below the maximum power of the high-power signal.

7.2.4 Averaging Methods

With averaging methods, reducing noise on a signal increases the accuracy of measuring low-level spurs. Averaging over several periods of a signal was used to eliminate random or white noise and converge to the real value of the signal.

7.2.5 Displayed Average Noise Floor

The apparent noise floor of the VNA can also be influenced by the resolution bandwidth (RBW) of the signal *(Agilent, 2000)*. This is another important specification that could affect the indication of the smallest detectable signal that the VNA can measure. The effect was investigated for a buried target in soil and the A-scan profile for 3 MHz (in blue), and 3 kHz (in red) are shown in Fig. 7.5. As can be seen in this case, there are no apparent differences between the two. Thus, measurements were taken at 3 MHz RBW since it provides a faster sweeping time.

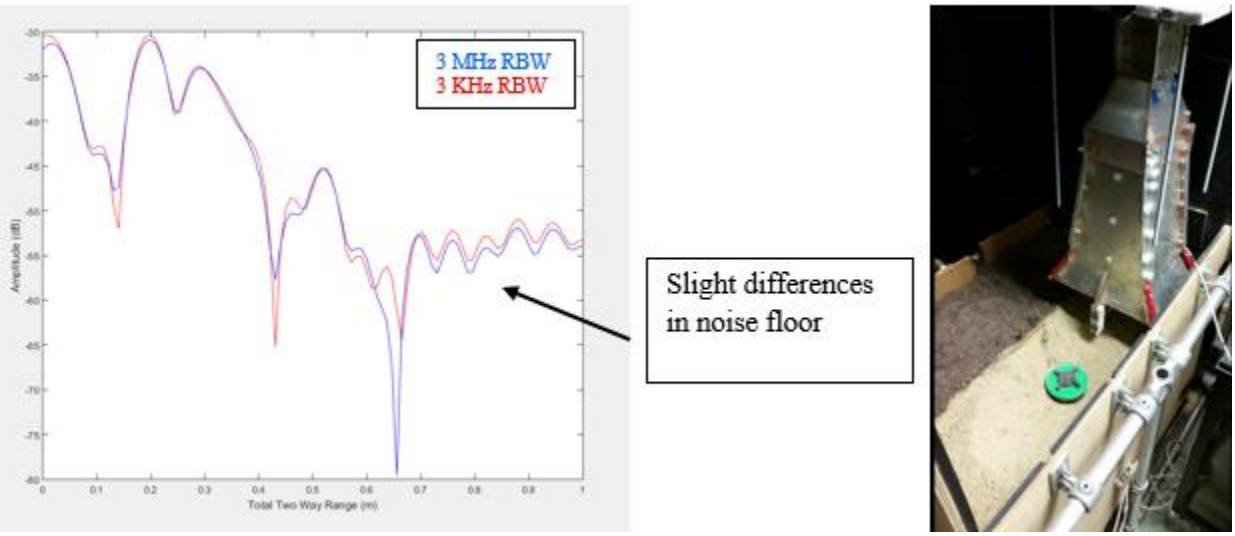

Figure 7-5: The effect of the RBW of VNA on A-scan profile of a buried target at 3 kHz (red) and 3 MHz (blue)

7.2.6 Calibration

To ensure the accuracy of measurements, the VNA is required to be calibrated before the antenna system is introduced. The first error comes from the attenuation of the waves in the cables from the VNA to the DUT (Device Under Test) and then from the DUT back to the VNA. The finite length of the cables also introduces a phase shift of the waves and these two factors both affect the accuracy of the measurements. The calibration process typically consists of a calibration kit, cables, and the VNA. The calibration process employs different techniques such as vector error correction, in which error terms are characterised using known standards so that they can be removed from actual measurements. Calibration is performed by sequentially making measurements using the calibration standards. Coaxial Calibration standards are Short (S), Open (O) and Match or Load (M/L). The first step is to make sure the right calibration kit is used for the specified VNA. The next step is to make sure the connectors and adaptors that connect the VNA,

cables, and the calibration kit are not damaged and in a good condition. If there are any physical damages in the inner pin of the adaptors, there will be undesirable effects in the calibration process, especially at high frequencies. Once the calibration kit is connected, the calibration process is performed. It is necessary to check each step to eliminate undesirable errors. Figure 7.6 shows the calibration kit that was used for each VNA. After each calibration, the quality of the calibration can be checked by measuring the reflection on a Smith chart while each calibration standard is connected. The quality of the cables can be inspected by checking the magnitude and phase while moving the cables around. A good cable offers a small amount of change in magnitude and phase when being moved.

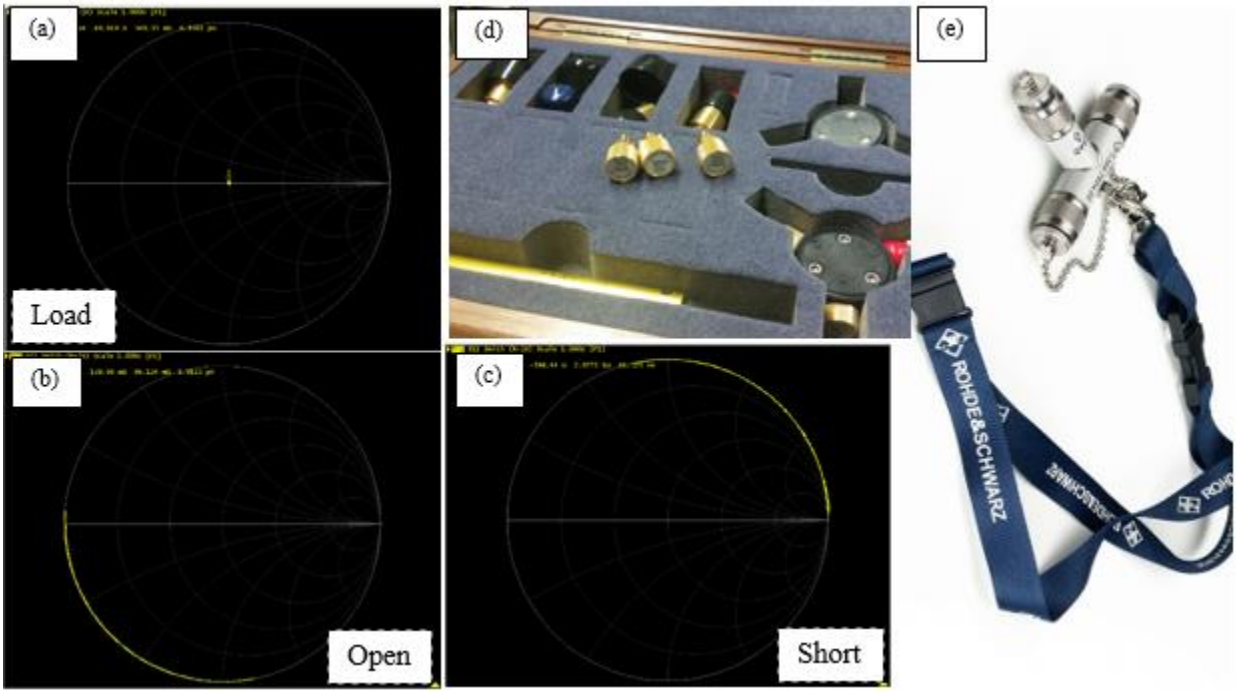

Figure 7-6: Calibration procedure – Smith chart when corrected calibration standard is connected for the load (a), open (b), short (c). The calibration kit for the VNA E5071C (d) and FSH8 (e)

7.3 Description of the Test Sandbox

The sandbox for the GPR measurements is made of wood. The interior structure of the box is covered with 10 mm natural rubber material to provide absorption of unwanted reflected waves. The bottom of the box is marked with a strip of copper tape to help in understating some of the peaks that appear in the range profile. The copper strip is used to provide a reference to the bottom of the box. The box is divided into four sections, and each section is filled with different earth materials. The dimension of the box is 1m by 1m and 2m in height. However, regarding weight

restrictions, only 60 cm of the box is filled with the earth materials. Figure 7.7 shows the sandbox and its contents.

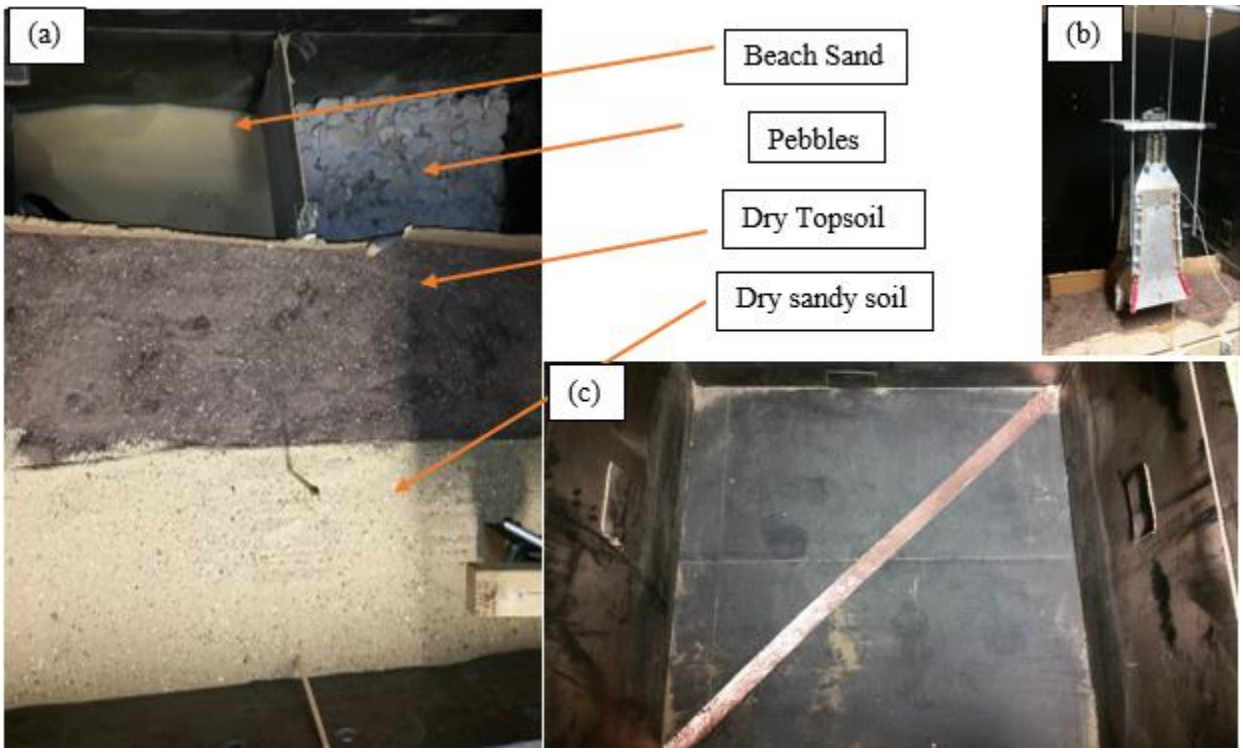

Figure 7-7: Sandbox used for GPR laboratory measurements, sandbox content (a), the GPR mount (b) and bottom of the box marked with a copper strip for calibration purposes (c)

The moving platform consists of a rail that is placed on top of the box. The antenna is mounted and secured underneath with adjustable height. The rail can support a B-scan with a relatively linear and stable movement of the platform that can cover a distance of 60 cm. Enough room is allowed so that the mount and the cables are moved together to avoid any measurement errors regarding phase differences.

7.4 Description of the Test Landmines

In order to validate the modelling and simulation results, a set of selected test objects, representing dummy AP landmines, false targets and landmine like objects are collected. To further improve the quality of the GPR measurements, efforts are made to model and fabricate 3D AP and AV landmines. As mentioned in Chapter 3, the models of the real AP and AV landmines are designed to exact dimensions and features. They are fabricated using CEL Robox and LulzBot TAZ 3D printers, which can support different printing materials. ABS plastic (ε_r = 2.1) is used to print most

of the landmines. Figure 7.8 shows the selection of targets including AP and AV landmines that are used for the measurements addressed in this thesis.

Figure 7-8: Landmine Targets

The AP landmines include VS-50, PMN-2, PMA-2 and PFM-1. The AV landmine is the TMRP-6, which was fabricated by 3D printer and metallised by copper paint. The AP landmines cover a range of dimensions and shapes. Also, other test objects were gathered that show similar geometry to landmines. These are tin cans in various diameters and heights. Experimental measurements were made on the material of the real landmines. This is to ensure the correct material is chosen for the modelled landmines. Access to real landmines was granted at Cranfield University and the Imperial War Museum where photos and measurements of real landmines were taken.

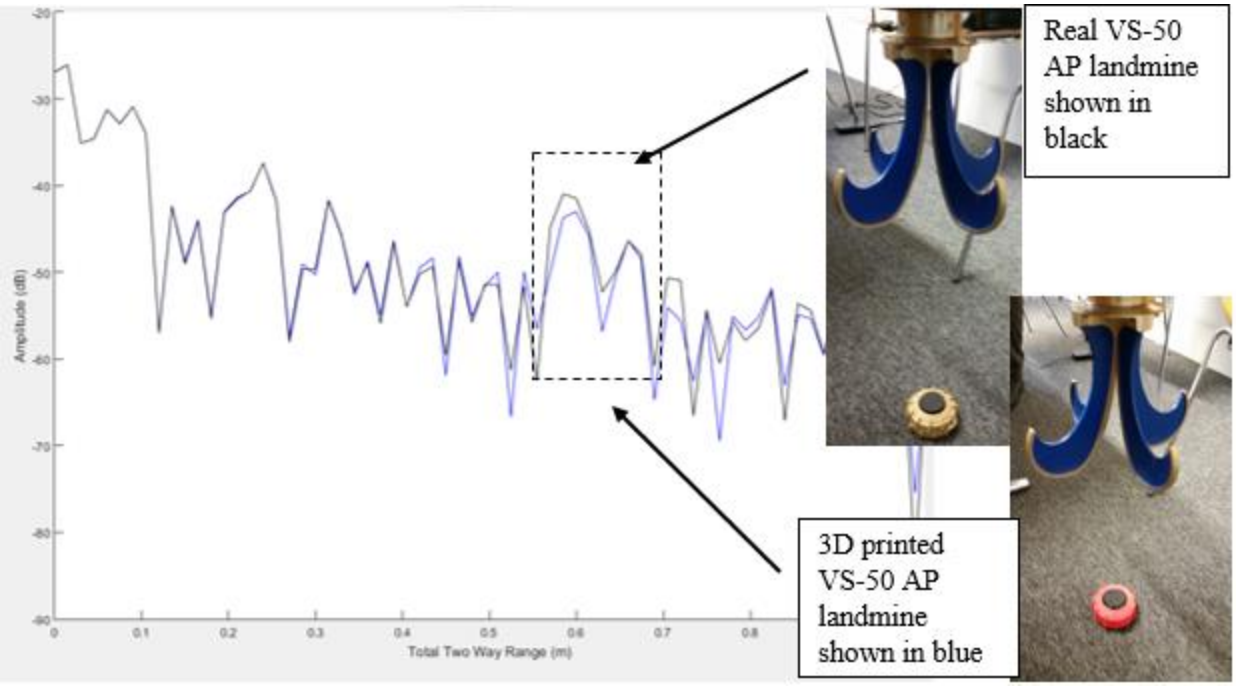

Figure 7-9: Test measurement for Real VS-50 landmine and 3D printed VS-50

Figure 7.9 shows an A-scan profile of both real (in black) and 3D printed (in blue) from a distance of 40 cm in free space. A quad-ridge horn antenna is used with a portable FSH8 VNA. The results show that the signature in the range profile for both landmines are similar. This means that the 3D printed landmine have been modelled to similar features and dimensions compared to the real one. The range profile for real VS-50 shows slightly higher reflectivity (in return signal) than the 3D printed one. This is due to the specific plastic material that is used for the casing. This was verified by measuring the dielectric properties of both the real and the 3D printed plastic material. The setup for the dielectric measurements has been discussed in Chapter 4. The results show that the dielectric constant of the material that is used to make the activator (top part) of the real VS-50 landmine is around 6 and the dielectric constant for the 3D printed material is around 2.5. The same measurements are performed for other real and 3D printed AP landmines, and the results suggest that the 3D printed models are quite similar to the real ones. In order to further increase the similarity of 3D printed landmines to real landmines found in the minefield, one can add a filling material that resembles the electrical characteristic of explosives. From the literature, it was found out that dried peanuts and Paraffin wax have similar dielectric properties in terms of ε_r and $tan\delta$ to that of RDX and TNT explosive materials. For experimental use, homogenous and isotropic explosive materials have been assumed. Therefore, the 3D printed models were filled

with a correct amount of peanuts and paraffin wax and densely packed to avoid air gaps. The fill factor, homogeneity, air gaps and other material properties will be studied and addressed in future work.

Dried peanuts have similar dielectric properties to TNT, and a combination of dried peanuts and paraffin wax (e.g. mixed) have similar dielectric properties to RDX. The preparation and characterisation of the 3D landmine models are shown in Fig. 7.10.

Figure 7-10: Dielectric properties testing and filling of 3D printed models of landmines with dried peanuts and paraffin wax

As shown in the figure, the dielectric properties of dried peanuts, wax and the 3D printed plastic material were measured. In consideration of the specification of the amount and mixture of the explosive materials in real landmines found in the literature, the 3D printed models were filled and prepared accordingly.

7.5 Laboratory GPR Measurements

The GPR laboratory setup was developed in the context of this thesis. The setup consists of the proposed antenna design, the two VNAs, test landmines and objects, soil box and laptop to acquire and archive the data. Numerous amount of experiments have been conducted, in this section, only a selected number of experiments are discussed and presented.

Before any measurements are taken, the antenna is calibrated regarding the range it introduces in the range profile. From the time that signal travels from the point of excitation to the point where the signal propagates out of the antenna, corresponds to a distance in the range profile. This time depends on a variety of antenna parameters, namely the length of the antenna, the group delay, etc. In order to correctly deduce the true range of the target (which is the distance from the aperture of the antenna to the target), the antenna is calibrated so the offset that introduces in the range profile can be subtracted from the raw data. This is illustrated in Fig. 7.11 and Eq. 7.1. The raw data collected from the antenna undergoes appropriate frequency to time domain conversion and signal processing to reconstruct the range profile. Once the total one-way range is constructed, the known antenna height, H_1, is subtracted from it and this leaves the overall 'antenna distance', D_{Ant}. This is the distance or offset in the range profile introduced by the antenna. The measurement is repeated for various antenna heights.

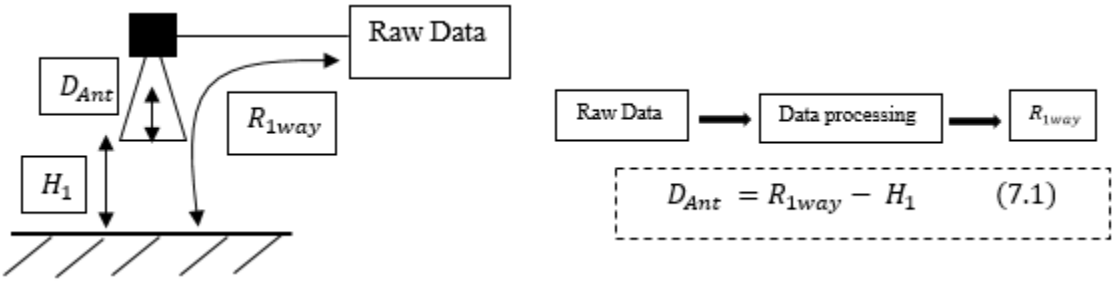

Figure 7-11: Antenna calibration method

An A–scan measurement is taken from a setup where the antenna is adjusted to a fixed height and is placed above the ground. The target to calibrate the antenna can be the ground reflection from the soil interface, a large metal sheet placed on the soil interface (increase reflectivity) or a buried flat sheet at a known depth. The results of a calibration procedure for the 0.5 GHz to 5.5 GHz antenna is shown in Fig. 7.12, where three traces from different antenna heights are recorded. It can be seen, a distance of 0.8 m corresponds to the range that is introduced by the antenna offset.

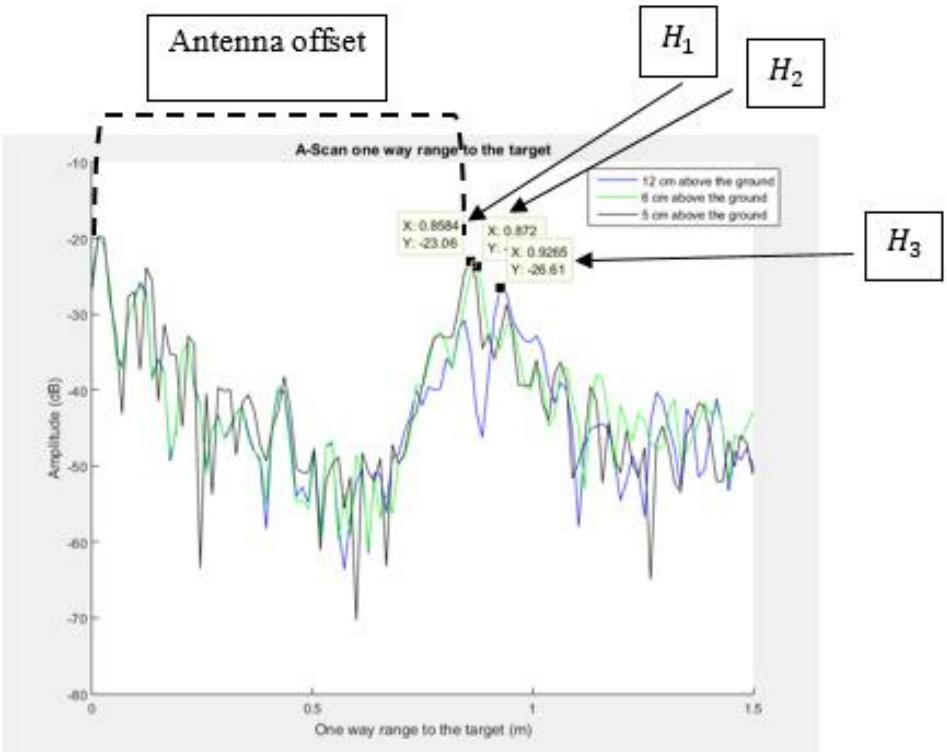

Figure 7-12: Antenna calibration results – 0.5 GHz-5.5 GHz antenna

7.5.1 Influence of the Antenna Height

As discussed before, the height of the antenna above the soil influences the footprint that the antenna imposes on the surface. At a particular height, the antenna may be coupled more efficiently into the ground, giving better return signals from the target and improving the resolution of the GPR images. Figure 7.11 (a) shows the A-scan profile operating at band 1 for a buried flat metal target from an antenna height of 18 cm (red), 12 cm (blue), 6 cm (green) and 5 cm (black) above the soil. The results show the antenna operating at band 1, provides a clearer indication of the soil interface from the target. As the antenna height is increased, the signal level from the soil interface is decreased, but the peaks from the soil interface and the target seem to have coincided and dispersed. An antenna height around 5 or 6 cm gives a clear indication of the soil interface and the target buried at 4 cm depth. Similar behaviour is seen for the antenna operating at band 2, figure 7.11 (b) shows the antenna height of 5 cm (red) and 2.5 cm (blue) for the same measurement setup. It can be seen that the antenna height of 2.5 cm gives a sharper and clearer peaks for the returns signals. The return signals from the soil and target are marked with grey and red arrows respectively.

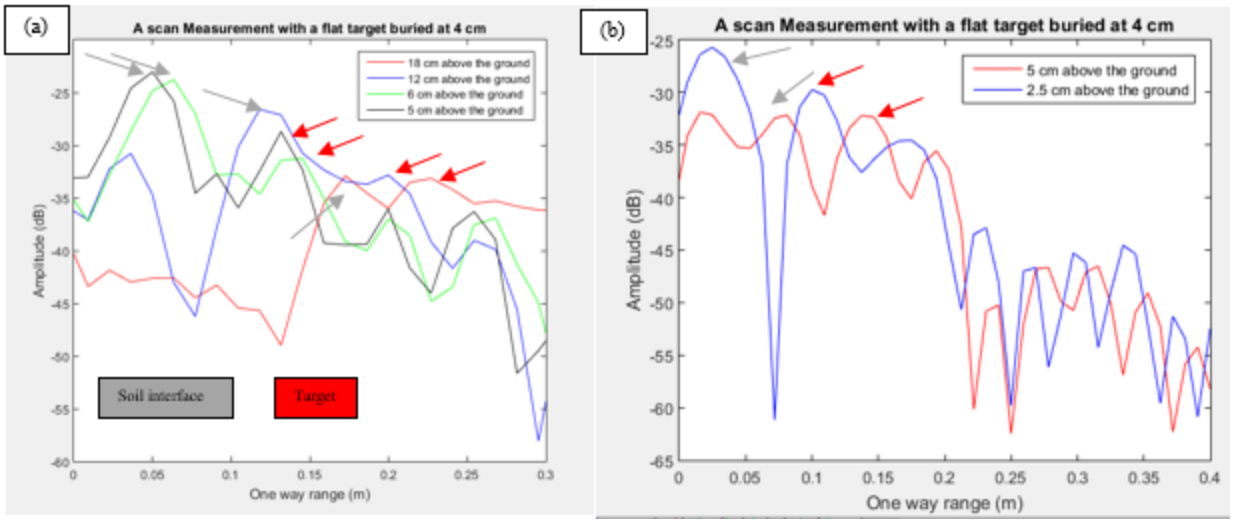

Figure 7-13: GPR measurement antenna height influence – 0.5 GHs – 5.5 GHz (a), 3.5 GHz – 7.5 GHz (b)

To understand the GPR images and the landmine targets, it is important to perform a measurement of the soil with no targets present, also known as background measurements. Figure 7.14 shows background measurements of dry sandy soil from the antenna operating at band 3 (3.5 – 7.5 GHz) before and after the soil is disturbed. Appropriate data processing is performed on the raw data to produce a time bin vs. cross range, intensity plot. The time bin (y axis) is the frequency to time domain conversion with applied hamming window and a padding factor. The cross range (x axis) is the points where the data is recorded.

In figure 7.12, the soil interface and the bottom of the box are clearly highlighted. Figure 7.12 (a) is the measurement of the soil undisturbed and 7.12 (b) disturbed. The undisturbed soil is the soil that is left over a period in the lab. As shown in the figure it can be seen that high returns below the surface of the soil and near the edge of the box are present (marked by arrows). The soil is then disturbed in a way where the entire volume of the soil to some depth is emptied and filled back in. The background measurements are performed again, and the result is shown in the Fig. 7.12 (b). The high returns from the undisturbed soil have disappeared and reappeared to some extend in different locations. This suggests that the soil density and its structure have an impact and may contribute to the high level of return signals. The high return signals may be resultant of highly packed soil grains as well as soil being moisturised.

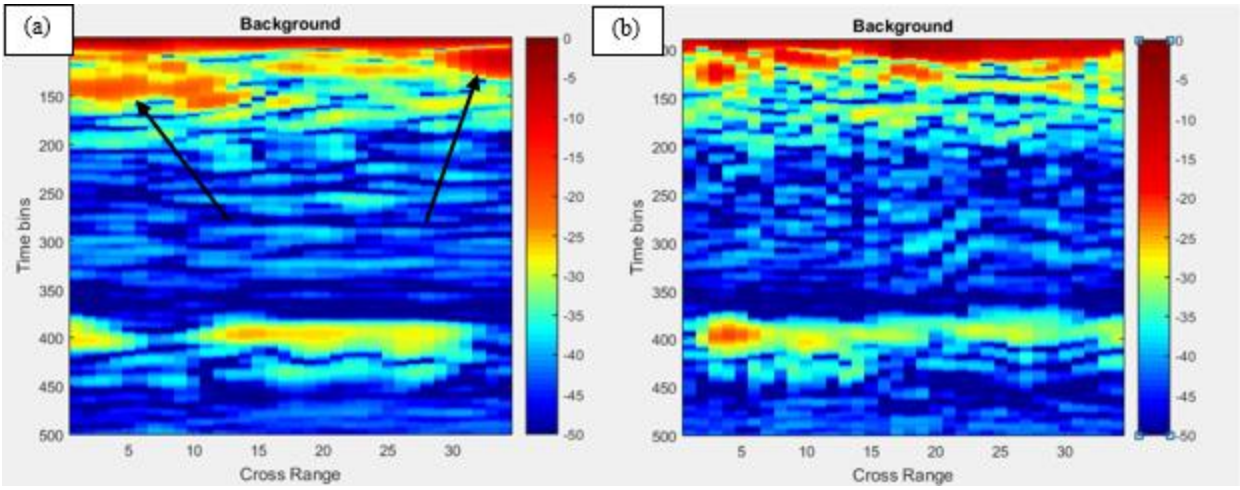

Figure 7-14: Undisturbed dry sandy soil (a) and disturbed dry sandy soil (b) at Band 3 (3.5 GHz- 7.5 GHz)

The shadows that are left in the same time bin at the bottom of the box are the resultant of the signals being masked by the return signals from the targets appearing above them. Figure 7.15 shows the background measurement of two types of soil materials, dry sandy soil (a) and loamy soil (b) from the antenna operating at band 1 (0.5 – 5.5 GHz). In the measurements from the disturbed soil at band 3, Fig.14 (b), there is small features present just below the soil interface. Also, there are groups of slightly high-intensity signals from each layer of the soil. However, in band 1, Fig. 7.15 (a), the overall layers of the soil across the box are more highlighted especially towards the bottom of the box. This suggests band 1 may have penetrated deeper in the soil. In comparison to loamy soil, in Fig.7.13 (b), band 1 signals have gone under more attenuation introduced by the dielectric properties of loamy soil. The lesser highlighted signals from the bottom of the box are the resultant of attenuation in the loamy soil. The loamy soil, in general, has a higher loss tangent than sandy soil.

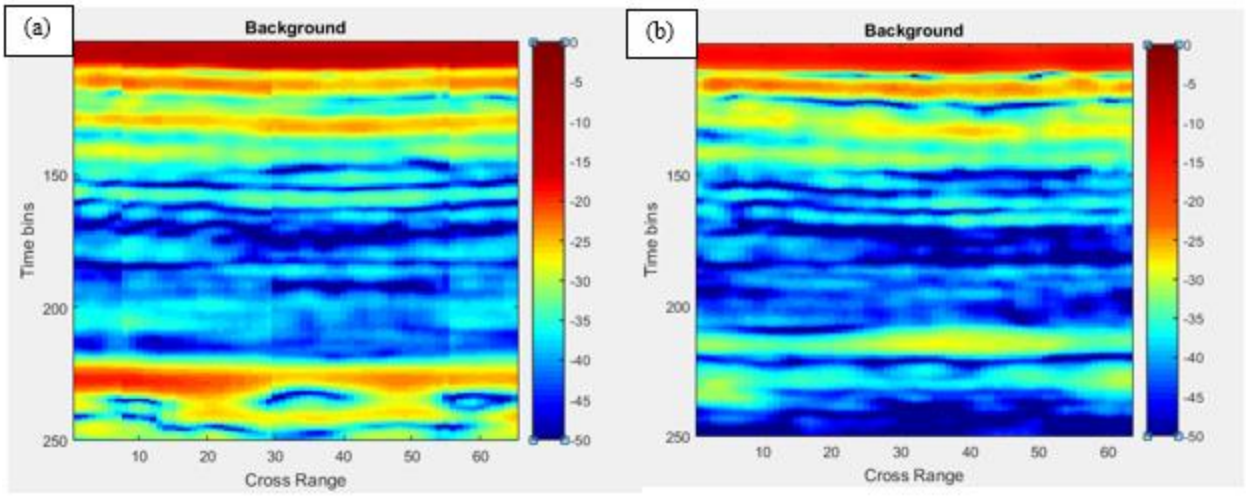

Figure 7-15: Dry Sandy Soil (a) and Dry Loamy Soil (b) at Band 1 (0.5 GHz – 5.5 GHz)

7.5.3 PMN-2 AP Landmine from Band 1 and Band 3

Figure 7.16 shows the measurements from a PMN-2 AP model landmine 4 cm buried in dry sandy soil. Figure 7.16 (a) is the image that is formed from the 3.5 GHz to 7.5 GHz, band 3. Figure 7.16 (b) is the image from the 0.5 GHz – 5.5 GHz, band 1. The PMN-2 target is present in both images and is marked by the arrows. In both images the hyperbola shape that is a common behaviour of the AP landmines can be seen. However, the overall signature of the target is slightly different in each of the bands. In band 1, the outer part of the landmine is highlighted as well as the linear layers of soil around it. In contrast, band 3 image shows features highlighted within the landmine. Both images include the shadowing that is left in the same time bin at the bottom of the box.

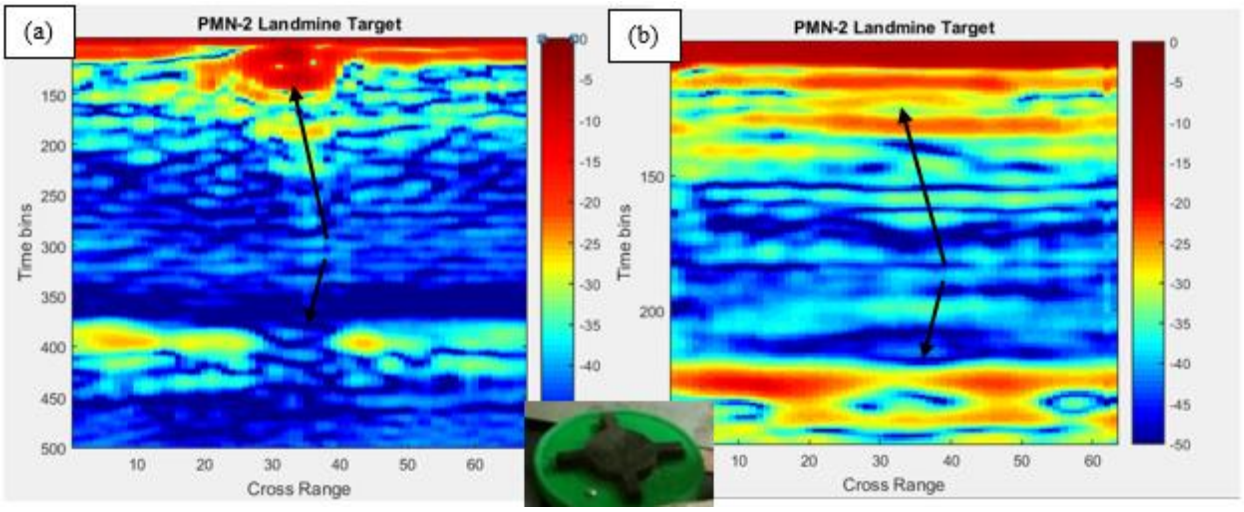

Figure 7-16: PMN-2 AP Mine buried at 4 cm taken from Band 3 (left) and Band 1 (right)

7.5.4 VS-50 and PMA-2 AP Landmines from Band 1 and 3

The VS-50 and PMA-2 landmine targets are imaged in band 3 (3.5 GHz – 7.5 GHz) and shown in Fig. 7.17 (a) and (b) respectively marked by the arrows. The VS-50 is buried at 4 cm depth and the PMA-2 at 8 cm. As well as the landmines, other features from the soil texture are present. The shadowing effect is also present which suggests a typical behaviour when operating at this particular band. The shape and the profile of the images obtained from these landmines in band 3, suggest, more features at a greater resolution in shallow depths can be archived. However, when landmines targets are buried at a greater depths, band 1 (0.5 GHz to 5.5 GHz) tend to dominate in performance. Figure 7.17 (c), shows the VS-50 landmine buried at 1 cm below the soil and the PMA-2 landmine at 10 cm.

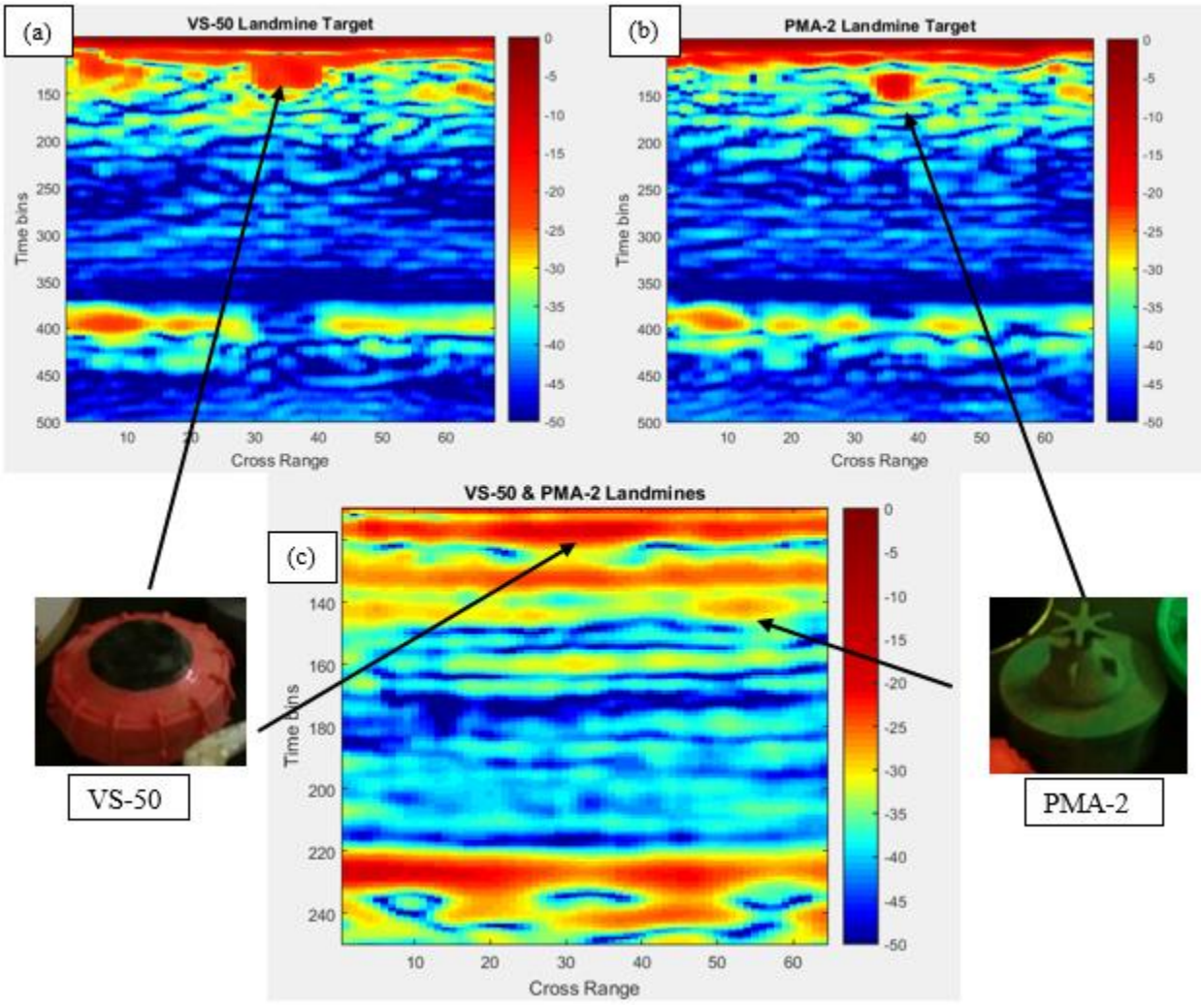

Figure 7-17: VS-50 landmine from band 3 (a), PMA-2 landmine from band 3(b), VS-50 & PMA-2 landmines from band 1

7.5.5 TMRP-6 AV Landmine

Most metal landmines totally reflect radar waves so that the signal detected by the radar depends primarily on the target geometry and the properties of any surrounding soil. Figure 7.18 (a) & (b) shows the radar data for the TMRP-6 AV landmine in band 3 and band 1 accordingly. The metal landmine is clearly discernible in the centre of the image in band 3. The high frequency and adequate range resolution allow clearer image of the landmine . The main geometrical features of the landmine such as the three stacked parts of the landmine are the dominant scatter of the radar data. The handle of the landmine which consists of a small linear bar (on the left of the landmine in the figure) is also detected. Moreover, there seem to be additional reflections surrounding the landmine, particularly from beneath. This may have been caused by multipath and radar scattering from the sharp edges of the landmine. In band 1 however, this multipath effect is not present but lesser features are detected, and the most of the radar signature is caused by the overall shape of the landmine.

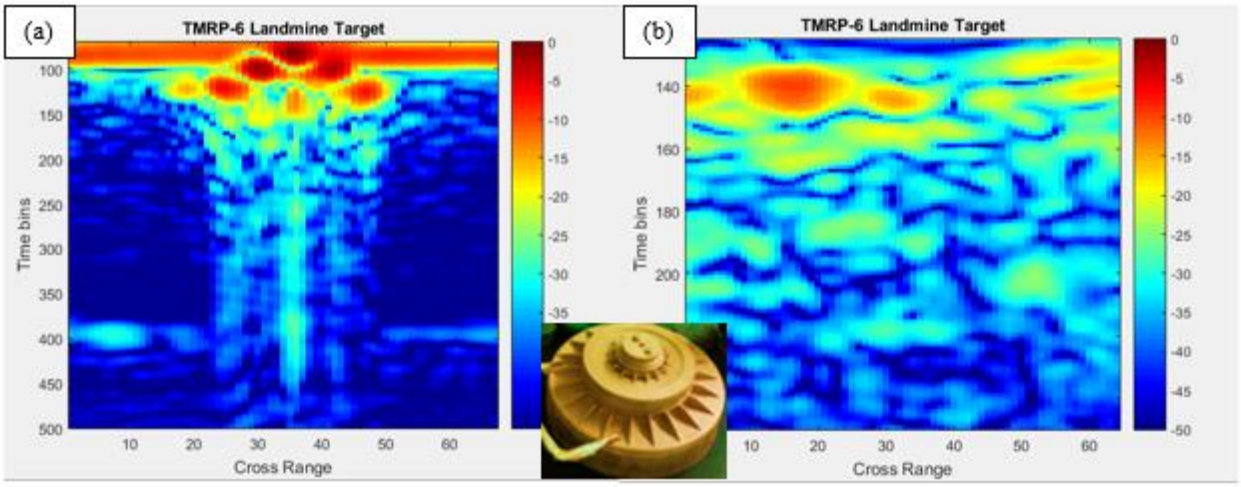

Figure 7-18: TMRP-6 from band 3 (a) and band 1(b)

7.5.6 Length Feature in Metal Targets

When a UWB radar signal illuminates a conducting target, it scatters the EM energy through reflection, diffraction and resonance mechanisms. Each scattering mechanism corresponds to particular target feature or a combination of features that could be useful for classification. Some features of both the target profile and the data may have advantages over the others in particular applications. The natural resonance feature associated with a conducting target is a result of the reverberation of surface currents induced by the incoming radar signal. Each reverberation is

accompanied by radiations that damp the resonance strength. Propagation causes further damping through conducting soils *(Chen et al., 2001).* Figure 7.19 (a) – (f), shows examples of a measured A-scan trace of flat linear targets with various lengths and diameters. The radar data is from the band 1 (0.5 GHz to 5.5 GHz) of the antenna, and the target is placed around 5 cm below the dry sandy soil. The traces for all the targets suggest when the radiated fields are received by the radar, the time response (frequency to time converted) appears as damped series of peaks with its fundamental frequency related to the target location under the soil. In the Figure 7.19 (a), the first peak corresponds to the soil interface positioned at 0 cm. The highest peak corresponds to reflected, and diffracted responses that occurred immediately after incoming radar signal hit the target body. This portion of the signal is usually referred to as the "early-time response". A damped resonant response that dominates the late-time region is also clearly observed. It should be noted that the distinction between the early-time and late-time regions are not always obvious for arbitrarily oriented targets. The resonance signature could provide a length or diameter estimations of the target. For instance, given a relative permittivity of 2.5, the distance from one of the resonant peaks to the early-time response peak predicts a 25 cm target length in (a), 41 cm in (b), 25 cm diameter in (c), 13 cm in (d) and 11 cm in (e). The resonant peak that corresponds to the prediction of the length seems to lie at an arbitrary point along the damping line that starts from the early-time response to the point where the damping ends.

The multiple resonant peaks in between the damping line seem to be periodic, and the distance between them is around 10 cm. This might correspond to the wavelength of the centre frequency of the band 1 (e.g. 3 GHz). Target (e) that is buried at 7 cm and is 7 cm in diameter does not provide any resonance behaviour, and this may be because the surrounding soil reflections become stronger than the target. This might also be the cause of the different level of the peaks that are shown for the soil interface and the early-time response. The larger the target, the higher the early-time response peak compared to the soil interface peak. As the target gets smaller, the soil properties are the dominant peaks.

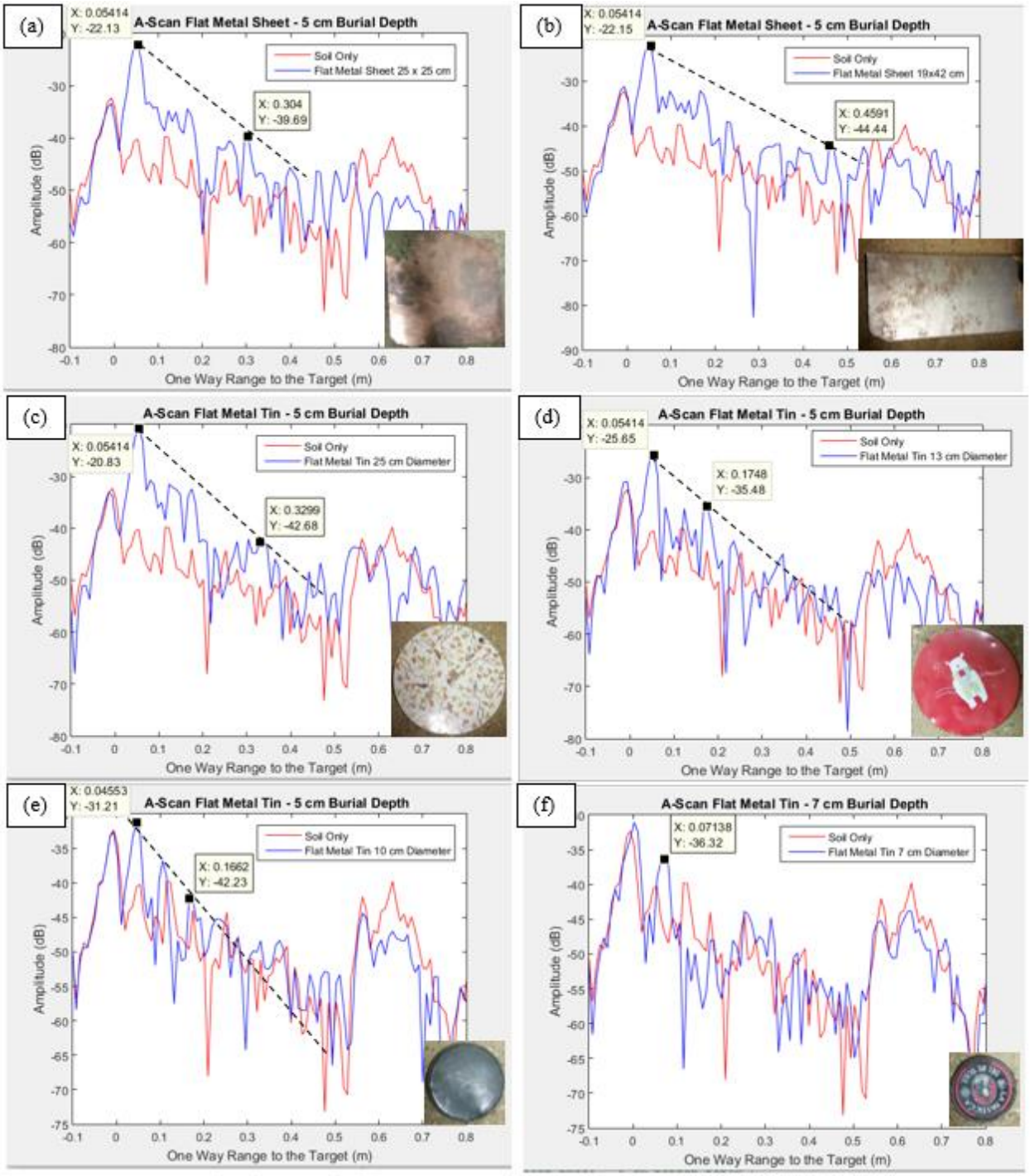

Figure 7-19: A-scan measurements and length feature prediction of various metal targets

7.5.7 Comparison of various Antenna Performances

Examples of dispersive and non-dispersive antennas that have been used in GPRs are summarised in Chapter 5. The performance of the proposed antenna is compared against a commercially available Archimedean spiral and a Quad ridge horn antenna. The Archimedean antenna operates between 1 to 4 GHz. The Quad ridge horn antenna operates between 0.8 GHz to 12 GHz. Figure 7.20 shows the results for two set of A-scan measurements for a 5 cm buried flat metal target under a dry sandy soil. The antennas are held at a height of 2 cm above the soil, and a trace of range profile from the radar data is constructed. In Figure 7.20 (a), all three antennas are operated from 1 to 4 GHz. The soil interface and the target peaks are visible. The signal to clutter ratio for these two peaks is measured as 8.6 dB for the spiral antenna, 8.1 dB for the quad-ridge antenna and 6 dB for the proposed antenna. This proposed antenna performance in terms of signal to noise ratio is not far off from the two commercial antennas and shows similar behaviour in the range profile. However, when the full band of the proposed antenna is used (0.5 GHz to 5.5 GHz, band 1), the range profile for the buried flat target shows extra information. This is shown in Figure 7.20 (b). The quad-ridge antenna is operated from 0.8 GHz to 5.5 GHz and spiral antenna from 1 to 4 GHz.

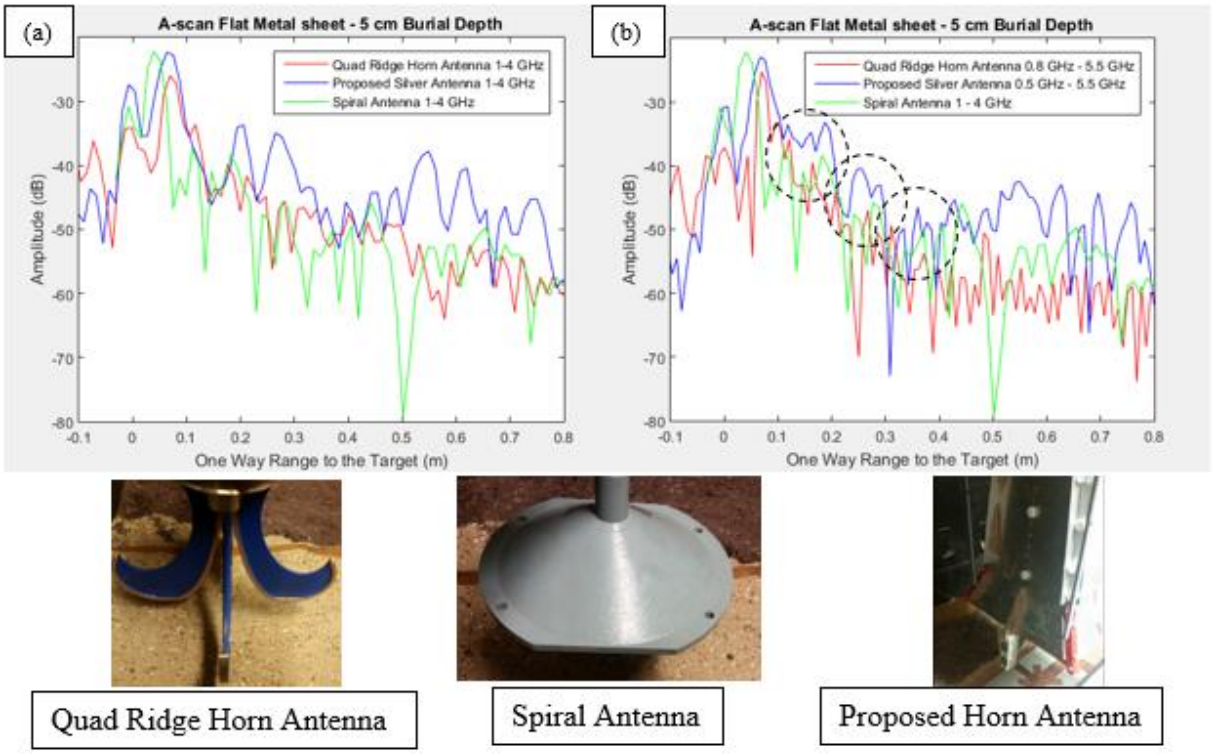

Figure 7-20: A-scan of buried metal sheet from various antennas operating at the same frequency band (a) and individual operating bands (b)

7.6 Outdoor GPR Measurements

The performance of the proposed antenna and the GPR system is measured in a different soil material, and the results are shown in the following sections. The soil environment is a dry sandy soil with different dielectric properties to that of the one in the lab. The sand pit is located at Cranfield University - MoD site. Figure 7.21 shows the layout of the sand pit and the map of targets with various sizes, shapes, and materials. These targets include electronic switches, mortar shells, strand wires, battery pack and main charges.

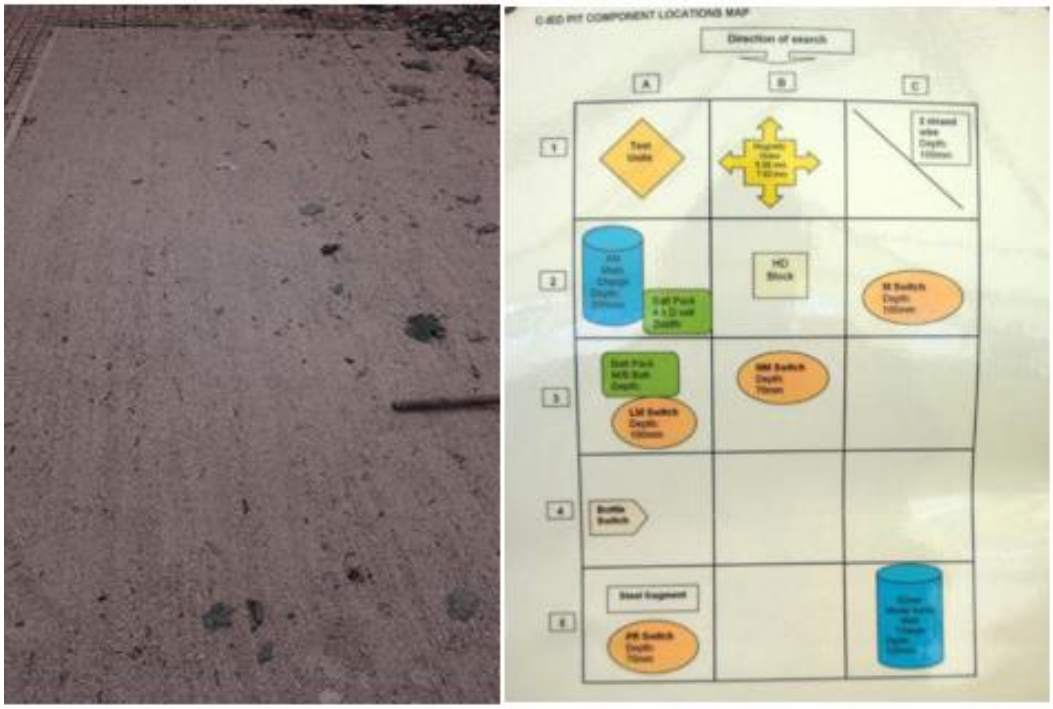

Figure 7-21: The sand pit at Cranfield University and the map of various buried targets in the sand pit

The GPR setup is shown in Fig. 7.22 (a). The GPR and the scanning platform are positioned across two adjacent sections of the sand pit. The antenna can cover a distance of 80 cm. The sampling step where the traces are recorded is varied for different experiments. The antenna is operated from Band 1 (0.5 GHz – 5.5 GHz) and Band 2 (2.5 GHz – 6 GHz, H-Pol) channels. The same channels are used to transmit and receive the radar data, i.e. Band 1 corresponds to VV (Vertical polarisation transmit, Vertical polarisation receive) and Band 2 to HH (Horizontal polarisation transmit, Horizontal polarisation receive). The targets are the real VS-50 and PFM-1 landmines (courtesy of Cranfield University) and the 3D printed VS-50, PMA-2, PMN-2 and the PFM-1 landmines.

These are shown in Figure 7.22 (b). In addition to these targets, a buried mortar shell in the sand pit is also measured.

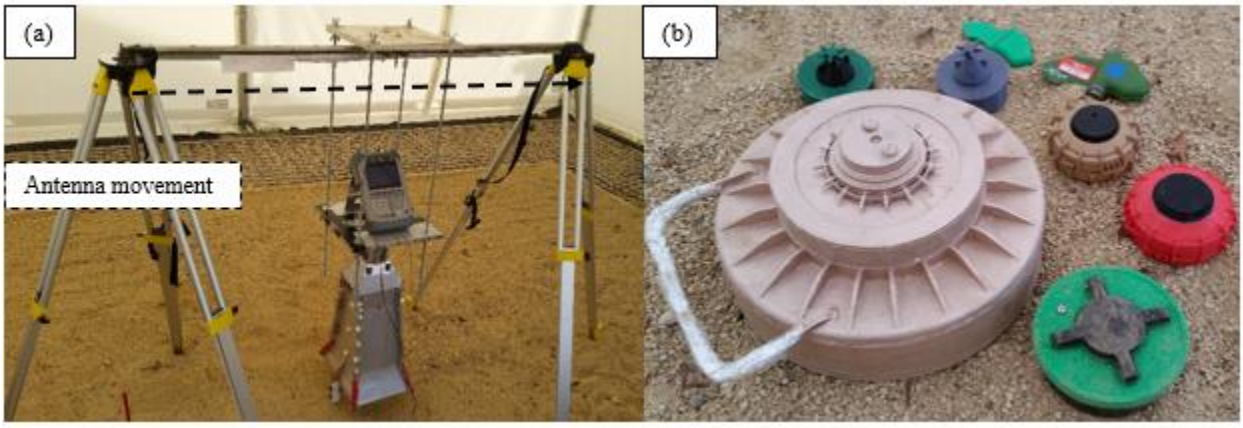

Figure 7-22: GPR measurement setup and the landmine targets

7.6.1 System Calibration

The radar is calibrated from 0.5 GHz to 5.5 GHz. The experimental measurements for the calibration techniques as discussed before, consists of taking two A–scan traces, one from a metal sheet laid on the surface and one without the metal sheet (soil only). This is shown in Figure 7.23 (a). The main calibration measurements are the antenna offset and the location of the bottom of the sand pit. The relative permittivity value of the sand material is measured by a dielectric probe technique described in Chapter 4. Figure 7.23 (b) shows the A–scans for metal sheet and soil only. The radar output power was measured as -18 dB. The return power level from the metal sheet was measured as -19 dB. The return power level from the soil surface (without the metal sheet) was measured around -32 dB. This suggests that -14 dB is penetrated into the ground. The power level of the two-way return signal from the bottom of the box is around -57 dB. Therefore the two-way attenuation for the distance between the soil interface and the bottom of the sand pit is around -43 dB, taking into account -14 dB input power into the soil and -57 dB return power. The depth of the sand pit is calculated as the difference in the distance from the soil interface to the peak corresponding to the bottom of the sand pit, divided by the square root of the relative permittivity. The bottom of the box, taking a relative permittivity of 2.3, appears at 1.5 metres below the soil interface. It is also noted that the damping line for the soil appears to be longer that the metal sheet.

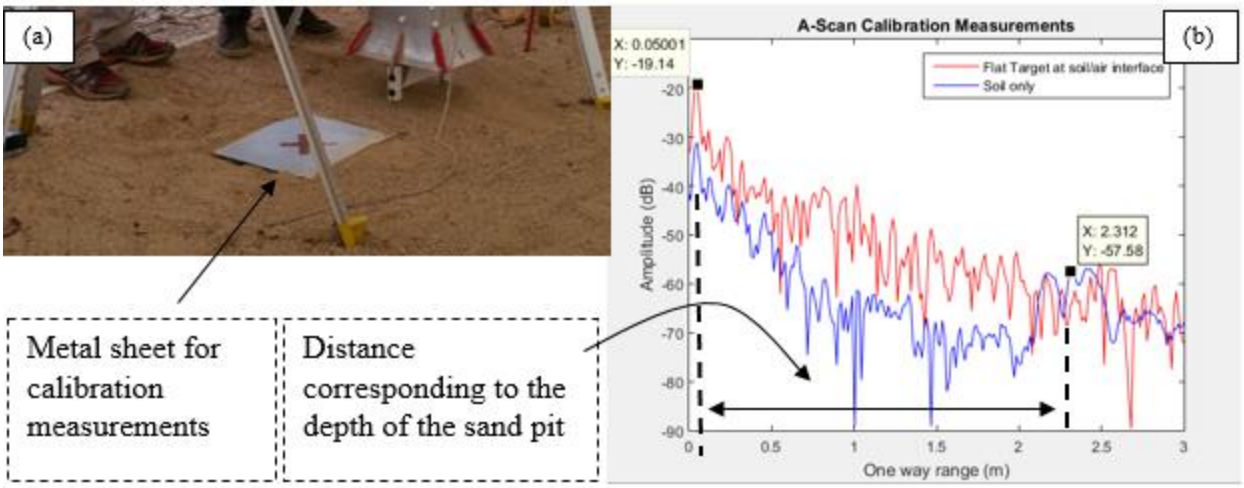

Figure 7-23: Calibration measurements (a) and the A-scans of metal sheet and soil only (b)

7.6.2 Dry Sandy Soil Pit – Band 1 and Band 2

The section under the test where the landmines are placed is first measured without any targets. Figure 7.24 shows the images of the B-scan radar data for the sand pit across 80 cm. The radar data is recorded in a 2 cm step. The measurements are performed by Band 1 and Band 2 simultaneously. Appropriate signal processing is performed to filter out the undesired frequencies according to the range of the frequency band 2.

Figure 7.25 (a) shows the image taken from Band 1 (0.5 GHz to 5.5 GHz) on a vertical polarisation (e.g. VV) and Figure 7.24 (b) is the image from Band 2 (2.5 GHz to 6 GHz) on a horizontal polarisation (e.g. HH). The image from band 1 shows a strong indication of the soil interface with the bottom of the box clearly visible. The non-linearity of the soil geometry across the area is also noted. In contrast, the image from band 2 does not show the bottom of the box. However, there are fewer reflections from the soil interface. This suggests that the polarisation has an impact on the soil properties, and the image acquired present different behaviour. The range profile data of all traces for the entire cross range has been shown in a 3D plot at the bottom of the figure.

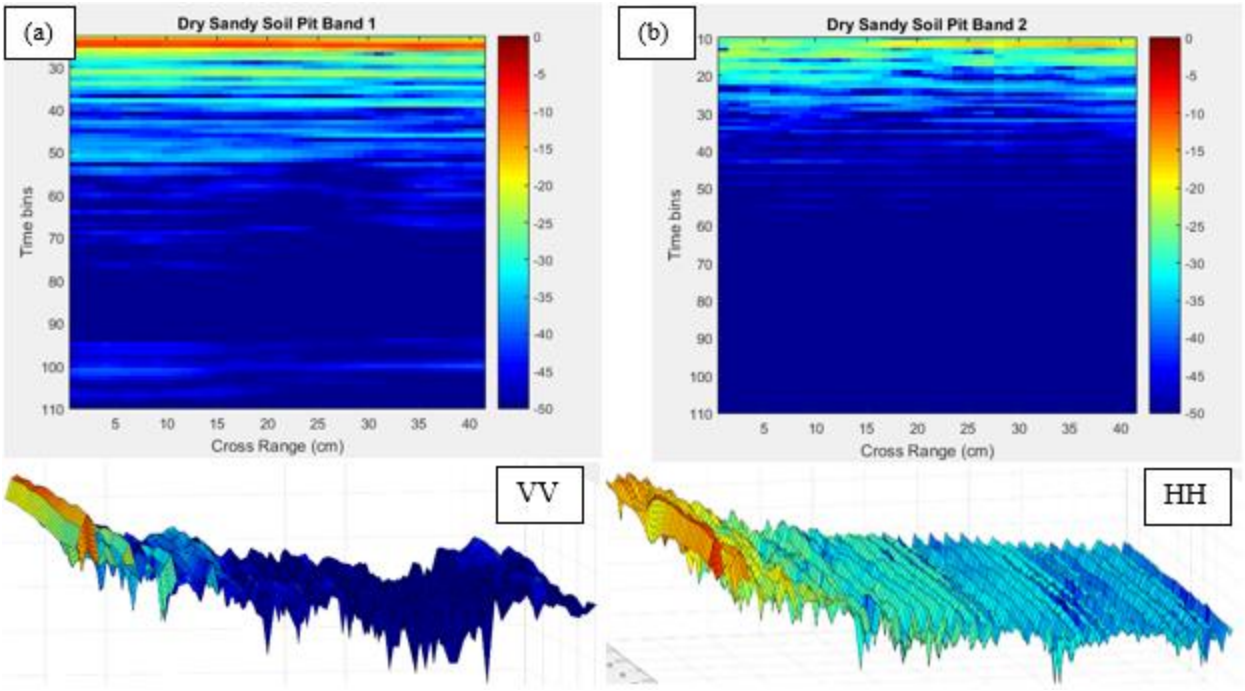

Figure 7-24: Dry Sandy Soil from Band 1 (0.5 GHz – 5.5 GHz, VV) and Band 2 (2.5 Hz – 6 GHz, HH)

7.6.3 TMRP-6 AV Landmine - Band 1 and Band 2

Figure 7.25 shows the measurement setup for the TMRP-6 AV landmine. The landmine is buried in the middle of the scanning line at the depth of 6 cm. The antenna is positioned at a distance of 5 cm above the soil interface and is oriented in vertical polarisation (e.g. in the same direction of the antenna movement). The B-scan measurements across the line marked by the arrow are then performed from Band 1 and Band 2 channels simultaneously. The radar is moved across 80 cm, and the data is recorded in a 2 cm step.

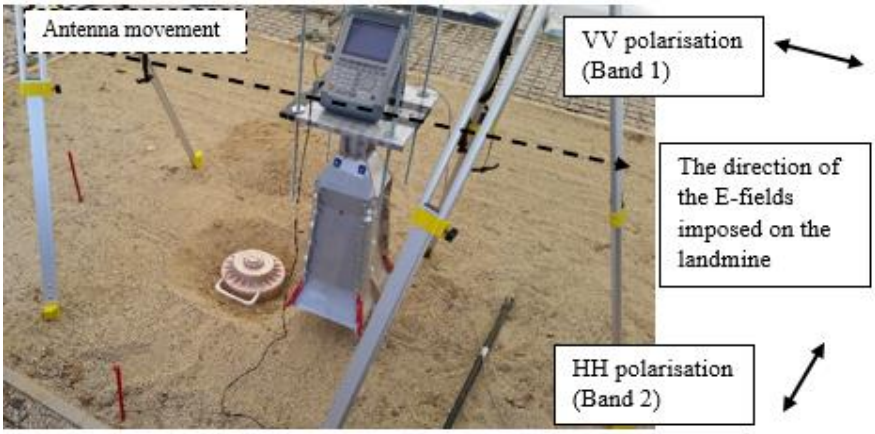

Figure 7-25: The GPR measurements of the TMRP-6 landmine buried at 6 cm in dry sandy soil

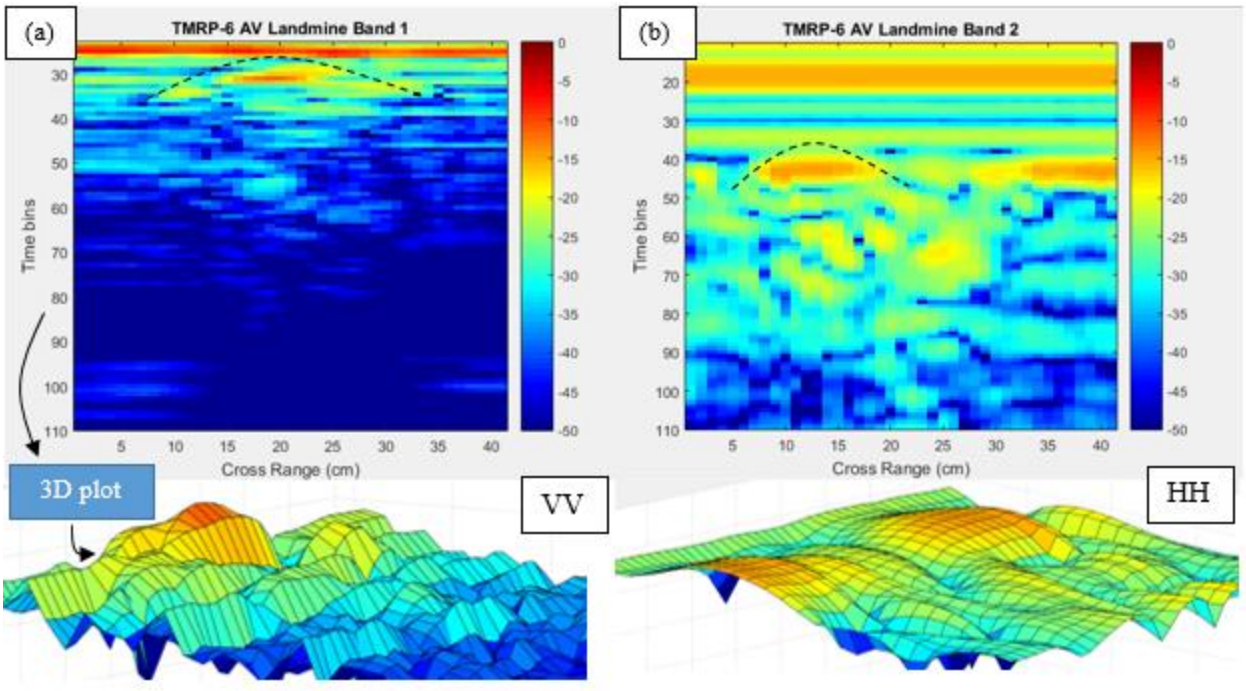

Figure 7-26: TMRP-6 AV Landmine from Band 1 (0.5 GHz – 5.5 GHz, VV) and Band 2 (2.5 Hz – 6 GHz, HH)

Figure 7.26 (a) shows the image for the TMRP-6 AV landmine from Band 1. The main body of the landmine is visible, and it reveals a hyperbola shape. The diameter of the landmine can be estimated from the cross range. In comparison to the image with no target (Figure 7.24 - a), there are reflections noted below the landmine that is known to be the late-time responses. The landmine image in band 1 suggests particular characteristics where most of the reflected signals tend to have been detected from the centre of the main body. There does not seem to be any indication of the handle of the landmine. The landmine handle is oriented perpendicular to this band as shown in Figure 7.25. In contrast, the image for the landmine from band 2 indicates multiple late-time responses which could indicate reflections from different parts of the landmine body. The main body of the landmine is noted with a slight offset in the location where it should appear due to the offset off the boresight for the radiation pattern of this band. The surf plot of the landmine suggests most of the reflected signals tend to have been collected from the direction aligned with the *H*-plane. Therefore, the asymmetrical pattern appearing in the image is likely to be caused by the handle of the landmine. The surf plot is a plot function in MATLAB that creates a 3D shaded surface from the z components in matrix z, using $x = 1:n$ and $y = 1:m$, where `[m,n] = size(z)`. The height, z, is a single-valued function defined over a geometrically rectangular

grid. Z specifies the colour data, as well as surface height, so colour is proportional to surface height (*MathWorks, 2016*)

7.6.4 Mortar Shell – Band 1

The deactivated mortar shell buried at 6 cm in the sand is measured in the band 0.5 GHz to 5.5 GHz. The measurement area is scanned across 60 cm, and the radar data is recorded in a 2 cm step. The mortar shell is 82 mm in diameter and 35 cm in length. Figure 7.27 (a) shows the mortar shell geometry. The antenna (band 1 – VV) is oriented in the same direction as the longest dimension of the mortar shell. Figure 7.28 (b) shows the image obtained from the radar data. The linear pattern across the cross range in the image is noted, and the dimension of the mortar can be estimated. The shape of the mortar shell consists of a tapered cone profile with the smallest diameter on the left-hand side of the Figure 7.27 (a).

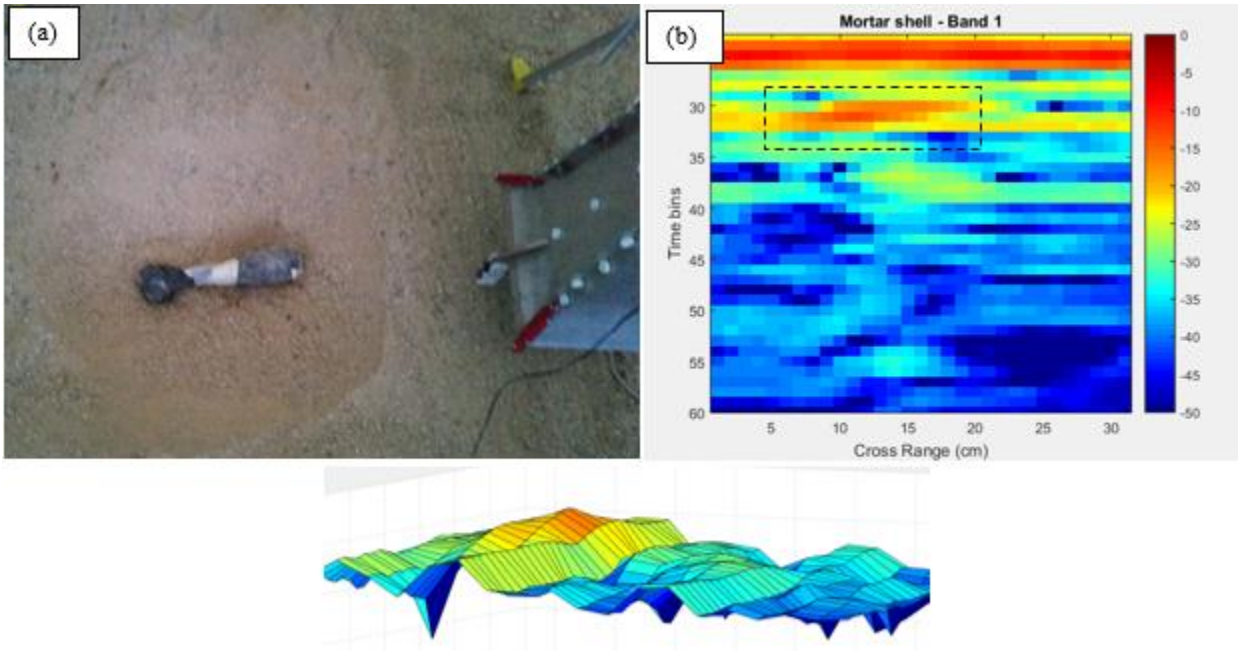

Figure 7-27: GPR measurements of Mortar shell buried at 6 cm in dry sandy soil from Band 1 (0.5 GHz – 5.5 GHz, VV)

7.6.5 Surface Roughness – Band 1

Detailed structural interpretation can be important for determining soil and bedrock characteristics in the shallow subsurface. It is reported that the effective dielectric constant of an inhomogeneous medium can be increased depending on its distribution. (*Chylek and Srivastava, 1983*). This suggests that when the medium is not homogeneous, stronger EM waves can be reflected by the soil. This condition is often found in minefields, and it causes strong clutter. In an experiment to

observe this from a medium with a dry sandy soil material, the test area is dug, and an uneven surface is introduced. The radar is moved across an area of 90 cm, and the radar traces are recorded in a 10 cm step. Figure 7.28 (a) shows the layout of the surface of the sand. Figure 7.28 (b) shows the resulting radar image measured in Band 1. The unevenness of the sand is clearly visible. Moreover, the bottom of the box is less highlighted, and this could be resultant of high attenuation introduced by the densely packed and inhomogeneous sand surface. The roughness level of the sand could also contribute to signal scattering, resulting in less amount of energy reflected back towards the radar. In order to examine this effect further, smaller step size should be used.

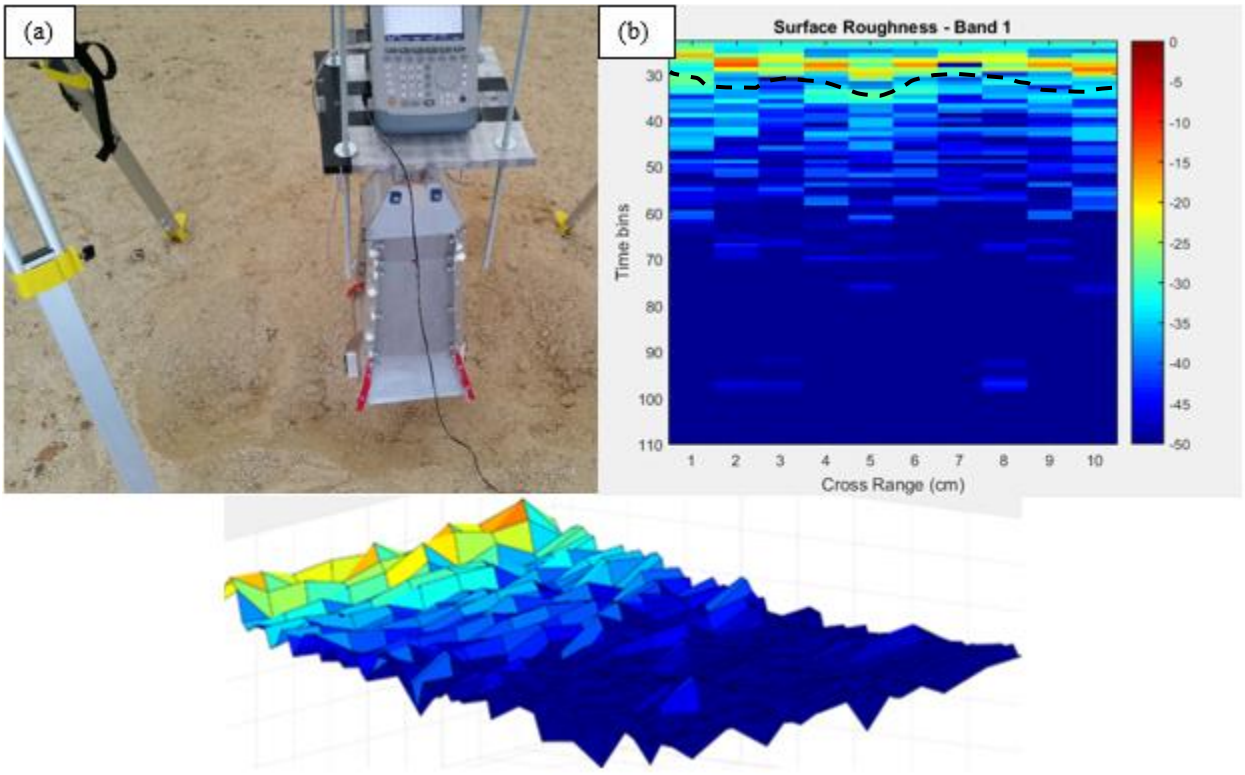

Figure 7-28: GPR measurements of dry sandy soil with a rough surface

7.6.6 Multi-Parameter GPR Environment – Band 1

In order to create a more realistic minefield scenario, the test environment was constructed to include various environmental conditions. These conditions were combined with multiple landmines of different types. Following summarises the environmental and buried target conditions:

- AP and AV landmines in close proximity
- Two AP landmines in close proximity
- Various burial depths
- Surface roughness
- Different attitudes of landmine (e.g. horizontal or vertical)
- Various sizes of landmines

Figure 7.29 shows the layout of the GPR environment. The landmine targets include a TMRP-6 AV landmine, a real VS-50 landmine, a 3D printed PMA-2 landmine, a mortar shell and a 3D printed PMN-2 landmine. These landmines are buried at 1 cm, 3 cm, 2 cm, 2 cm and 2 cm respectively. These are shown in the Figure 7.29 (a) from left to right.

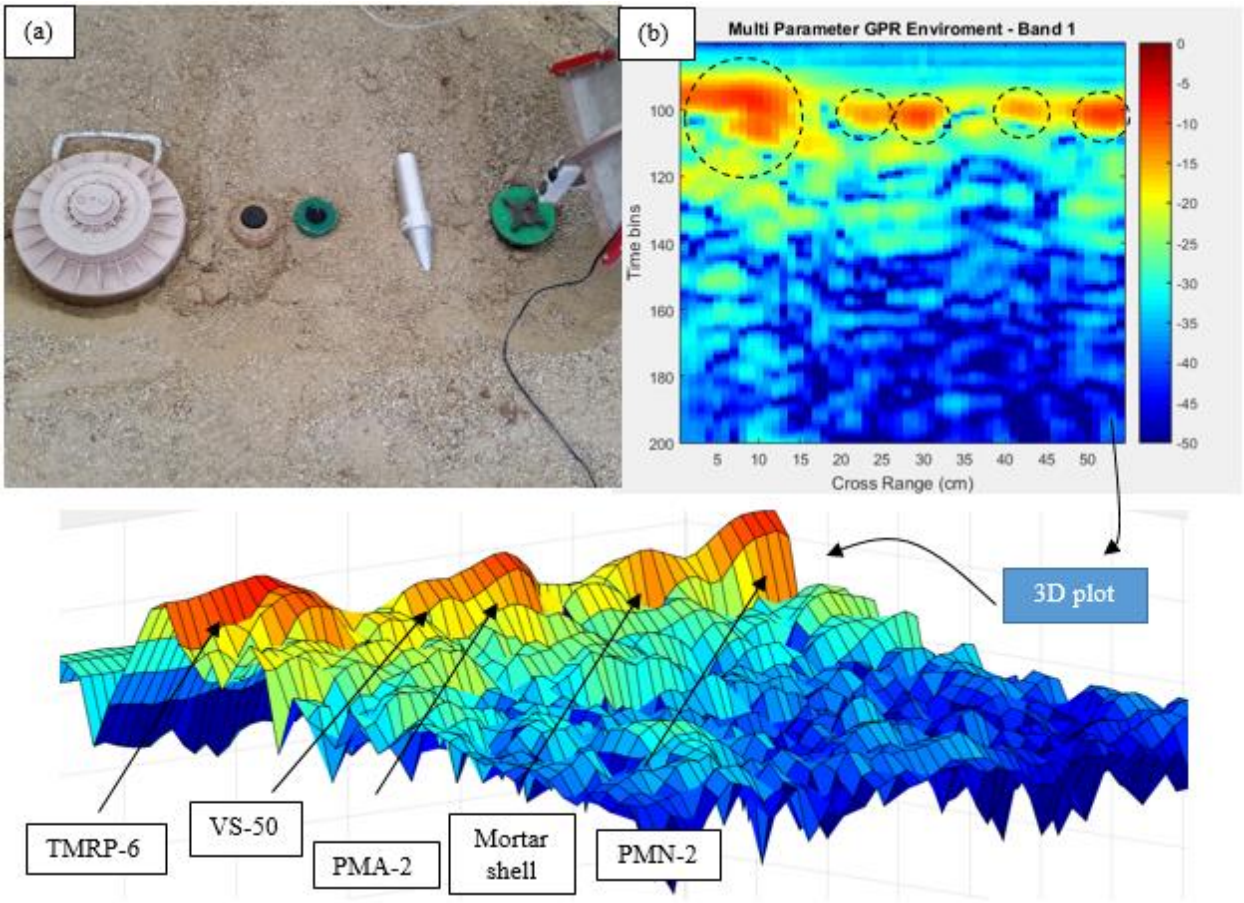

Figure 7-29: GPR measurements of a multi-parameter environment

Figure 7.29 (b) shows the image obtained by the radar that is moved 106 cm across the test environment. The radar traces were recorded in a step of 2 cm. The highest reflections from the

TMRP-6 landmine is evident. The peaks from the two AP landmines in the middle are to some extent apart from each other, enough to interpret them as two separate peaks. The distance between these two AP landmines is 3 cm. This suggests that narrower frequency band than band 1, will result in no distinguishing of these two peaks from each other as they will coincide. The reflection from the mortar shell, despite the perpendicular orientation to the vertical polarisation of the antenna from band 1 is noted. However, this reflection corresponds to the width of the mortar shell and only with an image obtained from a different polarisation it can be classified as a mortar shell. The PMN-2 landmine is contributed quite strong reflections and therefore it is evidently visible.

7.7 Summary

This chapter has introduced the GPR system that is used to collect experimental measurements from the buried landmines in various environmental conditions. The radar is a VNA based, SFCW type that can operate up to 8 GHz. Two types of VNA based radar systems are investigated. In addition, the effect of various radar systems parameters such as RBW, attenuation level, sampling points, and averaging methods on the GPR performance are evaluated. In order to test the proposed antenna in a realistic environment, a sandbox is constructed. The sandbox contains four types of materials including, dry sandy soil, dry loamy soil, beach sand and pebbles. Careful design of the box is considered to minimise unwanted reflections as well as providing calibration measurements. There are significant differences between most of the lab test sites used for landmine testing and real field conditions. Efforts are made to ensure the test lab environment included some degrees of actual real minefields. This included various ground materials and adequate depth. Model landmine targets that are described in Chapter 3, were fabricated using 3D printers. The material that is used to print these landmine has a relative permittivity close to that of the casing of the real landmines.

Two sets of GPR measurements are conducted, one in the lab at UCL and one in a sand pit at Cranfield University. The main aim of the measurements is to investigate the diversity of the signatures that the landmines show under various system parameters such as frequency, polarisation, illuminated footprint, ground clearance, etc. The proposed multifunctional antenna that is described in Chapter 5 is used to conduct the GPR experiments. Basic signal processing techniques are employed to construct radar images of various landmine targets. This chapter has provided examples of radar images that show, buried landmine can provide different signatures

under various system parameters. These system parameters are addressed as Band 1, Band 2 and Band 3. The results from one particular band show that some of the images contain much more information than others. The differences in the images from the same landmine show different features being highlighted under favourable environmental conditions. However, the increased information also entailed an increase in clutter. This chapter has also considered some of the issues that can give rise to false targets such as densely packed sand material as well as surface roughness.

Finally, this chapter has shown that the proposed antenna can provide adequate performance in detecting landmine targets under various environmental conditions.

7.8 References

Agilent. (2000). *Understanding and Improving Network Analyzer Dynamic Range*. Application Note [Online] Available from: http://cp.literature.agilent.com/litweb/pdf/5980-2778EN.pdf

Chen, C.C, Higgins, M.B, O'Neill, K. and Detsch, R. (2001). *Ultrawide-Bandwidth Fully-Polarimetric Ground Penetrating Radar Classification of Subsurface Unexploded Ordnance*. IEEE Transactions on Geoscience and Remote Sensing, Vol. 39, NO. 6.

Chylek, P., and Srivastava, V. (1983). *Dielectric constant of a composite inhomogeneous medium*. Physical Review B covering condensed matter and materials physics, Phys. Rev. B 27, 5098.

MathsWorks. (2016). *2D and 3D plots*. [Online] Available from: http://uk.mathworks.com/help/matlab/2-and-3d-plots.html

Nicolaescu I., Genderen P.V., Dongen K.W, Heijenoort J.V, Hakkaart P. (2003). *Stepped Frequency Continuous Wave Radar- Data Prepossessing*. 2nd International Workshop on Advanced GPR, the Netherlands.

Chapter 8

Ethics, Research, and Security

8.1 Introduction

This guide aims to set out the standards of performance and conduct expected of all those engaged in research and governance of detection and clearance of landmines and other types explosives devices (e.g. Improvised Explosive Devices and Unexploded Ordnances). The primary evaluation of the guide emphasises on identifying the associated ethical issues and concerns, analysing the level of risk and the ethical issues that might underlie those concerns and to respond effectively to those concerns.

The key elements of good professional judgment that form an engineer's professional ability and for those who are working in demanding roles and making important decisions based on a very wide range of different kinds of information are, prudently prioritising the ethical issues that have the most impact to stakeholders and value the possibility of such issues happening. The discussions below are intended as suggestions for possible actions that bear on an engineer's ethical responsibilities and the extent to which governments or other organisations should be taking into account.

There are over 100 million undetected terrestrial landmines scattered in approximately 70 countries including Europe. 70 people are injured every day of which 90% of the victims are civilians. There are emerging threats from more sophisticated explosive devices such as Improvised Explosive Devices (IEDs) and Unexploded Ordnance (UXOs), which tend to diminish the entire fabric of society. The overall political and legal framework covered by several treaties and conventions emphasise in eliminating landmines including IEDs and UXOs around the world. Therefore, a global effort in a multidisciplinary manner is required to address this issue. This ranges from improving a quality of the information on the threat and its impact, developing new survey and clearance procedures and deploying better equipment including improved sensors and detection techniques.

A new generation of electromagnetic sensors synthesises Ground Penetrating Radar (GPR) systems mounted on low flying Unmanned Aerial Vehicles (UAVs) for a remote contactless sensing in aggressive media as well as rapid and mobile surveying. The intended GPR system is

to operate adaptively to cope with the hostile environments in which some of the landmines are buried. This is achieved by designing and implementing smart and reconfigurable antennas that can accommodate adaptive radar systems.

One of the main activities of engineers is the design and implementation of technical products that act as a frontier to the problems we encounter. “Engineers invent the future, and their work affects the lives of millions of people, for better or worse. That raises enormous ethical issues in every branch of engineering, from computing through biotechnology and energy to civil and aeronautical”, engineering ethics in practice survey. There are two fundamental problems in identifying the ethical standards we are to follow, on what do we base our ethical standards and how do these standards get applied to the specific situations we face *(RAE, 2014)* The ethical frameworks that will be followed are based on the Statement of Ethical Principles (SEP) developed by The Royal Academy of Engineering in conjunction with the Engineering Council and a number of the leading professional engineering institutions (e.g. IEEE, IISP …). The four principles set out in the SEP are:

- Accuracy and rigour
- Honesty and integrity
- Respect for life, law, and the public good
- Responsible leadership including listening and informing

These four fundamental principles will be used for the ethical analysis and evaluation of the research that concerns the detection and clearance of landmines. Some of these principles address specific professions or those that have a stronger role to play in making judgments, working with new technologies and giving advice.

8.2 Engineering Standards

The first principle stated in SEP is accuracy and rigour which in general terms describes the accuracy of the knowledge that is relevant to the line of work in service of others. United Nations stated the 99.6% level of detection and clearance in landmine-contaminated areas as a standard for demining operations. Meeting this standard with current technologies and demining products that are provided to demining organisations require accurate and reliable detection. The contribution in capability and reliability of many methods and procedures are still in the process of testing, validation, and improvement *(Krstelj and Stepanic, 1999)*.

As a multidisciplinary field, the non-destructive detection and clearance of landmines benefit from capabilities that are developed in many other fields of science and technology leading to methods, techniques and instruments with greater sensitivity and higher accuracy. However, the applicability to complex materials and structures, realistic minefields and problems related to demining operations raise an issue of how accurate are these technologies. Highly motivated field teams under pressure to tackle the mine detection problem as soon as possible, often use unproven methods which may cause great material damage and in the worst case loss of life. It took 1 billion dollars to clean up the landmines that were left as a result of the recent conflict in Iraq and 90 people lost their lives in that demining effort due to the poorly equipped and inaccurate technology *(GICHD, 2014)*. Loss of life is not the only consequence of inaccuracies; there are also significant economic costs as well. For brave humanitarian and military demining personnel fortunate enough to survive, the cost is often in the form of expensive medical bills which can cost anywhere from 100 – 2000 pounds.

Accepting the reality that no single method can provide highly accurate systems, efforts should be made to integrate several methods to form a multi-sensor system that would take advantage of the complementary capabilities. It offers the better probability of detection and increases the functionality as well. The selected methods and inspection requirements depend on the inspected conditions, site-scan accessibility and characteristics of the part under examination. It must not be forgotten that implementation of demining methods in any field needs a general compliance of all system requirements i.e. systematic approach in transfer regarding demining operations and necessary system reliability assurance.

8.3 Ethics

The set of principles defined by SEP regarding the respect for life, law, and public good is rather the broadest of the four and arguably the one that covers the ethical issues most commonly associated with engineering ethics. The principle of safety of others is so central to engineering, but this set of principles is not limited to health and safety and also covers respect for the law and respect for the natural environment. The Ottawa Treaty that states "Convention on the Prohibition of the Use, Stockpiling, Production and Transfer of Anti-Personnel Mines and their Destruction" opened for signature in Ottawa on December 3, 1997. The two general obligations that this treaty takes the form of are, never under any circumstances to use, develop, produce, acquire, stockpile, retain or transfer APMs to anyone, directly or indirectly. And to destroy or ensure the destruction of all APMs, stockpiled or in mined areas *(UN, 2012)*. There is a list of states that have signed and ratified to the Ottawa Treaty (also known as the Mine Ban Treaty). The treaty came into force and closed for signature on March 1, 1999, with the ratification by 40 states including the United Kingdom and Germany. Since then, states that did not sign the treaty can now only accede to it. Currently, 160 states have ratified or acceded to the treaty, and two states have signed the treaty but not ratified it, and there are still 34 non-signatory states including the United States, China, and Egypt, who alone have one-quarter of the world's landmines buried in its deserts, most leftover from the Second World War. The approval of the treaty has not been worldwide, and most landmine production and incidents occur in countries that do not currently intend to ratify the treaty *(ICBL 2014)*.The ethical issues concern the danger to health and safety by these inhuman weapons that are indiscriminate activated by its many victims, whether civilians or combatants, on whom it causes superfluous injury and unnecessary suffering, often intended to maim rather than to kill. The problem is even more complicated when other types of explosives devices are considered. The Ottawa treaty does not cover all types of unexploded ordnance, Cluster bombs, for example, introduce the same problem as mines and they can also remain a hazard for civilians as well as animals long after a conflict has ended. There is a need for more effective treaties and conventions with pressure on states to adhere and its adoption globally.

Opponents of the treaty make several points that the mines are a cheap therefore cost effective way of defence. But the fact that landmines suffer from the ability to distinguish between targets make these points inadequate. In theory, landmines could be replaced by manually triggered claymore mines. The next generation of smart mines could be developed to self-destruct or self-deactivate

at the end of a conflict and designed to re-deploy themselves if its neighbours detonate or are removed *(DefenceTech, 2015)*. They could even incorporate sensory systems to recognise their targets reducing non-combatant and civilian injury. These technological advances also reflect the first set of principles by SEP, the accuracy, and rigour for if there are failures, lives of innocent victims will be at risk.

Under the principles of responsible leadership, the SEP encourages professional engineers to aspire high standards of leadership in the exploitation and management of technology. They are expected to demonstrate that they are seeking to serve wider society and to be sensitive to public concerns. The ethical considerations regarding the landmines concern perhaps the extent to which professional engineering organisations should be funding research into mine-clearing and funding mine-clearance programmes. One example of this is Egypt's allocation of funds and its limitation and insufficient resources when looking at the problem of landmines and UXOs laid throughout the country. In February 2000, Egypt announced that mine clearance had stopped due to a shortage of funds. In Albania where 2,700 cluster bombs were reported to have cleared by September 2000, The Swiss Foundation for Mine Action was ceased in 2004 due to lack of funds *(LM, 2008)*. These countries have asked for the help from those who are responsible for planting the mines in the form of funds or detection technologies. It may be acceptable for any individual engineer to choose not to be involved in political debate and high-profile policy issues; however there is a specific interpretation of leadership in the common code of practice and SEP. There is a duty that engineers have to be responsible leaders where they realize worldwide issues in need of solutions. Professional engineers should "be aware of the issues that engineering and technology raise for society, and listen to the aspirations and concerns of others." Engineering institutes, professional engineers with demanding roles and governments should remain committed to funding research and projects in mine clearance for nations that are heavily affected.

8.4 Summary

This guide has identified the ethical issues concerning the landmine detection and clearance. They are 1) accuracy of landmine clearing technologies 2) the need for non-signatory nations to follow landmine banning treaties and conventions. The guide has also tried to provide an ethical analysis within a framework set by the Statement of Ethical Principles (SEP) and where appropriate suggestions of possible actions to diminish the risks are considered.

8.5 References

GICHD. (2006). *Guidebook on Detection Technologies and Systems for Humanitarian Demining*. [Online] Available from: http://www.gichd.org/fileadmin/GICHDresources/recdocuments/Guidebook_Detection_2006.pdf [Accessed: 1st May 2015]

ICBL. (2015). *International to campaign ban landmines*. [Online] Available from: http://www.icbl.org/en-gb/home.aspx [Accessed: 20th June 2015]

The Royal Academy of Engineering. (2014). *Engineering Ethics in Practice.* [Online] Available from http://www.raeng.org.uk/societygov/engineeringethics/principles.htm

Krstelj, V., Stepanic J. (1999). *Non Destructive Testing in antipersonnel landmine detection*. Proceedings, International Conference; MATEST.

United Nations Treaty Collection. (2012). *Convention on the Prohibition of the Use, Stockpiling, Production and Transfer of Anti-Personnel Mines and on their Destruction*. [Online] Available from: https://treaties.un.org/pages/ViewDetails.aspx?src=TREATY&mtdsg_no=XXVI5&chapter=26&lang=en

DefenceTech. (2015). *Smart and Deadly: The New Breed of Smart Mines.* [Online] available from: http://www.military.com/soldiertech/0,14632,Soldiertech_Mines,,00.html

Landmine Monitor Fact Sheet. (2008). *Cluster Munition Contamination and Clearance.* [Online] Available from: http://www.themonitor.org/media/1774873/LM08_Cluster_Contamination_Clearance.pdf

Chapter 9

Conclusion and Future Work

9.1 Conclusion

Landmine detection and clearance represents a serious problem facing humanity today. The statistics and the nature of the problem have been discussed. Seventy countries are affected by landmines. 70 million landmines remain in the ground, and they have been identified as deadly threats to both physical security and development. Different types of landmine have been introduced and the environment and conditions these landmines are likely to be found have been shown. Having identified the severity of the problem, Chapter 1 goes on to describe different detection techniques, drawing the attention to the fact that no single method will be reliable enough to provide a complete solution by itself. Disadvantages and advantages of some of the current detection technologies have been listed and the need for a multi-sensor platform has been explained. It has also been discussed that the detection and removal systems take two distinct types; Military and Humanitarian. The military demining requirements are to breach the minefield quickly in order to create a safe path for the troops. Therefore only the lanes that the troops are planned to advance get cleared at a rapid pace. This method of landmine clearance is quicker but less exacting and often involve mass disturbance and damage to the land using carpet bombing or burning of the land. In contrast, it was elaborated that the humanitarian deeming involves precise detection and removal of all landmines in the land so the land may return to its normal use. The need for a reliable and affordable system have led to research and investigation into all fields of engineering. It was discussed that as a result of decades of research, GPR shows a promising solution. The literature review in Chapter 1 has provided the baseline for GPR technology to be evaluated in order to inform the research carried out during this study.

Ground Penetrating Radar can be one of the most challenging measurement techniques, but also one of the most rewarding and promising technologies, as it can map what is buried in the ground in three dimensions. Conditions, although, must be conducive for EM waves propagation in the ground, features must be distinct enough to be differentiated from propagating medium or soil, and at the depth that can be resolved within hardware capability. For all these variables to be met, the target and its environment which it is found must be studied so that the EM characteristics

within the ground can be correctly interpreted. In addition, an understanding of how reflections from targets are created and how acquisition and processing steps can enhance, or sometimes obscure these reflections is crucial.

The research work which has been presented in this thesis has introduced systematic investigation of GPR. It is supposed to be utilised for the detection of buried nonmetallic AP and metallic AV landmines. Chapter 2 considers the principle of operation of GPR systems. It then introduces the nature of EM propagation in GPR and the environmental conditions that affect it. Burial depth of the landmines, their size, shape and material and geological conditions they are buried have been discussed and identified as major parameters to consider when designing GPR systems. Different type of radar architectures have been discussed, and their advantages and disadvantages have been noted. Radiated power, penetration depth, side-lobe suppression, data acquisition time and scanning, hardware complexity, cost, etc., are the important factors in deciding the adequate radar system for a particular GPR application. Various visualisation and interpretation of GPR data have been introduced. Most common form of GPR data representation is B-scan. Chapter 2 considers the resolution provided by GPR as a function of system parameters, which makes the case for some of the vital parameters such as bandwidth and polarisation. The bandwidth of at least 5 GHz is needed to resolve features that are 3 cm apart in down range as well as cross range. Different type of resolution in GPR have been discussed, and their definitions have been defined. Finally, Chapter 2, draws the main design stages of the GPR systems. These include modelling techniques, material characterization, antenna design, radar design and signal processing.

3D EM field simulation package CST Microwave Studio (MWS) has been used to study the GPR environment and its parameters, namely, the wave propagation, path losses, scattering properties of typical AP and AV landmines, their return signal levels, and RCS patterns. The definition of electromagnetic soil parameter in the simulation of the GPR has been addressed, and the implementation of realistic physical soil properties such as the structure and its dielectric properties have been discussed in Chapter 3. Real AP and AV landmines have been used in the GPR simulations and study of their scattering behaviour.

In order to create realistic models of GPR environment, the model data of the soil properties, and the landmine casing have been simulated using real and measured data. A laboratory technique has been introduced, and a list of materials have been tested to investigate their dielectric

properties. The dielectric properties of landmine casing show a relative permittivity in a range of 2.2 to 8 across a band of 2 to 8 GHz. The corresponding loss tangent is shown as 0.05 to 0.25. The relative permittivity of dry sandy soil has been measured and falls in a range of 2 to 2.5 and loamy soil from 2 to 3.

The main contribution of the work presented has been the antenna design. The considerations of the effect of the system parameters have led to the design of the multifunctional, UWB, dual polarised antenna. Important antenna parameters such as the bandwidth of operating frequencies, polarisation, and the radiation pattern have been taken into account right from the beginning of the investigation. UWB design techniques have been studied and utilised to achieve adequate performance. New design modifications and techniques were introduced to enhance the performance of standard horn antennas. These included tapered profile and aperture match structure of the ridges and the antenna aperture. Further modifications have been introduced to minimise unwanted backward radiation and surface current that appear at the back of the horn antennas. Novel cancellation techniques in the form of corrugated walls with integrated RAMs have been introduced.

The dual polarisation of the antenna is based on a new technique that has been introduced. It allows the antenna to accommodate multiple channels that can be operated simultaneously or independently. It has been shown how additional channels can be added that can operate at a band up to 8 GHz. The overall operating band of the antenna is shown to be from 0.5 GHz to 8 GHz. The antenna has four channels and each channel and has its own characteristics, regarding operating frequency band, polarisation, radiation beamwidth, and gain. The antenna has been fabricated, and its fabrication process has been discussed. Its measured performance compared with the predictions has shown a good agreement. However, fabrication inaccuracies, mainly surface roughness walls of the antenna has been identified to be the main reason for the slight discrepancies between the measured and simulated antenna performance at some frequencies.

The use of the proposed antenna and its purpose in multi-band radar for detection and classification of landmine targets have been demonstrated. In addition, a fully operational GPR system have been developed to collect series of data from lab and field test sites. Signal processing techniques have been developed to collect the data by the GPR system and represent them in the form of an image. The antenna has provided a good performance in GPR applications, capable of detecting plastic AP landmines and AV landmines in vigorous environmental conditions.

From the GPR images of landmines that have collected from experimental measurements, it is evident that some AP landmines under certain circumstances such as depth and terrain roughness show better reflectivity when the antenna is operated from a particular channel. However, this may result in additional clutter and false targets. Images obtained from other channels provide minimised clutter effect at a cost of lower quality target indication. Therefore, the data from all channels provide a best of both worlds and improve the landmine presence while minimising the presence of false targets and clutter. The following interpretation of the results can be drawn:

- AP and AV landmines have characteristic scattering properties and hence different signature.
- Different features of the AP or AV landmines are more highlighted under different system parameters such as operating frequency band, polarisation, and ground footprint.
- Frequencies up to 8 GHz show, additional information from the target such as geometrical features, internal structures (in the case of AP landmines).
- When operated at 0.5 GHz (band 1), the penetration depth is about 1.5 metres in dry sand
- The frequency range of 500 MHz to 5.5 GHz shows minimised multipath effect and late-time responses.
- The results from Band 1 suggests, the main body of the landmine is mostly reflected, with less multipath and late-time responses.
- The results from Band 2 suggest, high reflection from the soil can be mitigated, but lesser penetration depth can be achieved.
- The results from Band 3 suggest, more features of the landmine is reflected but at a cost of increased multipath and late-time responses.
- To successfully detect landmines in close proximity (e.g. 3 cm apart), a bandwidth of 5 GHz is desirable.
- To successfully classify asymmetrical targets such as mortar shell, dual polarisation data is needed.
- Antenna height from the ground can influence the detection performance.

In consideration of the current GPR technologies, four major objectives have been addressed and investigated in this thesis. Firstly, the 3D EM field simulation of complete GPR environment and understanding the fundamental system parameters, the soil structure and the scattering properties of the buried landmines. Secondly, the design of a multifunctional antenna that can provide diversity in the system parameters. Thirdly, the evaluation of the proposed antenna in GPR measurements. Lastly, multi-band imaging and investigation into signatures of the landmine under different frequency band, polarisation and radiation footprint.

9.2 Future Work and Extensions

The subject of GPR is vast and in order to successfully detect a landmine at high detection rate, every effort is made to ensure the reliability of the equipment and the validity of the radar data. This places a requirement for researchers and engineers to improve every aspect of the GPR, including modelling techniques, material characterisation, signal processing and RF hardware.

The preliminary GPR results shown, suggests a positive outcome experienced in the work described in this thesis and will encourage further field research. Successful detection of landmines from the proposed antenna is shown. However, the test sites and the measurements were performed under controlled conditions, and tolerances were set. Therefore, it is necessary to refine the tolerances and improve the reliability of the GPR images by considering more realistic situations. The first improvement considers a thorough evaluation of the model landmine targets that are used in the experiments. Efforts are made to arrange access to real landmines through collaboration with Cranfield University and other researchers in the field. This will allow a thorough examination of the real landmines in order to refine the model targets. An investigation into the filling of the landmine needs to be considered. In order to understand the electrical properties of high explosives, meetings have been arranged with explosive experts to find out more about the nature of the explosives and how it can be modelled for GPR uses. Adequate RF characterisation of materials also needs to be considered to realise a realistic casing for the model landmines. Flat position has been assumed for the landmines throughout the GPR experiments. In realistic situations as discussed, landmines may rotate and introduce different physical orientation to the radar. Therefore, polarimetric measurements and analysis will be performed to investigate the signatures of the landmines under different orientations.

In regards to material characterisation, Future work will include further dielectric measurements including techniques other than the one mentioned in this thesis. This will include the waveguide technique. The infill of the material and the surface geometry will also be investigated to find out their effects on dielectric properties measurement. This includes the air gaps inside the material and the surface roughness.

The second improvement considers the signal processing and GPR data interpretation. Basic signal processing techniques constructed the GPR results shown in this thesis. No further data processing techniques, detection or discrimination algorithms have been applied. In order to evaluate the concept of image diversity in GPRs, future algorithms will be investigated. This will include image superposition using image stitching or overlaying techniques.

The third improvement will be made by enhancing the capability and operational needs of the GPR system in field trials. In order to speed up the data acquisition of the radar system, a real time data capturing technique will be employed. This will include the communication of VNA to LabVIEW, and the data will be recorded and processed automatically.

The last improvement will address the limitations of the hardware that were imposed by the current radar system. Improvements can be made to increase the number of sampling points in the radar, the number of ports so additional antenna channels can be connected and increasing the upper frequency of operation to 13 GHz. These improvements will be part of a new, portable and compact SFCW radar.